University of South Bohemia in České Budějovice

Faculty of Science

Application of Electronic Continuum Correction to Molecular Simulations of Nano/Bio Interfaces

Ph.D. Thesis

MSc. Denys Biriukov

Supervisor: doc. RNDr. Milan Předota, Ph.D.

Institute of Physics, Faculty of Science,

University of South Bohemia in České Budějovice, Czech Republic

České Budějovice 2020

This thesis should be cited as:
Biriukov, D., 2020: Application of Electronic Continuum Correction to Molecular Simulations of Nano/Bio Interfaces. Ph.D. Thesis Series, No. 10. University of South Bohemia, Faculty of Science, České Budějovice, Czech Republic, 212 pp.

Annotation

Nowadays it is almost impossible to imagine our life without nanotechnologies. They are present in smartphones and many other gadgets we use every day, while advanced nanoparticle-based devises are currently indispensable in medicine, engineering, and science. In the case of biomedical applications, the knowledge how a specific nanomaterial behaves and changes its properties in complex physiological medium is essential to guarantee the accomplishment of all specific goals facing a scientist or engineer. Some of physical and chemical processes occurring when a nanodevice enters biological environment are yet very difficult to fully detail without accurate computer simulations, so special attention needs to be focused on theoretical studies of nano–bio interactions.

In this thesis, molecular simulations were used to investigate the interactions between different nanomaterials (titanium dioxide, silicon dioxide, and gold) and aqueous solutions, which contain ions, organic molecules, and amino acids. The importance of this scope and particularly selected for this study materials and compounds is given in Introduction. To model nano/bio interfaces, we adopted and integrated recent theoretical approaches, which together with basic principles of molecular simulations are described in Methods. Obtained results are divided in four parts and address several important issues that are vital in deciphering molecular mechanisms, through which nanoparticles identify and bind various biomolecules. The simulation data are thoroughly discussed, compared to experiments, and used to explain some of experimental observations. Additionally, outcomes of this thesis serve as a springboard for further theoretical studies aimed to advance our understanding of nano–bio interactions.

Declaration [in Czech]

Prohlašuji, že svoji disertační práci jsem vypracoval samostatně pouze s použitím pramenů a literatury uvedených v seznamu citované literatury.

Prohlašuji, že v souladu s § 47b zákona č. 111/1998 Sb. v platném znění souhlasím se zveřejněním své disertační práce, a to v úpravě vzniklé vypuštěním vyznačených částí archivovaných Přírodovědeckou fakultou elektronickou cestou ve veřejně přístupné části databáze STAG provozované Jihočeskou univerzitou v Českých Budějovicích na jejích internetových stránkách, a to se zachováním mého autorského práva k odevzdanému textu této kvalifikační práce. Souhlasím dále s tím, aby toutéž elektronickou cestou byly v souladu s uvedeným ustanovením zákona č. 111/1998 Sb. zveřejněny posudky školitele a oponentů práce i záznam o průběhu a výsledku obhajoby kvalifikační práce. Rovněž souhlasím s porovnáním textu mé kvalifikační práce s databází kvalifikačních prací Theses.cz provozovanou Národním registrem vysokoškolských kvalifikačních prací a systémem na odhalování plagiátů.

České Budějovice, 12. 4. 2020

……

Denys Biriukov

Přírodovědecká
fakulta
Faculty
of Science

Financial Support

The research presented in this thesis was supported by grants from the Czech Science Foundation (13-08651S, 17-10734S, 20-02067Y) and the Ministry of Education of the Czech Republic (LTAUSA17163), and by institutional funding.

Acknowledgements

More than four years of my PhD study in the Czech Republic were an amazing life experience, and here I want to thank all the people helping and supporting me during that curious and fascinating time.

First of all, I would like to express the sincere gratitude to my supervisor, Milan Předota, who has been a wonderful boss, excellent mentor, and after all great person, who gave me a chance to become a part of his group. I am enormously thankful to all the given advices, learned experience, inspiring ideas, and fruitful discussions. I will never forget our joint visit of the conference in California, which was one of the most fantastic journeys I have ever had in my life. I hope that this thesis is not the completion, but just the beginning of the scientific partnership we are going to share together in the future.

I want to thank my parents and my grandma for their endless love and support. Without you, who pushed me out the comfort zone and challenged me to conquer the scientific world abroad, this thesis would never have seen the light of day.

I wish to thank all my friends, who have made my life in České Budějovice much more colorful, enthralling, and enjoyable. I will always remember all the fun we had together, which was so needed for a young fellow like me diving right into the life in a new unknown country. I am sure all the best is still waiting for us ahead!

I would like to thank all my colleagues, who have created a comfortable, pleasant, and friendly environment at my working place and around. All the pub meetings, barbeque parties, lunches together, and even short walks to Menza and back are indispensable things embracing the life of any PhD student.

Thanks to you all, guys! I believe that after resolving all the troubles faced the world in 2020, we will find an opportunity to wander into a pub and spend time together, loudly repeating the most magical words in the Czech language: “Ještě jedno”.

List of papers and author's contribution

This PhD thesis is based on the results from the five articles published in international peer-reviewed journals (DB1–DB5, listed in the chronological order), one submitted manuscript (DB6), and unpublished data. Other two currently submitted manuscripts (DB7–DB8) are closely related to the theoretical framework of this thesis, however, they do not contribute to nano–bio interactions. Therefore, these manuscripts are not included, though we will be referring to them during the discussion. Numbering DB1–DB8 is used throughout this thesis.

DB1) Biriukov, D.; Kroutil, O.; Předota M. Modeling of Solid–Liquid Interfaces using Scaled Charges: Rutile (110) Surfaces. *Physical Chemistry Chemical Physics* **2018**, *20* (37), 23954–23966; IF (2018) = 3.567
DB *prepared molecular models for both rutile surfaces and ions, performed all the molecular simulations, analyzed the results using pre-implemented and self-written utilities, and was the key person in the paper writing.*

DB2) Biriukov, D.; Kroutil O.; Kabeláč, M.; Ridley, M. K.; Machesky, M. L.; Předota, M. Oxalic Acid Adsorption on Rutile: Molecular Dynamics and ab Initio Calculations. *Langmuir* **2019**, *35* (24), 7617–7630; IF (2018) = 3.638
DB *built simulation setups containing oxalic acid anions and rutile surfaces, performed all the molecular dynamics simulations, prepared the initial equilibrated structures for ab initio calculations, analyzed the results using pre-implemented and self-written utilities, and was the key person in the paper writing.*

DB3) Machesky, M. L.; Ridley, M. K.; **Biriukov, D.**; Kroutil, O.; Předota, M. Oxalic Acid Adsorption on Rutile: Experiments and Surface Complexation Modeling to 150 °C. *Langmuir* **2019**, *35* (24), 7631–7640; IF (2018) = 3.638
DB *performed all the molecular simulations, analyzed the results using pre-implemented and self-written utilities, provided the data for surface complexation modeling, and participated in the paper writing*.

DB4) Marchioro, A.; Bischoff, M.; Lütgebaucks, C.; **Biriukov, D.**; Předota, M.; Roke, S. Surface Characterization of Colloidal Silica Nanoparticles by Second Harmonic Scattering: Quantifying the Surface Potential and Interfacial Water Order. *Journal of Physical Chemistry C* **2019**, *123* (33), 20393–20404; IF (2018) = 4.309
DB *performed all the molecular simulations, analyzed the results, and participated in the paper writing*.

DB5) Biriukov, D.; Fibich, P.; Předota, M. Zeta Potential Determination from Molecular Simulations. *Journal of Physical Chemistry C* **2020**, 124 (4), 3159–3170; IF (2018) = 4.309
DB *integrated the method of prediction the zeta potential from nonequilibrium molecular dynamics simulations into LAMMPS software, prepared all the computational models, performed all the molecular simulations, analyzed the results using pre-implemented and self-written utilities, and was the key person in the paper writing.*

DB6) Bischoff, M.; **Biriukov, D.**; Předota, M.; Roke, S.; Marchioro, A. Surface Potential and Interfacial Water Order at the Amorphous TiO_2 Nanoparticle/Aqueous Interface (*Manuscript*)
DB *performed all the molecular simulations, analyzed the results, and participated in the paper writing*.

DB7) Předota, M.; **Biriukov, D.** Electronic Continuum Correction without Scaled Charges (*Manuscript*)
DB *performed testing molecular simulations and participated in the paper writing*.

DB8) Rampal, N.; Wang, H.-W.; **Biriukov, D.**; Brady, A. B.; Neuefeind, J.; Předota, M.; Stack, A. G. Local Molecular Environment Drives Speciation and Reactivity of Ion Complexes in Concentrated Salt Solution (*Manuscript*)
DB *was one of the key persons in the force field development, performed a substantial part of the molecular dynamics simulations, analyzed the results using pre-implemented and self-written utilities, and participated in the paper writing*.

Contents

List of abbreviations

AA	Amino Acid
NP	Nanoparticle
Arg	Arginine
Asp	Aspartic Acid
Glu	Glutamic Acid
Gly	Glycine
Lys	Lysine
EDL	Electric Double Layer
IS	Inner-sphere
OS	Outer-sphere
PZC	Point of Zero Charge
SCD	Surface Charge Density
ZP	Zeta Potential
AIMD	Ab Initio Molecular Dynamics
CMD	Classical Molecular Dynamics
DFT	Density Functional Theory
ECC	Electronic Continuum Correction
FF	Force Field
LB	Lorentz-Berthelot
LJ	Lennard-Jones
MD	Molecular Dynamics
MUSIC–CD	MUltiSIte Complexation – Charge Distribution
NEMD	Nonequilibrium Molecular Dynamics
PMF	Potential of Mean Force
US	Umbrella Sampling
vdW	van der Waals

Посвящается маме, которая в нужный момент помогла принять сложное, но верное решение

1. Introduction

1.1 Motivation

Nanoparticles (NPs) are of huge interest for diverse applications in biophysics, biochemistry, and rapidly emerging field of bionanotechnology (**Figure 1-1**). Naturally occurring and artificially developed nanomaterials have been extensively utilized in many medical, technical, and scientific applications. For instance, nanobased biosensors with their unique optical, electrical, magnetic, thermal, or chemical signatures are perfect tools for diagnostic (e.g. early detection of progressing diseases) or/and therapeutic (local drug delivery to diseased cells) purposes [Giner-Casares, 2016; Kumar, 2017; Xin, 2017]. In both cases, the biostability and harmlessness of NPs are of particular importance in minimizing a collateral damage to healthy tissues. The fabrication of biocompatible implants as well as tissue reconstruction also strongly involves nanomaterials of certain structure and specific properties [Wang, 2016]. Additionally, different nanobiomarkers can detect an undesired accumulation of antibiotics in human body or waterways [Cristea, 2017; Lan, 2017]. Bionanotechnology also vastly engages NPs in electrochemical applications like surface coating or production of anticorrosion materials [Jain, 2020]. Natural and synthesized nanostructures with pronounced hydrophilic or hydrophobic properties can be used in wastewater treatment [Lu, 2016]. Finally, NPs are ubiquitous in many other important fields like energy storage, electronics, cosmetics, food industry, and agriculture [Zhang, 2013; Peters, 2016; Prasad, 2017; Huang, 2019].

All these applications and associated development of various nanodevices require the solid knowledge of properties of a utilizing nanomaterial in a specific environment, e.g. living organisms, and under certain conditions like temperature, ionic concentration, and pH. Molecular interactions of NPs with aqueous solutions of ions and organic molecules, e.g. peptides and proteins, significantly affect their structure, dynamics, and stability. Consequently, the comprehensive and

substantial understanding of interactions between NPs and biologically relevant compounds is of key importance for competent design of nanodevices.

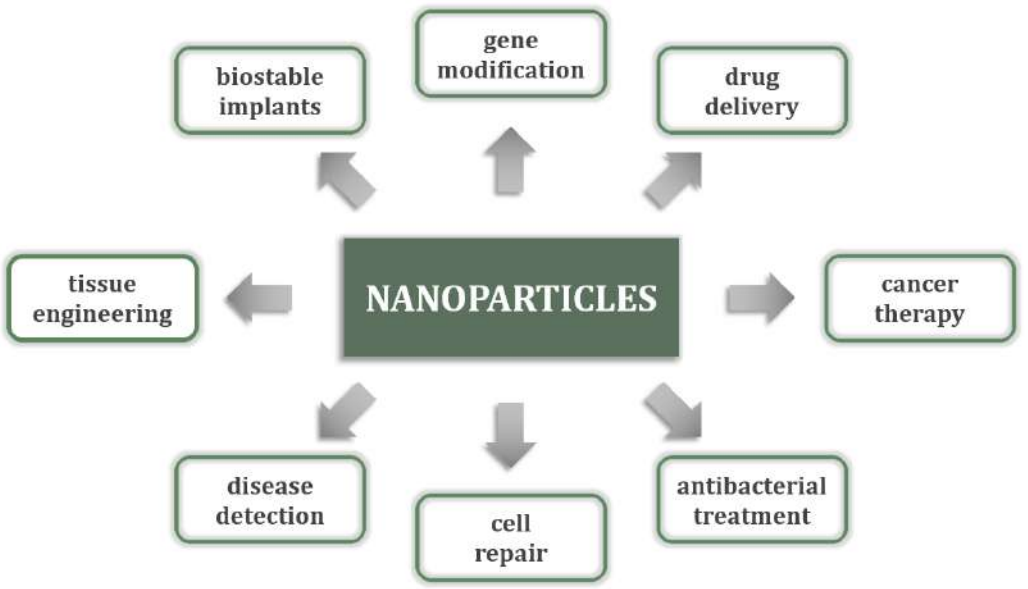

Figure 1-1. Bioapplications of nanoparticles.

The interactions between NPs and aqueous solutions occur in very narrow, usually only few nanometers wide region between the surface of a NP and surrounding medium. Physical and chemical processes in this border region, which is a special case of the solid/liquid interface, attract the largest scientific attention. Present experimental techniques can provide valuable information about molecular interactions at these interfaces. Those include X-ray reflectivity and X-ray standing wave measurements, nonlinear spectroscopy techniques like second harmonic scattering and sum-frequency generation, atomic force microscopy, surface plasmon resonance, and flow microcalorimetric measurements [Zaera, 2012]. At the same time, various computational methods like molecular dynamics (MD) simulations, *ab initio* molecular dynamics (AIMD), density functional theory (DFT), MD simulations with reactive force fields, hybrid

quantum mechanics/molecular mechanics approach, and coarse-grained modeling are gaining in popularity taking advantages of the continuously increasing computational power [Do, 2015]. It is also worth noting other theoretical models that include simplified descriptions of solid/liquid interfaces like the Gouy–Chapman and Stern models [Stern, 1924], and surface complexation modeling, e.g. MUltiSIte Complexation – Charge Distribution (MUSIC–CD) model [Hiemstra, 2006].

Even though modern experimental techniques are capable to look deep inside the molecular arrangement at solid/liquid interfaces, the full molecular picture cannot be captured yet without computational methods. This thesis, which is purely based on molecular simulations (although with direct connection and numerous comparisons with experimental data), details interactions of surfaces of three different nanomaterials with water and aqueous solutions of ions, small organic molecules, and amino acids (AAs). All these compounds are omnipresent in biological systems, and delicate interplay of their interactions determines the behavior of NPs. Moreover, this work includes novel methodological concepts that allow improving the performance of molecular models for biosimulations using recent advances in MD simulations of large-scale systems. This contribution adopts, develops, and integrates these innovations into simulations of solid–liquid interactions, and lays the foundation for further theoretical studies of nano/bio interfaces.

1.2 Nanosurfaces

In this thesis, we investigate interactions of aqueous solutions of relevant biocompounds with three different nanosurfaces, **Figure 1-2**: titanium dioxide (TiO_2), silicon dioxide (SiO_2), and gold (Au). In this section, we emphasize the importance of these materials and why their planar surfaces were selected for this computational work.

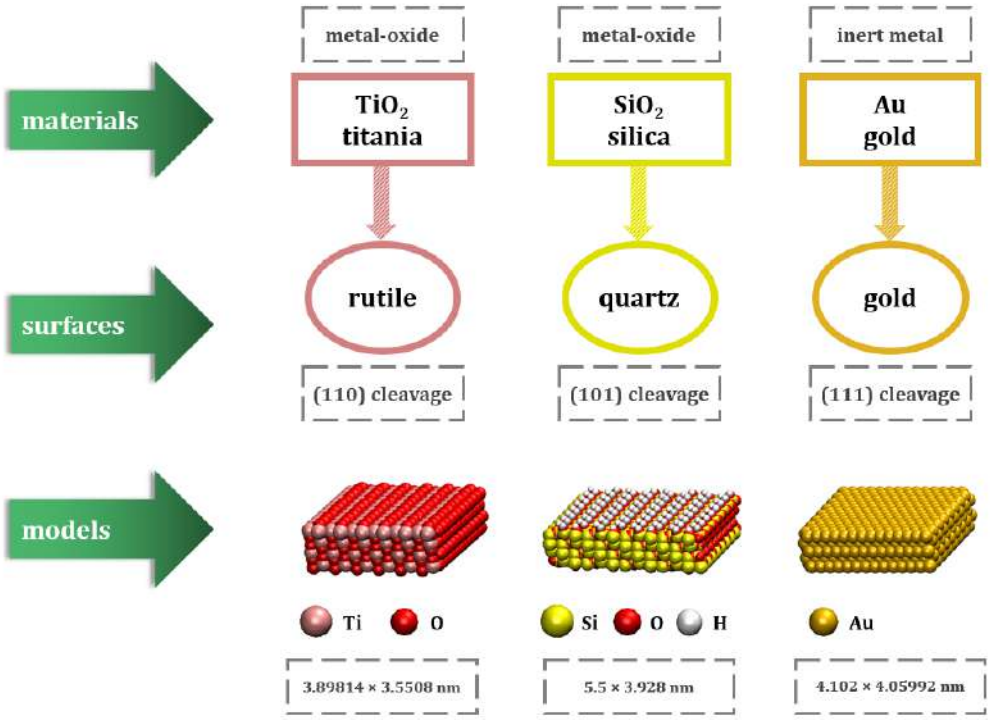

Figure 1-2. Modeled nanosurfaces.

1.2.1 Titanium dioxide

Titanium dioxide (TiO_2, also known as titania) is a naturally occurring material belonging to the family of metal-oxides. Since 1972, when Fujishima and Honda discovered the electrolysis of water on a TiO_2 electrode under ultraviolet light [Fujishima, 1972], huge attention has been paid to investigating the utilization of TiO_2 particles in many related areas like the decomposition of harmful pollutants [Wold, 1993], artificial photosynthesis [Yang, 2010], solar photovoltaic systems as a source of renewable energy [Bai, 2014b; Ma, 2014], atmospheric photochemistry [Chen, 2014], and sensor applications [Bai, 2014a]. Additionally, titania NPs are commonly used in the manufacturing of personal care products and food additives [Weir, 2012].

TiO_2 materials are well known for their high physical and chemical stability, low cost, and relative nontoxicity. All these factors have made this metal-oxide very attractive not only for large-scale productions in the chemical industry (one of the largest segments among inorganic materials [Gambogi, 2014]), but also for numerous medical applications [Shiba, 2010; Liu, 2014b; Rajh, 2014; Wu, 2014; Rehman, 2016]. For instance, TiO_2-based nanodevices can serve a role of cargo for the controlled and targeted drug delivery in cancer treatment [Ren, 2013; Du, 2015]. TiO_2 due to its high binding affinity is also a promising material for biosensing and genetic engineering [Tu, 2010; Yin, 2013]. Therefore, deciphering interaction mechanisms of proteins and their components with TiO_2 surfaces is an important matter for industrial, medical, and scientific applications.

There are three stable polymorphs of TiO_2 found in nature, namely rutile (tetragonal), anatase (also tetragonal), and brookite (orthorhombic) [Zhang, 2014]. In this thesis, we focus on rutile surfaces with (110) cleavage. First, rutile is the most thermodynamically stable form of titania under ambient conditions [Diebold, 2003]. Second, (110) crystal face is the predominant cut at rutile crystals and powders. Third, rutile (110) surfaces are well-established, strongly interacting with biomatter exteriors, so it is a proper candidate for testing new theoretical approaches in surface–bio simulations, which is one of the main outlines of this work. In fact, most of the data reported here have been obtained using the models of rutile (110) surfaces.

The rutile/water and rutile/bio interfaces have been a subject of numerous experimental and theoretical works [Zhang, 2004; Machesky, 2008; Kohli, 2009; Cleaves, 2010; Wu, 2010; Machesky, 2011; Kim, 2012b; Kim, 2013; Předota, 2013; Machesky, 2015; Futera, 2017; Hawkins, 2017; Wechler, 2018]. However, even now, several aspects about interactions of rutile surfaces with organic molecules and even water are subject to debates. For example, there is no solid inference yet about the impact of surface defects on the adsorption of biomolecules onto TiO_2 surfaces [Livi, 2013]. On the other hand, the strong adsorption of water on perfect crystal surfaces can significantly either inhibit or mediate the subsequent adsorption of peptides [Skelton, 2009; Kang, 2010]. Strongly binding to TiO_2 cations like Ca^{2+} are known to affect the adsorption of AAs [Lee, 2014]. However, the mechanisms promoting all these reactions are still not fully understood. This

thesis aims to address some of these shortcomings applying new rapidly evolving approaches in molecular simulations, which can expand our understanding of these and related phenomena.

1.2.2 Silicon dioxide

Silicon dioxide (SiO_2, also known as silica) is a clay material also classified as a metal-oxide. Clays are common in many scientific and industrial applications, e.g. petroleum refining [Murray, 1991], optoelectronics [Alabi, 2013], water splitting devices [Satterthwaite, 2016], surface coating [Medina, 2019], and photocatalysis [Liu, 2014a]. In general, clays are highly biocompatible and surface-reactive, which promotes their use in biosciences and medicine [Choy, 2007; Ghadiri, 2015; Hao, 2015]. Silicon dioxide is one of the most abundant clay materials in rocks, soils, and sand, and its only naturally occurring crystalline form, quartz, is widely present in the environment and one of the main components of Earth's crust [Flörke, 2000]. At the same time, a very popular quartz crystal microbalance technique that utilizes crystalline SiO_2 (as the name suggests) has been copiously used in electrochemistry [Deakin, 1989] and biological sciences [Marx, 2003].

Such a broad presence of SiO_2 in nature and various applications has initiated many experimental and theoretical investigations of SiO_2/water interfaces [Du, 1994; Kim, 2002; Schlegel, 2002; Van Duin, 2003; Ostroverkhov, 2004; Fogarty, 2010; Bandura, 2011; Skelton, 2011a; Skelton, 2011b; DelloStritto, 2014; Bellucci, 2015; Kroutil, 2015; DelloStritto, 2016; Ohno, 2016; Allen, 2017; Quezada, 2017; Rimsza, 2017; Bouhadja, 2018; Brkljača, 2018; Joutsuka, 2018; Quezada, 2018; Rimsza, 2018]. Despite the large scientific interest, the fundamental understanding of key physical and chemical processes, like e.g. dissolution of silica NPs, is still ambiguous [Kubicki, 2012; Crundwell, 2017]. The strength and manner of ionic adsorption on silica and quartz surfaces is also not fully characterized and systematized yet [Gaigeot, 2020], so additional, particularly computational studies are needed to remedy these deficiencies.

In this thesis, we explore the quartz (101)/fluid interfaces by molecular simulations. Since SiO_2 is also a metal-oxide, with several properties similar to titania, the modeling of SiO_2 allows the comparison of materials of similar type. For instance, we can assess how water and adsorbing ions behave at both studied interfaces under similar conditions, and how their interfacial structures can alter adsorption of biomolecules. The direct molecular simulations of SiO_2 surfaces interacting with large organic compounds like peptides and proteins are beyond the scope of this work; however, our simulation results about molecular interactions at SiO_2/aqueous interfaces significantly simplify the further implementation of tested SiO_2 models to surface–bio interactions.

1.2.3 Gold

Gold (Au) is the most inert and malleable of all metals. Its unique physical properties certainly attract both scientists and engineers, especially in the field of nanotechnology [Chakraborty, 2011]. In general, noble metals with their mostly chemically inactive surfaces can be used to investigate the electronic properties of biomolecules like proteins. At the same time, gold, silver, and platinum NPs demonstrate high antibacterial and antiviral activities [Rai, 2015]. Such characteristics are very promising in drug delivery applications, medical therapy, and clinical diagnosis [Panyala, 2009; Colombo, 2011; Kumar, 2012; Yang, 2015; Venditti, 2019]. A special place is taken by bioelectronics, since metalloproteins with incorporated transition metal cations can participate in charge transfer, when located at metal/organic and particularly gold/protein interfaces [Nitzan, 2003; Ruiz, 2017].

Over the last years, the adsorption of AAs and proteins on gold surfaces has been investigated in a number of experimental and computational studies [Bortolotti, 2007; Hnilova, 2008; Hoefling, 2010b; Feng, 2011; Feyer, 2012; Johnson, 2012; Aldeek, 2013; Siriwardana, 2013]. However, the absence of suitable reference data of atomic resolution complicates the description of gold/bio interfaces, since simulation results are sometimes remarkably inconsistent, though some general trends are preserved within most of the studies. The latest advances in the development of more accurate potentials for MD simulations supported by

increasingly feasible quantum chemical calculations of interfacial systems can help in overcoming this problem.

In this thesis, we evaluate the adsorption of AAs to gold (111) surface using MD simulations. These results will be discussed and compared to the adsorption data on rutile (110) surfaces. Contrasting texture and nature of these two nanosurfaces can provide valuable information about sorption properties of both materials, underlying benefits and disadvantages of using noble metals vs. metal-oxides in related nanoapplications. Moreover, the recently suggested new theoretical concept standing behind our molecular simulations (see **Section 2.1.3**) can give a more precise insight into gold–bio interactions in general.

1.3 Strategy and novelty of the work

The most common biological or natural environment of NPs is fluids. This is e.g. the case of nanosensors in human body or rocks interacting with water. To understand, how biologically relevant organic molecules, which are nearly always dissolved, interact with surfaces of NPs, one needs first to answer the following questions:

- How do these surfaces interact with the solvent (usually water)? How can it influence the adsorption of other molecules?
- How do these surfaces interact with ions, which are omnipresent in physiological and natural environments? Does their weak/strong adsorption enhance/inhibit the adsorption of other molecules?

Detailed characterization of surface–water and surface–ion interactions is a piece of puzzle, which should be addressed at the outset and before jumping to modeling the adsorption of large molecules like peptides or proteins.

It is well known that when a solid surface (even almost inert like gold) is in contact with liquid, the surface generates a surface charge through the charge transfer and ion/proton exchange reactions (the case of metal-oxides). This surface charge, (e.g. negative) is then compensated by counterions (e.g., positively charged Na^+) present in the solution. These two charged layers create the so-called electric

double layer (EDL) [Lyklema, 1995]. All interfacial phenomena including surface charge compensation, ionic adsorption, and peptide binding are directly related to the EDL formation. Since the width of EDL rarely exceeds a couple of nanometers, very few experimental techniques can detail molecular processes in this region. However, computational methods like MD simulations are among few tools that can provide information of atomic resolution (**Figure 1-3**), if carefully prepared molecular models are used.

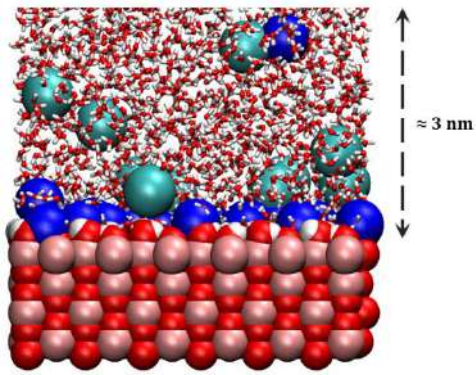

Figure 1-3. Representative example of a modeled solid/liquid interface: rutile (110) surface interacting with NaCl solution. Titanium atoms, surface oxygen atoms, surface hydrogen atoms, sodium ions, and chloride ions are shown as pink, red, white, blue, and cyan spheres, respectively. Water molecules (connected white and red small spheres) are also shown.

At the same time, current state of MD biosimulations is undergoing an era of significant changes due to recent ideas how to include polarization effects in nonpolarizable force fields (FFs). Historically, generic biological FFs like CHARMM [MacKerell, 2004], Amber [Lindorff-Larsen, 2010], and OPLS-AA [Kaminski, 2001] assign nominal (or "full") charges to ions and all other charged species. It means that any ion has integer charge regardless of its environment, e.g. sodium always has +1e, calcium has +2e, chloride has −1e, etc. However, such interpretation is only valid when an ion is put into vacuum. When the ion is solvated, its electronic environment changes reacting to the local electric field created by solvent molecules. The simplest and computationally cheapest way to reflect the response of the ion to this environment is to scale its charge applying the Electronic continuum correction, ECC [Leontyev, 2009; Leontyev, 2010a; Leontyev, 2010b; Leontyev, 2011; Pegado, 2012]. The same is true not only for simple monovalent ions like Na^+, Ca^{2+}, and Cl^-, but AAs, peptides, lipids, and

proteins charged at physiological pH. The models for neutral species, e.g. water, in turn remain the same (see **Section 2** for more theoretical details about ECC and MD simulations in general). Over the last almost ten years, the scaling of charges has given rise to a variety of new FFs for all types of species, and its performance in most cases has been proven far better than the performance of standard models. Obviously, the current generation of FFs for solid surfaces, especially charged ones, should react to such evolution of FFs for biomolecules.

This thesis is the first study, which integrates ECC ideas into MD simulations of solid/liquid interfaces. The main idea of the entire work is to step-by-step detail interactions of NPs with all components of complex biological medium (**Figure 1-4**). Numerous computational results were carefully analyzed and directly compared to experimental data. ECC has been implemented to FFs of solid surfaces, namely rutile (110) [DB1] and later quartz (101), also up to our knowledge for the first time. This allowed us to revisit the structure of studied solid/liquid interfaces using ECC models for all charged components in the system. We detailed the behavior of water molecules at TiO_2 and SiO_2 surfaces by means of computer simulations and compared our results to those from simulations with standard FFs and the experimental data collected by our collaborators or already available in the literature [DB1; DB4; DB6]. Then, we described the adsorption of ions and its effect on the water behavior, still using ECC for both surfaces and ions [DB1; DB4; DB5; DB6].

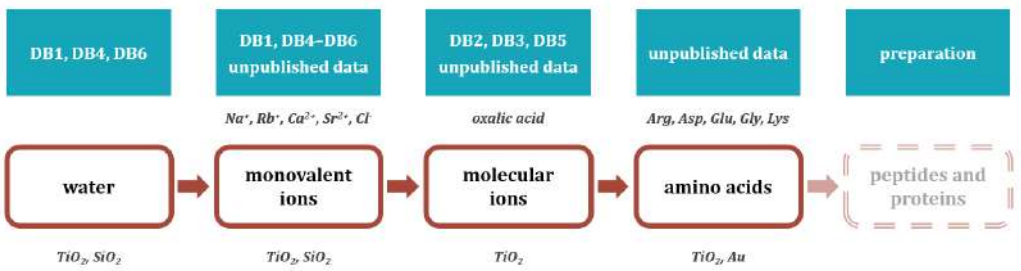

Figure 1-4. The structure of the work: modeled surfaces, investigated species, and future perspectives.

Another part of this work is devoted to the adsorption of oxalic acid by TiO_2 [DB2; DB3; DB5]. Oxalic acid $(COOH)_2$ is the simplest dicarboxylic acid with the unique structure of two covalently bound carboxyl groups. Carboxyl groups are omnipresent in biocompounds, and comprehension how a molecule like oxalic acid interacts with surfaces (in our case, rutile) significantly ameliorates our understanding of surface–bio interactions in general. Moreover, oxalate $(COO^-)_2$, a dianion of oxalic acid, is a compound with the pronounced need of ECC model, since being a molecule of six atoms only, it has a negative charge of −2e, so scaling charges significantly affects modeling of such a strongly reactive oxyanion [Kroutil, 2017].

Finally, the last part of this thesis is devoted to the adsorption of AAs. First, the basis for accurate simulations of surface–protein interactions is a careful treatment of the interactions at a single AA level. Second, we are not aware of any ECC simulations of AAs adsorbing to nanosurfaces. One of the driving factors in this adsorption are electrostatic interactions through charged side chain groups. Therefore, neglecting polarization effects in standard MD simulations significantly alters our imagination of processes like the formation of protein corona (dynamic coating of NPs by adsorbed proteins).

All these together, starting from surface–water interactions with smooth transition to characterizing the adsorption of AAs, sufficiently advances our understanding how NPs behave in biological environments, how we can simulate these processes, and what are real predictive capabilities of MD simulations.

2. Methods

2.1 Molecular dynamics simulations

2.1.1 Why MD simulations?

Molecular dynamics simulations are a viable tool to study complex natural and artificial phenomena at microscopic scale. The greatest advantage of using MD is ability to explore systems of a large size (~100 000 atoms) and for a long simulation time (~1 000 ns), which serves well for accurate large-scale modeling of biological phenomena. DFT calculations and AIMD simulations of such complex setups are still computationally expensive with realistic limits being about hundreds of atoms and dozens of picoseconds. In this aspect, MD simulations are much more preferable for the scope of this thesis.

The accuracy of results obtained by MD simulations is strictly dependent on a set of parameters (called a force field) that describe atomic interactions in the system. These parameters are usually invariable during a particular simulation and must be introduced in advance, which contrasts with quantum chemical calculations, where these interactions come from the direct solving of Schrödinger equations. Bearing in mind these nuances when developing FFs, one should consider a delicate balance between complexity and accuracy of a FF, which is usually validated by a comparison of selected microscopic or macroscopic properties calculated using the FF with experimental or *ab initio* benchmark, and its pace performance, which is one of the key features of MD simulations in studying large-scale systems. Nonpolarizable FFs, which are the most common in biosimulations, greatly fall within these criteria. Utilizing nonpolarizable FFs usually refers to classical MD simulations (CMD), in which chemical reactions, i.e. creating or breaking a covalent bond between atoms, are not allowed as well as any charge transfer.

2.1.2 Basics of MD simulations

The CMD simulations are based on a sequence of atomic configurations evolving over time by integration of Newton's equations of motions, where the atoms are modeled as spheres corresponding to their nuclei, while partial charges, located at the atomic or auxiliary sites, represent electron clouds. This treatment of atomic structure and molecular motion follows the Born-Oppenheimer approximation.

The fundamentals of MD simulations can be found elsewhere [Schlick, 2002], while here we focus on the description of nonbonded interactions. It is particularly important in the light of this thesis, since:

1. We model only the *physisorption* on the surfaces, i.e. without accompanying creation and/or disruption of chemical bonds. *Chemisorption* of organic molecules is beyond the scope of this work due to the nature of employed FFs.

2. Nonbonded (van der Waals and electrostatic) interactions define the physisorption.

3. The Electronic continuum correction also reconsiders only nonbonded interactions, particularly electrostatic forces between charged particles.

Van der Waals (vdW) interactions, which are described by Lennard-Jones (LJ) potential in most nonpolarizable FFs including those employed in this work, are calculated as:

$$\boldsymbol{U_{LJ}(r_{ij}) = 4\varepsilon_{ij}\left[\left(\frac{\sigma_{ij}}{r_{ij}}\right)^{12} - \left(\frac{\sigma_{ij}}{r_{ij}}\right)^{6}\right]} \qquad (2\text{-}1)$$

where r_{ij} is the distance between two atoms, σ_{ij} is the distance at which the potential between these two atoms is supposed to be zero, and ε_{ij} is the depth of the potential well.

Using commonly applied Lorentz-Berthelot (LB) combination rules, one can obtain the cross parameters for different species:

$$\sigma_{ij} = \frac{\sigma_{ii} + \sigma_{jj}}{2};\ \varepsilon_{ij} = \sqrt{\varepsilon_{ii}\varepsilon_{jj}} \tag{2-2}$$

Electrostatic interactions between charges particles are governed by Coulomb's law, which in general form could be written as:

$$U_{Coul}(r_{ij}) = \frac{q_i q_j}{4\pi\varepsilon_0 r_{ij}} \tag{2-3}$$

where q_i and q_j are atomic charges, and ε_0 is the relative permittivity of vacuum.

All the simulations performed in this work deal with the aforementioned interpretation of nonbonded interactions. The only exception is the usage of some predefined cross parameters in CHARMM and GoIP-CHARMM FFs (for amino acids and gold, respectively, see **Section 2.2.4**) without applying LB rules.

2.1.3 Electronic continuum model

The obvious drawback of nonpolarizable FFs is the absence of electronic screening of Coulombic interactions, which occurs when a charged molecule is put into liquid medium. This phenomenon is an important concern playing a fundamental role in many physical, chemical, and biological phenomena. In principle, we can treat the electronic polarization explicitly, and there are enough water polarizable models, e.g. with induced dipoles [Paricaud, 2004] and classical Drude oscillators [Lamoureux, 2003]. However, much less polarizable models are available for biomolecules, not to mention that the cost of computer simulations using explicit polarization models could be much higher, which is not a suitable solution for biosimulations.

Recently, an alternative approach has been suggested, originally aimed at improving the accuracy of biosimulations. The idea of the work by Leontyev and Stuchebrukhov [Leontyev, 2009; Leontyev, 2010a; Leontyev, 2010b; Leontyev, 2011] is to scale down ionic charges, which in a mean-field way reflects screening effects in the solution. The idea has been called as Molecular Dynamics in Electronic Continuum, or Electronic continuum model. Nowadays people usually

refer to it as Electronic Continuum Correction (ECC) theory [Pegado, 2012] or simply simulations with scaled charges. While in simulations with explicit polarization the electronic response is localized in the vicinity of atomic sites, the polarization in ECC simulations is uniform in space and eventually enters the equation of Coulombic interactions.

Macroscopically, electrostatic interactions in a solution are described as:

$$\boldsymbol{E}\,(\boldsymbol{r_{ij}}) = \frac{\boldsymbol{q_i q_j}}{\boldsymbol{4\pi\varepsilon_r\varepsilon_0 r_{ij}}} \tag{2-4}$$

Compared to the general form of the Coulomb's law, the relative permittivity of the solvent, ε_r, is added. This quantity has two contributions, namely electronic (or high-frequency) and nuclear:

$$\boldsymbol{\varepsilon_r = \varepsilon_r^{elec}\varepsilon_r^{nucl}} \tag{2-5}$$

In CMD simulations, only the nuclear part is explicitly present (molecular redistribution and reorientation as a response to the electric field), while the electronic part is missing:

$$\boldsymbol{E}\,(\boldsymbol{r_{ij}}) = \frac{\boldsymbol{q_i q_j}}{\boldsymbol{4\pi\varepsilon_r^{nucl}\varepsilon_0 r_{ij}}} \tag{2-6}$$

Leontyev and Stuchebrukhov [Leontyev, 2009; Leontyev, 2010a; Leontyev, 2011b; Leontyev, 2011] suggested that this problem could be solved by scaling partial charges of ionic species:

$$\boldsymbol{q^{ECC} = \frac{q}{\sqrt{\varepsilon_r^{elec}}};\ E\,(r_{ij}) = \frac{q_i^{ECC} q_j^{ECC}}{4\pi\varepsilon_r^{nucl}\varepsilon_0 r_{ij}}} \tag{2-7}$$

This eventually results in including both nuclear and electronic contributions in MD simulations, and what matters, at no additional computational cost.

The electronic permittivity can be calculated as the square of the refraction index, $\boldsymbol{\varepsilon_r^{ECC} = n^2}$, and in the case of water it equals 1.78. Consequently, if following

ECC theory, all ionic charges in aqueous solutions should be scaled down by a factor of 0.75. For most organic solvents, the electronic permittivity is about 2, so the scaling is closer to 70%.

Over the last years, a number of FFs that follow ECC approach and employ scaled charges have been developed. The examples include models for monovalent ions [Vazdar, 2012; Pluhařová, 2013; Kohagen, 2014; Pluharová, 2014; Kohagen, 2015; Behavides, 2017; Del Frate, 2017; Duboué-Dijon, 2018b; Martinek, 2018; Nikitin, 2018; Zeron, 2019; DB8], oxyanions (oxalate, sulfate, nitrate, and phosphate) [Pegado, 2012; Xie, 2014; Kroutil, 2017; Yadav, 2017; Bruce, 2018], biologically relevant molecular ions like carbonates [Mason, 2012], guanidine [Vazdar, 2013], imidazole [Duboué-Dijon, 2017], insulin [Březina, 2018; Duboué-Dijon, 2018a], calmodulin [Kohagen, 2014b], and even phospholipid bilayers [Melcr, 2018; Melcr, 2020]. Additionally, extended approaches like ECCR (Electronic Continuum Correction with Rescaling of vdW parameters) and ECCR-P (scaling charges of only charged groups of a molecule, see **Figure 2-1**) have been introduced [Kohagen, 2014a; Kohagen, 2014b; Kroutil, 2017].

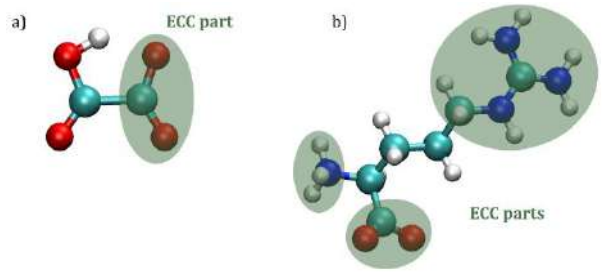

Figure 2-1. Examples of mixed ECCR-P approach: a) hydrogenoxalate ion and b) zwitterionic form of arginine.

It has been noticed that the largest benefit from using ECC is observed for ions with a high charge density. With standard molecular models, ion–ion and ion–water interactions are usually overestimated. This drawback was shown through the comparison of MD results against recent highly accurate *ab initio* and experimental reference data. Moreover, unphysical strong binding of cations to biomolecules has been systematically reported, and ECC scaling has been proven one of the possible solutions to address this issue [Melcr, 2018; Melcr, 2020; Tolmachev, 2020]. Dynamic properties in liquids are also better reproduced with the ionic charge scaling [Kann, 2014; Nguyen, 2018; Laage, 2019; Yue, 2019].

Nowadays, there is an ongoing heated debate how exactly ECC ideas should be integrated in MD simulations and FF development, while persistently acknowledging the need of including polarization to standard FFs, at least in a consistent effective way. Particularly, there are discussions about the limits of ECC to liquid solutions questioning its performance in other phases or dielectrically nonuniform space [Smith, 2018; Zeron, 2019]. Another dispute is the value of the ionic scaling factor, which is proposed to be either 75% as theoretically justified value [Leontyev, 2009; Leontyev, 2010a; Leontyev, 2010b; Leontyev, 2011], or water model dependent [Kann, 2014], or selected "in the battlefield" based on the performance of all possible values [Vega, 2015]. Even a completely different approach has been very recently suggested to avoid scaling partial charges at all, however still integrating ECC into CMD through implicit weakening of all electrostatic interactions [DB7]. The latter concept also stimulates the development of a new water model fully consistent with the ECC theory.

This thesis does not delve into these deliberations and, in turn, comprises the current state-of-art of the ECC approach, the first development of ECC models for solid surfaces, and performance of ECC in simulations of solid/liquid interfaces. Nevertheless, the ideas formulated here how to model surface–bio interactions with scaled charges are versatile and potentially able to react to the further evolution of the ECC theory and its applications.

2.2 Simulation models and techniques

2.2.1 Modeling charged surfaces

In aqueous environment, metal-oxide NPs like TiO_2 and SiO_2 are covered by hydroxyl groups formed through the dissociative chemisorption of water molecules. The surface hydroxylation is a fundamental process determining interfacial phenomena. The layer of hydroxyls on the one hand can serve as interaction sites for other adsorbing molecules, and on the other hand, contrary may not allow direct interactions with surface metal sites.

The nature and density of surface hydroxyls are fully determined by properties of a particular material. For quartz (101) surface, there are two types of surface hydroxyls, namely upper and lower silanols, **Figure 2-2a**. As the name suggests, the difference between them is in the position relative to the surface plane. The upper silanols are more accessible for interactions with the solution and consequently more acidic.

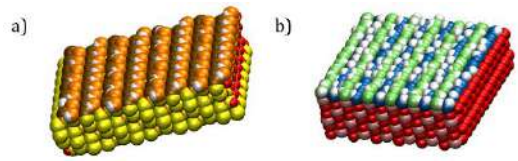

Figure 2-2. Surface hydroxyls of studied metal-oxides. a) Upper (orange oxygens) and lower (ochre oxygens) silanols of (101) quartz (–0.12 C/m^2) surface. b) Terminal (lime oxygens) and bridging (blue oxygens) hydroxyls of hydroxylated (110) rutile (–0.104 C/m^2) surface.

In the case of rutile (110) surface, one can distinguish terminal and bridging hydroxyls, **Figure 2-2b.** A single terminal hydroxyl is formed by five-coordinated Ti atom and OH group of chemisorbed water, while a bridging hydroxyl consists of six-coordinated titanium, surface two-coordinated oxygen, and water hydrogen. Interestingly, but particularly at rutile (110) surface, both chemi- and physisorption of water are almost equally significant adsorption mechanisms, with only the ratio of prevalence being a matter of debates [Diebold, 2017]. In the latter case, water adsorbs to a terminal site as an intact molecule, without donating a proton to a bridging oxygen.

This controversy historically led to two different approaches in modeling rutile (110)/water interfaces. A so-called nonhydroxylated model represents the rutile surface as it was in vacuum, i.e. free of surface hydroxyls, thus molecular water occupies all terminal sites, and bridging oxygens remain unprotonated. A hydroxylated model is the rutile surface fully covered by chemisorbed water. Modeling these two extreme cases of the surface hydroxylation resolves the dilemma and allows us to investigate adsorption phenomena taking into account both features. Note that models of quartz (101) surfaces in our MD simulations are only hydroxylated, with singly coordinated hydroxyl groups.

For each metal-oxide, the pH, at which the NP/surface bears no overall surface charge in the solution, is called the point of zero charge (PZC, also pH_{pzc}). For quartz particles, the PZC is about 2–4, while for TiO_2 polymorphs it lies between 5 and 6, particularly for rutile being closer to 5.5 [Kosmulski, 2002; Kosmulski, 2004]. The PZC is sensitive to ionic concentration of the solution, electrolyte composition, temperature, and changes of other thermodynamic conditions. Varying pH, surface hydroxyls exhibit ion exchange reactions releasing protons or hydroxyl ions, which eventually results in a negative or positive surface charge, respectively. These interfacial processes determine electrostatic interactions between solid surfaces and adsorbing ions. Simply put, a negatively charged surface preferentially interacts with positively charged ions, and vice versa. As we already indicated, adsorbed counterions together with a charged surface form the EDL at the interface. The strength of adsorption vastly depends on a degree of surface charging, which could differ for various materials under the same pH conditions. For instance, at the same pH around 9, the difference in surface charge density (SCD) of rutile (110) and quartz (101) surfaces could be about two-three times, see below.

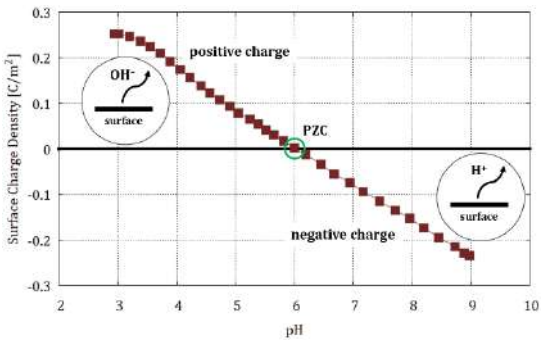

Figure 2-3. Surface charge titration data of rutile powders for 0.001 *m* oxalate in 0.3 *m* NaCl solution at 25 °C.

In CMD simulations, ion exchange reactions are not handled, so it is impossible to capture dynamic changing of pH. However, we can model a constant surface charge via a preset of (de)protonated hydroxyls at the surface. The resulting SCD can be further linked to corresponding pH value based on titration data, **Figure 2-3**. This approach has been proven successful for various systems including TiO_2 and SiO_2 surfaces [Vlček, 2007; Předota, 2013; Kroutil, 2015].

Table 2.1 summarizes the relation between modeled SCD and pH for the systems studied in this thesis. The reference titration data were either published

for the first time together with simulation results or found in the literature. For modeling the adsorption of AAs to TiO_2, we modeled only the negatively charged surface (SCD = –0.104 C/m^2) expected at physiological pH. In the case of gold, which is a noble metal, we investigated only neutral surface.

Table 2.1. Estimated Relation between the Surface Charge Density (SCD) and pH for Different Combinations of Metal-Oxide Surfaces and Aqueous Solutions Modeled in This Work[a]

SCD, C/m^2	pH			
	rutile (110)			
	NaCl, RbCl	$SrCl_2$	oxalic acid ions	amino acids
+0.208	–	–	3.7	–
+0.104	3	–	4.6	–
0	5.4	5.4	6	–
–0.104	7.4	7.1	7.7	~7.4
–0.208	8.9	8	–	–
–0.416	11.8	9.7	–	–
SCD, C/m^2	**quartz (101)**			
	NaCl, RbCl		**$CaCl_2$, $SrCl_2$**	
0	4		4	
–0.03	6.6		6	
–0.06	7.7		7.2	
–0.12	8.8		8.5	

[a]The data were compiled from different sources [Kitamura, 1999; Předota, 2013; DB3; DB5].

2.2.2 Modeling ECC surfaces

To model e.g. a negative surface charge, one should manually delete a proton or hydroxyl ion from the hydroxylated surface or add the opposite group to the nonhydroxylated surface. In most nonpolarizable FFs, the partial charge of a proton (hydrogen) is smaller than +1e and equals roughly +0.5e. Previously, removing this hydrogen was followed by the charge redistribution of remaining 0.5e between neighboring atoms (variable-charge atoms), which should eventually result in a change of surface charge by –1e. The same implies on designing a positive surface charge, where the removal of hydroxyl group does not result in +1e change itself (again only close to half an elementary charge), and additional modifications of partial charges are required.

With introducing ECC, this charge redistribution has been reconsidered. After removing a hydrogen/hydroxyl ion, only 0.25e charge should be distributed to obtain a reduced (scaled) charge of the surface with 75% of the nominal value. In this way, we treat a solid surface as a supermolecule, and analogically to large biomolecules, only surface atoms exposed to the solution carry ECC partial charges, **Figure 2-4**, following previously suggested ECCR-P approach [Kohagen, 2014b; Kroutil, 2017]. The same procedure can be applied, if one wants to apply ECC with another charge scaling factor, which in this thesis was done in the case quartz (101) surfaces, where the models with 85% scaling were also prepared.

Note that models of neutral surfaces (including gold) remain the same even if other, particularly the charged components of the system employ ECC scaling.

2.2.3 Modeling solid/liquid interfaces

Here, we briefly summarize general details of MD simulations performed within this work. Additional details of certain simulation setups are discussed later in the corresponding sections or can be found in already published/submitted works [DB1-DB6]. Description of fundamental MD concepts like thermostatting,

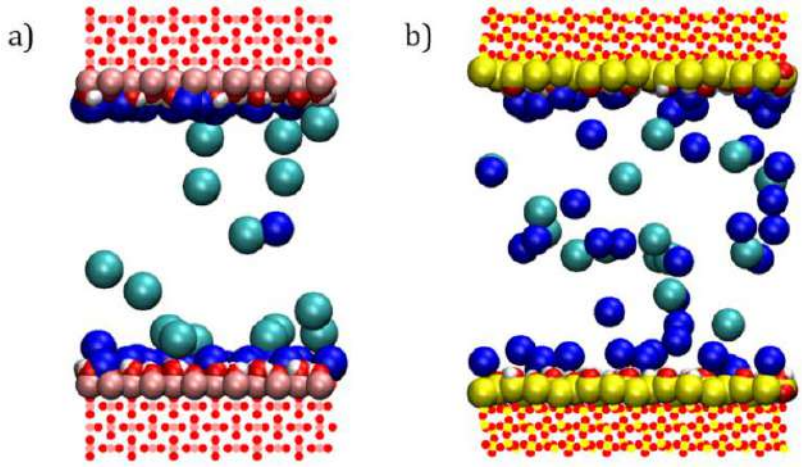

Figure 2-4. ECC systems of **a)** hydroxylated (110) rutile (–0.208 C/m^2) and **b)** (101) quartz (–0.12 C/m^2) surface. Only ions (blue Na^+ and cyan Cl^-) and ECC surface atoms are shown as spheres, while all other surface atoms are shown as points. Water is not shown for clarity. Bulk ionic concentrations are 0.25 and 0.34 M, respectively.

Ewald summation, or periodic boundary conditions can be found elsewhere [Schlick, 2002].

To model solid/liquid interfaces, we have chosen probably the most convenient method, when an aqueous solution is put between two identical planar solid surfaces. The system is periodically replicated in the lateral directions along the surface and, for technical reasons due to high efficiency of 3D Ewald summation, also in the perpendicular direction, though the perpendicular replicas are separated by large vacuum gaps to minimize interactions between the slabs. The results are usually averaged over the two identical interfaces. All the bulk atoms of modeled surfaces were frozen to prevent their displacement during MD simulations. The width of aqueous solution was around 5 nm in all cases, which is large enough to establish bulk properties in the middle of an aqueous slab (about 1.5 nm apart from each surface).

Most MD simulations were performed in Gromacs software [Van der Spoel, 2005] in the canonical NVT ensemble. Electrostatic interactions were treated by particle mesh Ewald summation method [Essmann, 1995] with the correction for systems with slab geometry [Yeh, 1999]. The total charge in all simulated systems was zero to converge long-range interactions. The selected temperature (usually 298.15 K) was controlled by Nosé-Hoover thermostat [Nosé, 1983; Hoover, 1985]. Hydrogen bonds and water geometry were constrained by LINCS algorithm [Hess, 1997]. Each simulation protocol consisted of equilibration and production parts of nanosecond scale, occasionally including short energy minimization at the beginning.

Simulations in LAMMPS software package [Plimpton, 1995] were performed only within the scope of DB5, and all the technical details can be found there.

2.2.4 Force fields

The first step of this work was to prepare surface models and embed ECC to make them compatible with a growing number of charge scaled FFs for ions and biomolecules.

The original, full charge FF for rutile was adopted from previous works of the Předota's group. This FF, which has started its way from the work by Matsui and Akaogi [Matsui, 1991], where bonded and nonbonded parameters for TiO_2 polymorphs were introduced, was adopted for MD simulations of rutile (110)/water interfaces after the partial charges for TiO_2 surface atoms were derived [Bandura, 2003]. Its performance has been repeatedly tested and verified in reproducing numerous structural and dynamics properties of TiO_2 systems over a wide range of pH and temperature conditions [Předota, 2004a; Předota, 2004b; Předota, 2007; Parez, 2012; Předota, 2013; Parez, 2014; Předota, 2016]. Recently, this FF originally defining vdW interactions in the form of Buckingham potential, which is not suitable for simulations in standard simulation packages and not compatible with generic FFs for biomolecules, was reparametrized to LJ form [Brandt, 2015]. The latter set of parameters was our starting point for ECC

simulations (with 75% scaling) and reference simulations with full charge models [DB1].

For neutral and negatively charged quartz (101) surfaces, we used the FF developed by Kroutil et al. [Kroutil, 2015]. This FF is an extension of very popular generic FF, ClayFF, for MD simulations of clay materials [Cygan, 2004], which was originally developed only for neutral surfaces. Since its first release and overall warm reception, a few updates have been recently added [Pouvreau, 2017; Pouvreau, 2019] to the original set of parameters. Despite a wide range of other available FFs for SiO_2 [De Leeuw, 1999; Lopes, 2006; Cole, 2007; Cruz-Chu, 2008; Hassanili, 2010; Butenuth, 2012; Heinz, 2013; Emami, 2014], only few of them are easily transferable and suitable for biosimulations, which is the case of Kroutil-FF [Kroutil, 2015].

For the purpose of this thesis, 75% and 85% modifications of Kroutil-FF have been prepared, to incorporate corresponding charge scaling for the surfaces. The latter type was required for compatibility with the recent ECC FF comprising 85% charge scaled models for ions [Zeron, 2019].

For gold, we selected GoIP-CHARMM FF [Wright, 2013] developed exclusively for exploring interactions of Au (111) and Au (100) surfaces with proteins, and, as the name suggests, compatible with generic CHARMM parameters [MacKerell, 2004]. This FF is a successor of GoIP FF [Iori, 2009] (compatible in turn with OPLS-AA [Kaminski, 2001]), which was among the first to include image charge effects for metal surfaces in MD simulations [Iori, 2008]. This amelioration makes GoIP-CHARMM more conceptually accurate than e.g. CHARMM-METAL FF [Heinz, 2008]. Recently, GoIP-CHARMM FF was complemented by Au–S bonded parameters [Futera, 2019], since sulfur-containing molecules preferentially create a covalent bond with gold surfaces. Although this addition is not of interest for our work and this parametrization was tested only for vacuum, the ongoing evolution of GoIP-CHARMM indicates that nowadays this FF is likely the most suitable choice for investigating gold/bio interfaces by MD simulations.

As we already mentioned, the selected FF for Au (111) model was not modified for ECC simulations, since only uncharged gold was studied. However,

future development of charged gold surfaces may include charge scaling according to ECC approach.

In this thesis, we worked with three rigid water models. In majority of the simulations, three-site SPC/E water model was employed [Berendsen, 1987]. For simulations with AAs, we adopted CHARMM-compatible TIP3P water model [MacKerell, 1998]. For modeling quartz (101)/water interfaces with 85% charge scaling, TIP4P/2005 water model [Abascal, 2005] compatible with the ionic 85% FF was used. Note that any water parameters were not changed for ECC simulations.

The models (both standard and ECC) of ions and AAs are listed in **Table 2-2**. Short summary of FFs for surfaces is also given. We refer only to those models used for obtaining the results presented in this thesis. However, in some of the already published works [DB1, DB5], additional FFs were employed and tested; we refer the reader directly to these publications for further information.

2.2.5 Analysis and post-processing

Gromacs provides a wide variety of post-processing tools, which enable to characterize adsorption processes in simulated systems. Those include computing axial density profiles, radial distribution functions, dipole orientation, etc. LAMMPS in turn gives a possibility to perform on-the-fly calculation and analysis of these and other properties including e.g. streaming velocity of water molecules and ions. Additionally, VMD software [Humphrey, 1996] allows to visualize simulated structures and provides a platform to prepare self-written scripts for advanced analysis of MD trajectories. All these possibilities were actively used during the data preparation for this thesis.

Table 2-2. Employed ECC Force Fields and Their Full Charge Ancestors

system	original full charge FF	ECC modification[a]
surfaces		
rutile (110)	[Předota, 2004a]; [Brandt, 2015]	DB1
quartz (101)	[Kroutil, 2015]	DB5 & this work
gold (111)	GoIP-CHARMM [Wright, 2013]	–
ions		
Na^+	[Joung, 2008]	75%: [Kohagen, 2015]; 85%: [Zeron, 2019]
Rb^+		DB1
Sr^{2+}	[Åqvist, 1990]	
Ca^{2+}	GROMOS96 [Oostenbrink, 2004]	75%: [Martinek, 2018]; 85%: [Zeron, 2019]
Cl^-	[Joung, 2008]	[Pluhařová, 2014]
oxalic acid anions	Amber ff99SB [Lindorff-Larsen, 2010]	[Kroutil, 2015]
amino acids (Arg, Asp, Glu, Gly, Lys)	Au: CHARMM22 [MacKerell, 2004]; TiO_2: CHARMM36m [Huang, 2016]	this work[b]
K^+ and Cl^-[c]	CHARMM [MacKerell, 2004]	this work

[a]75% models if not stated otherwise. [b]No modifications for neutral Glycine. [c]Only for simulations with AAs. Original parameters are identical in both CHARMM22 and CHARMM36 FFs.

2.3 Advanced MD simulations

2.3.1 Biased MD simulations

A serious problem that can appear in MD simulations is not satisfactory sampling of all possible energy states. This may happen if the energy landscape of the system consists of numerous energy barriers separating local minima. In this case, simulation time required for the system to converge could be larger than accessible.

There are several approaches that allow to overcome this problem, including so-called "biased" simulations. "Biased" actually means that during a MD simulation there is an artificial potential that forces the system to visit particular energy states. Probably, the most two popular methods for simulations with enhanced sampling are metadynamics and potential of mean force (PMF). Since in this thesis only the latter approach was used for particular goals, we focus on its description, while the metadynamics methodology can be found elsewhere [Laio, 2002; Barducci, 2011].

The idea of PMF lies in the dividing reaction coordinate, e.g. the distance between two ions (**Figure 2-5a**) or distance between adsorbing molecule and the surface, into several windows. Then, for each window, an independent simulation is carried out, and through the calculation of a mean force acting on the molecule to keep it at a particular point at the reaction coordinate, the free energy profile along this coordinate can be obtained from the collection of umbrella sampling (US) simulations. In Gromacs software [Van der Spoel, 2005], the Weighted Histogram Analysis Method allowing to compute a PMF is already included [Hub, 2006]. The US approach is only effective if the reaction coordinate is properly chosen and adequate sampling in overlapping windows is gained, **Figure 2-5b**. Fulfilling these criteria could be very challenging if the studied molecule exhibits several stable and highly reactive geometries. In fact, even several sets of US simulations may be needed, especially when exploring solid surfaces with different adsorption sites or biomolecules with several functional groups [DB2; YazdanYar, 2018].

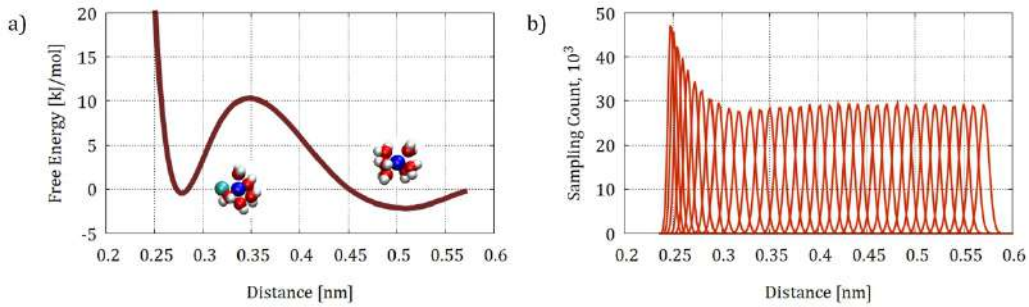

Figure 2-5. a) Free energy profile along the reaction coordinate (the distance between Ca^{2+} and Cl^- ions in aqueous solution) generated from the potential of mean force. b) Sampling histogram along the reaction coordinate. The data were generated following the methodology of the work by Martinek et al. [Martinek, 2018] using ECCR2 model (see the original reference).

Overall, advanced MD techniques are frequently used to estimate the adsorption free energy of biomolecules to different nanosurfaces [Hoefling, 2010a; Monti, 2010; Wright, 2012; Haldar, 2013; Mori, 2013; Nawrocki, 2014; Sultan, 2014; Sultan, 2016; YazdanYar, 2018], and their performance is quite efficient. In this work, the PMF approach was employed in the computational study of oxalate adsorption to rutile (full details about the performed US simulations can be found in the published work [DB2]) and investigating adsorption of selected AAs to gold surface (see **Section 3.4**).

2.3.2 Nonequilibrium MD simulations

Nonequilibrium molecular dynamics (NEMD) simulations are common in modeling electrokinetic phenomena at solid/liquid interfaces. A typical NEMD simulation is one with an applied external force, e.g. electric field, inducing the streaming motion of the liquid or NPs.

In this work, NEMD simulations were carried out to estimate the zeta potential (ζ-potential, ZP) of TiO_2 and SiO_2 surfaces under various conditions. The full description of the method can be found in the studies [Předota, 2016; DB5]

devoted to the formulation and further implementation of the method to common software packages like Gromacs [Van der Spoel, 2005] and LAMMPS [Plimpton, 1995]. Here, we just quickly overview the principles and significance of the suggested approach.

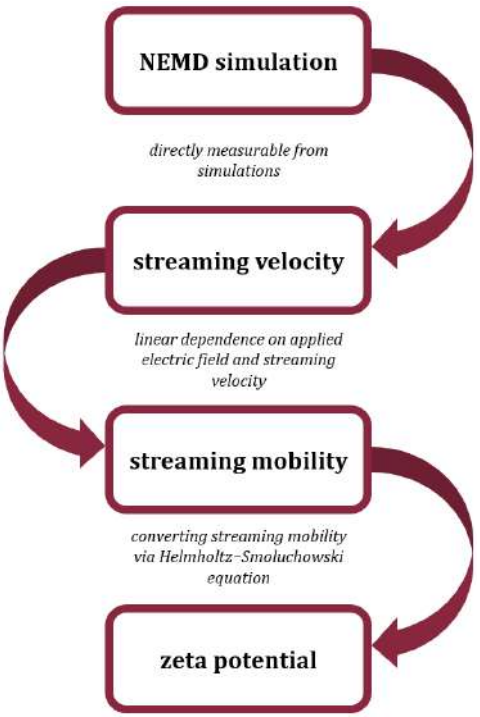

Figure 2-6. The scheme of the method to derive the zeta potential from nonequilibrium molecular dynamics simulations.

The ZP is a macroscopic physical property that characterizes the behavior of colloidal solutions. In a classical interpretation, the ZP is an electrostatic potential developing at an ill-defined border between a solid particle (including an immobile layer of strongly adsorbed species, which move together with the NP) and the rest of surrounding (static) solution. From the experimental point of view, the large absolute value of the ZP (more than 30 mV) usually indicates that particles in the solution are stable and do not aggregate, while smaller values (less than 30 mV) point to instability and quick sedimentation. From a theoretical standpoint, the ZP reflects how efficiently a surface charge is (over)compensated by counterions.

In the suggested NEMD method, **Figure 2-6**, an electric field is applied to aqueous solutions in the direction along the surfaces, while solids are immobile. This field generates a streaming motion of the fluid relative to the surface, i.e. eventually, we model electroosmosis. The streaming velocity is then converted to the streaming mobility, μ, and the ζ-potential can be derived from the latter using the Helmholtz-Smoluchowski equation:

$$\zeta = -\frac{\mu\eta}{\varepsilon_r\varepsilon_0} \tag{2-8}$$

where ε_0 is the vacuum permittivity, η and ε_r are the viscosity and relative permittivity of the solvent, respectively.

The value of the ZP is dictated by the sorption abilities of both NPs and ions. Simply, if the adsorption of ions is strong enough, then a surface charge is readily compensated by counterions present in the solution, and the overall charge and consequently the ZP are reaching low values. The weak adsorption in turn pronounces larger ZP values, since the surface charge is poorly screened. The anomalous behavior can occur at relatively high ionic concentrations of strongly adsorbing ions. In this case, the ZP has a sign opposite to the sign of the surface charge, i.e. the charge reversal is observed. Note the latter phenomenon is not expected for all nanomaterials and strongly depends on properties of both adsorbate and adsorbent. Moreover, it is not predictable by simplified theoretical models of EDL, i.e. could be either measured experimentally or estimated from MD simulations [Lyklema, 2009].

3. Results and Discussion

This section is divided into four parts: (i) water interactions with TiO_2 and SiO_2 surfaces; (ii) adsorption of ions to TiO_2 and SiO_2 surfaces; (iii) oxalic acid adsorption to TiO_2 surfaces; and (iv) interactions of AAs with TiO_2 and Au surfaces. The overview of published and unpublished data, effect of ECC, and relevance of the outputs are carefully summarized and discussed.

3.1 Water at TiO_2 and SiO_2/aqueous interfaces

This section is mostly based on the results from the papers DB4 and DB6. We will quickly overview main outcomes and outline the importance of these data for further parts of the thesis. Before that, we shortly describe the simulation setups and general information about properties of water close to nanosurfaces. More details about the performed MD simulations and full collection of simulation and experimental results can be found in the manuscripts [DB4; DB6].

3.1.1 Simulations details

We carried out two sets of simulations, one each for hydroxylated (110) rutile (–0.104 C/m^2) and (101) quartz (–0.104 C/m^2) surfaces. Similar SCD of both surfaces (though corresponding to different pH) and hydroxylated model of TiO_2 (as for SiO_2) allow to fairly compare the interfaces of both solids.

Each set consisted of three simulations with the identical number of particles (water and ions) in the system, however with varying restraints on ionic motion. The idea was to evaluate the effect of gradual adsorption of ions on the water structure at the interface. Only sodium ions were added to the system in order to reach the lowest ionic concentration as possible for systems of our size, and the total number of cations was set exactly to fully compensate the negative surface charge. This setup was chosen to provide closer comparison with the

experimental second harmonic scattering data performed at micromolar ionic concentrations.

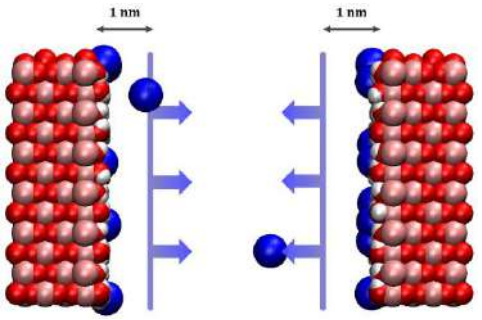

Figure 3-1. The idea of the setup with harmonic wall restraints. Harmonic walls do not allow ions (all or only some of them) get closer than 1 nm to the surface.

In the first simulation of each set, no restriction on the ions was applied, so they could freely move and adsorb to the surface or stay in the bulk solution. It means that a surface charge could be fully compensated by counterions. In the second simulation, half of the ions were forced to be further away from the surface (no closer than 1 nm) (**Figure 3-1**), while others did not have any restrictions, i.e. only 50% of the surface charge could be compensated. In the third simulation, all ions were limited to the motion only in the bulk phase (0% compensation of the surface charge).

3.1.2 Overview of the results

The properties of bulk and nanoconfined liquids including water are very different, especially at the molecular level. Generally, it is almost always true that close to a solid surface, the structure of water is more arranged, the translational and rotational mobilities of water molecules are significantly reduced and sometimes close to zero, and there is a preferential orientation of water dipoles, all dictated in first place by properties of the solid.

The molecular structure of water at both studied metal-oxide/fluid interfaces is quite similar. Looking at axial (in the direction perpendicular to the surface) number density profiles of water oxygens, see top graphs of **Figure 3-2**, one can see two distinct peaks close to the solid. The first peak is the water interacting directly with surface atoms (surface hydroxyls or deprotonated

oxygens that generate a negative surface charge). The water in the second layer interacts with the first water layer and is already less ordered. Moving away from the surface, the water gets less and less layered and eventually becomes bulk-like at around 1-1.5 nm. It is also known that in close vicinity of surfaces like TiO_2 and SiO_2, the mobility of water is significantly reduced [Předota, 2007; Bouhadja, 2018] and recovered to bulk values only within about 1.5-2 nm from the surface. The same is usually true for other liquids, particularly at rutile (110) [Parez, 2012].

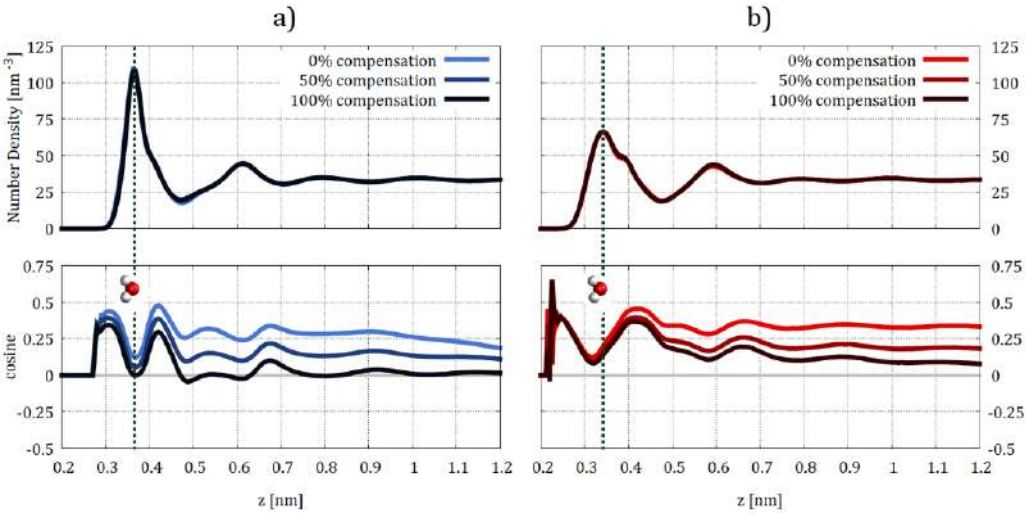

Figure 3-2. Axial number density profiles of water oxygens (top) and cosine of the angle between the inward-pointing surface normal and water dipole moment (bottom) at **a)** hydroxylated (110) rutile (–0.104 C/m^2) and **b)** (101) quartz (–0.12 C/m^2) surfaces under different conditions of possible surface charge screening. The zero height corresponds to the zero planes of the surfaces: the last row of Ti atoms if they were unrelaxed (the case of rutile) and the average position of surface top-layer silicon atoms (the case of quartz).

The fact that interfacial water is so firmly bound to the surface plays a crucial role in all phenomena happening at solid/liquid interfaces. Particularly, strongly adsorbed solvent may inhibit all the further adsorption processes (other

species must compete with water for adsorption surface sites) or contrary initiate/enhance the adsorption serving a role of mediator.

Here, we were aimed to identify the response of interfacial water to adsorbing ions. As you may already noticed, ionic adsorption does not lead to any visible changes in density profiles of water, top graphs of **Figure 3-2**. However, the preferred water orientation (bottom graphs of **Figure 3-2**) changes owing to this adsorption. Purely by electrostatics, a negatively charged surface drives water to be oriented with their hydrogens facing the solid, i.e. water molecules are hydrogen donors for deprotonated surface hydroxyls. However, when a counterion, e.g. sodium, adsorbs to a negatively charged site, i.e. compensates a surface charge, it pushes the water molecule out from a deprotonated site, and the "positive" orientation weakens. Moreover, surrounding water molecules also face their oxygens to the cation. This is observed for both TiO_2 and SiO_2.

However, TiO_2 and particularly rutile more effectively compensate a surface charge than quartz surfaces. If we compare the data for both metal-oxides under the condition, when there are enough ions to fully compensate either surface charge, already at the distance around 1 nm, water molecules almost do not have preferable orientation in the case of TiO_2, while in the case of SiO_2, water still has its hydrogens facing the solid, since the negative charge is not sufficiently screened. These results are in agreement with the experimental observations [DB4, DB6], and they highlight the difference in sorption affinities of studied metal-oxides.

Note that all the results in this section were obtained using ECC FFs (75% charge scaling) for both the surfaces and ions. Already in DB1, we stated that the effect of ECC on water properties is minor. Within the scope of DB1, DB4, and DB6, full charge FFs were also tested and results were almost identical. In principle, it is not a surprise, since water models were not reparametrized for ECC simulations and very small changes of surface partial charges should do not affect the water properties to any noticeable extent. However, as we will see in the next sections, for *charged* species, whose interactions are mostly localized in close vicinity of *charged* sites of the surface, the effect is more pronounced.

3.2 Ions at TiO_2 and SiO_2/aqueous interfaces

This section is based on the papers DB1 and DB5. Some yet unpublished data are also presented and discussed. Here, we will briefly describe the simulations details and overview the results. All the other data can be found in the manuscripts [DB1; DB5].

3.2.1 Simulations details

We performed a series of MD simulations for different aqueous solutions (NaCl, RbCl, $SrCl_2$, and $CaCl_2$) at rutile (110) and quartz (101) surfaces over a wide range of pH (de facto, SCD). Both full charge and ECC FFs were tested and results were compared. All CMD simulations were carried out exclusively in Gromacs, while NEMD simulations were performed using both Gromacs (equilibration simulations) and LAMMPS (production runs with an applied electric field). For the ZP calculations, NaCl solutions of similar concentrations (~0.4 M) were modeled at both solids.

Even though rubidium and strontium ions are rare in natural organic matter, the choice of studying these particular ions is dictated by availability of experimental X-ray and surface titration data [Zhang, 2004; Kohli, 2009], which can benchmark our adsorption data for TiO_2. Additionally, these ions represent important differences in sorption affinities. We can distinguish three types of cations within this work:

- Strongly adsorbing monovalent cations (Na^+)
- Weakly adsorbing monovalent cations (Rb^+)
- Strongly adsorbing divalent cations (Ca^{2+} and Sr^{2+})

Note that we do not detail the adsorption of Cl^- ions. First, the adsorption of this anion is overall weak; second, at physiological pH, surfaces are mostly negatively charged, and the adsorption is even weaker due to repulsive electrostatics.

3.2.2 Overview of the results

Earlier it was estimated that cations adsorb to quartz (101) surfaces 2-5 times weaker than to rutile (110), when comparing similar SCD [Kroutil, 2015], which supports our findings in the previous section. The difference would be even larger if compared at similar pH values. Obviously, this should affect the overall behavior of these NPs in aqueous environment. Using the methodology described in **Section 2.3.2**, we estimated the ZP of both surfaces in the presence of NaCl solution of a similar concentration.

As one can see from **Figure 3-3**, the shape of the ZP curves over pH is completely different for these metal-oxides. For quartz (101), the behavior is trivial and the ZP follows the buildup of SCD, i.e. negative ZP at negatively charged surfaces (we did not model positively charged SiO_2). Positive ZP was measured for neutral SiO_2, since fully hydroxylated surface repels positively charged cations, and the weakly adsorbing chlorides determine the ZP. All this indicates that a surface charge is never (over)compensated by counterions.

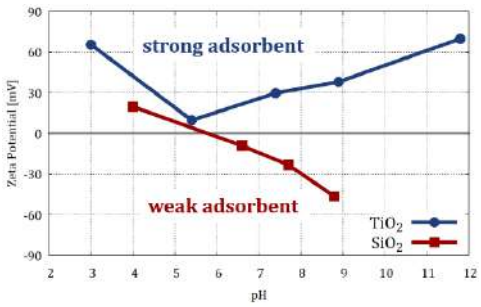

Figure 3-3. The zeta potential as a function of pH for (TiO_2) rutile (110) and (SiO_2) quartz (101) surfaces in ~0.4 M NaCl solution.

A completely different behavior is observed for rutile (110). At the studied concentration, the sodium adsorption is so strong that a surface charge is overcompensated at pH > PZC, and eventually the ZP is always positive. At lower ionic concentrations, the ZP should be rather similar to that of SiO_2 [Kosmulski, 1999; Gustafsson, 2000]. This anomalous behavior can dramatically affect the behavior of TiO_2-based NPs in biological environment. Physiological ionic concentration is quite high (0.15 M), so a negatively charged NP, targeted to bind

some positively charged peptides, may completely change its properties due to charge overcompensation, so a special care should be taken when designing such nanodevices.

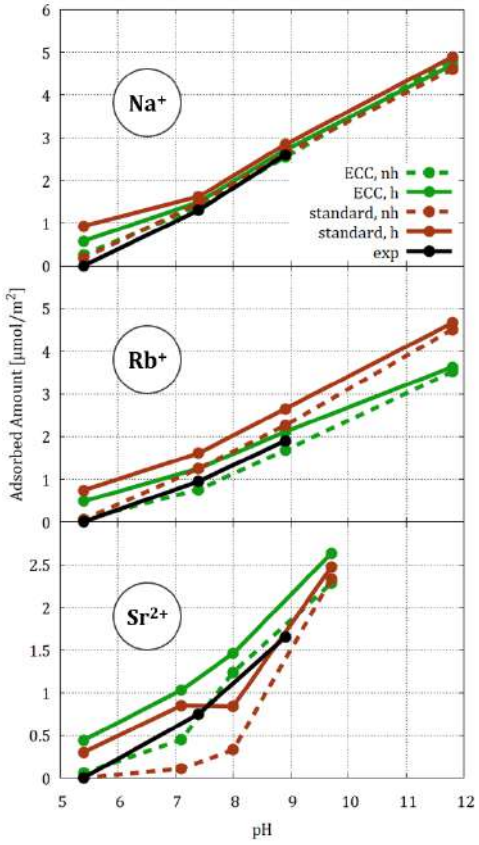

Figure 3-4. Amount of adsorbed cations to both nonhydroxylated ("nh") and hydroxylated ("h") rutile (110) surfaces using two types of force fields. Experimental data were taken from [Zhang, 2004]. Note different vertical scales.

It is worth stressing that modeling the ZP with ECC or full charge FFs does not change the conclusions (at least, for studied systems), though different absolute values of the ZP could be reported [DB5]. At the same time, ECC models better reproduce the amount of ions adsorbed. **Figure 3-4** shows that using ECC, predictions for Rb^+ and Sr^{2+} are in better agreement with the experimental data than using standard, full charge FFs. While for Rb^+ ECC estimates weaker adsorption compared to the standard models, for Sr^{2+} the effect is opposite. For Sr^{2+}, the explanation lies in its ability to dehydrate upon the adsorption. With full charges, ion–water interactions are exaggerated, which decreases ability of Sr^{2+} to dehydrate and adsorb to the surface. For Rb^+ the effect is rather opposite, i.e. a weakly adsorbing cation with a reduced positive charge adsorbs even weaker to negatively charged surfaces (with also reduced charges). Sodium adsorbs equally strong in both types of simulations. More details about the adsorption of cations to rutile surfaces (adsorption sites, distribution

among them, their height above the surface, etc.) can be found in the original manuscript [DB1].

The fact that ECC modeling gives more accurate insights about the adsorption of such small species like monoatomic ions should be treated as a solid indication that for larger molecules with several charged functional groups the lack of polarization in standard MD simulations could be even more dramatic, with significant impact on the geometry of the adsorption.

More interesting situation is observed for ionic adsorption on quartz (101) surfaces. In the literature, there is no solid inference about the nature of ionic adsorption on SiO_2, i.e. whether it is mostly inner-sphere (IS; direct interactions with surface silanol oxygens) or dominantly outer-sphere (OS; interactions with water layered at the surface). In the case of rutile (110), IS coordination is privileged, which in fact results in overall strong adsorption. For quartz (101) as a weak sorbent the situation is less clear.

From our simulations with three types of FFs (standard, ECC with 75% scaling, ECC with 85% scaling), we do not have consistent results, see **Figure 3-5**. As one can see from the density profiles, full charge and 75% FFs indicate dominant IS adsorption for both Na^+ and Ca^+ ions. Modeling with 85% charge scaling results in IS and OS being basically equal for sodium, while for calcium the IS adsorption is nearly zero.

These results raise an interesting topic about the development of FFs, particularly which target properties should be used during the parametrization. FFs with 75% scaling employed in this work were benchmarked against neutron scattering data, which provide highly accurate data about atomic distribution in the solution [Kohagen, 2015; Martinek, 2018]. The FFs with 85% charges [Zeron, 2019] were in turn fitted to reproduce the concentration dependence (up to 6 M) of density of NaCl and $CaCl_2$ solutions. We believe that the different approach in the development of the FFs is the reason for contradicting results in our simulations. Particularly, the bulk ionic concentration in our simulations does not exceed 0.4 M (experiments are rarely done at higher concentrations), so FFs targeted to match ion–water and ion–ion distances are probably more suitable for simulations of solid/liquid interfaces.

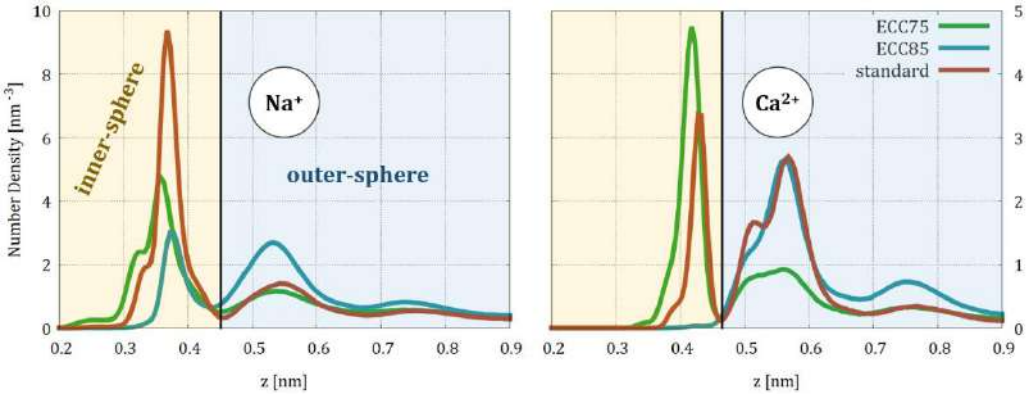

Figure 3-5. Axial number density profiles of cations at quartz (–0.12 C/m^2) surface from simulations with full charge ("standard") and ECC force fields with 75% and 85% charge scaling ("ECC75" and "ECC85", respectively). Note different vertical scales.

Anyway, this subject deserves further attention and is already beyond the scope of the thesis, while now we are moving to the adsorption of organic molecules on TiO_2.

3.3 Oxalic acid at TiO_2/aqueous interface

This section heavily relies on the data from DB2, DB3, and DB5. Here, we quickly overview simulations setups and briefly discuss the results, while a full pack of experimental and simulation data (two publications, DB2 and DB3, were devoted exclusively to this topic) together with the methodology can be found in the manuscripts [DB2, DB3, DB5].

3.3.1 Simulation details

We modeled rutile (110) surfaces interacting with solutions of oxalic acid anions, namely oxalate and hydrogenoxalate. These data were compared to titration adsorption data and served for further MUSIC–CD modeling

[Hiemstra, 2006]. Both hydroxylated and nonhydroxylated rutile surfaces were utilized for CMD simulations. For free energy calculations, only the nonhydroxylated model was used, since oxyanions are expected to bind to bare terminal sites. In the hydroxylated model, these sites are occupied by terminal hydroxyls, except for a few deprotonated to generate a positive surface charge.

3.3.2 Overview of the results

For many years, a primary hypothesis for the strong adsorption of (di)carboxylic acids and other molecules with reactive oxygens to TiO_2 has been that all these compounds adsorb as IS, i.e. their oxygens directly interact with surface metal atoms. This hypothesis, particularly in the case of oxalate, was supported by ATR-FTIR measurements and quantum chemical calculations [Hug, 1994; Weisz, 2002; Mendive, 2005; Hug, 2006; Mendive, 2006; Mendive, 2007; Mendive, 2008; Mendive, 2009; Young, 2009; Singh, 2013]. Contrary, adsorption as OS, i.e. interactions with surface hydrogens or adsorbed water molecules, has been considered as insignificant, especially compared to IS [Parikh, 2011; Savory, 2011].

However, the latest studies point that the real picture may be different. First of all, recent AIMD calculations showed that there is a large energy penalty to replace a water molecule at a terminal site, which therefore reduces the affinity of IS interactions [Klyukin, 2017]. Second, the strength of OS adsorption is probably significantly underestimated, since a molecule like oxalate with its four oxygens is evidently able to interact not only with metal sites, but also with surface hydrogens. Moreover, in most theoretical studies only the monolayer water coverage was modeled, which is not appropriate for OS adsorption. Third, the presence of surface defects like steps and kinks may be primarily responsible for the IS adsorption predicted by spectroscopic measurements, while such interpretation of the experimental data is not applicable for flawless surfaces [Livi, 2013].

The main goal of our study combining theoretical and experimental methods was to either support the original hypothesis or provide an alternative explanation for evidently strong adsorption of oxalate and similar compounds. The

mechanisms how organic molecules with carboxyl groups interact with TiO_2 surfaces are of substantial importance for simulations of bio–surface interactions. At physiological pH, many molecules like fulvic and humic acids, AAs, peptides, and proteins have deprotonated carboxyl groups carrying a negative charge, which often dictate the adsorption.

The main conclusion of the massive work performed within this study was that almost all the IS surface complexes suggested previously (see Figure 2 in DB2) were found energetically unfavorable, with some being completely unstable. Moreover, none of them were observed in CMD simulations (due to the energy barrier mentioned previously), so PMF calculations were required to estimate the adsorption free energy. Only IS monodentate complex (one oxalate oxygen interacts with one terminal Ti) was consistently proposed as stable by free energy calculations (**Figure 3-6**), *ab initio* simulations, and MUSIC–CD modeling [DB2; DB3], but still less favorable than OS adsorption.

At the same time, overall adsorption of oxalate anions was very strong owing to numerous OS complexes identified from CMD simulations (Figure 5 in DB2). Moreover, amount of adsorbed (hydrogen)oxalate predicted by MD simulations is in adequate agreement with both titration and MUSIC–CD data, **Figure 3-7**. ZP predictions from NEMD simulations (without IS adsorption) also indicate that oxalate as well as sodium is able to overcompensate a surface charge [DB5], which is supported by experimental measurements [Janusz, 2006]. All this together clearly contradicts with a common opinion that strong adsorption implies IS adsorption, while OS coordination means a weak adsorption.

The benefit of using ECC in all these simulations is that only ECC models of (hydrogen)oxalate ions were able to correctly describe ion–water interactions in pure water when compared to AIMD data [Kroutil, 2017]. Without ECC, simulations of the adsorption would be simply irrelevant and in any case inaccurate.

In fact, the entire story how even such highly charged ions like oxalate may not adsorb as IS complexes together with a clear warning that models for such molecules could be simply bad without ECC modification significantly changes our

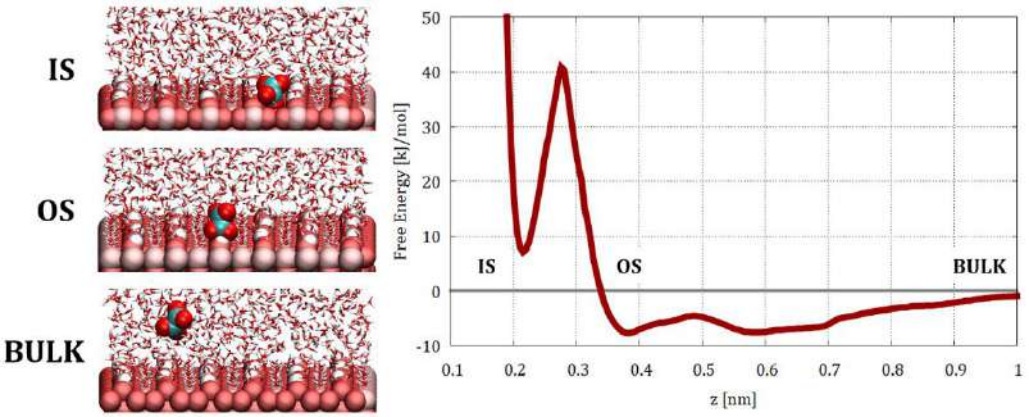

Figure 3-6. Free energy profile of oxalate at the nonhydroxylated (110) rutile (+0.208 C/m^2) surface with the monodentate inner-sphere (IS) coordination, i.e. one oxalate oxygen interacts with one Ti atom, compared to outer-sphere (OS) and bulk solution (BULK; reference zero energy).

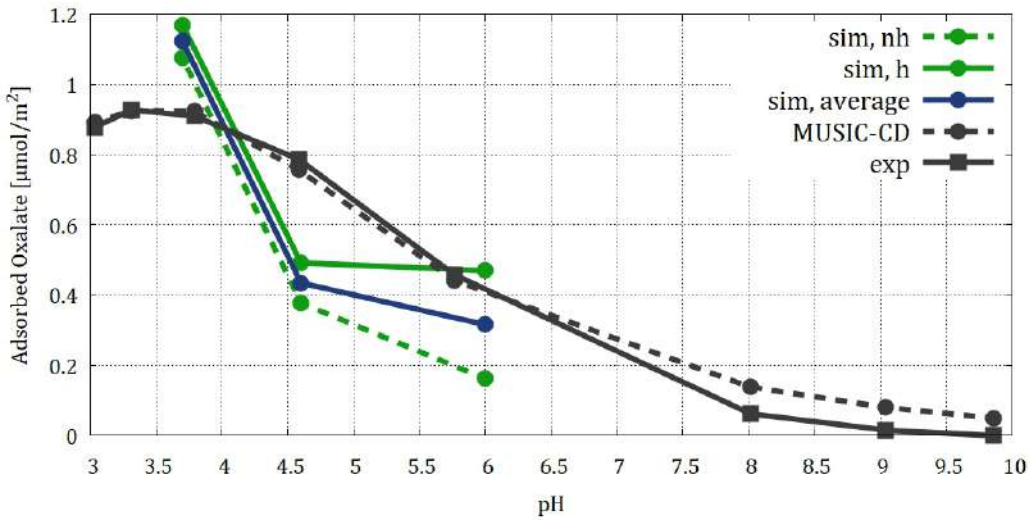

Figure 3-7. Amount of adsorbed oxalate to both nonhydroxylated ("nh") and hydroxylated ("h") rutile (110) surfaces compared to titration ("exp") and MUSIC–CD modeling ("MUSIC–CD") data. The average from simulations with different surface models is added for additional comparison.

imagination how any molecule with one or more carboxyl groups adsorbs to TiO_2. For example, glutamic and aspartic acids (negatively charged amino acids with two carboxyl groups in a zwitterionic form) are omnipresent in peptides and proteins, and our findings that these carboxyl groups may not interact with the surface via metal sites should give a rise to new theoretical studies of nano/bio interfaces.

3.4 Amino acids at TiO_2 and Au/aqueous interfaces

This section presents unpublished data that continue the storyline of interactions at nano/bio interfaces by estimating the adsorption of AAs onto rutile (110) and gold (111) surfaces. Simulation details, current results, and possible future outlines are summarized and discussed.

3.4.1 Simulation details

We studied five amino acids: four charged, namely arginine (Arg), aspartic acid (Asp), glutamic acid (Glu), and lysine (Lys), and neutral glycine (Gly, the smallest AA). This choice is motivated by the concept of ECC theory, which reconsiders only modeling of charged species. At physiological pH, Arg and Lys have a positive charge, while Glu and Asp are negatively charged. The results for Gly provide an additional comparison, how ECC modeling of rutile (110) surfaces affects the adsorption of neutral AAs. As shown in **Figure 3-8**, N and C-termini of each AA were capped by acetyl and N-methyl groups, respectively. Despite the fact that modeling of zwitterions most probably would result in a larger difference between the results from standard and ECC simulations (since all three functional groups of each AA are charged), we selected the current approach to stay close to future modeling of peptides, where usually side chains dictate the adsorption, while N and C-termini are involved in peptide bonds.

The primary test for both TiO_2/AA and Au/AA systems was to put a single AA between two identical surfaces and observe how it binds to the solids and how strong the adsorption is. The idea was to check, if there are any stuck interactions, i.e. AA binds to the surface and never detaches. Such behavior is likely expected in

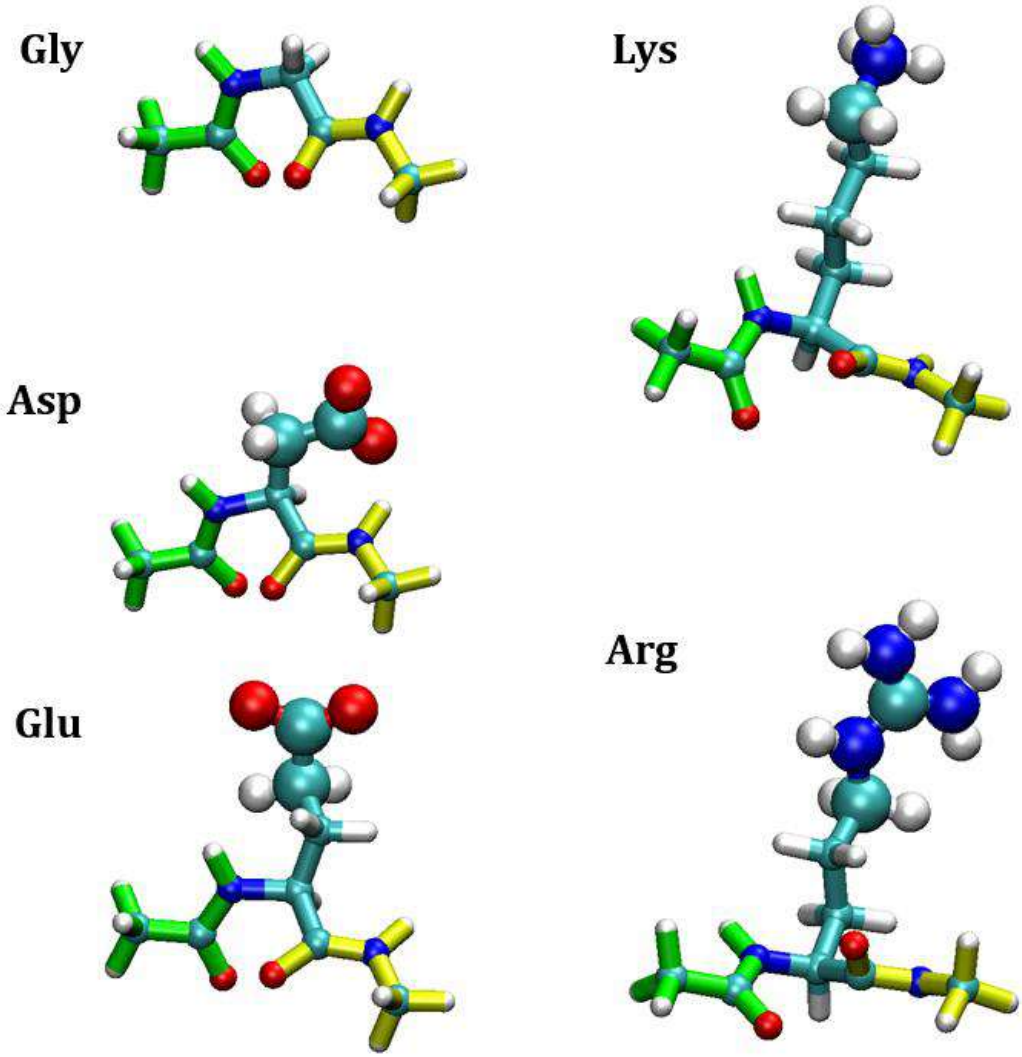

Figure 3-8. Modeled amino acids. Carbon, oxygen, nitrogen, and hydrogen atoms are shown as cyan, red, blue, and white spheres, respectively. Bonds in methylated N and C-termini ends are green and yellow, respectively. Bonds' colors in side chains reflect the colors of involved atoms. Enlarged spheres are atoms with ECC-modified charges.

full charge simulations, since similar problems, like e.g. overbinding of Ca^{2+} to charged phospholipid bilayers, have been previously reported as a drawback of nonpolarizable FFs [Melcr, 2018; Melcr, 2020; Tolmachev, 2020].

The setup for classical MD simulations was very similar to that in previous works [DB1−DB6]. A system net charge was compensated by uneven addition of K^+ and Cl^- ions (simulations with neutral gold) with resulting bulk concentration similar to physiological one, i.e. around 150 mM, or purely by K^+ (simulations with negatively charged rutile). Potassium was chosen over sodium to minimize the effect of heavily adsorbing Na^+ on the reported data for systems with TiO_2. For ECC simulations, K^+ and Cl^- charges were scaled down to 75% of the nominal value without modifications to CHARMM LJ parameters. CHARMM partial atomic charges of charged AAs were modified in accord with ECC theory: charges of either guanidino $HNCNH_2NH_2^+$, carboxyl COO^-, or amino NH_3^+ group together with the neighboring to it CH_2 group were scaled down to 75%, see again **Figure 3-8**, so the charge of an entire AA was also 75% of the nominal value.

In the case of gold, additional PMF calculations were carried out. Two sets of simulations with different initial structures were performed for each AA and type of FF, so here the average data are reported. The reaction coordinate (the *z*-component of the distance between the selected gold surface and the center of mass of an AA) was divided into more than 35 windows. A 0.02 nm step was chosen for distances from ~0.3 nm up to 0.7 nm, and 0.5 nm step was used further up to 1.5 nm away from the surface. A harmonic force with the force constant 500 $kJ.mol^{-1}.nm^{-2}$ was applied to keep the AA at a certain distance from the solid. Each umbrella sampling simulation was 11 ns long, with only the last 10 ns being analyzed.

3.4.2 Overview of the results

At the prevailing physiological pH, which is approximately 7.4, a TiO_2 surface is negatively charged (~ −0.1 C/m^2), so its main binding targets should be molecules containing positively charged residues, e.g. Arg with its guanidino group or Lys with its amino group. Contrary, negatively charged molecules are expected to be less attractive due to their own negative charge. However, as we showed by

an example of (hydrogen)oxalate anions, deprotonated carboxyl groups still can strongly interact with the surface water cover through the network of numerous hydrogen bonds. Basically, these expectations coincide with what we observe in our classical MD simulations, **Figure 3-9**.

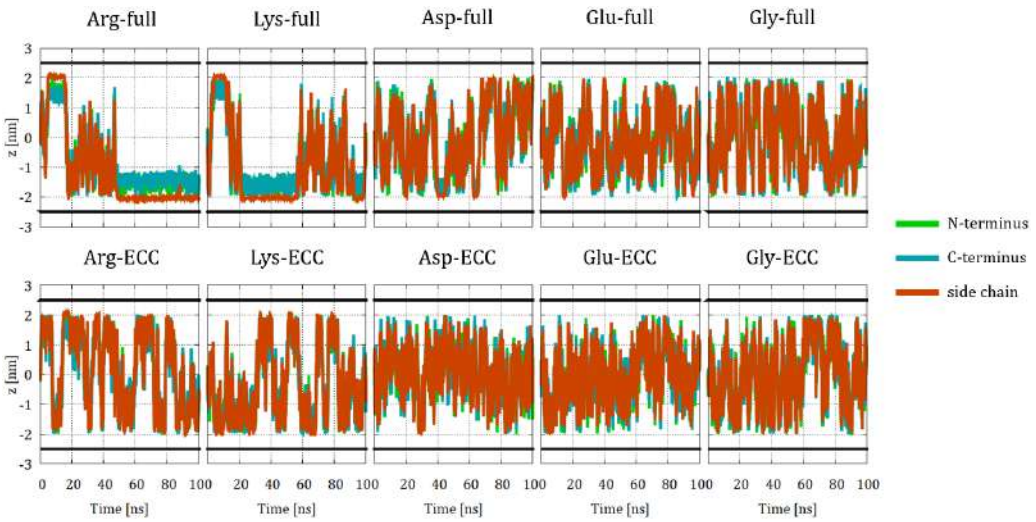

Figure 3-9. The *z*-position of the last carbon of each functional group of an AA as a function of time from simulations with rutile (110) surfaces and two types of FFs. The center of the box is set to $z = 0$. Solid black lines reflect the zero planes of two surfaces.

Monitoring the position of a molecule over the simulation time, one can clearly see that positively charged Arg and Lys have protracted interactions with rutile (110) surfaces through their side chains. At the same time, negatively charged Asp and Glu also actively interact with TiO_2 through carboxyl groups. All these interactions are actually oxygen−hydrogen bonds between AAs and the surface, and, similarly to (hydrogen)oxalate, carboxyl oxygens of Asp and Glu do not bind to metal sites.

Introducing ECC, the strength and lifetime of interactions are reduced, and particularly for Arg and Lys, the stuck periods, which are dozens nanoseconds long

in standard simulations, actually disappear. This is in line with previously reported effect of ECC on Coulombic interactions between ions and biomolecules, where rather unphysical overestimation of electrostatic interactions is resolved with scaling charges [Melcr, 2018; Melcr, 2020; Tolmachev, 2020]. For Gly, we observe neither strong adsorption nor significant changes with charge scaling.

A different situation is seen for gold–AA interactions, **Figure 3-10**. Long-lived adsorption is common here for all studied AAs and both types of FFs, and we suggest two reasons for this. First, all AAs easily interact directly with Au atoms, not adsorbed water. Second, the water adsorption seems to be not very strong itself, especially compared to that at TiO_2, i.e. AAs do not have to compete much for adsorption sites.

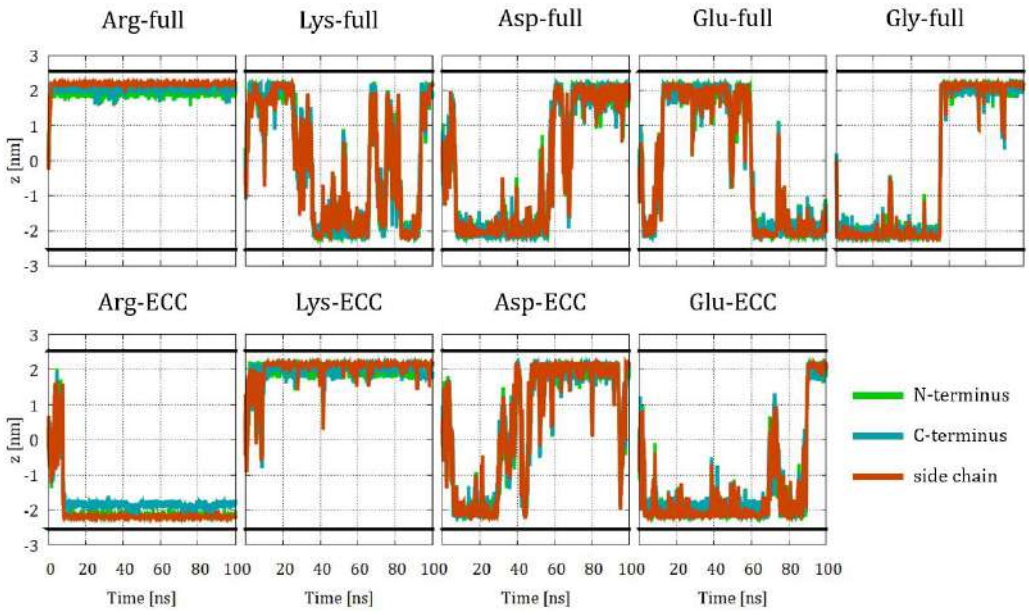

Figure 3-10. The z-position of the last carbon of each functional group of an AA as a function of time from simulations with gold (111) surfaces and two types of FFs. For glycine the full charge and ECC simulations coincide. The center of the box is set to z = 0. Solid black lines reflect the zero planes (the last row of Au atoms) of two surfaces.

This is clearly seen in the generated distance-dependent free energy profiles of AAs, **Figure 3-11**. For Arg, which is the most strongly adsorbing AA among studied (see below), there is a deep energy minimum close to the surface, and basically the AA has tiny chances to desorb. The most weakly adsorbing AA, Asp, is in a similar situation, however, the energy minimum is shallower, and additionally there is a small energy barrier (around 1.5 kJ/mol from simulations with full charges) preventing the adsorption to some extent.

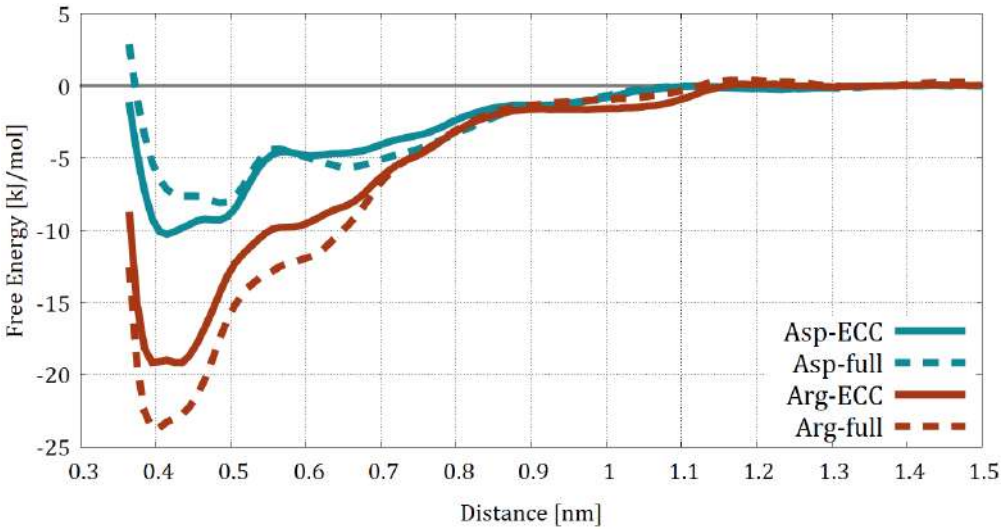

Figure 3-11. Free energy profiles for aspartic acid and arginine at gold (111) surface from simulations with full charge FFs. Zero energy corresponds to the position of an AA in the bulk.

All the adsorption free energies, calculated as a difference between the energies when the AA is adsorbed and when it is in the bulk, are given in **Table 3-1**. Interestingly that ECC scaling results in two opposite effects. For Arg, which has far larger adsorption energy than other AAs, scaling charges weakens the adsorption. For all other AAs, which have quite similar adsorption energies, the effect is opposite, i.e. all of them consistently adsorb stronger, with adsorption energy already being closer to that of neutral Gly.

Table 3-1. Adsorption Free Energies of Amino Acids to Au (111) Surface from the Potential of Mean Force Calculations with Two Types of Force Fields.

model	adsorption free energy, kJ/mo]				
	Arg	**Lys**	**Asp**	**Glu**	**Gly**
full	–23.9 ± 1.1	–10.1 ± 0.9	–8.2 ± 0.5	–9.9 ± 0.2	–13.9 ± 0.3
ECC	–19.5 ± 1.3	–13.1 ± 0.7	–10.3 ± 0.1	–11.7 ± 0.3	= full

The latter observation together with a careful look at **Figure 3-11** indicate that with full charges the side chains of Asp, Gly, and Lys disfavor the adsorption. With scaling charges, their detrimental influence is reduced, and particularly for Lys the interactions of the side chain with the surface even become the driving factor in the adsorption, i.e. similarly to Arg, which also has a positively charged side chain.

This actually means that ECC modeling not only weakens electrostatic interactions of charged species in solutions, which is essentially the idea of the theory and the most expected practical consequence of scaling charges, but also weakens the solute–solvent interactions, which can lead to stronger adsorption.

Unfortunately, we are not aware of direct reference data that can validate either results. Nevertheless, even if not making any preferences towards ECC or standard modeling, one should be aware that physically justified concept of the charge scaling should be taken into account or at least tested in molecular simulations of nano/bio interfaces, especially when knowing about numerous examples of apparent success of this approach for other systems.

4. Conclusions

Molecular description of nano/bio interfaces has been a challenging task for many years. Even now, interaction mechanisms, which are inherently manifold and complex at the atomic level, can hardly be revealed and detailed without computational methods, which together with modern experimental techniques rapidly evolve and advance. Molecular simulations and particularly molecular dynamics simulations are trustworthy and well-established theoretical methods that can shed the light on many experimentally observed biological phenomena and even further predict the behavior of complex biological systems under conditions of interest.

The simulation community continuously attempts to improve the accuracy of nonpolarizable force fields, which are the primary choice for biosimulations due to their simplicity, transferability, and applicability to big systems. Probably, the most perceptible and progressive idea among recent is the suggestion to scale ionic charges, following the Electronic continuum theory. This in a mean-field way reflects the electronic polarization effects, which are inconsistently incorporated into classical MD simulations with nonpolarizable FFs [DB7].

This thesis, up to our knowledge, is a pioneering study in integrating the idea of charge scaling into molecular simulations of solid surfaces. Starting from modeling the adsorption of ions on (TiO_2) rutile (110) surfaces [DB1], we moved to studying the interactions of oxalic acid anions with TiO_2 surfaces [DB2, DB3]. Later, the comparison of simulation results with the second harmonic scattering data on the water orientation on TiO_2 and SiO_2 particles allowed us to estimate how the ionic adsorption disturbs the water structure at both rutile (110) and (SiO_2) quartz (101) surfaces [DB4, DB6]. Analyzing these data, we also confirmed that TiO_2 materials are stronger sorbents than SiO_2, and these foundations were further supported by our study on the zeta potential predictions [DB5]. Integrating a simple, but yet accurate method of predicting the ZP from nonequilibrium MD simulations, we not only provided important insights about the molecular phenomena at both rutile and quartz/water interfaces, but also generalized this

NEMD approach making it easily applicable for modeling other systems and available for the large scientific community.

The final part of this thesis was devoted to the adsorption of several, mostly charged amino acids to TiO_2 and Au surfaces. In the former case, simulations with scaled charges resulted in anticipated weakening of sometimes unphysically exaggerated electrostatic interactions, which are observed in standard simulations, while in the latter case, ambivalent effects were noted. Although this topic deserves deeper investigation, already now we can evidently give credence to the statement that ECC is more important and simultaneously more complicated for molecular ions and ions with a high charge density. While for monoatomic ions the charge scaling usually trivially loosens Coulombic interactions, for molecular ions the resulting effect may change the adsorption geometry of an entire molecule, like it was in this study for lysine adsorbing to gold.

Overall, our numerous simulation results show that ECC can bring significant improvements to molecular modeling of nano/bio interfaces. With scaled charges, theoretical predictions even for simple monoatomic ions are in better agreement with the experimental titration data. Without ECC, modeling oxalate and hydrogenoxalate ions at TiO_2/aqueous interface would be simply wrong, since only ECC models can provide solvation structure of these ions in water in agreement with AIMD calculations. Moreover, our results revealed that previously suggested adsorption mechanisms for molecules with charged carboxyl groups could be incomplete or even erroneous. The role of charged side chains in the adsorption of both single amino acids and large peptides may be also incorrectly interpreted from classical simulations, while a real picture is probably better described by ECC simulations.

We believe that this thesis, which was aimed to bring something conceptually new to the field of modeling nano/bio interfaces, fairly accomplished this goal. The characterization of nano–bio interactions, which stand behind many natural and artificial processes tremendously important in biosciences and medicine, has a high priority, and results presented here not only significantly contribute to this topic, but also build a platform for future theoretical studies targeted to advance our understanding of these and related phenomena.

5. References

Abascal, J. L. F.; Vega, C. A General Purpose Model for the Condensed Phases of Water: TIP4P/2005. *J. Chem. Phys.* **2005**, *123* (23), 234505. https://doi.org/10.1063/1.2121687

Alabi, T. R.; Yuan, D.; Bucknall, D.; Das, S. Silicon Oxide Nanowires: Facile and Controlled Large Area Fabrication of Vertically Oriented Silicon Oxide Nanowires for Photoluminescence and Sensor Applications. *ACS Appl. Mater. Interfaces* **2013**, *5* (18), 8932–8938. https://doi.org/10.1021/am401787c

Aldeek, F.; Safi, M.; Zhan, N.; Palui, G.; Mattoussi, H. Understanding the Self-Assembly of Proteins onto Gold Nanoparticles and Quantum Dots Driven by Metal-Histidine Coordination. *ACS Nano* **2013**, *7* (11), 10197-10210. https://doi.org/10.1021/nn404479h

Allen, A.; Machesky, M.; Wesolowski, D. J.; Kabengi, N. Calorimetric Study of Alkali and Alkaline-Earth Cation Adsorption and Exchange at the Quartz-Solution Interface. *J. Coll. Interface Sci.* **2017**, *504*, 538–548. https://doi.org/10.1016/j.jcis.2017.06.005

Åqvist, J. Ion-Water Interaction Potentials Derived from Free Energy Perturbation Simulations. *J. Phys. Chem.* **1990**, *94* (21), 8021–8024. https://doi.org/10.1021/j100384a009

Bai, J.; Zhou, B. Titanium Dioxide Nanomaterials for Sensor Applications. *Chem. Rev.* **2014**, *114* (19), 10131–10176. https://doi.org/10.1021/cr400625j

Bai, Y.; Mora-Seró, I.; Angelis, F. D.; Bisquert, J.; Wang, P. Titanium Dioxide Nanomaterials for Photovoltaic Applications. *Chem. Rev.* **2014**, *114* (19), 10095–10130. https://doi.org/10.1021/cr400606n

Bandura, A. V.; Kubicki, J. D. Derivation of Force Field Parameters for TiO_2–H_2O Systems from ab Initio Calculations. *J. Phys. Chem. B* **2003**, *107* (40), 11072–11081. https://doi.org/10.1021/jp034093t

Bandura, A. V.; Kubicki, J. D.; Sofo, J. O. Periodic Density Functional Theory Study of Water Adsorption on the α-Quartz (101) Surface. *J. Phys. Chem. C* **2011**, *115* (13), 5756–5766. https://doi.org/10.1021/jp1106636

Barducci, A.; Bonomi, M.; Parrinello, M. Metadynamics. *WIREs Comput. Mol. Sci.* **2011**, *1* (5), 826–843. https://doi.org/10.1002/wcms.31

Benavides, A. L.; Portillo, M. A.; Chamorro, V. C.; Espinosa, J. R.; Abascal, J. L. F.; Vega, C. A Potential Model for Sodium Chloride Solutions Based on the TIP4P/2005 Water Model. *J. Chem. Phys.* **2017**, *147* (10), 104501. https://doi.org/10.1063/1.5001190

Bellucci, F.; Lee, S. S.; Kubicki, J. D.; Bandura, A.; Zhang, Z.; Wesolowski, D. J.; Fenter, P. Rb^+ Adsorption at the Quartz(101)−Aqueous Interface: Comparison of Resonant Anomalous X-Ray Reflectivity with Ab Initio Calculations. *J. Phys. Chem. C* **2015**, *119* (9), 4778−4788. https://doi.org/10.1021/jp510139t

Berendsen, H. J. C.; Grigera, J. R.; Straatsma, T. P. The Missing Term in Effective Pair Potentials. *J. Phys. Chem.* **1987**, *91* (24), 6269−6271. https://doi.org/10.1021/j100308a038

Bortolotti, C. A.; Borsari, M.; Sola, M.; Chertkova, R.; Dolgikh, D.; Kotlyar, A.; Facci, P. Orientation-Dependent Kinetics of Heterogeneous Electron Transfer for Cytochrome *c* Immobilized on Gold: Electrochemical Determination and Theoretical Prediction. *J. Phys. Chem. C* **2007**, *111* (32), 12100−12105. https://doi.org/10.1021/jp072813g

Bouhadja, M.; Skelton, A. A. Dynamical Properties of Water and Ions at the Quartz (101)−Water Interface at a Range of Solution Conditions: A Classical Molecular Dynamics Study. *J. Phys. Chem. C* **2018**, *122* (3), 1535−1546. https://doi.org/10.1021/acs.jpcc.7b08214

Brandt, E. G.; Lyubartsev, A. P. Systematic Optimization of a Force Field for Classical Simulations of TiO_2−Water Interfaces. *J. Phys. Chem. C* **2015**, *119* (32), 18110−18125. https://doi.org/10.1021/acs.jpcc.5b02669

Březina, K.; Duboué-Dijon, E.; Palivec, V.; Jiráček, J.; Křížek, T.; Viola, C. M.; Ganderton, T. R.; Brzozowski, A.M.; Jungwirth, P. Can Arginine Inhibit Insulin Aggregation? A Combined Protein Crystallography, Capillary Electrophoresis, and Molecular Simulation Study. *J. Phys. Chem. B* **2018**, *122* (44), 10069−10076. https://doi.org/10.1021/acs.jpcb.8b06557

Brkljača, Z.; Namjesnik, D.; Lützenkirchen, J.; Předota, M.; Preočanin, T. Quartz/Aqueous Electrolyte Solution Interface: Molecular Dynamic Simulation and Interfacial Potential Measurements. *J. Phys. Chem. C* **2018**, *122* (42), 24025−24036. https://doi.org/10.1021/acs.jpcc.8b04035

Bruce, E.; van der Vegt, N. F. A. Does an Electronic Continuum Correction Improve Effective Short-Range Ion–Ion Interactions in Aqueous Solution? *J. Chem. Phys.* **2018**, *148* (22), 222816. https://doi.org/10.1063/1.5017101

Butenuth, A.; Moras, G.; Schneider, J.; Koleini, M.; Koppen, S.; Meißner, R.; Wright, L. B.; Walsh, T. R.; Ciacchi, L. C. Ab Initio Derived Force-field Parameters for Molecular Dynamics Simulations of Deprotonated Amorphous-SiO_2/Water Interfaces. *Phys. Status Solidi B* **2012**, *249* (2), 293–305. https://doi.org/10.1002/pssb.201100786

Chakraborty, M.; Jain, S.; Rani, V. Nanotechnology: Emerging Tool for Diagnostics and Therapeutics. *Appl. Biochem. Biotechnol.* **2011**, *165*, 1178–1187. https://doi.org/10.1007/s12010-011-9336-6

Chen, H.; Nanayakkara, C. E.; Grassian, V. H. Titanium Dioxide Photocatalysis in Atmospheric Chemistry. *Chem. Rev.* **2012**, *112* (11), 5919–5948. https://doi.org/10.1021/cr3002092

Choy, J.-H.; Choi, S.-J.; Oh, J.-M.; Park, T. Clay Minerals and Layered Double Hydroxides for Novel Biological Applications. *Appl. Clay Sci.* **2007**, *36* (1–3), 122–132. https://doi.org/10.1016/j.clay.2006.07.007

Cleaves, H. J.; Jonsson, C. M.; Jonsson, C. L.; Sverjensky, D. A.; Hazen, R. M. Adsorption of Nucleic Acid Components on Rutile (TiO_2) Surfaces. *Astrobiology* **2010**, *10* (3), 311–323. https://doi.org/10.1089/ast.2009.0397

Cole, D. J.; Payne, M. C.; Csányi, G.; Spearing, M. S.; Ciacchi, L. C. Development of a Classical Force Field for the Oxidized Si Surface: Application to Hydrophilic Wafer Bonding. *J. Chem. Phys.* **2007**, *127* (20), 204704. https://doi.org/10.1063/1.2799196

Colombo, M.; Mazzucchelli, S.; Collico, V.; Avvakumova, S.; Pandolfi, L.; Corsi, F.; Porta, F.; Prosperi, D. Protein-Assisted One-Pot Synthesis and Biofunctionalization of Spherical Gold Nanoparticles for Selective Targeting of Cancer Cells. *Angew. Chem., Int. Ed.* **2012**, *124* (37), 9406–9409. https://doi.org/10.1002/anie.201204699

Cristea, C.; Tertis, M.; Galatus, R. Magnetic Nanoparticles for Antibiotics Detection. *Nanomaterials* **2017**, *7* (6), 119. https://doi.org/10.3390/nano7060119

Crundwell, F. K. On the Mechanism of the Dissolution of Quartz and Silica in Aqueous Solutions. *ACS Omega* **2017**, *2* (3), 1116–1127. https://doi.org/10.1021/acsomega.7b00019

Cruz-Chu, E. R.; Aksimentiev, A.; Schulten, K. Water-Silica Force Field for Simulating Nanodevices. *J. Phys. Chem. B* **2006**, *110* (43), 21497–21508. https://doi.org/10.1021/jp063896o

Cygan, R. T.; Liang, J.-J.; Kalinichev, A. G. Molecular Models of Hydroxide, Oxyhydroxide, and Clay Phases and the Development of a General Force Field. *J. Phys. Chem. B* **2004**, *108* (4), 1255–1266. https://doi.org/10.1021/jp0363287

De Leeuw, N. H.; Higgins, F., M.; Parker, S. C. Modeling the Surface Structure and Stability of α-Quartz. *J. Phys. Chem. B* **1999**, *103* (8), 1270–1277. https://doi.org/10.1021/jp983239z

Deakin, M. R.; Buttry, D. A. Electrochemical Applications of the Quartz Crystal Microbalance. *Anal. Chem.* **1989**, *61* (20), 1147A-1154A. https://doi.org/10.1021/ac00195a001

Del Frate, G.; Nikitin, A. Including Electronic Screening in Classical Force Field of Zinc Ion for Biomolecular Simulations. *ChemistrySelect* **2018**, *3* (43), 12367–12370. https://doi.org/10.1002/slct.201802864

DelloStritto, M. J.; Kubicki, J. D.; Sofo, J. O. Density Functional Theory Simulation of Hydrogen-Bonding Structure and Vibrational Densities of States at the Quartz (101)-Water Interface and its Relation to Dissolution as a Function of Solution pH and Ionic Strength. *J. Phys.: Condens. Matter* **2014**, *26* (24), 244101–244112. https://doi.org/10.1088/0953-8984/26/24/244101

DelloStritto, M. J.; Kubicki, J. D.; Sofo, J. O. Effect of Ions on H-Bond Structure and Dynamics at the Quartz(101)–Water Interface. *Langmuir* **2016**, *32* (44), 11353–11365. https://doi.org/10.1021/acs.langmuir.6b01719

Diebold, U. The Surface Science of Titanium Dioxide. *Surf. Sci. Rep.* **2003**, *48* (5–8), 53–229. https://doi.org/10.1016/S0167-5729(02)00100-0

Diebold, U. Perspective: A Controversial Benchmark System for Water–Oxide Interfaces: H_2O/TiO_2(110). *J. Chem. Phys.* **2017**, *147* (4), 040901. https://doi.org/10.1063/1.4996116

Do, T. N.; Jalkanen, J.; Karttunen, M. Molecular-Scale Computational Techniques in Interfacial Science. In *Computational Methods for Complex Liquid-Fluid Interfaces (Progress in Colloid and Interface Science)*; CRC Press, 2015. https://doi.org/10.1201/b19337

Du, Q.; Freysz, E.; Shen, Y. R. Vibrational Spectra of Water Molecules at Quartz/Water Interfaces. *Phys. Rev. Lett.* **1994**, *72* (2), 238–241. https://doi.org/10.1103/PhysRevLett.72.238

Du, Y.; Ren, W.; Li, Y.; Zhang, Q.; Zeng, L.; Chi, C.; Wu, A.; Tian, J. The Enhanced Chemotherapeutic Effects of Doxorubicin Loaded PEG Coated TiO_2 Nanocarriers in an Orthotopic Breast Tumor Bearing Mouse Model. *J. Mater. Chem. B* **2015**, *3* (8), 1518–1528. https://doi.org/10.1039/C4TB01781A

Duboué-Dijon, E.; Mason, P. E.; Fischer, H. E.; Jungwirth, P. Changes in the Hydration Structure of Imidazole upon Protonation: Neutron Scattering and Molecular Simulations. *J. Chem. Phys.* **2017**, *146* (18), 185102. https://doi.org/10.1063/1.4982937

Duboué-Dijon, E.; Delcroix, P., Martinez-Seara, H.; Hladílková, J.; Coufal, P.; Křížek, T.; Jungwirth, P. Binding of Divalent Cations to Insulin: Capillary Electrophoresis and Molecular Simulations. *J. Phys. Chem. B* **2018**, *122* (21), 5640−5648. https://doi.org/10.1021/acs.jpcb.7b12097

Duboué-Dijon, E.; Mason, P. E.; Fischer, H. E.; Jungwirth, P. Hydration and Ion Pairing in Aqueous Mg^{2+} and Zn^{2+} Solutions: Force-Field Description Aided by Neutron Scattering Experiments and Ab Initio Molecular Dynamics Simulations. *J. Phys. Chem. B* **2018**, *122* (13), 3296–3306. https://doi.org/10.1021/acs.jpcb.7b09612

Emami, F. S.; Puddu, V.; Berry, R. J.; Varshney, V.; Patwardhan, S. V.; Perry, C. C.; Heinz, H. Force Field and a Surface Model Database for Silica to Simulate Interfacial Properties in Atomic Resolution. *Chem. Mater.* **2014**, *26* (8), 2647−2658. https://doi.org/10.1021/cm500365c

Essmann, U.; Perera, L.; Berkowitz, M. L.; Darden, T.; Lee, H.; Pedersen, L. G. A Smooth Particle Mesh Ewald Method. *J. Chem. Phys.* **1995**, *103* (19), 8577−8593. https://doi.org/10.1063/1.470117

Feng, J.; Pandey, R. B.; Berry, R. J.; Farmer, B. L.; Naik, R. R.; Heinz, H. Adsorption Mechanism of Single Amino Acid and Surfactant Molecules to Au {111} Surfaces in Aqueous Solution: Design Rules for Metal-Binding Molecules. *Soft Matter* **2011**, *7* (5), 2113−2120. https://doi.org/10.1039/C0SM01118E

Feyer, V.; Plekan, O.; Ptasińska, S.; Iakhnenko, M.; Tsud, N.; Prince, K. C. Adsorption of Histidine and a Histidine Tripeptide on Au(111) and Au(110) from Acidic Solution. *J. Phys. Chem. C* **2012**, *116* (43), 22960−22966. https://doi.org/10.1021/jp307463z

Flörke, O. W.; Graetsch, H. A.; Brunk, F.; Benda, L.; Paschen, S.; Bergna, H. E.; Roberts, W. O.; Welsh, W. A.; Libanati, C.; Ettlinger, M.; et al. Silica. *In Ullmann's Encyclopedia of Industrial Chemistry;* Wiley-VCH Verlag GmbH & Co. KGaA: **2000**. https://doi.org/10.1002/14356007.a23_583.pub3

Fogarty, J. C.; Aktulga, H. M.; Grama, A. Y.; van Duin, A. C. T.; Pandit, S. A. A Reactive Molecular Dynamics Simulation of the Silica-Water Interface. *J. Chem. Phys.* **2010**, *132* (17), 174704. https://doi.org/10.1063/1.3407433

Fujishima, A; Honda, K. Electrochemical Photolysis of Water at a Semiconductor Electrode. *Nature* **1972**, *238*, 37–38. https://doi.org/10.1038/238037a0

Futera, Z.; English, N. J. Exploring Rutile (110) and Anatase (101) TiO_2 Water Interfaces by Reactive Force–Field Simulations. *J. Phys. Chem. C* **2017**, *121* (12), 6701–6711. https://doi.org/10.1021/acs.jpcc.6b12803

Futera, Z.; Blumberger, J. Adsorption of Amino Acids on Gold: Assessing the Accuracy of the GolP-CHARMM Force Field and Parametrization of Au–S Bonds. *J. Chem. Theory Comput.* **2019**, *15* (1), 613–624. https://doi.org/10.1021/acs.jctc.8b00992

Gaigeot, M.-P.; Sulpizi, M. Structure and Dynamics of Solid/Liquid Interfaces. *In Surface and Interface Science: Volume 7: Liquid and Biological Interfaces.* Wiley-VCH Verlag GmbH & Co. KGaA: 2020. https://doi.org/10.1002/9783527680597.ch50

Gambogi, J. *Mineral commodity summaries;* US Geological Survey, **2014**; p 172.

Ghadiri, M.; Chrzanowski, W.; Rohanizadeh, R. Biomedical Applications of Cationic Clay Minerals. *RSC Adv.* **2015**, *5* (37), 29467–29481. https://doi.org/10.1039/C4RA16945J

Giner-Casares, J. J.; Henriksen-Lacey, M.; Coronado-Puchau, M.; Liz-Marzán, L. M. Inorganic Nanoparticles for Biomedicine: Where Materials Scientists Meet Medical Research. *Mater. Today* **2016**, *19* (1), 19–28. https://doi.org/10.1016/j.mattod.2015.07.004

Gustafsson, J.; Mikkola, P.; Jokinen, M.; Rosenholm, J. B. The Influence of pH and NaCl on the Zeta Potential and Rheology of Anatase Dispersions. *Colloids Surf., A* **2000**, *175* (3), 349–359. https://doi.org/10.1016/S0927-7757(00)00634-8

Haldar, S.; Spiwok, V.; Hobza, P. On the Association of the Base Pairs on the Silica Surface Based on Free Energy Biased Molecular Dynamics Simulation and Quantum Mechanical Calculations. *J. Phys. Chem. C* **2013**, *117* (21), 11066–11075. https://doi.org/10.1021/jp400198h

Hao, X.; Hu, X.; Zhang, C.; Chen, S.; Li, Z.; Yang, X.; Liu, H.; Jia, G.; Liu, D.; Ge, K.; Liang, X.-J.; Zhang, J. Hybrid Mesoporous Silica-Based Drug Carrier Nanostructures with Improved Degradability by Hydroxyapatite. *ACS Nano* **2015**, *9* (10), 9614–9625. https://doi.org/10.1021/nn507485j

Hassanili, A. A.; Zhang, H.; Knight, C.; Shin, Y. K.; Singer, S. J. The Dissociated Amorphous Silica Surface: Model Development and Evaluation. *J. Chem. Theory Comput.* **2010**, *6* (11), 3456–3471. https://doi.org/10.1021/ct100260z

Hawkins, T.; Allen, N.; Machesky, M. L.; Wesolowski, D. J.; Kabengi, N. Ion Exchange Thermodynamics at the Rutile–Water Interface: Flow Microcalorimetric Measurements and Surface Complexation Modeling of Na–K–Rb–Cl–NO_3 Adsorption. *Langmuir* **2017**, *33* (20), 4934–4941. https://doi.org/10.1021/acs.langmuir.7b00867

Heinz, H.; Vaia, R. A.; Farmer, B. L.; Naik, R. R. Accurate Simulation of Surface and Interfaces of Face-Centered Cubic Metals using 12–6 and 9–6 Lennard-Jones Potentials. *J. Phys. Chem. C* **2008**, *112* (44), 17281–17290. https://doi.org/10.1021/jp801931d

Heinz, H.; Lin, T.-J.; Mishra, R. K.; Emami, F. S. Thermodynamically Consistent Force Fields for the Assembly of Inorganic, Organic, and Biological Nanostructures: The INTERFACE Force Field. *Langmuir* **2013**, *29* (6), 1754–1765. https://doi.org/10.1021/la3038846

Hess, B.; Bekker, H.; Berendsen, H. J. C.; Fraaije, J. G. E. M. LINCS: A Linear Constraint Solver for Molecular Simulations. *J. Comput. Chem.* **1997**, *18* (12), 1463–1472. https://doi.org/10.1002/(SICI)1096-987X(199709)18:12<1463::AID-JCC4>3.0.CO;2-H

Hiemstra, T.; Van Riemsdijk, W. H. On the Relationship between Charge Distribution, Surface Hydration, and the Structure of the Interface of Metal Hydroxides. *J. Colloid Interface Sci.* **2006**, *301* (1), 1–18. https://doi.org/10.1016/j.jcis.2006.05.008

Hnilova, M.; Oren, E. E.; Seker, U. O. S.; Wilson, B. R.; Collino, S.; Evans, J. S.; Tamerler, C.; Sarikaya, M. Effect of Molecular Conformations on the Adsorption Behavior of Gold-Binding Peptides. *Langmuir* **2008**, *24* (21), 12440–12445. https://doi.org/10.1021/la801468c

Hoefling, M.; Iori, F.; Corni, S.; Gottschalk, K.-E. Interaction of Amino Acids with the Au(111) Surface: Adsorption Free Energies from Molecular Dynamics Simulations. *Langmuir* **2010**, *26* (11), 8347–8351. https://doi.org/10.1021/la904765u

Hoefling, M.; Iori, F.; Corni, S.; Gottschalk, K. E. The Conformations of Amino Acids on a Gold (111) Surface. *ChemPhysChem* **2010**, *11* (8), 1763–1767. https://doi.org/10.1002/cphc.200900990

Hoover, W. G. Canonical dynamics: Equilibrium phase-space distributions. *Phys. Rev. A* **1985**, *31* (3), 1695–1697. https://doi.org/10.1103/PhysRevA.31.1695

Huang, J.; Rauscher, S.; Nawrocki, G.; Ran, T.; Feig, M.; De Groot, B. L.; Grubmüller, H.; MacKerell, A. D. J. CHARMM36m: An Improved Force Field for Folded and Intrinsically Disordered Proteins. *Nat. Methods* **2016**, *14*, 71–73. https://doi.org/10.1038/nmeth.4067

Huang, Q.; Zhu, Y. Printing Conductive Nanomaterials for Flexible and Stretchable Electronics: A Review of Materials, Processes, and Applications. *Adv. Mater. Technol.* **2019**, *4*, 1800546. https://doi.org/10.1002/admt.201800546

Hub, J. S.; de Groot, B. L.; van der Spoel, D. g_wham—A Free Weighted Histogram Analysis Implementation Including Robust Error and Autocorrelation Estimates. *J. Chem. Theory Comput.* **2010**, *6* (12), 3713–3720. https://doi.org/10.1021/ct100494z

Hug, S. J.; Sulzberger, B. In Situ Fourier Transform Infrared Spectroscopic Evidence for the Formation of Several Different Surface Complexes of Oxalate on TiO_2 in the Aqueous Phase. *Langmuir* **1994**, *10* (10), 3587–3597. https://doi.org/10.1021/la00022a036

Hug, S. G.; Bahnemann, D. Infrared Spectra of Oxalate, Malonate and Succinate Adsorbed on the Aqueous Surface of Rutile, Anatase and Lepidocrocite Measured with in situ ATR-FTIR. *J. Electron Spectrosc. Relat. Phenom.* **2006**, *150* (2–3), 208–219. https://doi.org/10.1016/j.elspec.2005.05.006

Humphrey, W.; Dalke, A.; Schulten, K. VMD: Visual Molecular Dynamics. *J. Mol. Graphics* **1996**, *14*, 33–38. https://doi.org/10.1016/0263-7855(96)00018-5

Iori, F.; Corni, S. Including Image Charge Effects in the Molecular Dynamics Simulations of Molecules on Metal Surfaces. *J. Comput. Chem.* **2008**, *29* (10), 1656–1666. https://doi.org/10.1002/jcc.20928

Iori, F.; Di Felice, R.; Molinari, E.; Corni, S. GolP: An Atomistic Force-Field to Describe the Interaction of Proteins With Au(111) Surfaces in Water. *J. Comput. Chem.* **2009**, *30* (9), 1465–1476. https://doi.org/10.1002/jcc.21165

Jain, P.; Patidar, B.; Bhawsar, J. Potential of Nanoparticles as a Corrosion Inhibitor: A Review. *J. Bio Tribo Corros.* **2020**, *6*, 43. https://doi.org/10.1007/s40735-020-00335-0

Janusz W.; Matysek, M. Coadsorption of Cd(II) and Oxalate Ions at the TiO_2/Electrolyte Solution Interface. *J. Colloid Interface Sci.* **2006**, *296* (1), 22–29. https://doi.org/10.1016/j.jcis.2005.08.067

Johnson, B. N.; Mutharasan, R. pH Effect on Protein G Orientation on Gold Surfaces and Characterization of Adsorption Thermodynamics. *Langmuir* **2012**, *28* (17), 6928–6934. https://doi.org/10.1021/la3009128

Joung, I. S.; Cheatham, T. E. Determination of Alkali and Halide Monovalent Ion Parameters for Use in Explicitly Solvated Biomolecular Simulations. *J. Phys. Chem. B* **2008**, *112* (30), 9020–9041. https://doi.org/10.1021/jp8001614

Joutsuka, T.; Hirano, T.; Sprik, M.; Morita, A. Effect of Third-Order Susceptibility in Sum Frequency Generation Spectroscopy: Molecular Dynamics Study in Liquid Water. *Phys. Chem. Chem. Phys.* **2018**, *20* (5), 3040–3053. https://doi.org/10.1039/C7CP01978E

Kaminski, G. A.; Friesner, R. A.; Tirado-Rives, J.; Jorgensen, W. L. Evaluation and Reparametrization of the OPLS-AA Force Field for Proteins via Comparison with Accurate Quantum Chemical Calculations on Peptides. *J. Phys. Chem. B* **2001**, *105* (28), 6474–6487. https://doi.org/10.1021/jp003919d

Kang, Y.; Li, X.; Tu, Y.; Wang, Q.; Ågren, H. On the Mechanism of Protein Adsorption onto Hydroxylated and Nonhydroxylated TiO_2 Surfaces. *J. Phys. Chem. C* **2010**, *114* (34), 14496–14502. https://doi.org/10.1021/jp1037156

Kann, Z. R.; Skinner, J. L. A Scaled-Ionic-Charge Simulation Model that Reproduces Enhanced and Suppressed Water Diffusion in Aqueous Salt Solutions. *J. Chem. Phys.* **2014**, *141* (10), 104507. https://doi.org/10.1063/1.4894500

Kim, J.; Kim, G.; Cremer, P. S. Investigations of Polyelectrolyte Adsorption at the Solid/Liquid Interface by Sum Frequency Spectroscopy: Evidence for Long-Range Macromolecular Alignment at Highly Charged Quartz/Water Interfaces. *J. Am. Chem. Soc.* **2002**, *124* (29), 8751–8756. https://doi.org/10.1021/ja0263036

Kim, S. Y.; van Duin, A. C. T.; Kubicki, J. D. Molecular Dynamics Simulations of the Interactions between TiO_2 Nanoparticles and Water with Na^+ and Cl^-, Methanol, and Formic Acid using a Reactive Force Field. *J. Mater. Res.* **2012**, *28* (3), 513–520. https://doi.org/10.1557/jmr.2012.367

Kim, S.-Y.; Kumar, N.; Persson, P.; Sofo, J.; van Duin, A. C. T.; Kubicki, J. D. Development of a ReaxFF Reactive Force Field for Titanium Dioxide/Water Systems. *Langmuir* **2013**, *29* (25), 7838–7846. https://doi.org/10.1021/la4006983

Kitamura, A.; Fujiwara, K.; Yamamoto, T.; Nishikawa, S.; Moriyama, H. Analysis of Adsorption Behavior of Cations onto Quartz Surface by Electrical Double-layer Model. *J. Nucl. Sci. Technol.* **1999**, *36* (12), 1167–1175. https://doi.org/10.1080/18811248.1999.9726312

Klyukin, K.; Alexandrov, V. CO_2 Adsorption and Reactivity on Rutile TiO_2(110) in Water: An Ab Initio Molecular Dynamics Study. *J. Phys. Chem. C* **2017**, *121* (19), 10476–10483. https://doi.org/10.1021/acs.jpcc.7b02777

Kohagen, M.; Mason, P. M.; Jungwirth, P. Accurate Description of Calcium Solvation in Concentrated Aqueous Solutions. *J. Phys. Chem. B* **2014**, *118* (28), 7902–7909. https://doi.org/10.1021/jp5005693

Kohagen, M.; Lepsik, M.; Jungwirth, P. Calcium Binding to Calmodulin by Molecular Dynamics with Effective Polarization. *J. Phys. Chem. Lett.* **2014**, *5* (22), 3464–3469. https://doi.org/10.1021/jz502099g

Kohagen, M.; Mason, P. E.; Jungwirth, P. Accounting for Electronic Polarization Effects in Aqueous Sodium Chloride via Molecular Dynamics Aided by Neutron Scattering. *J. Phys. Chem. B* **2015**, *120* (8), 1454–1460. https://doi.org/10.1021/acs.jpcb.5b05221

Kohli, V.; Zhang, Z.; Park, C.; Fenter, P. Rb^+ and Sr^{2+} Adsorption at the TiO_2 (110)−Electrolyte Interface Observed with Resonant Anomalous X-ray Reflectivity. *Langmuir* **2009**, *26* (2), 950–958. https://doi.org/10.1021/la902419z

Kosmulski, M.; Gustafsson, J.; Rosenholm, J. B. Ion Specificity and Viscosity of Rutile Dispersions. *Colloid Polym. Sci.* **1999**, *277*, 550–556. https://doi.org/10.1007/s003960050423

Kosmulski, M. The pH-Dependent Surface Charging and the Points of Zero Charge. *J. Colloid Interface Sci.* **2002**, *253* (1), 77–87. https://doi.org/10.1006/jcis.2002.8490

Kosmulski, M. The pH-Dependent Surface Charging and Points of Zero Charge. *J. Colloid Interface Sci.* **2004**, *275* (1), 214–224. https://doi.org/10.1016/j.jcis.2004.02.029

Kroutil, O.; Chval, Z.; Skelton, A. A.; Předota, M. Computer Simulations of Quartz (101)–Water Interface over a Range of pH Values. *J. Phys. Chem. C* **2015**, *119* (17), 9274–9286. https://doi.org/10.1021/acs.jpcc.5b00096

Kroutil, O.; Předota, M.; Kabeláč, M. Force Field Parametrization of Hydrogenoxalate and Oxalate Anions with Scaled Charges. *J. Mol. Model.* **2017**, *23*, 327. https://doi.org/10.1007/s00894-017-3490-x

Kubicki, J. D.; Sofo, J. O.; Skelton, A. A.; Bandura, A. V. A New Hypothesis for the Dissolution Mechanism of Silicates. *J. Phys. Chem. C* **2012**, *116* (33), 17479–17491. https://doi.org/10.1021/jp300623v

Kumar, A.; Ma, H. L.; Zhang, X.; Huang, K. Y.; Jin, S. B.; Liu, J.;Wei, T.; Cao, W. P.; Zou, G. Z.; Liang, X. J. Gold Nanoparticles Functionalized with Therapeutic and Targeted Peptides for Cancer Treatment. *Biomaterials* **2012**, *33* (4), 1180–1189. https://doi.org/10.1016/j.biomaterials.2011.10.058

Kumar, B.; Jalodia, K.; Kumar, P.; Gautam, H. K. Recent Advances in Nanoparticle-Mediated Drug Delivery. *J. Drug Delivery Sci. Technol.* **2017**, *41*, 260–268. https://doi.org/10.1016/j.jddst.2017.07.019

Laage, D.; Stirnemann, G. Effect of Ions on Water Dynamics in Dilute and Concentrated Aqueous Salt Solutions. *J. Phys. Chem. B* **2019**, *123* (15), 3312–3324. https://doi.org/10.1021/acs.jpcb.9b01053

Laio, A.; Parrinello, M. Escaping Free-Energy Minima. *Proc. Natl. Acad. Sci. U.S.A.* **2002**, *99* (20), 12562–15566. https://doi.org/10.1073/pnas.202427399

Lamoureux, G.; MacKerell Jr., A. D. A Simple Polarizable Model of Water Based on Classical Drude Oscillators. *J. Chem. Phys.* **2003**, *119* (10), 5185–5197. https://doi.org/10.1063/1.1598191

Lan, L.; Yao, Y.; Ping, J.; Ying, Y. Recent Advances in Nanomaterial-Based Biosensors for Antibiotics Detection. *Biosens. Bioelectron.* **2017**, *91*, 504–514. https://doi.org/10.1016/j.bios.2017.01.007

Lee, N.; Sverjensky, D. A.; Hazen, R. M. Cooperative and Competitive Adsorption of Amino Acids with Ca^{2+} on Rutile (α-TiO_2). *Environ. Sci. Technol.* **2014**, *48* (16), 9358–9365. https://doi.org/10.1021/es501980y

Leontyev, I. V.; Stuchebrukhov, A. A. Electronic Continuum Model for Molecular Dynamics Simulations. *J. Chem. Phys.* **2009**, *130* (8), 085102. https://doi.org/10.1063/1.3060164

Leontyev, I. V.; Stuchebrukhov, A. A. Electronic Continuum Model for Molecular Dynamics Simulations of Biological Molecules. *J. Chem. Theory Comput.* **2010**, *6* (5), 1498–1508. https://doi.org/10.1021/ct9005807

Leontyev, I. V.; Stuchebrukhov, A. A. Electronic Polarizability and the Effective Pair Potentials of Water. *J. Chem. Theory Comput.* **2010**, *6* (10), 3153–3161. https://doi.org/10.1021/ct1002048

Leontyev, I.; Stuchebrukhov, A. A. Accounting for Electronic Polarization in Non-Polarizable Force Fields. *Phys. Chem. Chem. Phys.* **2011**, *13* (7), 2613–2626. https://doi.org/10.1039/C0CP01971B

Lindorff-Larsen, K.; Piana, S.; Palmo, K.; Maragakis, P.; Klepeis, J. L.; Dror, R. O.; Shaw, D. E. Improved Side-Chain Torsion Potentials for the Amber Ff99SB Protein Force Field. *Proteins Struct. Funct. Bioinforma.* **2010**, *78* (8), 1950–1958. https://doi.org/10.1002/prot.22711

Livi, K. J. T.; Schaffer, B.; Azzolini, D.; Seabourne, C. R.; Hardcastle, T. P.; Scott, A. J.; Hazen, R. M.; Erlebacher, J. D.; Brydson, R. B.; Sverjensky, D. A. Atomic-Scale Surface Roughness of Rutile and Implications for Organic Molecule Adsorption. *Langmuir* **2013**, *29* (23), 6876–6883. https://doi.org/10.1021/la4005328

Liu, J.; Zhang, G. Recent Advances in Synthesis and Applications of Clay-Based Photocatalysts: a Review. *Phys. Chem. Chem. Phys.* **2014**, *16* (18), 8178–8192. https://doi.org/10.1039/C3CP54146K

Liu, K.; Cao, M.; Fujishima, A.; Jiang, L. Bio-Inspired Titanium Dioxide Materials with Special Wettability and Their Applications. *Chem. Rev.* **2014**, *114* (19), 10044–10094. https://doi.org/10.1021/cr4006796

Lopes, P. E. M.; Murashov, V.; Tazi, M.; Demchuk, E.; MacKerell, A. D. Development of an Empirical Force Field for Silica. Application to the Quartz–Water Interface. *J. Phys. Chem. B* **2006**, *110* (6), 2782–2792. https://doi.org/10.1021/jp055341j

Lu, H.; Wang, J.; Stoller, M.; Wang, T.; Bao, Y.; Hao, H.; Kanchi, S. An Overview of Nanomaterials for Water and Wastewater Treatment. *J Env. Anal Chem.* **2016**, *2016*, 1–10. https://doi.org/10.1155/2016/4964828

Lui, J. Adsorption of DNA onto gold nanoparticles and graphene oxide: surface science and applications. *Phys. Chem. Chem. Phys.* **2012**, *14* (30), 10485–10496. https://doi.org/10.1039/C2CP41186E

Lyklema, J. In *Fundamentals of Interface and Colloid Science*; Academic Press, **1995**; Vol. 2, pp 1–232.

Lyklema, J. Quest for Ion-ion Correlations in Electric Double Layers and Overcharging Phenomena. *Adv. Colloid Interface Sci*. **2009**, *147–148*, 205–213. https://doi.org/10.1016/j.cis.2008.12.002

Ma, Y.; Wang X.; Jia, Y.; Chen, X.; Han, H.; Li, C. Titanium Dioxide-Based Nanomaterials for Photocatalytic Fuel Generations. *Chem. Rev.* **2014**, *114* (19), 9987–10043. https://doi.org/10.1021/cr500008u

Machesky, M. L.; Předota, M.; Wesolowski, D. J.; Vlcek, L.; Cummings, P. T.; Rosenqvist, J.; Ridley, M. K.; Kubicki, J. D.; Bandura, A. V.; Kumar, N.; Sofo, J. O. Surface Protonation at the Rutile (110) Interface: Explicit Incorporation of Solvation Structure within the Refined MUSIC Model Framework. *Langmuir* **2008**, *24* (21) 12331–12339. https://doi.org/10.1021/la801356m

Machesky, M.; Wesolowski, D.; Rosenqvist, J.; Předota, M.; Vlcek, L.; Ridley, M.; Kohli, V.; Zhang, Z.; Fenter, P.; Cummings, P.; Lvov, S.; Fedkin, M.; Rodriguez-Santiago, V.; Kubicki, J.; Bandura, A. Comparison of Cation Adsorption by Isostructural Rutile and Cassiterite. *Langmuir* **2011**, *27* (8), 4585–4593. https://doi.org/10.1021/la1040163

Machesky, M. L.; Předota, M.; Ridley, M. K.; Wesolowski, D. J. Constrained Surface Complexation Modeling: Rutile in RbCl, NaCl, and $NaCF_3SO_3$ Media to 250 °C. *J. Phys. Chem. C* **2015**, *119* (27), 15204–15215. https://doi.org/10.1021/acs.jpcc.5b02841

MacKerell, A. D., Jr.; Bashford, D.; Bellott, M.; Dunbrack, R. L.,Jr.; Evanseck, J. D.; Field, M. J.; Fischer, S.; Gao, J.; Guo, H.; Ha, S.; et al. All-Atom Empirical Potential for Molecular Modeling and Dynamics Studies of Proteins. *J. Phys. Chem. B* **1998**, *102* (18), 3586–3616. https://doi.org/10.1021/jp973084f

MacKerell, A. D.; Feig, M.; Brooks, C. L. Extending the Treatment of Backbone Energetics in Protein Force Fields: Limitations of Gas-Phase Quantum Mechanics in Reproducing Protein Conformational Distributions in Molecular Dynamics Simulation. *J. Comput. Chem.* **2004**, *25* (11), 1400–1415. https://doi.org/10.1002/jcc.20065

Marx, K. A. Quartz Crystal Microbalance: A Useful Tool for Studying Thin Polymer Films and Complex Biomolecular Systems at the Solution−Surface Interface. *Biomacromolecules* **2003**, *4* (5), 1099–1120. https://doi.org/10.1021/bm020116i

Martinek, T.; Duboué-Dijon, E.; Timr, S.; Mason, P. E.; Baxová, K.; Fischer, H. E.; Schmidt, B.; Pluhařová, E.; Jungwirth, P. Calcium Ions in Aqueous Solutions: Accurate Force Field Description Aided by Ab Initio Molecular Dynamics and Neutron Scattering. *J. Chem. Phys.* **2018**, *148* (22), 222813. https://doi.org/10.1063/1.5006779

Mason P. E.; Wernersson E.; Jungwirth P. Accurate Description of Aqueous Carbonate Ions: An Effective Polarization Model Verified by Neutron Scattering. *J. Phys. Chem. B* **2012**, *116* (28), 8145–8153. https://doi.org/10.1021/jp3008267

Matsui, M.; Akaogi, M. Molecular Dynamics Simulation of the Structural and Physical Properties of the Four Polymorphs of TiO_2. *Mol. Simul.* **1991**, *6* (4–6), 239–244. https://doi.org/10.1080/08927029108022432

Medina, L.; Ansari, F.; Carosio, F.; Salajkova, M.; Berglund, L. A. Nanocomposites from Clay, Cellulose Nanofibrils, and Epoxy with Improved Moisture Stability for Coatings and Semistructural Applications. *ACS Appl. Nano Mater.* **2019**, *2* (5), 3117–3126. https://doi.org/10.1021/acsanm.9b00459

Melcr, J.; Martinez-Seara, H.; Nencini, R.; Kolafa, J.; Jungwirth, P.; Ollila, O. H. S. Accurate Binding of Sodium and Calcium to a POPC Bilayer by Effective Inclusion of Electronic Polarization. *J. Phys. Chem. B* **2018**, *122* (16), 4546–4557. https://doi.org/10.1021/acs.jpcb.7b12510

Melcr, J.; Ferreira, T. M.; Jungwirth, P.; Ollila, O. H. S. Improved Cation Binding to Lipid Bilayers with Negatively Charged POPS by Effective Inclusion of Electronic Polarization. *J. Chem. Theory Comput.* **2020**, *16* (1), 738-748. https://doi.org/10.1021/acs.jctc.9b00824

Mendive, C. B.; Bahnemann, D. W.; Blesa, M. A. Microscopic Characterization of the Photocatalytic Oxidation of Oxalic Acid Adsorbed onto TiO_2 by FTIR-ATR. *Catal. Today* **2005**, *101* (3–4), 237–244. https://doi.org/10.1016/j.cattod.2005.03.016

Mendive, C. B.; Bredow, T.; Blesa, M. A.; Bahnemann, D. W. ATR-FTIR Measurements and Quantum Chemical Calculations Concerning the Adsorption and Photoreaction of Oxalic Acid on TiO_2. *Phys. Chem. Chem. Phys.* **2006**, *8* (27), 3232–3247. https://doi.org/10.1039/B518007B

Mendive, C. B.; Blesa, M. A.; Bahnemann, D. W. The Adsorption and Photodegradation of Oxalic Acid at the TiO_2 Surface. *Water Sci. Technol.* **2007**, *55* (12), 139–145. https://doi.org/10.2166/wst.2007.398

Mendive, C. B.; Bredow, T.; Feldhoff, A.; Blesa, M. A.; Bahnemann, D. W. Adsorption of Oxalate on Rutile Particles in Aqueous Solutions: a Spectroscopic, Electron-Microscopic and Theoretical Study. *Phys. Chem. Chem. Phys.* **2008**, *10* (14), 1960–1974. https://doi.org/10.1039/B800140P

Mendive, C. B.; Bredow, T.; Feldhoff, A.; Blesa, M. A.; Bahnemann, D. W. Adsorption of Oxalate on Anatase (100) and Rutile (110) Surfaces in Aqueous Systems: Experimental Results vs. Theoretical Predictions. *Phys. Chem. Chem. Phys.* **2009**, *11* (11), 1794–1808. https://doi.org/10.1039/B814608J

Monti, S.; Walsh, T. R. Free Energy Calculations of the Adsorption of Amino Acid Analogues at the Aqueous Titania Interface. *J. Phys. Chem. C* **2010**, *114* (50), 22197–22206. https://doi.org/10.1021/jp107859q

Mori, T.; Hamers, R. J.; Pedersen, J. A.; Cui, Q. An Explicit Consideration of Desolvation is Critical to Binding Free Energy Calculations of Charged Molecules at Ionic Surfaces. *J. Chem. Theory Comput.* **2013**, *9* (11), 5059–5069. https://doi.org/10.1021/ct400487e

Murray, H. H. Overview – Clay Mineral Applications. *Appl. Clay Sci.* **1991**, *5* (5–6), 379–395. https://doi.org/10.1016/0169-1317(91)90014-Z

Nawrocki, G.; Cieplak, M. Aqueous Amino Acids and Proteins Near the Surface of Gold in Hydrophilic and Hydrophobic Force Fields. *J. Phys. Chem. C* **2014**, *118* (24), 12929–12943. https://doi.org/10.1021/jp5030558

Nguyen, M.; Rick, S. W. The Influence of Polarizability and Charge Transfer on Specific Ion Effects in the Dynamics of Aqueous Salt Solutions. *J. Chem. Phys.* **2018**, *148* (22), 222803. https://doi.org/10.1063/1.5012682

Nikitin, A.; Del Frate, G. Development of Nonbonded Models for Metal Cations using the Electronic Continuum Correction. *J. Comp. Chem.* **2018**, *40* (28), 2464–2472. https://doi.org/10.1002/jcc.26021

Nitzan, A.; Ratner, M. A. Electron Transport in Molecular Wire Junctions. S*cience* **2003**, *300* (5624), 1384–1389. https://doi.org/10.1126/science.1081572

Nosé, S. A Molecular Dynamics Method for Simulations in the Canonical Ensemble. *Mol. Phys.* **1983**, 5*2* (2), 255–268. https://doi.org/10.1080/00268978400101201

Ohno, P. E.; Saslow, S. A.; Wang, H.-F.; Geiger, F. M.; Eisenthal, K. B. Phase-Referenced Nonlinear Spectroscopy of the α-Quartz/Water Interface. *Nat. Commun.* **2016**, *7*, 13587. https://doi.org/10.1038/ncomms13587

Oostenbrink, C.; Villa, A.; Mark, A. E.; Van Gunsteren, W. F. A Biomolecular Force Field Based on the Free Enthalpy of Hydration and Solvation: The GROMOS Force-Field Parameter Sets 53A5 and 53A6. *J. Comput. Chem.* 2004, *25* (13), 1463–1472. https://doi.org/10.1002/jcc.20090

Ostroverkhov, V.; Waychunas, G. A.; Shen, Y. R. Vibrational Spectra of Water at Water/α-Quartz (0001) Interface. *Chem. Phys. Lett.* **2004**, *386* (1–3), 144–148. https://doi.org/10.1016/j.cplett.2004.01.047

Panyala, N. R.; Peña-Méndez, E. M.; Havel, J. Gold and Nano-Gold in Medicine: Overview, Toxicology and Perspectives. *J. Appl. Biomed.* **2009**, *7*, 75–91. https://doi.org/10.32725/jab.2009.008

Parez, S.; Předota, M. Determination of the Distance-Dependent Viscosity of Mixtures in Parallel Slabs using Non-Equilibrium Molecular Dynamics. *Phys. Chem. Chem. Phys.* **2012**, *14* (10), 3640–3650. https://doi.org/10.1039/C2CP22136E

Parez, S.; Předota, M.; Machesky, M. L. Dielectric Properties of Water at Rutile and Graphite Surfaces: Effect of Molecular Structure. *J. Phys. Chem. C* **2014**, *118* (9), 4818–4834. https://doi.org/10.1021/jp4128012

Paricaud, P.; Předota, M.; Chialvo, A. A.; Cummings, P. T. From Dimer to Condensed Phases at Extreme Conditions: Accurate Predictions of the Properties of Water by a Gaussian Charge Polarizable Model. *J. Chem. Phys.* **2004**, *122* (24), 244511. https://doi.org/10.1063/1.1940033

Parikh, S. J.; Kubicki, J. D.; Jonsson, C. M.; Jonsson, C. L.; Hazen, R. M.; Sverjensky, D. A.; Sparks, D. L. Evaluating Glutamate and Aspartate Binding Mechanisms to Rutile (α-TiO2) via ATR-FTIR Spectroscopy and Quantum Chemical Calculations. *Langmuir* **2011**, *27* (5), 1778–1787. https://doi.org/10.1021/la103826p

Pegado, L.; Marsalek, O.; Jungwirth, P.; Wernersson, E. Solvation and Ion-Pairing Properties of the Aqueous Sulfate Anion: Explicit *versus* Effective Electronic Polarization. *Phys. Chem. Chem. Phys.* **2012**, *14* (29), 10248–10257. https://doi.org/10.1039/C2CP40711F

Peters, R. J. B.; Bouwmeester, H.; Gottardo, S.; Amenta, V.; Arena, M.; Brandhoff, P.; Marvin, H. J. P.; Mech, A.; Moniz, F. B.; Pesudo, L. Q.; et al. Nanomaterials for Products and Application in Agriculture, Feed and Food. *Trends Food Sci. Technol.* **2016**, *54*, 155–164. https://doi.org/10.1016/j.tifs.2016.06.008

Plimpton, S. Fast Parallel Algorithms for Short-Range Molecular Dynamics. *J. Comput. Phys.* **1995**, *117* (1), 1–19. https://doi.org/10.1006/jcph.1995.1039

Pluhařová, E.; Mason P. E.; Jungwirth P. Ion Pairing in Aqueous Lithium Salt Solutions with Monovalent and Divalent Counter–Anions. *J. Phys. Chem. A* **2013**, *117* (46), 11766–11773. https://doi.org/10.1021/jp402532e

Pluhařová, E.; Fischer, H. E.; Mason, P. E.; Jungwirth, P. Hydration of the Chloride Ion in Concentrated Aqueous Solutions using Neutron Scattering and Molecular Dynamics. *Mol. Phys.* **2014**, *112* (9–10), 1230–1240. https://doi.org/10.1080/00268976.2013.875231

Pouvreau, M.; Greathouse, J. A.; Cygan, R. T.; Kalinichev, A. G. Structure of Hydrated Gibbsite and Brucite Edge Surfaces: DFT Results and Further Development of the ClayFF Classical Force Field with Metal–O–H Angle Bending Terms. *J. Phys. Chem. C* **2017**, *121* (27), 14757–14771. https://doi.org/10.1021/acs.jpcc.7b05362

Pouvreau, M.; Greathouse, J. A.; Cygan, R. T.; Kalinichev, A. G. Structure of Hydrated Kaolinite Edge Surfaces: DFT Results and Further Development of the ClayFF Classical Force Field with Metal–O–H Angle Bending Terms. *J. Phys. Chem. C* **2019**, *123* (18), 11628–11638. https://doi.org/10.1021/acs.jpcc.9b00514

Prasad, R.; Bhattacharyya, A.; Nguyen, Q. D. Nanotechnology in Sustainable Agriculture: Recent Developments, Challenges, and Perspectives. *Front. Microbiol.* **2017**, *8*, 1014. https://doi.org/10.3389/fmicb.2017.01014

Předota, M.; Bandura, A. V.; Cummings, P. T.; Kubicki, J. D.; Wesolowski, D. J.; Chialvo, A. A.; Machesky, M. L. Electric Double Layer at the Rutile (110) Surface. 1. Structure of Surfaces and Interfacial Water from Molecular Dynamics by Use of ab Initio Potentials. *J. Phys. Chem. B* **2004**, *108* (32), 12049–12060. https://doi.org/10.1021/jp037197c

Předota, M.; Zhang, Z.; Fenter, P.; Wesolowski, D. J., Cummings, P. T. Electric Double Layer at the Rutile (110) Surface. 2. Adsorption of Ions from Molecular Dynamics and X-ray Experiments. *J. Phys. Chem. B* **2004**, *108* (32), 12061–12072. https://doi.org/10.1021/jp037199x

Předota, M.; Vlček, L. Comment on Parts 1 and 2 of the Series "Electric Double Layer at the Rutile (110) Surface". *J. Phys. Chem. B* **2007**, *111* (5), 1245–1247. https://doi.org/10.1021/jp068250a

Předota, M.; Cummings, P. T; Wesolowski, D. J. Electric Double Layer at the Rutile (110) Surface. 3. Inhomogeneous Viscosity and Diffusivity Measurement by Computer Simulations. *J. Phys. Chem. C* **2007**, 111 (7), 3071–3079. https://doi.org/10.1021/jp065165u

Předota, M.; Machesky, M. L.; Wesolowski, D. J.; Cummings, P. T. Electric Double Layer at the Rutile (110) Surface. 4. Effect of Temperature and pH on the Adsorption and Dynamics of Ions. *J. Phys. Chem. C* **2013**, *117* (44), 22852–22866. https://doi.org/10.1021/jp407124p

Předota, M.; Machesky, M. L.; Wesolowski, D. J. Molecular Origins of the Zeta Potential. *Langmuir* **2016**, *32* (40), 10189–10198. https://doi.org/10.1021/acs.langmuir.6b02493

Quezada, G. R.; Rozas, R. E.; Toledo, P. G. Molecular Dynamics Simulations of Quartz (101)–Water and Corundum (001)–Water Interfaces: Effect of Surface Charge and Ions on Cation Adsorption, Water Orientation, and Surface Charge Reversal. *J. Phys. Chem. C* **2017**, *121* (45), 25271–25282. https://doi.org/10.1021/acs.jpcc.7b08836

Quezada, G. R.; Jeldres, R. I.; Fawell, P. D.; Toledo, P. G. Use of Molecular Dynamics to Study the Conformation of an Anionic Polyelectrolyte in Saline Medium and its Adsorption on a Quartz Surface. *Minerals Engineering* **2018**, *129*, 102–105. https://doi.org/10.1016/j.mineng.2018.09.025

Rai, M.; Ingle, A. P.; Gupta, I.; Brandelli, A. Bioactivity of noble metal nanoparticles decorated with biopolymers and their application in drug delivery. *Int. J. Pharm.* **2015** *496* (2), 159-172. https://doi.org/10.1016/j.ijpharm.2015.10.059

Rajh, T.; Dimitrijevic, N. M.; Bissonnette, M.; Koritarov, T.; Konda, V. Titanium Dioxide in the Service of the Biomedical Revolution. *Chem. Rev.* **2014**, *114* (19), 10177–10216. https://doi.org/10.1021/cr500029g

Rehman, F. U.; Zhao, C.; Jiang, H.; Wang, X. Biomedical Applications of Nano-Titania in Theranostics and Photodynamic Therapy. *Biomater. Sci.* **2016**, *4* (1), 40–54. https://doi.org/10.1039/C5BM00332F

Ren, W.; Zeng, L.; Shen, Z.; Xiang, L.; Gong, A.; Zhang, J.; Mao, C.; Li, A.; Paunesku, T.; Woloschak, G. E.; et al. Enhanced Doxorubicin Transport to Multidrug Resistant Breast Cancer Cells via TiO_2 Nanocarriers. *RSC Adv.* **2013**, *3* (43), 20855–20861. https://doi.org/10.1039/C3RA42863J

Rimsza, J. M.; Jones, R. E.; Criscenti, L. J. Surface Structure and Stability of Partially Hydroxylated Silica Surfaces. *Langmuir* **2017**, *33* (15), 3882–3891. https://doi.org/10.1021/acs.langmuir.7b00041

Rimsza, J. M.; Jones, R. E.; Criscenti, L. J. Interaction of NaOH Solutions with Silica Surfaces. *J. Coll. Interface Sci.* **2018**, *516*, 128–137. https://doi.org/10.1016/j.jcis.2018.01.049

Ruiz, M. P.; Aragones, A. C.; Camarero, N.; Vilhena, J. G.; Ortega,M.; Zotti, L. A.; Perez, R.; Carlos Cuevas, J.; Gorostiza, P.; Diez-Perez, I. Bioengineering a Single-Protein Junction. *J. Am. Chem. Soc.* **2017**, *139* (43), 15337–15346. https://doi.org/10.1021/jacs.7b06130

Satterthwaite, P. F.; Scheuermann, A. G.; Hurley, P. K.; Chidsey, C. E. D.; McIntyre, P. C. Engineering Interfacial Silicon Dioxide for Improved Metal–Insulator–Semiconductor Silicon Photoanode Water Splitting Performance. *ACS Appl. Mater. Interfaces* **2016**, *8* (20), 13140–13149. https://doi.org/10.1021/acsami.6b03029

Savory, D. M.; Warren, D. S.; McQuillan, A. J. Shallow Electron Trap, Interfacial Water, and Outer-Sphere Adsorbed Oxalate IR Absorptions Correlate during UV Irradiation of Photocatalytic TiO_2 Films in Aqueous Solution. *J. Phys. Chem. C* **2011**, *115* (4), 902–907. https://doi.org/10.1021/jp102723u

Schlegel, M. L.; Nagy, K. L.; Fenter, P.; Sturchio, N. C. Structures of Quartz (1010)- and (1011)-Water Interfaces Determined by X-ray Reflectivity and Atomic Force Microscopy of Natural Growth Surfaces. *Geochim. Cosmochim. Acta* **2002**, *66* (17), 3037–3054. https://doi.org/10.1016/S0016-7037(02)00912-2

Schlick, T. *Molecular Modeling and Simulation: an Interdisciplinary Guide;* Springer: New York, NY, **2002**. https://doi.org/10.1007/978-1-4419-6351-2

Shiba, K. Exploitation of Peptide Motif Sequences and Their Use in Nanobiotechnology. *Curr. Opin. Biotechnol.* **2010**, *21* (4), 412–425. https://doi.org/10.1016/j.copbio.2010.07.008

Singh, J.; Gusain, A.; Saxena, V.; Chauhan, A. K.; Veerender, P.; Koiry, S. P.; Jha, P.; Jain, A.; Aswal, D. K.; Gupta, S. K. XPS, UV–Vis, FTIR, and EXAFS Studies to Investigate the Binding Mechanism of N719 Dye onto Oxalic Acid Treated TiO_2 and Its Implication on Photovoltaic Properties. *J. Phys. Chem. C* **2013**, *117* (41), 21096–21104. https://doi.org/10.1021/jp4062994

Siriwardana, K.; Wang, A.; Vangala, K.; Fitzkee, N.; Zhang, D. Probing the Effects of Cysteine Residues on Protein Adsorption onto Gold Nanoparticles using Wild-Type and Mutated GB3 Proteins. *Langmuir* **2013**, *29* (35), 10990–10996. https://doi.org/10.1021/la402239h

Skelton, A. A.; Liang, T.; Walsh, T. R. Interplay of Sequence, Conformation, and Binding at the Peptide–Titania Interface as Mediated by Water. *ACS Appl. Mater. Interfaces* **2009**, *1* (7), 1482–1491. https://doi.org/10.1021/am9001666

Skelton, A. A.; Fenter, P.; Kubicki, J. D.; Wesolowski, D. J.; Cummings, P. T. Simulations of the Quartz(1011)/Water Interface: A Comparison of Classical Force Fields, Ab Initio Molecular Dynamics, and X-ray Reflectivity Experiments. *J. Phys. Chem. C* **2011**, *115* (5), 2076–2088. https://doi.org/10.1021/jp109446d

Skelton, A. A.; Wesolowski, D. J.; Cummings, P. T. Investigating the Quartz (1010)/Water Interface using Classical and Ab Initio Molecular Dynamics. *Langmuir* **2011**, *27* (14), 8700–8709. https://doi.org/10.1021/la2005826

Smith, W. R.; Nezbeda, I.; Kolafa, J.; Moučka, F. Recent Progress in the Molecular Simulation of Thermodynamic Properties of Aqueous Electrolyte Solutions. *Fluid Phase Equilib.* **2018**, *466*, 19–30. https://doi.org/10.1016/j.fluid.2018.03.006

Stern, H. O. Zur theorie der elektrolytischen doppelschicht. *Zeitschrift für Elektrochemie Angew. Phys. Chemie* **1924**, 30 (21–22), 508–516. https://doi.org/10.1002/bbpc.192400182

Sultan, A. M.; Hughes, Z. E.; Walsh, T. R. Binding Affinities of Amino Acid Analogues at the Charged Aqueous Titania Interface: Implications for Titania-Binding Peptides. *Langmuir* **2014**, *30* (44), 13321–13329. https://doi.org/10.1021/la503312d

Sultan, A. M.; Westcott, Z. C.; Hughes, Z. E.; Palafox-Hernandez, J. P.; Giesa, T.; Puddu, V.; Buehler, M. J.; Perry, C. C.; Walsh, T. R. Aqueous Peptide–TiO2 Interfaces: Isoenergetic Binding via Either Entropically or Enthalpically Driven Mechanisms. *ACS Appl. Mater. Interfaces* **2016**, *8* (28), 18620–18630. https://doi.org/10.1021/acsami.6b05200

Tolmachev, D. A.; Boyko, O. S.; Lukasheva, N. V.; Martinez-Seara, H.; Karttunen, M. Overbinding and Qualitative and Quantitative Changes Caused by Simple Na^+ and K^+ Ions in Polyelectrolyte Simulations: Comparison of Force Fields with and without NBFIX and ECC Corrections. *J. Chem. Theory Comput.* **2020**, *16* (1), 677–687. https://doi.org/10.1021/acs.jctc.9b00813

Tu, W.; Dong, Y.; Lei, J.; Ju, H. Low-Potential Photoelectrochemical Biosensing using Porphyrin-Functionalized TiO_2 Nanoparticles. *Anal. Chem.* **2010**, *82* (20), 8711–8716. https://doi.org/10.1021/ac102070f

Van der Spoel, D.; Lindahl, E.; Hess, B.; Groenhof, G.; Mark, A. E.; Berendsen, H. J. C. GROMACS: Fast, Flexible, and Free. *J. Comput. Chem.* **2005**, *26* (16), 1701–1718. https://doi.org/10.1002/jcc.20291

Van Duin, A. C. T.; Strachan, A.; Stewman, S.; Zhang, Q.; Xu, X.; Goddard, W. A. $ReaxFF_{SiO}$ Reactive Force Field for Silicon and Silicon Oxide Systems. *J. Phys. Chem. A* **2003**, *107* (19), 3803–3811. https://doi.org/10.1021/jp0276303

Vazdar, M.; Pluhařová E.; Mason, P. E.; Vacha, P.; Jungwirth, P. Ions at Hydrophobic Aqueous Interfaces: Molecular Dynamics with Effective Polarization. *J. Phys. Chem. Lett.* **2012**, *3* (15), 2087–2091. https://doi.org/10.1021/jz300805b

Vazdar M.; Jungwirth P.; Mason P. E. Aqueous Guanidinium–Carbonate Interactions by Molecular Dynamics and Neutron Scattering: Relevance to Ion–Protein Interactions. *J. Phys. Chem. B* **2013**, *117* (6), 1844–1848. https://doi.org/10.1021/jp310719g

Vega, C. Water: One Molecule, Two Surfaces, One Mistake. *Mol. Phys.* **2015**, *113* (9–10), 1145–1163. https://doi.org/10.1080/00268976.2015.1005191

Venditti, I. Engineered Gold-Based Nanomaterials: Morphologies and Functionalities in Biomedical Applications. A Mini Review. *Bioengineering* **2019** *6* (2), 53–78. https://doi.org/10.3390/bioengineering6020053

Vlček, L.; Zhang, Z.; Machesky, M. L.; Fenter, P.; Rosenqvist, J.; Wesolowski, D. J.; Anovitz, L. M.; Předota, M.; Cummings, P. T. Electric Double Layer at Metal Oxide Surfaces: Static Properties of the Cassiterite–Water Interface. *Langmuir* **2007**, *23* (9), 4925–4937. https://doi.org/10.1021/la063306d

Wang, Q.; Yan, J.; Yang, J.; Li, B. Nanomaterials Promise Better Bone Repair. *Mater. Today* **2016**, *19* (8), 451–463. https://doi.org/10.1016/j.mattod.2015.12.003

Wechsler, D.; Fernández, C. C.; Steinrück, H.-P.; Lytken, O.; Williams, F. J. Covalent Anchoring and Interfacial Reactions of Adsorbed Porphyrins on Rutile TiO_2(110). *J. Phys. Chem. C* **2018**, *122* (8), 4480–4487. https://doi.org/10.1021/acs.jpcc.7b12717

Weir, A.; Westerhoff, P.; Fabricius, L.; Hristovski, K.; Goetz, N. Titanium Dioxide Nanoparticles in Food and Personal Care Products. *Environ. Sci. Technol.* **2012**, *46* (4), 2242–2250. https://doi.org/10.1021/es204168d

Weisz, A. D.; Rodenas; L. G.; Morando, P. J.; Regazzoni, A. E.; Blesa, M. A. FTIR Study of the Adsorption of Single Pollutants and Mixtures of Pollutants onto Titanium Dioxide in Water: Oxalic and Salicylic Acids. *Catal. Today* **2002**, *76* (2–4), 103–112. https://doi.org/10.1016/S0920-5861(02)00210-9

Wold, A. Photocatalytic Properties of Titanium Dioxide (TiO_2). *Chem. Mater.* **1993**, *5* (3), 280–283. https://doi.org/10.1021/cm00027a008

Wright, L. B.; Walsh, T. R. Facet Selectivity of Binding on Quartz Surfaces: Free Energy Calculations of Amino-Acid Analogue Adsorption. *J. Phys. Chem. C* **2012**, *116* (4), 2933–2945. https://doi.org/10.1021/jp209554g

Wright, L. B.; Rodger, P. M.; Corni, S.; Walsh, T. R. GolP-CHARMM: First-Principles Based Force Fields for the Interaction of Proteins with Au(111) and Au(100). *J. Chem. Theory Comput.* **2013**, *9* (3), 1616–1630. https://doi.org/10.1021/ct301018m

Wu, C.; Chen, M.; Xing, C. Molecular Understanding of Conformational Dynamics of a Fibronectin Module on Rutile (110) Surface. *Langmuir* **2010**, *26* (20), 15972–15981. https://doi.org/10.1021/la103010c

Wu, S.; Weng, Z.; Liu, X.; Yeung, K. W. K.; Chu, P. K. Functionalized TiO_2 Based Nanomaterials for Biomedical Applications. *Adv. Funct. Mater.* **2014**, *24* (35), 5464–5481. https://doi.org/10.1002/adfm.201400706

Xie, W. J.; Zhang, Z.; Gao; Y. Q. Ion Pairing in Alkali Nitrate Electrolyte Solutions. *J. Phys. Chem. B* **2016**, *120* (9), 2343–2351. https://doi.org/10.1021/acs.jpcb.5b10755

Xin, Y. R.; Yin, M. M.; Zhao, L. Y.; Meng, F. L.; Luo, L. Recent Progress on Nanoparticle-Based Drug Delivery Systems for Cancer Therapy. *Cancer Biol. Med.* **2017**, *14* (3), 228–241. https://doi.org/10.20892/j.issn.2095-3941.2017.0052

Yadav, S.; Chandra, A. Preferential Solvation, Ion Pairing, and Dynamics of Concentrated Aqueous Solutions of Divalent Metal Nitrate salts. *J. Chem. Phys.* **2017**, *147* (24), 244503. https://doi.org/10.1063/1.4996273

Yang, C.; Yu, Y.; Linden, B.; Wu J. C. S.; Mul, G. Artificial Photosynthesis over Crystalline TiO_2-Based Catalysts: Fact or Fiction? *J. Am. Chem. Soc.* **2010**, *132* (24), 8398–8406. https://doi.org/10.1021/ja101318k

Yang, X.; Yang, M.; Pang, B.; Vara, M.; Xia, Y. Gold Nanomaterials at Work in Biomedicine. *Chem. Rev.* **2015**, *115* (19), 10410–10488. https://doi.org/10.1021/acs.chemrev.5b00193

YazdanYar, A.; Aschauer, U.; Bowen, P. Adsorption Free Energy of Single Amino Acids at the Rutile (110)/Water Interface Studied by Well-Tempered Metadynamics. *J. Phys. Chem. C* **2018**, *122* (21), 11355–11363. https://doi.org/10.1021/acs.jpcc.7b12614

Yeh, I.-C.; Berkowitz, M. L. Ewald Summation for Systems with Slab Geometry. *J. Chem. Phys.* **1999**, *111* (7), 3155–3162. https://doi.org/10.1063/1.479595

Yin, Z. F.; Wu, L.; Yang, H. G.; Su, Y. H. Recent Progress in Biomedical Applications of Titanium Dioxide. *Phys. Chem. Chem. Phys.* **2013**, *15* (14), 4844–4858. https://doi.org/10.1039/C3CP43938K

Young, A. G.; McQuillan, A. J. Adsorption/Desorption Kinetics from ATR-IR Spectroscopy. Aqueous Oxalic Acid on Anatase TiO_2. *Langmuir* **2009**, *25* (6), 3538–3548. https://doi.org/10.1021/la803116n

Yue, S.; Panagiotopoulos, A. Z. Dynamic Properties of Aqueous Electrolyte Solutions from Non-Polarisable, Polarisable, and Scaled-Charge Models. *Mol. Phys.* **2019**, 117 (23–24), 3538–3549. https://doi.org/10.1080/00268976.2019.1645901

Zaera, F. Probing Liquid/Solid Interfaces at the Molecular Level. *Chem. Rev.* **2012**, *112* (5), 2920–2986. https://doi.org/10.1021/cr2002068

Zeron, I. M.; Abascal, J. L. F.; Vega, C. A Force Field of Li^+, Na^+, K^+, Mg^{2+}, Ca^{2+}, Cl^-, and SO_4^{2-} in Aqueous Solution Based on the TIP4P/2005 Water Model and Scaled Charges for the Ions. *J. Chem. Phys.* **2019**, *151* (13), 134504. https://doi.org/10.1063/1.5121392

Zhang, H.; Banfield, J. F. Structural Characteristics and Mechanical and Thermodynamic Properties of Nanocrystalline TiO_2. *Chem. Rev.* **2014**, *114* (19), 9613–9644. https://doi.org/10.1021/cr500072j

Zhang, Q.; Uchaker, E.; Candelaria, S. L.; Cao, G. Nanomaterials for Energy Conversion and Storage. *Chem. Soc. Rev*. **2013**, *42* (7), 3127–3171. https://doi.org/10.1039/C3CS00009E

Zhang, Z.; Fenter, P.; Cheng, L.; Sturchio, N. C.; Bedzyk, M. J.; Předota, M.; Bandura, A.; Kubicki, J. D.; Lvov, S. N.; Cummings, P. T.; et al. J. Ion Adsorption at the Rutile–Water Interface: Linking Molecular and Macroscopic Properties. *Langmuir* **2004**, *20* (12), 4954–4969. https://doi.org/10.1021/la0353834

Article DB1

Biriukov, D.; Kroutil, O.; Předota M.

Modeling of Solid–Liquid Interfaces using Scaled Charges: Rutile (110) Surfaces

Physical Chemistry Chemical Physics **2018**, *20* (37), 23954–23966;
IF (2018) = 3.567

Participation of Denys Biriukov:

DB prepared molecular models for both rutile surfaces and ions, performed all the molecular simulations, analyzed the results using pre-implemented and self-written utilities, and was the key person in the paper writing.

DOI: 10.1039/C8CP04535F.

PCCP

PAPER

Cite this: *Phys. Chem. Chem. Phys.*, 2018, **20**, 23954

Modeling of solid–liquid interfaces using scaled charges: rutile (110) surfaces†

Denys Biriukov, [a] Ondřej Kroutil [ab] and Milan Předota *[a]

Received 17th July 2018,
Accepted 31st August 2018

DOI: 10.1039/c8cp04535f

rsc.li/pccp

Electronic continuum correction (ECC) has been proven to bring significant improvement in the modeling of interactions of ions (especially multivalent) in aqueous solutions. We present a generalization and the first application of this approach to modeling solid–liquid interfaces, which are omnipresent in physical chemistry, geochemistry, and biophysics. Scaling charges of the top layer of surface atoms makes the existing solid models compatible with the ECC models of ions and molecules, allowing the use of modified force fields for a more accurate investigation of interactions of various metal and metal-oxide surfaces with aqueous solutions, including complex biomolecules and multivalent ions. We have reparametrized rutile (110) models with different surface charge densities (from 0 to −0.416 C m^{-2}) and adopted/developed scaled charge force fields for ions, namely Na^+, Rb^+, Sr^{2+}, and Cl^-. A good agreement of the obtained molecular dynamics (MD) data with X-ray experiments and previously reported MD results was observed, but changes in the occupancy of various adsorption sites were observed and discussed in detail.

1. Introduction

Solid–liquid interfaces attract a lot of scientific attention due to the ubiquitous occurrence of adsorption processes in a wide range of natural and industrial environments, since the surface of any material is the principal pathway for its interaction with the surrounding environment. It is well known that chemical reactions between mineral surfaces and aqueous solutions play a crucial role in corrosion, soil production, chemical weathering, degradation of building materials, and transformation of environmental contaminants and pollutants. Therefore, the examination of these phenomena is a challenging task for today's scientists. Many experimental techniques like resonant anomalous X-ray reflectivity and X-ray standing wave measurements,[1,2] nonlinear spectroscopy,[3,4] and flow microcalorimetric measurements[5] have been applied to explore the properties of different compounds at mineral–fluid interfaces. On the other hand, theoretical approaches such as density functional theory, *ab initio* molecular dynamics, and classical molecular dynamics (MD) greatly improved the molecular-level understanding of processes occurring at interfaces.[6–10]

Titanium dioxide has been a subject of numerous works due to its simplicity and importance in comparison with other minerals being used in nanotechnology and nanoscience.[11] High physical and chemical stability makes TiO_2 nanoparticles of particular interest for many applications in biosensors,[12] consumer production,[13] and medicine.[14,15] Moreover, different forms of titanium surfaces show a high photocatalytic activity.[16] The rutile surface, which is the most stable form of titanium dioxide under ambient conditions,[17] and in particular its predominant (110) stable crystal face, has been a subject of many theoretical and experimental studies, separately and in combination. Numerous studies measured the pH dependence of the surface charge and the point of the zero net charge,[18] multilayer formation of the adsorbed water on the surface,[19] and an electric double layer (EDL) at the interface.[20] Further studies were aimed at the adsorption of ions[21,22] and organic compounds, *e.g.* dicarboxylic acids, amino acids, and nucleic acids.[23–25] Particular attention was devoted to the hydration of the surface, *i.e.* water molecules physically adsorbed on the bare terminal Ti atoms or dissociatively chemisorbed to form OH groups at both bridging and terminal sites.[26,27] Other works also provided information about the surface steps and the influence of such defects on the adsorption processes.[28,29] Great contribution to the understanding of the TiO_2–water interface has been made by MD simulations,[30] both with a classical approach[31,32] and using a reactive force field, where the formation and breaking of covalent bonds are allowed.[33–35]

Here, we continue our series of articles focused on modeling α-rutile (110) surfaces interacting with aqueous solutions.

[a] *Institute of Physics, Faculty of Science, University of South Bohemia, Branišovská 1760, 370 05, České Budějovice, Czech Republic. E-mail: predota@prf.jcu.cz; Tel: +420 387776258*

[b] *Faculty of Chemistry, Materials Research Centre, Brno University of Technology, Purkyňova 118, 612 00 Brno, Czech Republic*

† Electronic supplementary information (ESI) available: Gromacs simulation files, comparison of Matsui–Akaogi and Brandt–Lyubartsev potentials for TiO_2 surfaces, ion–water distances from simulations, numbers of species in simulations, additional density profiles of water and ions at rutile surfaces of different surface charge densities, and height of ions at surface adsorption sites. See DOI: 10.1039/c8cp04535f

From the development of the force field for TiO_2,[36] we presented results on the structure of water and ions at the interface by MD simulations.[37–39] Later, we described the distance dependence of the viscosity and diffusivity of water,[40] characterized dielectric properties of water,[41] investigated the effect of the temperature and surface charge on ion adsorption,[42] applied classical MD to constrain the CD-MUSIC surface complexation model,[43] and predicted the zeta potential from nonequilibrium MD simulations.[44]

The recently developed electronic continuum correction (ECC)[45,46] method has been introduced to improve the accuracy of classical MD. It addresses a well-known problem that electrostatic interatomic interactions are overestimated with fully charged models, since polarization effects of electrons are missed in standard force fields. The idea of ECC is to take into account this issue by scaling partial atomic charges by the inverse square root of the electronic part of the dielectric constant of the solvent. In the case of water, this factor is approximately 0.75. Since the standard Lennard-Jones (LJ) parameters are fitted to standard charges, they also should be refined to provide reasonable interatomic distances.[47] Therefore, the so-called ECCR (electronic continuum correction with rescaling) method combines rescaling of both charges and van der Waals parameters. The importance of incorporating polarization effects using ECCR into classical MD simulations was demonstrated in numerous works focused on hydration and ion pairing of monovalent and divalent monoatomic ions in aqueous solutions.[47–52] Appropriate force fields with scaled charges were created for phosphates,[53] carbonate ions,[54] guanidinium ions,[55] calmodulin,[56] imidazole,[57] insulin,[58] phospholipid bilayers,[59] and oxalate ions.[60] Moreover, reduced charges are commonly used in classical MD simulations of ionic liquids.[61,62] The development and applications of scaled charges have recently been reviewed in the context of thermodynamic properties.[63] Generally, it was shown that charge scaling is important mainly for molecules with a high charge density, *e.g.* multivalent ions (Ca^{2+}, Mg^{2+},...), proteins, and nucleic acids, due to the strong polarization of surrounding water molecules. As an example, Kroutil *et al.* proved[60] that only a model with scaled charges describes the interactions of oxalate with molecular water properly, while a model with full charges leads to overestimated electrostatic interactions between solute and water molecules. In the case of small monoatomic ions, the effect of ECCR is less important.[47] However, ions with a lower charge density, *e.g.* sodium, are often present in simulations of complex systems as counterions; thereby, ECCR models for these ions should also be prepared to have a consistent simulation force field.

The main motivation for this study and our first application of the ECCR approach to mineral surfaces has been our ongoing investigation of the adsorption of oxalic acid on rutile. To study interactions of the ECCR models of oxalate (COO^-)$_2$, scaled charge $-1.5e$, and hydrogenoxalate ($HOOCCOO^-$), scaled charge $-0.75e$,[60] with rutile surfaces, we need a compatible surface model developed here.

Both nonhydroxylated and hydroxylated types of the rutile slab were modeled. ECCR models of ions were either adopted from the available literature or prepared by us to yield reasonable bulk properties, namely the ion–water structure and diffusivity of ions in water. In this way, the obtained parameters for both ions and rutile surfaces resulted in a new ECCR force field, which was used to model the TiO_2–liquid interface for a range of surface charge densities (from 0 to -0.4 C m^{-2}) corresponding to pH values from the point of zero charge (5.4) to about 10 for Sr^{2+} and nearly 12 for monovalent ions.[5,42] As far as we are aware, this is the first time that the ECC methodology (scaling charges) is applied to simulations of surface interactions. We describe in detail the structure of interfacial ions, Na^+, Rb^+, Sr^{2+}, representing small monovalent, large monovalent, and large divalent cations, respectively. Results are compared against experimental data, outcomes from the same system without applying ECCR, and our previously published results. We demonstrated that the developed force field gives good agreement with data obtained from X-ray reflectivity analysis, calorimetric experiments, and CD-MUSIC modeling. Hence, the present work extends our previous knowledge about molecular modeling of the rutile–electrolyte interfaces and provides new capabilities in computer simulations of interactions with metal-oxide surfaces.

2. ECCR parametrization

2.1 Water

As in our previous works on simulating interfaces, we have used the rigid nonpolarizable SPC/E model of water[64] as a solvent. This model adequately reproduces the structural and thermodynamic properties of bulk water, and even the kinetic properties are rather accurate. In our previous works,[37–40,42–44] the choice of SPC/E was greatly motivated by the availability of ionic parameters[65,66] optimized with this model; note that our work in this field started prior to *e.g.* publishing of the popular Joung and Cheatham parameters of ions[67] or development of even more accurate water models, *e.g.* TIP4P/2005.[68] Moreover, most of the recently developed 75% scaled models discussed in the Introduction section were parameterized in SPC/E solvent. The performance with the TIP4P/2005 model[68] also was studied for a few scaled force fields,[47,48,50] where the results with TIP4P/2005 and SPC/E models did not show a big difference, indicating good transferability of scaled ionic models. Continuing to use the same SPC/E water model in this study we guarantee that the observed changes are due to the ECC approach to the modeling of ions and surfaces and are not caused by switching to another water model.

It is important to note that we did not apply any modifications to this model, because (i) the SPC/E model is from its conception designed to include the average effect of polarization, and (ii) consequently, it already features reduced charges ($q_H = 0.4238e$, $q_O = -0.8476e$). We also kept the original LJ parameter values for both oxygen ($\sigma_O = 3.16557$ Å, $\varepsilon_O = 0.650629$ kJ mol^{-1}) and hydrogen ($\sigma_H = \varepsilon_H = 0$) atoms.

2.2 Ions

As a first step in the modeling of the force field for rutile–ion interactions, we adopted the ECCR approach for the ions in

solutions, namely Na^+, Rb^+, Sr^{2+}, and Cl^-, which are our main concern due to their importance and availability of experimental adsorption data. We scaled all atomic charges by a factor of 0.75, which resulted in either negative or positive charge amounting to $0.75e$ for monovalent ions, and $+1.5e$ for divalent strontium. LJ parameters for fully charged models of Na^+, Rb^+, and Cl^- were adopted from the work of Joung and Cheatham,[67] while a set of parameters for fully charged Sr^{2+} was chosen on the basis of a recent spectroscopic work,[69] where a good agreement between theoretical XANES spectra (obtained from classical MD using the aforementioned model[70]) and experimental data has been demonstrated. Refined ECCR LJ parameters were either adopted from the literature[47] (for Na^+ and Cl^-) or obtained by us (for Rb^+ and Sr^{2+}). In the latter case, we rescaled only the van der Waals radii σ (by a factor of $\sim$4% to match the ion–water distances), keeping the original energy term ε of van der Waals interactions. Results from simulations with scaled charges and optimized radii are hereafter denoted as 'ECCR'; results obtained using full charges are denoted as 'full'; for additional comparison, we also performed simulations with one more set of parameters[65,66] used in our previous works,[38–40,42–44] referred to by the abbreviation 'EDL'. All parameters of the ions are summarized in Table 1.

To verify the performance of the force fields before running simulations of the solid–liquid interface, we measured ion–water distances and self-diffusion constants in aqueous solutions in the absence of surfaces for all studied ions, and compared the obtained values with experimental data. The simulation cell initially comprised 4222 water molecules. Then, a number of water molecules were replaced by a selected number of cations (either 30 monovalent Na^+ or Rb^+, or 15 divalent Sr^{2+}). To neutralize the system, a required number of negatively charged chloride ions were added, *i.e.* 30 anions. Hence, we obtained aqueous solutions with average salt concentrations of 0.4 M and 0.2 M, respectively, *i.e.* similar to those usually maintained in macroscopic pH titration measurements.[42] Due to differences in the adsorption of different cations and the effect of surface charge, the resulting bulk concentrations away from the interface, which are best compared with experimental conditions, are about 0.1 M to 0.6 M with the extreme cases occurring for the most negatively charged surface and the strongly adsorbing (Na^+) and weakly adsorbing (Rb^+) ions, respectively.

Table 1 Charges and Lennard-Jones parameters of ions

Atom	Model	q (e)	σ (Å)	ε (kJ mol^{-1})
Na^+	ECCR[a]	+0.75	2.11500	0.544284
	Full[b]	+1	2.15954	1.475450
	EDL[d]	+1	2.58300	0.418400
Rb^+	ECCR[f]	+0.75	2.97000	1.862310
	Full[b]	+1	3.09498	1.862310
	EDL[d]	+1	3.52800	0.418400
Sr^{2+}	ECCR[f]	+1.5	2.97000	0.494700
	Full[c]	+2	3.10300	0.494700
	EDL[e]	+2	3.31410	0.418400
Cl^-	ECCR[a]	−0.75	4.10000	0.492800
	Full[b]	−1	4.83045	0.053492
	EDL[d]	−1	4.44010	0.418400

[a] Kohagen *et al.*[47] [b] Joung and Cheatham.[67] [c] Aqvist.[70] [d] Lee and Rasaiah.[65] [e] Palmer *et al.*[66] [f] Our own parametrization.

All classical MD simulations in this contribution were carried out using the Gromacs 5.1.4 program package.[71] The prepared simulation box was energy minimized with the steepest descent algorithm to avoid unphysical intersections after the water replacement. Then, each system was equilibrated with the isothermal–isobaric ensemble (*NPT*). With a Nosé–Hoover thermostat[72] at 298.15 K (coupling time 0.5 ps) and a Parrinello–Rahman barostat[73] at 1 bar (coupling time 0.5 ps), the equilibration phase was followed by a *NVT* production run of 30 ns with a time step of 1 fs. Electrostatic interactions were treated by the particle-mesh Ewald algorithm[74] using a cut-off of 12 Å. Bonds and angles of rigid water were constrained by the LINCS algorithm.[75] For all LJ pairs, Lorentz–Berthelot combining rules were applied.

The radial distribution functions for all ion–oxygen pairs using different models are depicted in Fig. 1. Available experimental values[76] were directly compared with the position of the first peak of each ion–oxygen pair correlation function (see Table S1 in ESI†). To evaluate the effect of ECCR modifications, corresponding values were obtained for all aforementioned models. For chloride, only data from the system with Na^+ are present, because there is no effect of cation on the anion–oxygen distances at targeted salt concentrations. As one can see, all models give very good agreement with the literature data with a deviation of less than 4% from the experimental value. At the same time, the first peak of the radial distribution function is slightly broader and lower for 'ECCR' models, which is a direct consequence of the weaker Coulombic interactions between ions and the surrounding water molecules.

To investigate the dynamic properties of ions, we measured their self-diffusion constants in aqueous solutions. Since experimental

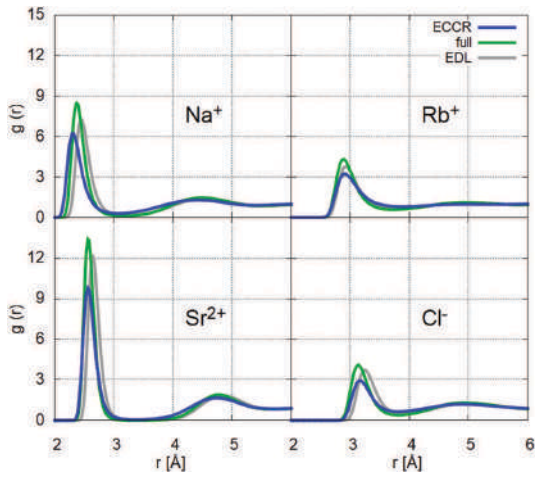

Fig. 1 Radial distribution functions of cations with water oxygens for all sets of parameters used in this work.

data are reported in the limit of the infinite dilution of the solute, we performed additional simulations at salt concentrations in the range between 0.2 M and 0.4 M, *i.e.* we replaced water molecules in the original water box by different numbers of cation–anion pairs. An approximately linear dependence of the diffusion *vs.* concentration was observed, and therefore we also report diffusivities extrapolated to zero concentrations. The self-diffusion constants were calculated from the mean square displacement (MSD) of ions *versus* time. The slope of the linear fit of MSD gives the self-diffusion constant using Einstein's relation. Since the linear behavior of MSD *versus* time can be affected by poor sampling, we looped the diffusion coefficient calculation 120 times, *i.e.* each iteration was calculated over a 250 ps window. Such a length of the timeframe was found long enough to avoid the ballistic regime, which might happen at short simulation times, and small enough to have more MSD curves for better statistics. The final diffusivity values were obtained from the average of all iterations. A comparison of simulated diffusion constants with experimental data,[77] Table 2, reveals that the impact of scaling charges on the mobility of ions is dramatic. Reducing charges and weakening interatomic electrostatic interactions lead to increased diffusivities. With 'full' models, diffusion constants of Na^+, Rb^+, and Sr^{2+} are smaller by 10%, 7%, and 15%, respectively, than the experimental values, whereas using the 'EDL' model they are smaller by 1%, 10%, and 15%. With ECCR, the inconsistency is opposite and diffusion constants are significantly larger than the experimental values by 59%, 23%, and 22%, respectively. We observed this artifact of overestimated diffusivity also for calcium and magnesium ions, when they carry reduced charges. Using models from ref. 51 (for Ca^{2+}) and ref. 52 (for Mg^{2+}), we obtained the diffusion constants of 0.92 and 0.83×10^{-9} m^2 s^{-1}, respectively, which are higher by 16% and 17% than the experimental values (0.79 and 0.71×10^{-9} m^2 s^{-1}). The higher diffusivity of ECCR models is a weakness of these models, which we could not resolve with reasonable fits of the ionic structure. However, as proved by a comparison with neutron scattering data and *ab initio* molecular dynamics,[47,51,52,60] the ECCR force fields are able to describe ion hydration and pairing more accurately than force fields with full charges. Moreover, scaled ionic charges can capture the ''structure-breaking'' properties of some salt solutions, for which the diffusivity of water should increase with increasing concentration of the salt.[78] All common fully charged nonpolarizable force fields fail to reproduce this behavior.[79] Our ECCR model of RbCl solution (Rb^+ is the only ''structure-breaking'' cation[80] we study here) shows the independence of water diffusivity on salt concentration, which is a positive trend and comparable to that obtained before.[79] For other models, higher concentration leads to lower water diffusivity, including all NaCl and $SrCl_2$ simulations, where this behavior is correct and follows ''structure-making'' effects. Particularly for the current structural study of equilibrium adsorption of ions on surfaces, the accuracy of structure overweighs the larger deviations in diffusivities, even though our observations must be considered in future works. Concerning the diffusivity of chloride, we observe similar behavior to cations, *i.e.* lower diffusivity with full charges, and higher (in fact, a bit closer to the experiment) diffusivity with ECCR. Moreover, we observed that generally the lower the diffusivity of cations in the system, the lower the diffusivity of chloride, that is, the mobility of Cl^- is affected by the ion pairing with the corresponding cations. Despite the difference in diffusion coefficients with experiment, the trend in diffusion, $Sr^{2+} < Na^+ < Cl^- < Rb^+$, is conserved for all models.

Table 2 Diffusion coefficients (D) of ions from simulations and experiment[a]

	D (10^{-9} m^2 s^{-1})			
Atom	ECCR	Full	EDL	Experiment
Na^+	2.11	1.20	1.32	1.33
Rb^+	2.55	1.93	1.86	2.07
Sr^{2+}	0.96	0.67	0.67	0.79
Cl^-	2.36,[b] 2.32,[c] 2.24[d]	1.51,[b] 1.72,[c] 1.54[d]	1.63,[b] 1.72,[c] 1.64[d]	2.03

[a] Simulated diffusion coefficients at selected salt concentrations were extrapolated to infinite dilution. Experimental values from ref. 77. [b] For the system with Na^+. [c] For the system with Rb^+. [d] For the system with Sr^{2+}.

2.3 Rutile surfaces

The force field of the rutile surface used previously in our research[37] has been updated in several steps. Primarily, the model was transferred from our self-written and hard to generalize simulation code into the Gromacs software package.[71] Originally, we kept the same force field as in our previous publications[44] including combination of LJ potentials with the Buckingham (exp-6) potential for Ti–O interactions, which had to be implemented in a form of user-defined tabulated potentials. In the ESI,† we prove that such simulations closely reproduced our previous results obtained with our own code. However, all the other new results were obtained using recently derived LJ reparameterization[81] of the Matsui and Akaogi (MA) force field[82] to allow simulations in Gromacs without the need for user-defined tabulated potentials (see Table 3). The values from ref. 37 were used for the equilibrium bond distance parameters r_0. The O–H spring constant k^b was adopted from the generic CLAYFF[83] and is furthermore not important due to the applied LINCS algorithm, see below. The spring constant k^b for the Ti–O bond was doubled from the value 4226 kJ mol^{-1} $Å^{-2}$ reported by Brandt and Lyubartsev[81] to bring the bond lengths closer to the equilibrium distances derived *ab initio*.[37] The angle-bending potential acting on the terminal and bridging hydroxyls (summing the two Ti–O–H contributions in the latter case) as in ref. 37 was applied by grouping the hydroxyls and underlying Ti atoms into pseudo-molecules. With the rows of bridging oxygens, the simulation had to be run with a switch 'periodic-molecules = yes' to correctly handle the angular terms across the periodic cell.

In an analogy to treatment of neutral and charged molecules,[56,60] ECCR was employed only for charged surfaces *via* rescaling the partial charges on only the top layer of the negatively charged surfaces (see Fig. 2). The other surface atoms like bulk crystal titanium and bulk crystal oxygen

Table 3 Parameters of rutile surface atoms

Non-bonded Lennard-Jones parameters[a]		
Atom	σ (Å)	ε (kJ mol^{-1})
Ti	1.958	2.5422
O	2.875	1.3897
H	0.000	0.0000
Bonded parameters[b], $V_b(r_{ij}) = \frac{1}{2}k_{ij}^b(r_{ij} - r_{0,ij})^2$; $V_a(\theta_{ijk}) = \frac{1}{2}k_{ijk}^\theta(\theta_{ijk} - \theta_{0,ijk})^2$		
Bond	r_0 (Å)	k (kJ mol^{-1} A^{-2})
Ti_b–O_b(H)	2.022	8452.00
Ti_b–O_b	1.872	8452.00
O_b–H_b	0.994	4637.00
Ti_t–O_t	1.895	8452.00
O_t–H_t	0.983	4637.00
Angle	θ_0 (deg)	k (kJ mol^{-1} rad^{-2})
Ti_b–O_b–H_b	90.85	59.15
Ti_t–O_t–H_t	90.85	59.15

[a] Parameters are taken from ref. 81. [b] Force constant for Ti–O bonds is twice as large as that reported in ref. 81. Force constant for O–H bonds is taken from ref. 83. Reference bond values and angle parameters are taken from ref. 37.

retained their original charges from the initial force field,[37,78] see Table 4. Thus, we modified only the charges of the variable-charge atoms as identified in ref. 37, *i.e.* terminal and bridging hydroxyls (or just bridging oxygens when not protonated) and Ti atoms in the last surface layer. With the standard approach used so far, the variable charges were modified in such a way that a deprotonation of the surface resulted in a change of surface charge by $-1e$. Specifically, the drop by about $0.5e$ was caused by removing the surface hydrogen (a value corresponding to its partial charge), and the change of variable-charge atoms was responsible for the decrease of the surface charge additionally by about $0.5e$. With the ECCR approach, the removal of surface hydrogen (still carrying a partial charge of about $0.5e$) should result in a change of the surface charge by only $-0.75e$, *i.e.* the variable-charge surface atoms are responsible for the additional decrease by only about $0.25e$. In other words, only about half of the 'missing charge', discussed in ref. 37, needs to be distributed over the variable-charge atoms when ECCR is applied, adding these charges to the same basic charges as reported in Table 3 of ref. 37. Due to a number of variable-charge atoms, the charges of each of them do not change much with respect to their values at neutral surfaces, and their LJ parameters are not modified in combination with ECCR, which is consistent with our previous simulations (where the modifications of charges of variable-charge atoms were greater as discussed above) and common independence of van der Waals parameters on small variations of partial charges in classical molecular force fields.

2.4 Rutile–liquid interface

In simulations with rutile surfaces, we used the same methodology as in our previous studies,[44] *i.e.* each simulation cell was composed of two identically charged, periodic rutile slabs with the lateral size 38.891 Å × 35.508 Å. The aqueous solution consisting of water molecules and a selected number of ions (Na^+, Rb^+, Sr^{2+}, Cl^-) was located between the surfaces. The width of the liquid phase was about 50 Å. Hence, we had two identical interfacial regions of about 15 Å at each surface and an approximately 20 Å thick bulk region in the middle of the simulation box (see Fig. 2), where the bulk properties of both water and ions are observed.[44] The obtained results (density profiles, the occupancy of adsorption sites) are averaged over both identical interfaces. Numbers of ions present in the systems, given in Table S2 (ESI†), are the same as in our previous work.[42] In the case of negatively charged surfaces, the total surface charge was compensated for by a surplus of positive ions in the solution. The amount of water was around 2000 molecules resulting in a bulk water density of about 1 g cm^{-3}.

We investigated the adsorption of cations (Na^+, Rb^+, or Sr^{2+}) on neutral and negatively charged surfaces (-0.104 C m^{-2}, -0.208 C m^{-2}, and -0.416 C m^{-2}), corresponding to pH values of 5.4, 7.4, 8.9, and 11.8 for monovalent ions (Na^+, Rb^+), and about 5.4, 7.1, 8, and 9.7 for Sr^{2+}, which has a steeper charging curve.[42] For brevity, these surface charge densities are hereinafter referred to as 0.0, -0.1, -0.2, and -0.4 C m^{-2}. Surface charge densities are fixed in all simulations and surface oxygen protonation/

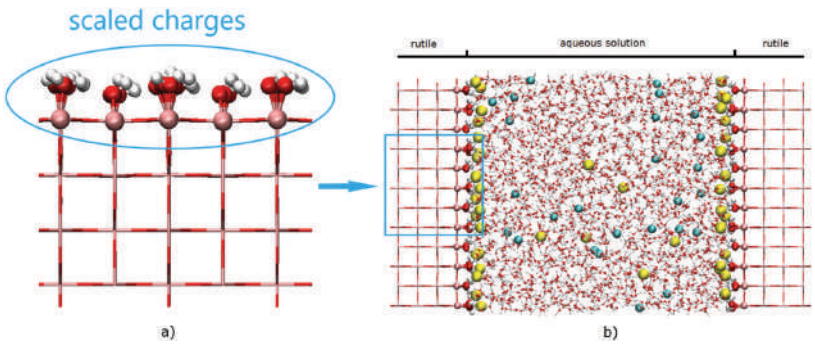

Fig. 2 Simulation setup. (a) A piece of hydroxylated rutile cluster. Only atoms with reduced charges are shown as spheres. (b) A typical simulation cell: two rutile slabs with aqueous $SrCl_2$ (yellow and green spheres, respectively) solution in between.

Table 4 Charges of rutile surface atoms from the original force field and ECCR theory[a]

	Surface charge density σ (C m^{-2})							
	−0.416		−0.208		−0.104		0	
Atom	nh[b]	h[c]	nh[b]	h[c]	nh[b]	h[c]	nh[b]	h[c]
Full								
Bulk Ti	2.196	2.196	2.196	2.196	2.196	2.196	2.196	2.196
Bulk O	−1.098	−1.098	−1.098	−1.098	−1.098	−1.098	−1.098	−1.098
Surface Ti	2.094	2.112	2.121	2.134	2.137	2.146	2.196	2.196
Bridging unproton O	−1.079	−1.063	−1.053	−1.039	−1.037	−1.028	−1.098	—
Bridging proton O	—	−1.009	—	−0.985	—	−0.976	—	−1.035
Bridging H	—	0.410	—	0.434	—	0.444	—	0.486
Terminal O	−1	−0.984	−0.974	−0.960	−0.956	−0.949	—	−1.008
Terminal H	0.37	0.385	0.394	0.409	0.412	0.420	—	0.459
Total surface charge	−72		−36		−18		0	
ECCR								
Bulk Ti	2.196	2.196	2.196	2.196	2.196	2.196	2.196	2.196
Bulk O	−1.098	−1.098	−1.098	−1.098	−1.098	−1.098	−1.098	−1.098
Surface Ti	**2.126**	**2.134**	**2.139**	**2.145**	**2.147**	**2.151**	2.196	2.196
Bridging unproton O	**−1.048**	**−1.039**	**−1.036**	**−1.028**	**−1.028**	**−1.022**	−1.098	—
Bridging proton O	—	**−0.986**	—	**−0.975**	—	**−0.970**	—	−1.035
Bridging H	—	**0.433**	—	**0.445**	—	**0.450**	—	0.486
Terminal O	**−0.970**	**−0.961**	**−0.955**	**−0.949**	**−0.947**	**−0.944**	—	−1.008
Terminal H	**0.400**	**0.408**	**0.413**	**0.420**	**0.421**	**0.425**	—	0.459
Total surface charge	**−54**		**−27**		**−13.5**		0	

[a] Modified charges are given in bold. [b] Nonhydroxylated surface. [c] Hydroxylated surface.

deprotonation reactions are prohibited due to the nondissociative force field. The relation between surface charge densities and solution pH with rutile powders was previously demonstrated in our research.[42] Note that to model *e.g.* surface charge density −0.1 C m^{-2}, we deprotonate the same corresponding number of surface hydrogens as with full charges, *i.e.* the geometry of surfaces is identical regardless of whether ECCR or full charges are applied. The actual surface charge density is in fact only 75% of the nominal value, but that is perfectly in line with the ECCR modeling of ions, where the nominal charges of ions are also reported (*e.g.* Ca^{2+}), though the model charge is only +1.5*e*. While making the step from full charges to ECCR charges, there was no need to modify the numbers of any species.

All production runs in the presence of rutile surfaces were 25 ns long after 5 ns equilibration run in the *NVT* ensemble. The time step was set to 2 fs in both cases. A Nosé–Hoover thermostat[72] at 298.15 K was applied. The particle-mesh Ewald algorithm[74] with the correction for slab geometry[84] was employed for long-range electrostatic interactions. The LINCS algorithm[75] was used to constrain the bonds involving water and surface hydrogens. Bulk crystal atoms together with 5-fold and 6-fold surface titanium atoms were kept immobile during all simulations to prevent a surface displacement, which would smear the axial density profiles of water and ions. At the same time, bridging and terminal hydroxyl groups were flexible in all cases. All other simulation settings reflect the setup for bulk simulations.

3. Results

Due to the availability of X-ray experimental data[20,21] for Rb^+ and Sr^{2+} adsorption at rutile–water interfaces at pH above 10, we restrict the discussion of our results to corresponding simulations with the most negatively charged (−0.4 C m^{-2}) rutile surfaces. Moreover, our previous MD results[42] included adsorption data at the −0.4 C m^{-2} surface for Sr^{2+}, but not for Na^+ or Rb^+. The results for lower surface charge densities (0, −0.1, −0.2 C m^{-2}), which are given in the ESI,† reveal no principal difference in pH dependence between 'ECCR' and 'full' models, except the trends identified for −0.4 C m^{-2} surfaces or mentioned here. The behavior of interfacial water is almost independent of the type of cation–anion pair and the method of modeling their charges; therefore, these data are not discussed. The discussion of adsorption of Cl^- is also omitted because of nearly zero adsorption at the studied surfaces. Nevertheless, density profiles of water oxygens, water hydrogens, and chloride ions at −0.4 C m^{-2} surfaces can be found in the ESI.†

Fig. 3 shows the axial number density profiles of sodium, rubidium, and strontium ions at −0.4 C m^{-2} surfaces, *i.e.* distribution of cations as a function of distance from the surface. The zero height is set to the position that the surface layer of Ti atoms would occupy in the unrelaxed crystal termination. The positions of the first peaks of these profiles are given and compared with the data from X-ray experiments[20,21] in Table 5. All models of ions ('ECCR', 'full', and 'EDL'), discussed in the ECCR parametrization section, were examined in simulations with two types of the rutile slab, *i.e.* nonhydroxylated (molecular water adsorbed at terminal sites except deprotonated, *i.e.* hydroxylated sites; abbreviated as nh in the tables and figures) and hydroxylated (hydroxyl groups at terminal sites; abbreviated as h in the tables and figures). The rutile force field with original 'full' charges[37] was employed in combination with 'full' and 'EDL' models of the ions, while the modified force

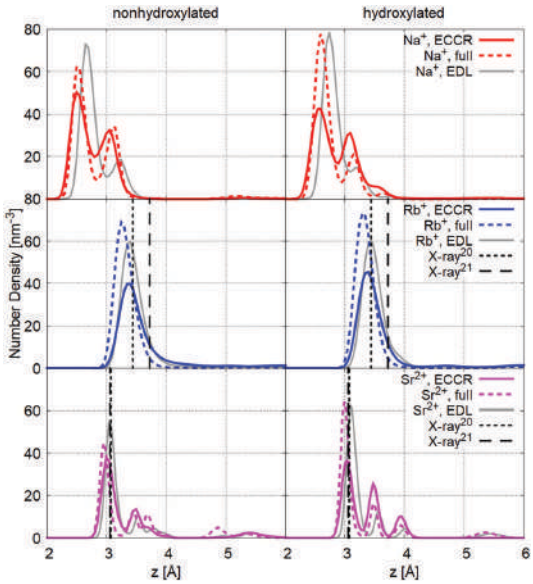

Fig. 3 Axial number density profiles of ions for the system with the most negatively charged (σ = −0.416 C m^{-2}) nonhydroxylated (left) and hydroxylated (right) rutile surfaces. Results for all discussed models of cations are shown. Comparison with X-ray data[20,21] is shown for Rb^+ and Sr^{2+}.

field (with scaled variable charges in the top layer) was used with 'ECCR' models. Note again that both surface force fields of rutile coincide for neutral surfaces.

As one can see from Fig. 3, all cations strongly adsorb on the rutile surfaces, in agreement with our previous MD results and surface titration measurements.[42] For sodium, two peaks can be distinguished at the nonhydroxylated surface with all models, while at the hydroxylated surface a small third peak emerges with 'full' and 'ECCR' models. With full charges, the first peak strongly dominates regardless of whether the 'full' or 'EDL' model is applied. With 'ECCR' charges, the first peak gets smaller, while the population of the second peak gets larger. This difference comes from the weaker electrostatics between deprotonated bridging or terminal oxygens and a cation, which leads to larger occupancy of the more distant and more hydrated adsorption sites, because water molecules, unlike surface atoms, still carry the same charges. The positions of these two peaks are different for all described models. With 'EDL' parameters, the peaks are further from the surface. Comparing 'ECCR' with 'full', the position of the first peak is closer to the surface for 'ECCR' at the nonhydroxylated surface, and the same at the hydroxylated surface for both models (Table 5), whereas the second peak of adsorbed Na^+ is closer to the surface in the case of the 'ECCR' model.

Table 5 Positions (in Å) of the first peaks of density profiles of ions for the most negatively charged (σ = −0.416 C m^{-2}) rutile surface

	nh-0.4			h-0.4			
	ECCR	Full	EDL	ECCR	Full	EDL	X-ray
Na^+	2.51	2.51	2.65	2.60	2.60	2.74	—
Rb^+	3.38	3.24	3.38	3.40	3.33	3.43	3.44 ± 0.03,[a] 3.72 ± 0.03[b]
Sr^{2+}	3.03	2.96	3.05	3.02	2.99	3.09	3.07 ± 0.07,[a] 3.05 ± 0.16[b]

[a] Zhang *et al.*[20] [b] Kohli *et al.*[21]

In contrast to Na^+, the density profiles of Rb^+ have only one peak regardless of the model. In fact, the shape and position of the rubidium density profile are almost independent of not only the ionic charge, but also of the temperature and pH, as shown in our previous research,[42] and confirmed in this work (see the pH dependence of density profiles in ESI,† Fig. S4 and S5). With 'ECCR', the adsorption peak is a bit wider and lower, and its position is in better agreement with experimental data in comparison with the 'full' model. Interestingly, the 'EDL' model results in even slightly better agreement with experiment relative to 'ECCR', while the more recent and currently more recommended full charge model[64] results in a peak at significantly shorter position.

The density profiles of strontium at both nonhydroxylated and hydroxylated surfaces are characterized by three peaks with the first peak more pronounced than the others. The effect of ECCR is similar to that for Na^+, that is, the difference in the height of peaks gets smaller, especially in the case of hydroxylated surfaces. For the 'ECCR' model, the distribution of strontium ions among these three peaks is more uniform, without a big change in the peaks' positions with respect to the 'full' model. Moreover, the 'ECCR' model gives the position of the first peak in good agreement with experiment, while the 'full' model slightly underestimates this value.

The peaks and their relative amplitudes can be linked to different adsorption sites of cations. In previous contributions,[20,21,42] six possible sites of inner-sphere adsorption on the rutile (110) surface were proposed and discussed (see ref. 21 and Fig. 1 therein). These sites include two monodentate sites (one bond with either bridging or terminal oxygen of the rutile slab), three bidentate sites (interactions with two oxygens, either both terminal (TOTO) or bridging (BOBO), or one bridging and one terminal (BOTO)), and one tetradentate site (TD, requires two terminal and two bridging oxygens). In this work, we performed additional analysis of simulated trajectories using the VMD molecular program[85] to determine relative occupancies of the adsorption sites using 'ECCR' and 'full' models. This analysis was based on the number of bonds formed by a cation with surface oxygens. The position of the first minimum of the bulk cation–oxygen radial distribution function, namely 3.1 Å (Na^+–O), 3.8 Å (Rb^+–O), and 3.4 Å (Sr^{2+}–O), was used as a cut-off value to distinguish the inner-sphere bonding of a cation with surface oxygens.

The relative occupancies of the adsorption sites for studied cations are summarized in Table 6. The average heights of cations at those sites can be found in the ESI.† Only four adsorption sites are detailed in results, namely all bidentate sites (BOBO, BOTO, TOTO) and the tetradentate site (TD). Monodentate and other less populated surface complexes, *e.g.* transition modes like a tridentate site with two bridging and one terminal oxygens, are omitted in the table, since their relative individual contribution to the inner-sphere adsorption never exceeded 5% and is usually negligible.

Table 6 Relative populations (in %) of tetradentate (TD) and bidentate (BOBO, BOTO, TOTO) adsorption sites of ions at the most charged (σ = −0.416 C m^{-2}) rutile surface[a]

		nh-0.4		h-0.4	
Ion	Type	ECCR	Full	ECCR	Full
Na^+	TD	**54.7**	**55.9**	**48.0**	**66.4**
	BOBO	[b]	3.5	6.0	5.8
	BOTO	**35.2**	**37.5**	**33.9**	**24.1**
	TOTO	[b]	[b]	6.4	[b]
Rb^+	TD	**78.4**	**83.5**	**84.2**	**81.5**
	BOBO	[b]	4.9	[b]	6.8
	BOTO	10.0	4.8	9.2	8.3
	TOTO	[b]	[b]	[b]	[b]
Sr^{2+}	TD	**58.2**	**48.2**	**48.9**	**71.2**
	BOBO	8.1	5.4	5.8	4.9
	BOTO	**27.3**	**31.8**	**28.8**	**16.1**
	TOTO	[b]	5.0	10.0	4.9

[a] Less occupied adsorption sites are not included in this table. Predominant surface complexes are shown in bold. [b] The relative contribution of the adsorption site is lower than 3%.

Our analysis revealed that the TD and BOTO sites are the most preferred adsorption sites for all studied cations at −0.4 C m^{-2} surfaces. In the case of rubidium, this domination is most obvious, in agreement with previous simulations and new experimental results,[5,42] where this site dominated even at smaller surface charge densities and lower bulk concentrations. The contribution of the other adsorption sites, when Rb^+ has at least one bond with surface oxygens, is only ∼20%. Scaling charges does not change the picture significantly, only a redistribution from the BOBO site to the BOTO site is observed. The overall inner-sphere adsorption of Rb^+ is smaller with 'ECCR' models (see Fig. 4) compared to the 'full' charge model. For such weakly interacting ions, it is quite easy to (partially) dehydrate even when using full charges, so the reduction of the surface charges is the leading factor behind decreased inner-sphere adsorption. More importantly, new microcalorimetric measurements together with SCM modeling[5] confirmed previous experimental results,[20] namely, in the whole range of pH, Na^+ is a stronger adsorbent than Rb^+. In our simulations, only 'ECCR' models reproduced this tendency, whereas with 'full' models, Rb^+ has a comparable adsorption to Na^+. The total amount of the adsorbed Rb^+ per rutile surface area is also nicely compared to experiment in the case of 'ECCR' models, while with 'full' models these values are larger (see Fig. 5). Note that the experimental data from ref. 5 are smaller than those from our simulations, which is in accord with the larger bulk concentrations used in our simulations. However, our previous works[42,44] have confirmed the dominant role of surface charge on the amount of adsorbed ions, while the effect of bulk concentration is minor.

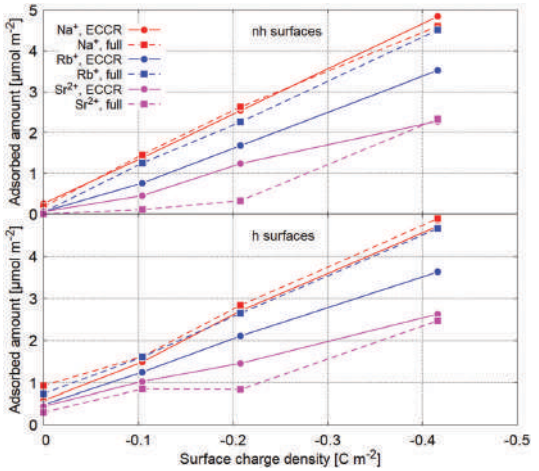

Fig. 4 Dependence of the inner-sphere adsorption of the cations on surface charge density at nonhydroxylated (top) and hydroxylated (bottom) surfaces.

Unlike Rb^+, sodium cations strongly prefer both TD and BOTO sites. Our previous MD results, which were limited to the −0.2 C m^{-2} surface, predicted only the TOTO site as preferable.[42] Here, at the −0.4 C m^{-2} surface, this site is observed only at the hydroxylated surface with 'ECCR' charges, and not at the nonhydroxylated surface. In fact, an analysis of current results at the −0.2 C m^{-2} surface (*cf.* Fig. S4 and S5, ESI†) confirms that at lower pH the TOTO site has the largest coverage at hydroxylated surfaces, but only with 'full' models. With 'ECCR', BOTO and TD sites are dominant; however, the TOTO site still has a sufficient coverage of ∼20%. At nonhydroxylated surfaces and under lower pH conditions, the BOTO site is the most preferred with both 'full' and 'ECCR', whereas the TD site is less occupied. These significant changes of adsorption geometry of interfacial Na^+ due to a shift to a higher pH have not been modeled before. Recent experimental data[5] also revealed the tendency of the TD site to be more occupied with increased pH, which supports our new simulation data.

The analysis of Sr^{2+} inner-sphere binding identifies that TD and BOTO sites are significantly occupied in all simulated systems, while the coverage of BOBO and TOTO sites is rather small. Moreover, the outer-sphere adsorption is considerably smaller with scaled charges compared to full charges; therefore, inner-sphere adsorption is larger with 'ECCR' models (see Fig. 4), and in better agreement with experimental data than using 'full' models (Fig. 5). This trend is most pronounced at the −0.2 C m^{-2} surface, where Sr^{2+} is evidently most frustrated between surface attraction and hydration and therefore sensitive to parameterization. Under these conditions, the effect of scaling charges promoting easier (partial) dehydration of ions upon adsorption is stronger than the effect of reduction of charges of surface groups. At the −0.4 C m^{-2} surface, the charge density is already strong enough to force Sr^{2+} to adsorb as an inner-sphere complex in a similar amount using both models. Generally, as demonstrated by Na^+ and Sr^{2+}, scaling of charges mostly affects the occupancy of the sites at hydroxylated surfaces. With 'ECCR', there is a significant drop in the occupancy of the TD site, which leads to the larger occupancy of other more distant sites. This can be explained by the fact that with 'ECCR' at the hydroxylated surface all atoms of terminal

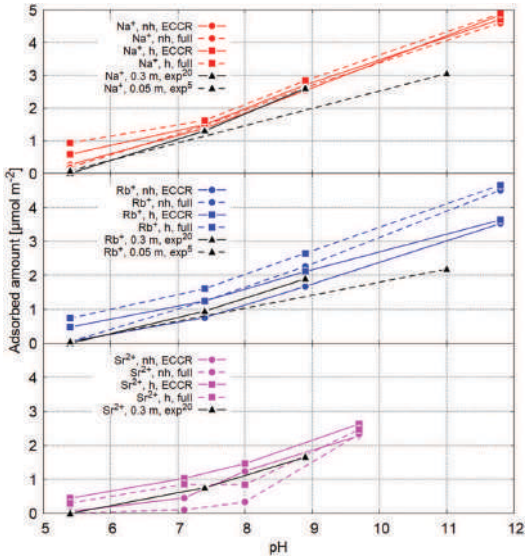

Fig. 5 The pH dependence of the inner-sphere adsorption of cations from simulations (this work) and experiment (ref. 5 and 20).

hydroxyl groups carry reduced charges, while at the nonhydroxylated surface at least one of the bare terminal Ti atoms interacting with an ion is occupied by molecular SPC/E water, a model which is the same in all simulations.

4. Conclusions

For many ions, mainly divalent, it has already been proven that the ECCR approach in aqueous environment, scaling charges to 75% of their nominal values, brings significant improvement in the structure of ion–water interactions, free energy profiles, ion–ion pairing, and ion dynamics.[45–60] The structural improvement was observed particularly when combining the neutron diffraction data *vs.* simulation data using full or ECCR charges. The standard potentials with full charges are typically designed to predict correctly the peak positions of X-ray diffraction data, but less attention has often been paid to the agreement in the heights of these peaks and the valleys which separate them – either due to the lack of more detailed information from experiments or simply because the fitted potentials failed to produce them accurately at the same time. Nowadays, the advance of X-ray and neutron diffraction experiments as well as comparison with *ab initio* MD shows often overstructuring of the peaks when full charges are applied.

The main aim of this manuscript is to pave the way for the application of the ECCR approach to charged surfaces. Without that, the studies of interactions of charged surfaces with ions and molecules described by scaled charges would be impossible or inconsistent. The ECCR modeling of surfaces enables the study of the adsorption and interactions with surfaces of those molecules, which were found to be more accurately represented in bulk systems using ECCR models – including multivalent ions and highly charged molecules.

We developed a new force field for the rutile (110) surfaces in accord with the ECCR approach and compared its performance to the existing ones with full charges. Similarly to the treatment of large molecules by ECCR, where charges of only part of the molecule (charged residuum) are affected by scaling, only the surface atoms of surfaces are affected. In this aspect, the surface is treated as a supermolecule. The problem of distribution of the 'missing charge' upon protonating or deprotonating the surface is significantly reduced with ECCR, since the proton carries a partial charge of about 0.5*e* and only the remaining charge of about 0.25*e* has to be distributed on other surface atoms in the case of ECCR, as opposed to about 0.5*e* in the case of full charges. Except for this difference, the scenario for assignment of partial surface charges to atoms on charged surfaces remains the same as with full charges.

The results of adsorption of Rb^+ on (110) neutral to negatively charged nonhydroxylated and hydroxylated surfaces did not change significantly when the charges of ions both in the aqueous phase and surface groups were reduced to 75%; however, there are several improvements. The agreement of the peaks' positions between MD and X-ray is better with ECCR compared to 'full' charges. The total amount of adsorbed Rb^+ is lower with ECCR in contrast to full charges and also in comparison with our ECCR Na^+ simulations. This behavior is now in better accord with experimental adsorption data. The adsorption of Sr^{2+} is more homogeneously distributed among the adsorption sites with ECCR, but the positions of peaks did not change significantly. For Na^+, where unfortunately the X-ray data are lacking due to similar scattering of Na^+ and water molecules, the effect of ECCR is larger, increasing the population of the second peak at the cost of the first peak compared to 'full' charges.

Overall the effect of charge scaling is more pronounced on hydroxylated surfaces dominated by terminal and bridging hydroxyls (except for deprotonated bridging sites), while at nonhydroxylated surfaces the terminal sites are occupied by nondissociated water molecules (except for selected hydroxylated terminal sites), which carry the same charge in all cases. Particularly, scaling the charges of hydroxylated surfaces decreases the population of the tetradentate sites interacting with several scaled down surface hydroxyls or bridging oxygens and increases the population of the bidentate sites interacting with more water molecules.

As a by-product, we found that the diffusivities of ECCR ions are overestimated compared to experimental values – often more significantly than these values are underestimated with full charge models. This deficiency deserves further attention, since it is likely to negatively affect the simulated dynamic properties including residence times and mobilities of ions in electric fields influencing *e.g.* electrokinetic effects (zeta potentials). The superior structural performance of ECCR models, together with weakening of the electrostatic interactions (compared to full charge models, where they are exaggerated), is however essential in studies of adsorption and interactions of ions with surfaces.

The scaling factor 0.75 (theoretically justified for water by Leontyev and Stuchebrukhov[45,46]) leads to very high ionic diffusivities and better agreement might be reached when this factor is increased. The idea to release (increase) the scaling factor from the value of 0.75 and tune it using the dielectric properties of a water model was found to improve the concentration dependence of ionic diffusivities of alkali halides.[78] However, using our recently developed oxalate model with a scaling factor of 0.75 (we note here that an unpublished version of this model with a scaling factor of 0.8 was also rather good) and adopting some of the ionic parameters also applying the same scaling factor, we had to be consistent and fix the scaling factor to 0.75. Future works devoted to ECC will enlighten whether a constant charge scaling factor (be it 0.75, 0.8, or other value) and consistent model sets of ions, molecules, and surfaces with such a fixed scaling factor will prove to be the best (not only in terms of accuracy, but also transferability), or whether a consistent methodology to modify the charges of charged groups will be developed (as also represented in this manuscript), allowing the scaling factor to vary based on the solvent model, temperature, solvent density (all influencing the dielectric properties), or other factors. The second approach definitely offers better transferability with respect to different, even non-aqueous solvents.

The approach detailed here for (110) rutile surfaces can be straightforwardly applied to other surfaces by recalculating the charges of variable-charge surface atoms. Our ongoing work on modeling of Ca^{2+} interacting with (101) quartz surfaces[6] shows improved agreement of MD and *ab initio* results when the ECCR approach is applied to both ions and surface atoms.

Conflicts of interest

There are no conflicts to declare.

Acknowledgements

The authors were supported by the Czech Science Foundation, project 17-10734S. Computational resources were provided by the CESNET LM2015042 and the CERIT Scientific Cloud LM2015085, provided under the program ''Projects of Large Research, Development, and Innovations Infrastructures''.

References

1 F. Bellucci, S. S. Lee, J. D. Kubicki, A. Bandura, Z. Zhang, D. J. Wesolowski and P. Fenter, Rb^+ Adsorption at the Quartz(101)–Aqueous Interface: Comparison of Resonant Anomalous X-Ray Reflectivity with *Ab Initio* Calculations, *J. Phys. Chem. C*, 2015, **119**(9), 4778–4788.

2 J. N. Bracco, S. S. Lee, J. E. Stubbs, P. J. Eng, F. Heberling, P. Fenter and A. G. Stack, Hydration Structure of the Barite (001)–Water Interface: Comparison of X-ray Reflectivity with Molecular Dynamics Simulations, *J. Phys. Chem. C*, 2017, **121**(22), 12236–12248.

3 P. E. Ohno, S. A. Saslow, H.-F. Wang, F. M. Geiger and K. B. Eisenthal, Phase-Referenced Nonlinear Spectroscopy of the α-Quartz/WaterInterface, *Nat. Commun.*, 2016, **7**, 13587.

4 A. Tuladhar, S. M. Piontek and E. Borguet, Insights on Interfacial Structure, Dynamics, and Proton Transfer from Ultrafast Vibrational Sum Frequency Generation Spectroscopy of the Alumina(0001)/Water Interface, *J. Phys. Chem. C*, 2017, **121**(9), 5168–5177.

5 T. Hawkins, N. Allen, M. L. Machesky, D. J. Wesolowski and N. Kabengi, Ion Exchange Thermodynamics at the Rutile–Water Interface: Flow Microcalorimetric Measurements and Surface Complexation Modeling of Na–K–Rb–Cl–NO_3 Adsorption, *Langmuir*, 2017, **33**(20), 4934–4941.

6 O. Kroutil, Z. Chval, A. A. Skelton and M. Předota, Computer Simulations of Quartz(101)–Water Interface over a Range of pH Values, *J. Phys. Chem. C*, 2015, **119**(17), 9274–9286.

7 M. J. DelloStritto, J. D. Kubicki and J. O. Sofo, Effect of Ions on H-Bond Structure and Dynamics at the Quartz(101)–Water Interface, *Langmuir*, 2016, **32**(44), 11353–11365.

8 Z. Li, A. K. Van Dyk, S. J. Fitzwater, K. A. Fichthorn and S. T. Milner, Atomistic Molecular Dynamics Simulations of Charged Latex Particle Surfaces in Aqueous Solution, *Langmuir*, 2016, **32**(2), 428–441.

9 L. Fu, S. Merabia and L. Joly, What Controls Thermo-osmosis? Molecular Simulations Show the Critical Role of Interfacial Hydrodynamics, *Phys. Rev. Lett.*, 2017, **119**, 214501.

10 M. Bouhadja and A. A. Skelton, Dynamical Properties of Water and Ions at the Quartz(101)–Water Interface at a Range of Solution Conditions: A Classical Molecular Dynamics Study, *J. Phys. Chem. C*, 2018, **122**(3), 1535–1546.

11 X. Chen, Introduction: Titanium Dioxide (TiO_2) Nanomaterials, *Chem. Rev.*, 2014, **114**(19), 9281–9282.

12 K. Shiba, Exploitation of Peptide Motif Sequences and Their Use in Nanobiotechnology, *Curr. Opin. Biotechnol.*, 2010, **21**(4), 412–425.

13 A. Weir, P. Westerhoff, L. Fabricius, K. Hristovski and N. Goetz, Titanium Dioxide Nanoparticles in Food and Personal Care Products, *Environ. Sci. Technol.*, 2012, **46**(4), 2242–2250.

14 Z. F. Yin, L. Wu, H. G. Yang and Y. H. Su, Recent progress in biomedical applications of titanium dioxide, *Phys. Chem. Chem. Phys.*, 2013, **15**(14), 4844–4858.

15 F. U. Rehman, C. Zhao, H. Jiang and X. Wang, Biomedical Applications of Nano-Titania in Theranostics and Photodynamic Therapy, *Biomater. Sci.*, 2016, **4**(1), 40–54.

16 M. Buchalska, M. Kobielusz, A. Matuszek, M. Pacia, S. Wojtyła and W. Macyk, On Oxygen Activation at Rutile– and Anatase–TiO_2, *ACS Catal.*, 2015, **5**(12), 7424–7431.

17 U. Diebold, The Surface Science of Titanium Dioxide, *Surf. Sci. Rep.*, 2003, **48**, 53–229.

18 M. L. Machesky, D. A. Palmer and D. J. Wesolowski, Hydrogen Ion Adsorption at the Rutile–Water Interface to 250 °C, *Geochim. Cosmochim. Acta*, 1994, **58**(24), 5627–5632.

19 C. Zhang and P. J. D. Lindan, Multilayer Water Adsorption on Rutile TiO_2 (110): A First-Principles Study, *J. Chem. Phys.*, 2003, **118**(10), 4620–4630.

20 Z. Zhang, P. Fenter, L. Cheng, N. C. Sturchio, M. J. Bedzyk, M. Předota, A. Bandura, J. D. Kubicki, S. N. Lvov, P. T. Cummings, A. A. Chialvo, M. K. Ridley, P. Bénézeth, L. Anovitz, D. A. Palmer, M. L. Machesky and D. J. Wesolowski, Ion Adsorption at the Rutile–Water Interface: Linking Molecular and Macroscopic Properties, *Langmuir*, 2004, **20**(12), 4954–4969.

21 V. Kohli, Z. Zhang, C. Park and P. Fenter, Rb^+ and Sr^{2+} Adsorption at the TiO_2 (110)–Electrolyte Interface Observed with Resonant Anomalous X-ray Reflectivity, *Langmuir*, 2009, **26**(2), 950–958.

22 A. V. Bandura, J. O. Sofo and J. D. Kubicki, Adsorption of Zn^{2+} on the (110) Surface of TiO_2 (Rutile): A Density Functional Molecular Dynamics Study, *J. Phys. Chem. C*, 2011, **115**(19), 9608–9614.

23 S. G. Hug and D. Bahnemann, Infrared Spectra of Oxalate, Malonate and Succinate Adsorbed on the Aqueous Surface of Rutile, Anatase and Lepidocrocite Measured with in situ ATR-FTIR, *J. Electron Spectrosc. Relat. Phenom.*, 2006, **150**(2–3), 208–219.

24 H. J. Cleaves, C. M. Jonsson, C. L. Jonsson, D. A. Sverjensky and R. M. Hazen, Adsorption of Nucleic Acid Components on Rutile (TiO_2) Surfaces, *Astrobiology*, 2010, **10**(3), 311–323.

25 N. Lee, D. A. Sverjensky and R. M. Hazen, Cooperative and Competitive Adsorption of Amino Acids with Ca^{2+} on Rutile (α-TiO_2), *Environ. Sci. Technol.*, 2014, **48**(16), 9358–9365.

26 L. Agosta, E. G. Brandt and A. P. Lyubartsev, Diffusion and Reaction Pathways of Water near Fully Hydrated TiO_2 Surfaces from *Ab Initio* Molecular Dynamics, *J. Chem. Phys.*, 2017, **147**(2), 024704.

27 U. Diebold, Perspective: A Controversial Benchmark System for Water-Oxide Interfaces: H_2O/TiO_2 (110), *J. Chem. Phys.*, 2017, **147**(4), 040901.

28 K. Livi, B. Schaffer, D. Azzolini, C. R. Seabourne, T. P. Hardcastle, A. J. Scott, R. M. Hazen, J. D. Erlebacher, R. B. Brydson and D. A. Sverjensky, Atomic-Scale Surface Roughness of Rutile and Implications for Organic Molecule Adsorption, *Langmuir*, 2013, **29**(23), 6876–6883.

29 T. Zheng, C. Wu, M. Chen, Y. Zhang and P. T. Cummings, A DFT Study of Water Adsorption on Rutile TiO_2 (110) Surface: The Effects of Surface Steps, *J. Chem. Phys.*, 2016, **145**(4), 044702.

30 A. YazdanYar, U. Aschauer and P. Bowen, Interaction of Biologically Relevant Ions and Organic Molecules with Titanium Oxide (Rutile) Surfaces: A Review on Molecular Dynamics Studies, *Colloids Surf., B*, 2018, **161**, 563–577.

31 G. Okeke, R. B. Hammond and S. J. Antony, Molecular Dynamics Simulation of Anatase TiO_2 Nanoparticles, *J. Nanosci. Nanotechnol.*, 2013, **13**(2), 1047–1052.

32 S. Mushnoori, L. Chong and M. Dutt, Molecular Dynamics Study of Water over Pt/TiO_2 Surfaces, *Materials Today: Proceedings*, 2016, **3**(2), 513–517.

33 S. Kim, A. C. T. van Duin and J. D. Kubicki, Molecular Dynamics Simulations of the Interactions between TiO_2 Nanoparticles and Water with Na^+ and Cl^-, Methanol, and Formic Acid Using a Reactive Force Field, *J. Mater. Res.*, 2012, **28**(3), 513–520.

34 S.-I. Kim, N. Kumar, P. Persson, J. Sofo, A. C. T. van Duin and J. D. Kubicki, Development of a ReaxFF Reactive Force Field for Titanium Dioxide/Water Systems, *Langmuir*, 2013, **29**(25), 7838–7846.

35 Z. Futera and N. J. English, Exploring Rutile (110) and Anatase (101) TiO_2 Water Interfaces by Reactive Force–Field Simulations, *J. Phys. Chem. C*, 2017, **121**(12), 6701–6711.

36 A. V. Bandura and J. D. Kubicki, Derivation of Force Field Parameters for TiO_2–H_2O Systems from *Ab Initio* Calculations, *J. Phys. Chem. B*, 2003, **107**(40), 11072–11081.

37 M. Předota, A. V. Bandura, P. T. Cummings, J. D. Kubicki, D. J. Wesolowski, A. A. Chialvo and M. L. Machesky, Electric Double Layer at the Rutile (110) Surface. 1. Structure of Surfaces and Interfacial Water from Molecular Dynamics by Use of *Ab Initio* Potentials, *J. Phys. Chem. B*, 2004, **108**(32), 12049–12060.

38 M. Předota, Z. Zhang, P. Fenter, D. J. Wesolowski and P. T. Cummings, Electric Double Layer at the Rutile (110) Surface. 2. Adsorption of Ions from Molecular Dynamics and X-ray Experiments, *J. Phys. Chem. B*, 2004, **108**(32), 12061–12072.

39 M. Předota and L. Vlček, Comment on Parts 1 and 2 of the Series "Electric Double Layer at the Rutile (110) Surface", *J. Phys. Chem. B*, 2007, **111**(5), 1245–1247.

40 M. Předota, P. T. Cummings and D. J. Wesolowski, Electric Double Layer at the Rutile (110) Surface. 3. Inhomogeneous Viscosity and Diffusivity Measurement by Computer Simulations, *J. Phys. Chem. C*, 2007, **111**(7), 3071–3079.

41 S. Parez, M. Předota and M. L. Machesky, Dielectric Properties of Water at Rutile and Graphite Surfaces: Effect of Molecular Structure, *J. Phys. Chem. C*, 2014, **118**(9), 4818–4834.

42 M. Předota, M. L. Machesky, D. J. Wesolowski and P. T. Cummings, Electric Double Layer at the Rutile (110) Surface. 4. Effect of Temperature and pH on the Adsorption and Dynamics of Ions, *J. Phys. Chem. C*, 2013, **117**(44), 22852–22866.

43 M. L. Machesky, M. Předota, M. K. Ridley and D. J. Wesolowski, Constrained Surface Complexation Modeling: Rutile in RbCl, NaCl, and $NaCF_3SO_3$ Media to 250 °C, *J. Phys. Chem. C*, 2015, **119**(27), 15204–15215.

44 M. Předota, M. L. Machesky and D. J. Wesolowski, Molecular Origins of the Zeta Potential, *Langmuir*, 2016, **32**(40), 10189–10198.

45 I. V. Leontyev and A. A. Stuchebrukhov, Electronic Continuum Model for Molecular Dynamics Simulations of Biological Molecules, *J. Chem. Theory Comput.*, 2010, **6**(5), 1498–1508.

46 I. Leontyev and A. A. Stuchebrukhov, Accounting for Electronic Polarization in Non-Polarizable Force Fields, *Phys. Chem. Chem. Phys.*, 2011, **13**(7), 2613–2626.

47 M. Kohagen, P. E. Mason and P. Jungwirth, Accounting for Electronic Polarization Effects in Aqueous Sodium Chloride via Molecular Dynamics Aided by Neutron Scattering, *J. Phys. Chem. B*, 2015, **120**(8), 1454–1460.

48 M. Kohagen, P. M. Mason and P. Jungwirth, Accurate Description of Calcium Solvation in Concentrated Aqueous Solutions, *J. Phys. Chem. B*, 2014, **118**(28), 7902–7909.

49 M. Vazdar, E. Pluharova, P. E. Mason, P. Vacha and P. Jungwirth, Ions at Hydrophobic Aqueous Interfaces: Molecular Dynamics with Effective Polarization, *J. Phys. Chem. Lett.*, 2012, **3**(15), 2087–2091.

50 E. Pluhařová, P. E. Mason and P. Jungwirth, Ion Pairing in Aqueous Lithium Salt Solutions with Monovalent and Divalent Counter–Anions, *J. Phys. Chem. A*, 2013, **117**(46), 11766–11773.

51 T. Martinek, E. Duboué-Dijon, S. Timr, P. E. Mason, K. Baxová, H. E. Fischer, B. Schmidt, E. Pluharova and P. Jungwirth, Calcium Ions in Aqueous Solutions: Accurate Force Field Description Aided by *Ab Initio* Molecular Dynamics and Neutron Scattering, *J. Chem. Phys.*, 2018, **148**(22), 222813.

52 E. Duboué-Dijon, P. E. Mason, H. E. Fischer and P. Jungwirth, Hydration and Ion Pairing in Aqueous Mg^{2+} and Zn^{2+} Solutions: Force-Field Description Aided by Neutron Scattering Experiments and *Ab Initio* Molecular Dynamics Simulations, *J. Phys. Chem. B*, 2018, **122**(13), 3296–3306.

53 E. Bruce and N. F. A. van der Vegta, Does an Electronic Continuum Correction Improve Effective Short-Range Ion–Ion Interactions in Aqueous Solution?, *J. Chem. Phys.*, 2018, **148**(22), 222816.

54 P. E. Mason, E. Wernersson and P. Jungwirth, Accurate Description of Aqueous Carbonate Ions: An Effective Polarization Model Verified by Neutron Scattering, *J. Phys. Chem. B*, 2012, **116**(28), 8145–8153.

55 M. Vazdar, P. Jungwirth and P. E. Mason, Aqueous Guanidinium–Carbonate Interactions by Molecular Dynamics and Neutron Scattering: Relevance to Ion–Protein Interactions, *J. Phys. Chem. B*, 2013, **117**(6), 1844–1848.

56 M. Kohagen, M. Lepsik and P. Jungwirth, Calcium Binding to Calmodulin by Molecular Dynamics with Effective Polarization, *J. Phys. Chem. Lett.*, 2014, **5**(22), 3464–3469.

57 E. Duboue-Dijon, P. E. Mason, H. E. Fischer and P. Jungwirth, Changes in the Hydration Structure of Imidazole upon Protonation: Neutron Scattering and Molecular Simulations, *J. Chem. Phys.*, 2017, **146**(18), 185102.

58 E. Duboué-Dijon, P. Delcroix, H. Martinez-Seara, J. Hladílková, P. Coufal, T. Křížek and P. Jungwirth, Binding of Divalent Cations to Insulin: Capillary Electrophoresis and Molecular Simulations, *J. Phys. Chem. B*, 2018, **122**(13), 3296–3306.

59 J. Melcr, H. Martinez-Seara, R. Nencini, J. Kolafa, P. Jungwirth and O. H. S. Ollila, Accurate Binding of Sodium and Calcium to a POPC Bilayer by Effective Inclusion of Electronic Polarization, *J. Phys. Chem. B*, 2018, **122**(16), 4546–4557.

60 O. Kroutil, M. Předota and M. Kabeláč, Force Field Parametrization of Hydrogenoxalate and Oxalate Anions with Scaled Charges, *J. Mol. Model.*, 2017, **23**, 327.

61 X. Zhong, Z. Liu and D. Cao, Improved Classical United–Atom Force Field for Imidazolium-Based Ionic Liquids: Tetrafluoroborate, Hexafluorophosphate, Methylsulfate, Trifluoromethylsulfonate, Acetate, Trifluoroacetate, and Bis(trifluoromethylsulfonyl)amide, *J. Phys. Chem. B*, 2011, **115**(33), 10027–10040.

62 C. Schroder, Comparing Reduced Partial Charge Models with Polarizable Simulations of Ionic Liquids, *Phys. Chem. Chem. Phys.*, 2012, **14**(9), 3089–3102.

63 W. R. Smith, I. Nezbeda, J. Kolafa and F. Moučka, Recent progress in the molecular simulation of thermodynamic properties of aqueous electrolyte solutions, *Fluid Phase Equilib.*, 2018, **466**, 19–30.

64 H. J. C. Berendsen, J. R. Grigera and T. P. Straatsma, The Missing Term in Effective Pair Potentials, *J. Phys. Chem.*, 1987, **91**(24), 6269–6271.

65 S. H. Lee and J. C. Rasaiah, Molecular Dynamics Simulation of Ion Mobility. 2. Alkali Metal and Halide Ions Using the SPC/E Model for Water at 25 °C, *J. Phys. Chem.*, 1996, **100**(4), 1420–1425.

66 B. J. Palmer, D. M. Pfund and J. L. Fulton, Direct Modeling of EXAFS Spectra from Molecular Dynamics Simulations, *J. Phys. Chem.*, 1996, **100**(32), 13393–13398.

67 I. S. Joung and T. E. Cheatham, Determination of Alkali and Halide Monovalent Ion Parameters for Use in Explicitly Solvated Biomolecular Simulations, *J. Phys. Chem. B*, 2008, **112**(30), 9020–9041.

68 J. L. F. Abascal and C. Vega, A General Purpose Model for the Condensed Phases of Water: TIP4P/2005, *J. Chem. Phys.*, 2005, **123**, 234505.

69 P. D'Angelo, V. Migliorati, F. Sessa, G. Mancini and I. Persson, XANES Reveals the Flexible Nature of Hydrated Strontium in Aqueous Solution, *J. Phys. Chem. B*, 2016, **120**(17), 4114–4124.

70 J. Aqvist, Ion-Water Interaction Potentials Derived from Free Energy Perturbation Simulations, *J. Phys. Chem.*, 1990, **94**(21), 8021–8024.

71 D. Van der Spoel, E. Lindahl, B. Hess, G. Groenhof, A. E. Mark and H. J. C. Berendsen, GROMACS: Fast, Flexible, and Free, *J. Comput. Chem.*, 2005, **26**(16), 1701–1718.

72 W. G. Hoover, Canonical dynamics: Equilibrium phase-space distributions, *Phys. Rev. A: At., Mol., Opt. Phys.*, 1985, **31**(3), 1695–1697.

73 M. Parrinello and A. Rahman, Polymorphic Transitions in Single-Crystals – a New Molecular-Dynamics Method, *J. Appl. Phys.*, 1981, **52**(12), 7182–7190.

74 U. Essmann, L. Perera, M. L. Berkowitz, T. Darden, H. Lee and L. G. Pedersen, A Smooth Particle Mesh Ewald Method, *J. Chem. Phys.*, 1995, **103**(19), 8577–8593.

75 B. Hess, H. Bekker, H. J. C. Berendsen and J. G. E. M. Fraaije, LINCS: A Linear Constraint Solver for Molecular Simulations, *J. Comput. Chem.*, 1997, **18**(12), 1463–1472.

76 R. Heyrovska, Dependence of Ion–Water distances on Covalent Radii, Ionic Radii in Water and Distances of Oxygen and Hydrogen of Water from Ion/Water Boundaries, *Chem. Phys. Lett.*, 2006, **429**(4–6), 600–605.

77 *CRC Handbook of Chemistry and Physics*, ed. D. R. Lide, 89th edn, 2009.

78 Z. R. Kann and J. L. Skinner, A Scaled-Ionic-Charge Simulation Model that Reproduces Enhanced and Suppressed Water Diffusion in Aqueous Salt Solutions, *J. Chem. Phys.*, 2014, **141**, 104507.

79 J. S. Kim, Z. Wu, A. R. Morrow, A. Yethiraj and A. Yethiraj, Self-Diffusion and Viscosity in Electrolyte Solutions, *J. Phys. Chem. B*, 2012, **116**, 12007–12013.

80 Y. Marcus, Effect of Ions on the Structure of Water: Structure Making and Breaking, *Chem. Rev.*, 2009, **109**(3), 1346–1370.
81 E. G. Brandt and A. P. Lyubartsev, Systematic Optimization of a Force Field for Classical Simulations of TiO_2–Water Interfaces, *J. Phys. Chem. C*, 2015, **119**(32), 18110–18125.
82 M. Matsui and M. Akaogi, Molecular Dynamics Simulation of the Structural and Physical Properties of the Four Polymorphs of TiO_2, *Mol. Simul.*, 1991, **6**, 239–244.
83 R. T. Cygan, J.-J. Liang and A. G. Kalinichev, Molecular Models of Hydroxide, Oxyhydroxide, and Clay Phases and the Development of a General Force Field, *J. Phys. Chem. B*, 2004, **108**(4), 1255–1266.
84 I.-C. Yeh and M. L. Berkowitz, Ewald Summation for Systems with Slab Geometry, *J. Chem. Phys.*, 1999, **111**(7), 3155–3162.
85 W. Humphrey, A. Dalke and K. Schulten, VMD – Visual Molecular Dynamics, *J. Mol. Graphics*, 1996, **14**, 33–38.

Article DB2

Biriukov, D.; Kroutil O.; Kabeláč, M.; Ridley, M. K.;
Machesky, M. L.; Předota, M.

Oxalic Acid Adsorption on Rutile: Molecular Dynamics and ab Initio Calculations

Langmuir **2019**, *35* (24), 7617–7630;
IF (2018) = 3.638

Participation of Denys Biriukov:

DB built simulation setups containing oxalic acid anions and rutile surfaces, performed all the molecular dynamics simulations, prepared the initial equilibrated structures for *ab initio* calculations, analyzed the results using pre-implemented and self-written utilities, and was the key person in the paper writing.

DOI: 10.1021/acs.langmuir.8b03984; Copyright 2019 American Chemical Society.

LANGMUIR
Cite This: Langmuir 2019, 35, 7617−7630
Article
pubs.acs.org/Langmuir

Oxalic Acid Adsorption on Rutile: Molecular Dynamics and ab Initio Calculations

Denys Biriukov,*[,†] Ondřej Kroutil,[†,§] Martin Kabeláč,[‡] Moira K. Ridley,[∥] Michael L. Machesky,[⊥] and Milan Předota*[,†]

[†]Institute of Physics, Faculty of Science and [‡]Institute of Chemistry, Faculty of Science, University of South Bohemia, Branišovská 1760, 370 05, České Budějovice, Czech Republic

[§]Faculty of Chemistry, Materials Research Centre, Brno University of Technology, Purkyňova 118, 612 00 Brno, Czech Republic

[∥]Department of Geosciences, Texas Tech University, Lubbock, Texas 79409-1053, United States

[⊥]Illinois State Water Survey, University of Illinois, 1506 Coral Cove Drive, Champaign, Illinois 61821, United States

Supporting Information

ABSTRACT: Detailed analysis of the adsorption of oxalic acid ions, that is, oxalate and hydrogenoxalate, on the rutile (110) surface was carried out using molecular dynamics augmented by free energy calculations and supported by ab initio calculations. The predicted adsorption on perfect nonhydroxylated and hydroxylated surfaces with surface charge density from neutral to +0.208 C/m^2 corresponding to pH values of about 6 and 3.7, respectively, agrees with experimental adsorption data and charge-distribution multisite ion complexation model predictions obtained using the most favorable surface complexes identified in our simulations. We found that outer-sphere complexes are the most favorable, owing to strong hydrogen binding of oxalic acid ions with surface hydroxyls and physisorbed water. The monodentate complex, the most stable among inner-sphere complexes, was about 15 kJ/mol higher in energy, but separated by a large energy barrier. Other inner-sphere complexes, including some previously suggested in the literature as likely adsorption structures such as bidentate and chelate complexes, were found to be unstable both by classical and by ab initio modeling. Both the surfaces and (hydrogen)oxalate ions were modeled using charges scaled to 75% of the nominal values in accord with the electronic continuum theory and our earlier parameterization of (hydrogen)oxalate ions, which showed that nominal charges exaggerate ion−water interactions.

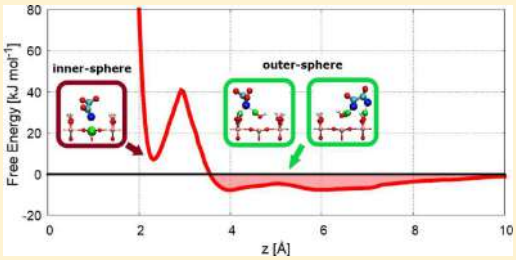

INTRODUCTION

Titanium dioxide is a well-known naturally occurring mineral, which is of particular interest for many scientific and technological applications.[1] TiO_2 nanoparticles are extensively used in a wide range of biomedical fields including photodynamic therapy, drug delivery systems, and genetic engineering due to their relative inertness, facile synthesis, and low cost.[2−4] Moreover, the biocompatibility, chemical stability, and nontoxicity of TiO_2 materials have led to applications in biosensors and tissue reconstruction.[5,6] Besides these advantages, TiO_2 is considered a promising semiconductor in photocatalysis due to its strong photooxidative properties. Since Fujishima et al.[7] discovered the photocatalytic splitting of water on a TiO_2 electrode under ultraviolet light, tremendous attention has been paid to investigating the utilization of TiO_2 particles in a number of related promising areas. Examples include the decomposition of harmful pollutants,[8] solar photovoltaic systems,[9] artificial photosynthesis,[10] and atmospheric photochemistry.[11] These examples highlight the importance of obtaining a comprehensive molecular-level description of processes happening at the interface between TiO_2 and either gas or liquid phases. Consequently, the rutile−vapor and rutile−water interfaces, and especially the predominant (110) crystal face,[12,13] have been the subject of many theoretical and experimental studies,[14−20] which have resulted in substantial understanding of interfacial phenomena.

In recent years, our research group has intensively studied the rutile (110) surface interacting with aqueous solutions by classical molecular dynamics (CMD) simulations.[21−27] As an outcome, we successfully described the structure of water and ions (primarily cations) on neutral and charged surfaces,[21−23] characterized the local viscosity and diffusivity of water molecules between surface slabs,[24] described the effect of temperature and pH on the adsorption and dynamics of ions,[25] and investigated in detail the molecular origin of the ζ

Received: November 29, 2018
Revised: April 24, 2019
Published: May 22, 2019

DOI: 10.1021/acs.langmuir.8b03984
Langmuir 2019, 35, 7617−7630

potential via nonequilibrium MD simulations.[26] When analyzing the adsorption of ions, we studied occupancy of several inner-sphere complexes of ions directly interacting with surface metal-oxide atoms, as well as outer-sphere adsorption of ions fully hydrated by water molecules. Finally, our most recent work[27] focused on modeling the solid−liquid interface by applying scaled charges in accord with the electronic continuum correction (ECC) theory.[28,29] A good agreement of our results with experimental data allowed us to extend the range of investigated systems and perform simulations with larger molecules like organic acids. It is well known that the adsorption and decomposition of carboxylic and dicarboxylic acids have a significant impact on many environmental and geochemical processes, for example, mineral dissolution and the transport of colloids. Moreover, the adsorption of complex compounds containing carboxyl groups, including amino acids and complex components of natural organic matter like humic and fulvic acids, can significantly influence the competitive adsorption of other pollutants.[30]

Here, we detail the adsorption of oxalic acid anions (shown in Figure 1) on charged and neutral rutile (110) surfaces and compare our results with ab initio calculations and experimental data. Oxalic acid $(COOH)_2$, the simplest and smallest dicarboxylic acid, is normally present in dissociated forms under ambient pH conditions due to its low pK_a values. The unique structure with a direct bond between two carboxyl carbons makes this ligand of significant scientific interest. In an early work, Apelblat et al.[31] presented results on the solubility of hydroxycarboxylic and dicarboxylic acids, and in particular oxalic acid, in water for a range of different temperatures. Kettler et al.[32] characterized the thermodynamic properties of oxalic acid to 175 °C using potentiometric titrations. Specifically, they measured the dissociation constants of oxalic acid in different ionic media over a range of ionic strengths. The microsolvation of oxalic acid in pure water was examined by ab initio calculations.[33,34] The important role of $(NH_4)_2SO_4$ in oxalic acid solvation processes resulted in the solubility of oxalic acid salts being measured.[35] The dissociated forms of oxalic acid (Figure 1), namely, oxalate dianion $(COO^-)_2$, abbreviated henceforth as *ox*-2 to indicate its charge, and hydrogenoxalate (also known as bioxalate) $H(COO^-)_2$, abbreviated as *ox*-1, have also been studied. For example, Dean[36] described the stability of different conformers of *ox*-2, whereas Mohajeri et al.[37] were interested in intramolecular hydrogen bonding of *ox*-1 and neutral oxalic acid in the gas phase. Kroutil et al.[34,38] studied the structures of both *ox*-1 and *ox*-2 using classical and ab initio MD simulations. They showed that ab initio optimized geometries depend on the number of water molecules considered to form the solvation shell. In the presence of an explicit solvent, both *ox*-2 and *ox*-1 prefer a staggered structure,[38] whereas a planar structure is typical for a vacuum phase or an implicit solvent. For hydrogenoxalate, because of a possible hydrogen bond between the COOH hydrogen and either COO^- oxygen or water oxygen, the planar geometry is more prevalent compared with that of oxalate, although the staggered structure remains the most preferred.

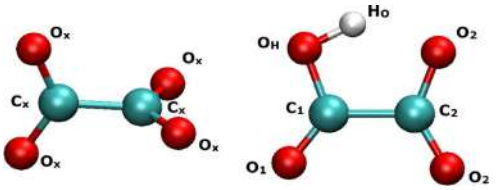

Figure 1. Molecules of oxalate, *ox*-2 (left), and hydrogenoxalate, *ox*-1 (right).

Strong binding ability to metal oxides and the photocatalytic properties of oxalic acid have motivated investigations of its behavior in combination with TiO_2 particles for pollutant removal applications.[39] The photocatalytic reduction of nitrate to ammonia in aqueous suspensions of TiO_2 in the presence of oxalic acid as a hole scavenger was demonstrated by Li and Wagestian.[40] Similarly, adding oxalic acid as a hole scavenger significantly accelerated the decomposition of perfluorooctanoic acid to CO_2 and fluoride ions by TiO_2 under UV light and a nitrogen atmosphere.[41]

Special attention has been given to surface complexation, and especially to the most reactive oxalate species. In the pioneering study in this area,[42] Fahmi et al. presented results of periodic quantum chemical calculations on the adsorption of oxalic acid and its deprotonated species on rutile and anatase

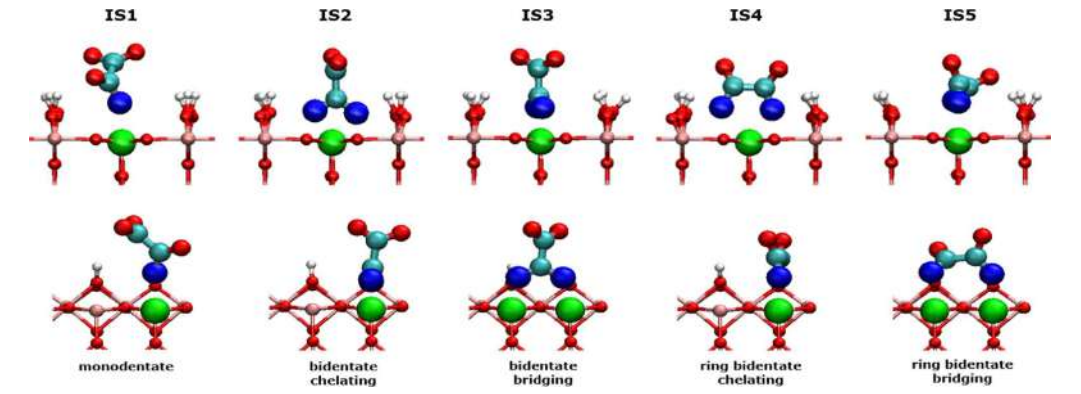

Figure 2. Proposed surface structures of inner-sphere adsorbed oxalate: front (top) and side (bottom) views. Interacting oxygen atoms of oxalate are shown in blue; interacting metal sites are shown in green.

DOI: 10.1021/acs.langmuir.8b03984
Langmuir 2019, 35, 7617−7630

surfaces in the gas phase. Using TiO_2 modeled as one-dimensional polymers, they indicated that the dissociative adsorption of oxalic acid (an electron pair is transferred from an oxygen atom of oxalic acid to a metal site) is more favorable than molecular adsorption (a proton is transferred to an oxygen of the oxide, and the carboxylate adsorbs on a Ti atom). The oxalate chemisorbed to two metal sites by two oxygen atoms of different COO^- groups was found to be the most stable surface complex, whereas adsorption through two oxygen atoms of the same carboxyl group was predicted as unstable. Subsequent experimental studies[43] proposed several possible inner-sphere structures at the TiO_2–water interface. The most predominant of those inner-sphere complexes, labeled IS1–IS5 in Figure 2, comprise a monodentate structure (one oxygen bound to one Ti atom, IS1), a bidentate chelating structure (both oxygen atoms of the same COO^- group bound to a metal site, IS2), a bidentate bridging structure (each oxygen of the same COO^- bound to different Ti atoms, IS3), a ring bidentate chelating structure (two oxygen atoms from different COO^- groups bound to a metal site, IS4), and a ring bidentate bridging structure (one oxygen from each COO^- group bound to different Ti atoms, IS5). Note that in terms of anion adsorption by metal-oxide surfaces, and particularly oxalate by rutile, inner-sphere adsorption specifically involves a direct bond(s) between the adsorbed anion and a surface metal atom(s), that is, fivefold coordinated Ti, whereas interactions with only surface hydroxyls are not treated as inner-sphere.

Hug et al.[43,44] have made significant contributions to understanding TiO_2–oxalic acid interactions by attenuated total reflectance Fourier transform infrared spectroscopy (ATR-FTIR). In their studies, the spectral differences between the bulk and adsorbed species were interpreted as strong evidence of inner-sphere adsorption. They concluded that ring bidentate chelating and ring bidentate bridging surface complexes, with one oxygen of each carboxyl group coordinated to titanium atoms, are the most favorable surface structures (IS4 and IS5). Similar conclusions were made by Weisz et al.[45] in their analogous spectroscopic study. In addition, Weisz et al. found surface complexes involving one or two oxygen atoms of the same COO^- group as less stable compared with those with two oxygen atoms of different groups (ring structures). Similar behavior was suggested for more complex dicarboxylic acids like malonate and succinate.[43] In the case of monocarboxylic acids (formate and acetate), the bridging bidentate structure was identified as predominant.[46]

Another series of articles reporting on the adsorption of oxalate on both rutile and anatase surfaces have been carried out by Mendive et al.[47−51] They employed a combination of ATR-FTIR experiments and quantum chemical calculations, comparing the spectra derived from the infrared measurements with calculated spectra for several different configurations of the adsorbed ligand. For rutile, the suggested structures were similar to those identified previously. According to their results, the presence of an aqueous phase greatly changes the stability of surface complexes. With water present in the system, monodentate structures were found to be thermodynamically more stable than bidentate species, whereas in vacuum the trend was opposite. In the case of anatase, monodentate structures followed by both types of bidentate complexes (C–C bond either parallel or perpendicular to the surface) were recognized as the main contributors. Other studies are varied in terms of the stability of surface complexes. An FTIR study by Singh et al.[52] revealed that oxalic acid binds to TiO_2 particles through bidentate bridging coordination with both COO^- groups involved. Young et al.[53] concluded that the ring bidentate chelating complex was the most strongly bound to anatase. Inner-sphere binding was also suggested as the predominant complexation for oxalate at (α-Al_2O_3) corundum (ring bidentate chelating)[54] and (γ-FeO(OH)) lepidocrocite (monodentate and ring bidentate chelating) surfaces.[55] Returning to TiO_2, a few inner-sphere complexes are hypothesized for glutamate ("lying down", with both carboxyl groups involved, and "standing up", with only one carboxyl group bound to the surface)[56] and formaldehyde (bidentate and monodentate adsorption, with possible spontaneous switching between these states).[57]

It should be noted that in all of the works summarized above, purely hydrogen-bonded outer-sphere adsorption (hereinafter referred to as outer-sphere), that is, hydrogen binding of acids or their ions to surface hydroxyl groups or inner-sphere adsorbed water, was not fully described or even considered at all. Few studies attempted to correlate IR spectroscopic data with outer-sphere adsorption of oxalate at lepidocrocite, and glutamate and aspartate at rutile,[55,56] and it was possible to correlate outer-sphere complexes to the observed spectra. In addition, oxalate has been proposed to form outer-sphere complexes at the TiO_2–water interface, which diminish with time as the coordinated oxalate decreases the positive surface charge.[58] Recent work[59] suggests that surface defects can play a major role in the adsorption of organic molecules, and inner-sphere adsorption may be based upon the presence of surface steps, at which most inner-sphere coordination occurs. At present, the role and impact of outer-sphere adsorption are still unclear, particularly at perfect crystal surfaces. Our research was aimed at addressing this shortcoming through both experimental and theoretical methods.

EXPERIMENTAL METHODS

The adsorption of oxalic acid anions onto rutile was investigated using potentiometric titrations, which have been described in detail previously.[60−64] Titration solutions were prepared with 0.001 *m* $(COO^-)_2$ (where *m* is moles of $(COO^-)_2$ per kg water) and sufficient NaCl to give ionic strengths of 0.03 or 0.3 *m*. The rutile powder used in all titrations came from Tioxide Corporation. This rutile has a distinct and dominant (110) crystal face and a N_2-Brunauer–Emmett–Teller surface area of about 17 m^2/g. Prior to use, the rutile was hydrothermally pretreated following Machesky et al.[65] At each experimental condition (i.e., varying ionic strengths), two independent sets of titrations were completed. In the first, at each titration point the proton excess or deficit in solution was calculated as a function of m^2 of the rutile area. The excess/deficit of protons per m^2 may then be expressed in terms of net proton surface charge (σH, C/m^2), where the relationship is negative Faraday constant per equivalent moles of proton excess/deficit. In the second set of titrations, samples were periodically withdrawn from the test solution. The withdrawn samples were filtered; then, the total dissolved oxalate concentration was analyzed by ion chromatography. The concentrations of oxalic acid anions adsorbed to the rutile surface were determined by difference.

COMPUTATIONAL DETAILS

Molecular Dynamics Force Field. The force field of the system consists of models of the rutile surface, oxalic acid, background ions, and explicit water.

Models of oxalate (*ox*-2) and hydrogenoxalate (*ox*-1) (Figure 1) were adopted from the recent study of Kroutil et al.[38] The force field, implementing scaled charges according to the ECC theory, describes interactions with water in very good

DOI: 10.1021/acs.langmuir.8b03984
Langmuir 2019, 35, 7617−7630

agreement with ab initio MD simulations, whereas the standard model with the full restrained electrostatic potential (RESP) charges results in overstructuring of the water envelope and too strong electrostatic interactions. For oxalate, all RESP charges were scaled down by a factor of 0.75. For hydrogenoxalate, a hybrid approach (called ECCR-P[38,66]) was applied; the charges of the COOH group were adopted from the neutral oxalic acid model without scaling, whereas the charges of the COO^- group are the same as for oxalate with scaled charges. For large molecules, reduction of only the charges of the charged functional groups, while keeping the RESP charges of the remainder of the molecule, has already been applied with success for proteins,[66−68] where either deprotonation or charging has a rather local effect on partial charges. It was therefore somewhat surprising that this combination works well even for an ion as small as hydrogenoxalate. The nonbonded parameters of this force field are given in Table 1, and the corresponding atom labels can be found in Figure 1. The full force field with bonded and angle terms can be found in the Supporting Information of ref 38.

Table 1. Nonbonded Parameters for Water, Ions, and Oxalic Acid Anions

atom	σ (Å)	ε (kJ/mol)	q (e)
	Water[a]		
O_w	3.16557	0.650629	−0.8476
H_w	0.00000	0.000000	0.4238
	Ions[b]		
Na^+	2.11500	0.544284	0.75
Cl^-	4.10000	0.492800	−0.75
	Oxalate, *ox*-2[c]		
C_x	3.39967	0.359824	0.53516
O_x	3.04600	0.878640	−0.64258
	Hydrogenoxalate, *ox*-1[c]		
C_1	3.39967	0.359824	0.70168
O_1	3.04600	0.878640	−0.52824
O_H	3.06647	0.880314	−0.64505
H_O	0.00000	0.000000	0.47160
C_2	3.39967	0.359824	0.53516
O_2	3.04600	0.878640	−0.64258

[a]Berendsen.[69] [b]Kohagen et al.[70] [c]Kroutil et al.[38]

Within the ECC concept, consistent parameters for the other system components were required. The aqueous solvent was represented by the rigid, nondissociative extended simple point charge (SPC/E) model,[69] which assigns partial charges to the oxygen and two hydrogens and applies a Lennard-Jones (LJ) potential to the oxygen site. This model was successfully used in our previous studies[21−27] since it can adequately reproduce thermodynamic and dielectric properties for a wide range of temperature and pH conditions. Note that the SPC/E model without any modifications is fully compatible with the ECC theory, since effective partial charges are used, and the ECC scaling applies only to charged molecules (or their functional groups as mentioned above). The charges of background ions, sodium and chloride, were scaled to $0.75e$ and $-0.75e$, respectively. The LJ potentials for Na^+ and Cl^- were adopted from Kohagen et al.,[70] where an adjustment of the van der Waals coefficients was performed after charge rescaling. The parameters for water and ions are also summarized in Table 1.

The force field for rutile surfaces was prepared in the same way as in our earlier works[21−26] except for two changes that have been discussed in more detail recently.[27] The first change was technical to unify the functional form of all nonbonded interactions to the LJ form, allowing easier implementation of the force field in simulation software, GROMACS.[71] For this reason, the Buckingham (exp-6) terms for Ti−O interactions[72] were replaced by their refitted LJ parameters.[73] The second change, implementing the ECC theory to model rutile surfaces, follows the same mechanism for distribution of excess surface charge as in our previous studies. However, reducing excess charge to 75% of its nominal value is a fundamentally new approach, representing the first application of the ECC theory to surfaces. We scaled the partial charges of only the top layer of the surface (terminal Ti_t and bridging Ti_b hydroxyls), whereas bulk titanium and oxygen atoms retained their normal charges (Table 2). The only difference in the present work is that we used positively charged surfaces prepared from neutral surfaces by partial protonation of selected bridging oxygen atoms (starting from the neutral nonhydroxylated surface) or by partial protonation of selected terminal hydroxyls, that is, their replacement by physisorbed water molecules (starting from the neutral hydroxylated surface). Note that the nominal +0.104 or +0.208 C/m^2 surface charge densities represent the surface charge densities linked to the surface occupancy of protonating protons and experimental data, although the actual surface charge density in the ECC simulations is only 75% of that value due to the charge of only $+0.75e$ for each protonated group. This is fully consistent with the fact that in the ECC approach, all ions (including charged surfaces, which can be treated as charged supermolecules) are modeled with 75% total charge compared to their nominal values (e.g., Na^+ is represented by a model with a charge of $+0.75e$). Note that for neutral surfaces no modifications to partial charges were applied.

Table 2. ECC Charges of Rutile Surface Atoms

	surface					
atom	*nh* + 0.0	*nh* + 0.1	*nh* + 0.2	*h* + 0.0	*h* + 0.1	*h* + 0.2
bulk Ti	2.196	2.196	2.196	2.196	2.196	2.196
bulk O	−1.098	−1.098	−1.098	−1.098	−1.098	−1.098
Ti_t, Ti_b	2.196	2.165	2.175	2.196	2.162	2.167
O_t				−1.008	−0.936	−0.927
H_t				0.459	0.434	0.441
unprotonated O_b	−1.098	−1.007	−1.001			
protonated O_b		−0.954	−0.945	−1.035	−0.958	−0.954
H_b		0.465	0.474	0.486	0.461	0.466

DOI: 10.1021/acs.langmuir.8b03984
Langmuir 2019, 35, 7617−7630

Table 3. Numbers of Ions in the Systems

		oxalic acid anions		background ions	
surface	surface charge to compensate [e], nominal (scaled)	*ox*-2 (−1.5*e*)	*ox*-1 (−0.75*e*)	Na^+ (+0.75*e*)	Cl^- (−0.75*e*)
neutral	0	10		32	12
+0.104 C/m^2	18 (13.5)	10		14	12
+0.208 C/m^2	36 (27)	15	10	16	12

We stress that no adjustment of the force field for the sake of (or during) the current study was performed. The models of oxalic acid ions were adopted from our recent publication,[38] where only bulk oxalic acid−water interactions were investigated. The parameters of background ions (Na^+, Cl^-) were adopted from the literature.[70] The ECC model of the rutile surface follows the development described above and was used for the first time for the study of monoatomic cation adsorption on neutral and negatively charged surfaces.[27] The ECC model of the positively charged +0.104 C/m^2 surface is used here for the first time since this surface charge density was studied by us only using full charges.[25,26] The +0.208 C/m^2 surface has not been explored by us before because only for our oxalic acid adsorption studies was this charge state attained.

Molecular Dynamics Setup. A four-layer TiO_2 slab on the liquid-facing side was either hydroxylated, mimicking chemisorption of dissociatively adsorbed water molecules, or nonhydroxylated, representing physisorption of associatively adsorbed water molecules at bare terminal Ti atoms. The first adsorption layer, L1, thus consists of surface terminal hydroxyls and SPC/E water molecules strongly bound to bare terminal Ti atoms. Oxygens of L1 are close to positions where rutile oxygen atoms would be if the mineral structure was not terminated. The second layer, L2, is formed by water molecules found close to bridging groups and interacting with them as well as with terminal water/hydroxyls and other water molecules; see, for example, Figure 1 in ref 74.

Charged surfaces were obtained from neutral surfaces either by a partial removal of terminal hydroxyl hydrogen atoms (hydroxylated surfaces) or by addition of bridging hydrogen atoms (nonhydroxylated surfaces), as detailed in the previous section. Six different systems were studied: hydroxylated or nonhydroxylated rutile surfaces, each of which was either neutral or positively charged (+0.104 or +0.208 C/m^2 surface charge density). Hereafter, the six systems are abbreviated as *nh* + 0.0, *nh* + 0.1, *nh* + 0.2, *h* + 0.0, *h* + 0.1, and *h* + 0.2 to indicate the type of surface and its charge density. These surface charge densities correspond to experimentally determined pH values of about 6, 4.6, and 3.7, respectively, from our oxalate adsorption studies.[75] This approach, successfully applied in all of our previous studies not only for rutile[21−27] but also for quartz[76] and cassiterite,[77] is dictated by the use of nonreactive MD force fields, where acid−base reactions and water dissociation are prohibited and must be taken into account by the preset partial coverage of surfaces by protonated/deprotonated bridging and terminal groups.

The simulation box consists of two equally charged rutile slabs with lateral dimensions of 38.9814 Å × 35.508 Å separated by the aqueous solution comprising water molecules and a selected number of oxalic acid anions and background salt (Table 3). In the *z* direction, replicas were separated by a sufficiently large vacuum gap to exclude surface−surface interactions. As a result, at each surface, we observed two identical inhomogeneous interfaces with widths of approximately 15 Å, followed by the 20 Å-thick bulk region formed in the center of the simulation cell. Previously, we proved that such width is sufficient to establish bulk aqueous solution properties.[26] Since both surfaces are equivalent, the presented results are averages over both interfaces. The ratio of oxalate and hydrogenoxalate in the system was selected in accord with pK_a values of the oxalic acid (pK_{a1} = 1.25 and pK_{a2} = 4.27).[78] Therefore, at neutral and +0.104 C/m^2 charged surfaces, no hydrogenoxalate ions were present, as they are negligible species at these pH conditions, whereas at +0.208 C/m^2 surfaces, the number of oxalate and hydrogenoxalate ions was set to produce a ratio of bulk concentrations of those species near that based on pK_a values (with the oxalate bulk concentration of 0.02−0.06 M for all systems, except for the least attractive *nh* + 0.0 surface, where it was around 0.2 M). The amount of oxalic acid was sufficiently large to fully compensate the positive surface charge. At neutral surfaces, the negative net charge of oxalate was compensated by a surplus of Na^+ ions. Sodium and chloride ions were added in an amount resulting in around 0.3 M bulk concentration as in the experiments. Bulk water density in the center of the simulation box was about 1 g/cm^3.

Classical MD simulations were performed using the Gromacs 5.1.4 software package[71] employing periodic boundary conditions in all three dimensions. A 2 fs step was used, and the cutoff distance was set to 12 Å for both short-range and long-range interactions. A three-dimensional particle mesh Ewald summation[79] with the correction for slab geometry (EW3DC)[80] was applied. The total charge of the system was zero to converge long-range interactions. The temperature was maintained at 298.15 K by the Nosé−Hoover thermostat[81] with a coupling time of 0.5 ps. The Lincs algorithm[82] was used to constrain hydrogen bonds. All surface atoms except for bridging and terminal groups were kept immobile during all MD simulations to prevent displacement of the surfaces.

The systems for unbiased simulations were minimized with the steepest descent algorithm. Subsequently, a 5 ns equilibration stage was followed by a 50 ns production run in the canonical NVT ensemble. Biased simulations are detailed in the next section.

Energy Calculations. Free energy calculations are an efficacious tool for detailed description of molecular interactions at an interface. A straightforward way to characterize the adsorption of a molecule on the surface is to calculate the free energy difference between the energy of a molecule bound at the surface and the energy corresponding to the molecule present in the bulk. Theoretically, it is possible to obtain the energy profile from the probability histogram obtained by counting the times when the particular states of the system are occupied from standard, unbiased molecular dynamics simulations. In practice, this approach can be inefficient because of the time needed for the system to visit all possible states, particularly when significant energy barriers are present. To circumvent these limitations, the system must

DOI: 10.1021/acs.langmuir.8b03984
Langmuir 2019, 35, 7617−7630

be forced to visit all states along the reaction coordinate. There are two popular approaches with artificially biased sampling to overcome the potential barriers present in the system. One of those is the umbrella sampling method, which restricts a system to a set of windows along the reaction coordinate, and then an independent simulation is carried out within each window with a harmonic biasing potential. The free energy profile (potential of mean force, PMF) along this reaction coordinate can be extracted from a series of umbrella sampling simulations using the WHAM algorithm.[83] The other popular method used to sample the free energy surface is metadynamics.[84] The principle of this method is to use collective variables (such as geometric (position, distance), or a number of water molecules in the surrounding shell) in conjunction with a time-dependent biasing potential. This potential prevents the system from exploring regions visited previously, which helps the system to escape from the traps of free energy minima and/or penetrate through the high-energy barriers. Such an approach is efficient for simulating interfaces since the adsorbate is biased to move along the surface and sample all adsorption sites. Both PMF and metadynamics approaches have already been successfully used to study rutile,[85−88] quartz,[89,90] and calcite[91] surfaces.

In this study, we focused on the PMF method to compare inner-sphere and outer-sphere adsorption of oxalic acid anions on the rutile (110) surface. Since the number of studied systems is large, and this method requires a lot of computational time, we restricted ourselves to studying only oxalate adsorption at the most positively charged (+0.208 C/m^2) nonhydroxylated (with bare terminal Ti sites) surface, that is, we chose the most reactive anion interacting with the most attractive surface for anion binding.

A common approach of using a distance between the surface and the center of a molecule as a reaction coordinate did not produce a reasonable energy profile because of the symmetric and hard-to-sample structure of the oxalate molecule and energy barriers present in the system. Similar problems of convergence were observed in metadynamics simulations. Therefore, we performed several series of umbrella sampling calculations, varying the choice of ligand reference, and reflecting the most promising inner-sphere configurations. We selected three types of reaction coordinates: (a) distance between the surface and one oxygen of oxalate, to model the monodentate structure; (b) distance between the surface and the center of mass (COM) of the oxygen atoms of the same COO^- group, to model bridging and chelating bidentate structures; and (c) distance between the surface and the COM of two oxygen atoms of the opposite COO^- groups, to model ring bidentate structures. A selected oxalate molecule with a chosen reference point was pulled toward the surface along the *z*-coordinate (reaction coordinate) to obtain initial configurations for umbrella sampling simulations. To finish in a desired inner-sphere state, an oxalate molecule was pulled to either one surface terminal Ti atom or to the COM of two terminal Ti atoms. For example, if the COM of the oxygen atoms of the same COO^- group is dragged to one terminal Ti site, the bidentate chelating structure (IS2) will be achieved. That means we had to run five pulling simulations to generate the five inner-sphere structures shown in Figure 2. A reaction coordinate, in all cases a distance between a ligand reference and the zero height of the surface (defined as the position of the last layer of Ti atoms, if they were unrelaxed), was divided into at least 33 windows up to 10 Å above the surface. In inner-sphere (hereinafter L1, or first layer) and outer-sphere (L2, or second layer) regions, the width of each window was around 0.1−0.2 Å; at larger distances, it was about 0.5 Å. These widths (together with carefully selected positions of reference distances) secured a sufficient overlap of the histograms of distribution of reference points of the oxalate ion, which is essential for correct determination of the whole free energy profile. An independent NVT run for each window was 10 ns long. Final energy profiles were obtained using the WHAM algorithm[83] implemented in the Gromacs simulation package.[71] Other simulation settings were the same as for the classical MD simulations described above.

Ab Initio Calculations. The quantum chemistry calculations were carried out using the Gaussian 16 program[92] using the B3PW91 density functional, similarly as in Kevorkyants et al.[93] Our model system contained a $Ti_{15}O_{30}$ cluster with one of the bridging oxygens protonated and an oxalate anion solvated by eight water molecules. The number of water molecules was limited to the first solvation shell because of high computational cost to reproduce full solvation as in our MD simulations. The structures representing different binding motifs of hydrated oxalate to the rutile surface were extracted from representative MD snapshots obtained using umbrella sampling simulations. During the optimization procedure, the geometry of the rutile surface was kept fixed, except for the bridging hydrogen, whereas no restrictions were applied for the optimization of the rest of the system. The LANL2DZ basis set was applied for titanium atoms, the 6-31G(d,p) basis set was applied for oxygen atoms of rutile and water atoms, and the 6-31++G(d,p) basis set was employed for oxalate atoms to properly describe the behavior of the anion. The missing dispersion energy in the density functional theory (DFT) was compensated by an empirically treated Grimme's GD3 dispersion term.[94] Water was treated implicitly by the polarizable continuum model.[95] The superposition error for calculations of interaction energies was eliminated by the counterpoise method of Boys and Bernardi.[96]

RESULTS AND DISCUSSION

A first step in our characterization of oxalic acid adsorption at rutile (110) surfaces was to run classical (unbiased) molecular dynamics (CMD) simulations using the aforementioned force field. Figure 3 shows axial density profiles of oxygen atoms of oxalate, hydrogenoxalate, and water, obtained from classical MD simulations for all studied systems with the number of species given in Table 3. One can clearly see that only water adsorbs inner-spherically, with its oxygen atoms in the L1 layer (about 2.14 and 2.27 Å above fivefold coordinated terminal (Ti_V) atoms for *nh* and *h* surfaces, respectively), except in the case of a neutral hydroxylated surface, where all terminal sites are hydroxylated. Oxalate and hydrogenoxalate, in turn, adsorb only as outer-sphere complexes, but in amounts close to the experimental results (Figure 4) for all three simulated charge densities. The independence of simulation results on the discrimination of adsorbed molecules is shown in the Supporting Information (SI). The positions of the peaks for water and (hydrogen)oxalate oxygen atoms in L2 are nearly the same. While the L1 layer located above the terminal sites is the only one offering a direct inner-sphere interaction of oxygens with Ti atoms (namely, terminal Ti_V atoms), the L2 layer located in the vicinity of bridging sites offers hydrogen binding opportunities for water and oxalic acid ions with surface sites. These bonds can be either between bridging

DOI: 10.1021/acs.langmuir.8b03984
Langmuir 2019, 35, 7617−7630

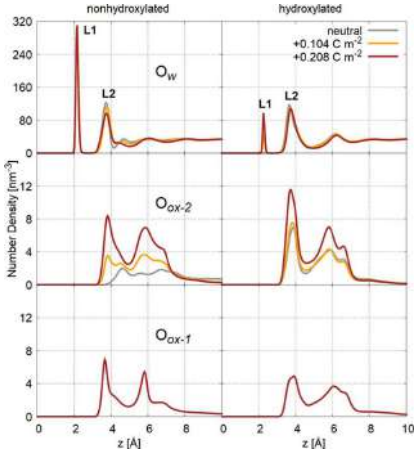

Figure 3. Axial number density profiles of water oxygen atoms of water (top), oxalate (middle), and hydrogenoxalate (bottom) at nonhydroxylated (left) and hydroxylated (right) rutile surfaces from unbiased MD simulations. Note the different vertical scales.

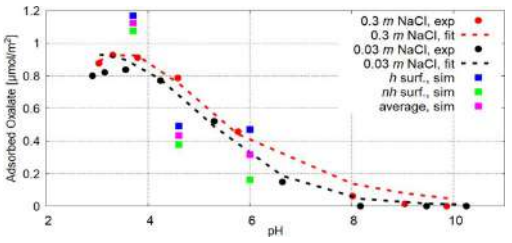

Figure 4. Adsorption pH edges for 0.001 *m* oxalic acid in NaCl electrolyte (0.3 *m* and 0.03 *m*) from experiment, charge-distribution multisite ion complexation (CD-MUSIC) surface complexation modeling (using OS1 and OS2 outer-sphere complexes; see ref 75 for details), and CMD simulations (*nh* and *h* surfaces, and average data from those).

oxygen and hydrogen of hydrogenoxalate or water or between oxygen atoms of (hydrogen)oxalate or water and hydrogens of terminal or bridging (if protonated) groups. Due to the full coordination of carbon atoms in oxalic acid, as well as steric hindrance of these atoms by carboxylic oxygen atoms, carbon atoms cannot directly interact with surface oxygen atoms. The only possibility (not allowed in the standard CMD model) would be if the surface bridging oxygen replaced the carboxyl oxygen; however, considering the strength of Ti−O and C−O bonds, this is a very unlikely scenario.

Obviously, with increasing surface charge, more oxalate adsorbs because of the strong electrostatic attraction of negatively charged oxalate and the positively charged surface. Note that much more oxalate adsorbs on the *h* + 0.0 surface compared with that on the *nh* + 0.0 surface since the hydroxylated surface offers both bridging (H_b) and terminal (H_t) hydrogen atoms for hydrogen binding with oxalate oxygen atoms. The nonhydroxylated surface offers in fact an equal number of hydrogens as emphasized in SI, but in the form of L1 water molecules, which are less attractive. This variance is no longer significant for charged surfaces due to partial protonation of bridging oxygen atoms on nonhydroxylated surfaces generating positive surface charge. Hydrogenoxalate, present only in simulations at +0.208 C/m^2 surfaces, is a weaker adsorbate than oxalate due to its lower negative charge. Our additional test simulations with the same number of oxalate and hydrogenoxalate species in the system confirmed this tendency; therefore, a major part of the following results, particularly energy calculations, is devoted to oxalate.

Detailed analysis of MD trajectories was carried out in a similar way as in our study of cation adsorption at neutral and negatively charged rutile surfaces.[27] This analysis was performed in the VMD program package[97] to identify the most preferable outer-sphere complexes. A criterion to define these complexes was the number of hydrogen bonds between a ligand and the surface. All L1 water molecules, which are strongly physisorbed at the surface (their exchange by another water molecule or a chloride ion was a rare event in the whole course of our MD simulations), were also treated as surface (terminal) species for this purpose. This inclusion not only acknowledges the strong interaction between L1 water molecules and the surface but also helps to fairly compare the results for nonhydroxylated and hydroxylated surfaces. With the inclusion of L1 water molecules as surface species, nonhydroxylated and hydroxylated surfaces contain the same number of oxygen and hydrogen atoms for each charge density.

Since oxalate has no hydrogen, and hydrogenoxalate rarely forms a bond with an oxalate molecule through its hydrogen, the outer-sphere complexes were distinguished by the number of hydrogen bonds between oxygen atoms of (hydrogen)-oxalate (O_x) and either bridging or terminal hydrogens including molecular L1 water. We adopt the simplest geometric criterion of a hydrogen bond, namely, each pair within the first minimum of the bulk radial distribution function between an oxygen of oxalate (O_x) and hydrogen of water (H_w) is considered as hydrogen bonded, that is, O_x−H_w distance smaller than 2.45 Å is the only criterion for hydrogen bonding. For simplicity and consistency, we chose this uniform distance, since the actual minima for O_x−H_b and O_x−H_t pairs were in a very close range for different systems (2.25−2.45 Å); moreover, small variations of this value have a negligible effect on the results. For hydrogenoxalate, we also monitored binding of the hydrogenoxalate hydrogen with surface oxygens (within the same cutoff of 2.45 Å), which can stabilize some complexes by an additional very strong bond (1.5−1.55 Å) with a bridging oxygen. Outer-sphere complexes identified by this analysis are summarized in Figure 5, where we indicate the six most prominent structures (OS1−OS6) differing in the amount and type of hydrogen bonds. Their relative populations (within acid anions forming at least one bond with surface groups) are given in Table 4, together with additional information about less-favorable structures (OS1−, OS2+, etc.). For example, OS2+ represents the population of complexes with the same number of bonds with bridging groups as the OS2 complex, that is, only one, but with three or more bonds with terminal groups. OS1−, in turn, refers to a complex with the same number of bonds with bridging groups, that is, one, but without binding to terminal groups.

At charged nonhydroxylated surfaces, OS1 and OS2 complexes are dominant, whereas less hydrogen-bonded OS3 and OS4 complexes have a smaller, but still considerable coverage. The dominant OS1 and OS2 structures, together

DOI: 10.1021/acs.langmuir.8b03984
Langmuir 2019, 35, 7617−7630

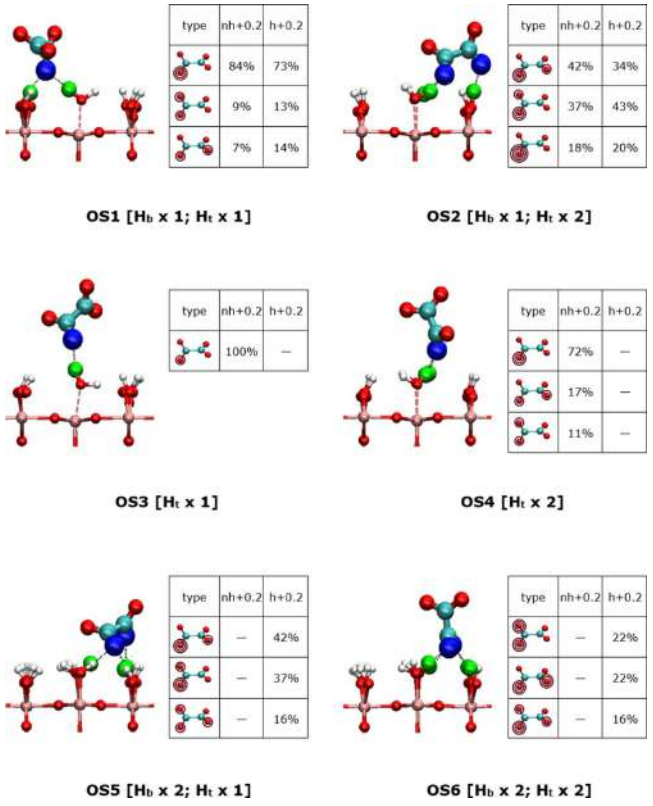

Figure 5. Examples of outer-sphere adsorbed complexes of oxalate distinguished by the number of hydrogen bonds of oxalate oxygens with terminal (H_t) and bridging (H_b) hydrogens as given in square brackets. Interacting oxygens of oxalate are shown in blue; interacting surface hydrogens are shown in green. Black dashed lines are hydrogen bonds between oxygen atoms of oxalate and surface hydrogens. For nonhydroxylated surfaces (OS1−OS4 structures), red dashed lines indicate strong noncovalent interactions between L1 water molecules and terminal Ti atoms (the case of nonhydroxylated surfaces shown for OS1−OS4 structures; hydroxylated surfaces are shown for OS5 and OS6). Hydrogens of water molecules at terminal sites are treated as terminal hydrogens. Note that complexes with several hydrogen bonds can be realized by many structural alternatives differing in the positions of interacting oxygens and surface hydrogen atoms. A table to the right of each complex shows a distribution of the formed bonds among oxygen atoms of an interacting oxalate molecule, that is, a number of circles around an oxygen atom corresponds to a number of formed bonds by this oxygen.

Table 4. Relative Population (in %) of the Outer-Sphere Adsorption Complexes of Oxalic Acid at Rutile Surfaces[a]

	oxalate						hydrogenoxalate[b]	
surface complex	*nh* + 0.0	*nh* + 0.1	*nh* + 0.2	*h* + 0.0	*h* + 0.1	*h* + 0.2	*nh* + 0.2	*h* + 0.2
OS1−	[c]	13.5	4.2	16.0	6.8	4.1	3.2 (8.7)	10.1 (42.9)
OS1	[c]	**20.2**	**25.7**	**18.3**	14.6	16.1	11.9 (15.3)	**28.6 (47.0)**
OS2	[c]	**18.4**	**22.7**	11.6	13.0	**17.2**	11.0 (44.1)	**17.9 (22.8)**
OS2+	[c]	8.8	14.2	3.5	4.9	7.6	6.8 (70.1)	4.6 (4.8)
OS3	**43.2**	15.0	11.0	[d]	[d]	[d]	**17.1 (33.1)**	8.4 (39.8)
OS4	**46.8**	15.8	11.5	[d]	[d]	[d]	**18.9 (58.8)**	4.5 (25.8)
OS4+	10.0	3.2	[d]	[d]	[d]	[d]	**28.0 (95.7)**	[d]
OS5−	[c]	[d]	[d]	10.0	7.5	3.4	[d]	3.7 (29.2)
OS5	[c]	[d]	[d]	**17.0**	**18.3**	12.3	[d]	8.8 (23.1)
OS6	[c]	[d]	4.5	11.9	**17.5**	**17.2**	[d]	7.6 (3.7)
OS6+	[c]	[d]	[d]	4.2	8.2	11.2	[d]	[d]

[a]Only cases when a molecule has at least one hydrogen bond are considered. Dominant complexes are shown in bold. [b]Values in parentheses show the relative subpopulation of the complexes forming an additional hydrogen bond between the hydrogenoxalate hydrogen and a deprotonated bridging oxygen. [c]Complex is not observed. [d]Complex is populated less than 3%.

DOI: 10.1021/acs.langmuir.8b03984
Langmuir 2019, 35, 7617−7630

with the average length of hydrogen bonds within these structures (which can be found in the SI of this paper), were successfully used for CD-MUSIC modeling of oxalate adsorption and provided good agreement with experimental adsorption data.[74] At the hydroxylated surface, structures with two bridging hydroxyls bound to a ligand are somewhat more prevalent (OS5 and OS6), although the OS1 and OS2 complexes have comparable populations. Importantly, for the surface charge densities explored, there are no adjacent bridging hydroxyls at nonhydroxylated surfaces, so OS5 and OS6 complexes are unfavorable at these surfaces. Since real surfaces are in between the extreme scenarios of surface hydroxylation studied here, that is, nonhydroxylated and hydroxylated surfaces,[98,99] OS1 and OS2 are considered to be predominant outer-sphere complexes for a wide range of pH and temperature.[75] This is also true for hydrogenoxalate, which favors the OS1 and OS2 structures at both nonhydroxylated and hydroxylated surfaces. In contrast to oxalate, the OS5 and OS6 complexes are less preferable for hydrogenoxalate even at hydroxylated surfaces because the hydrogenoxalate hydrogen weakens the binding capacity of its connected oxygen to surface hydrogens. In addition to the complexes given in Figure 5, adsorbed hydrogenoxalate can form another very stable complex at the nonhydroxylated surface (similar to OS4) forming three bonds between its oxygens and terminal (and/or L1 water) hydrogens and no bonds with bridging groups [$H_b \times 0$; $H_t \times 3$]. Hydrogenoxalate hydrogen plays a key role in this complexation because (i) it forms an additional hydrogen bond in the majority of structures of this type and (ii) because the abundance of this complex is high for hydrogenoxalate (~23%) but small for oxalate.

The hydrogenoxalate hydrogen (or its absence) influences the orientation of a molecule at the interface. Figure 6 shows

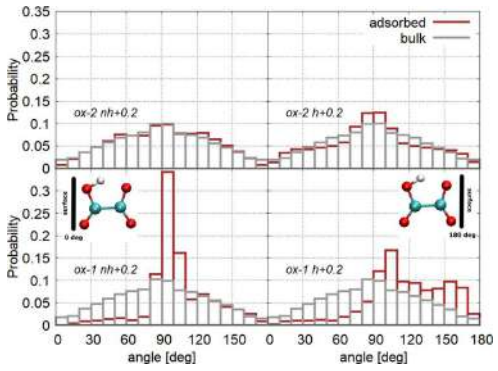

Figure 6. Histograms of the angular distribution between the C−C bond of oxalic acid anions and the surface normal vector at the most positively charged (+0.208 C/m^2) surfaces.

the angular distribution between the C−C vector of the adsorbed oxalic acid anion and the surface normal. This distribution was compared with the same distribution from an independent bulk simulation without rutile surfaces in the simulation box (the *xy* plane was used as an imaginary surface). For oxalate, the C−C bond orientation, in relation to the surface plane, changes only slightly compared to the isotropic (sine) distribution observed in the bulk. Only at the hydroxylated surface, there is a small shift to a more pronounced parallel orientation, which allows involvement of both COO^- groups in forming more hydrogen-bonded outer-sphere complexes like OS5 and OS6. Hydrogenoxalate, in turn, behaves significantly differently. At nonhydroxylated surfaces, where a hydrogenoxalate hydrogen can easily form a bond with a bare bridging oxygen, a parallel orientation with respect to the surface greatly dominates. This conclusion is also supported by the density profiles of hydrogenoxalate atoms (Figure S1 in the SI), which shows that while the COO^- group of hydrogenoxalate interacts with the surface more often than the COOH group, the hydrogen of the latter can form a clearly distinguishable hydrogen bond with a bare bridging oxygen. For hydroxylated surfaces, nearly perpendicular orientations with the COOH group facing the bulk solution are much more favorable compared with nonhydroxylated surfaces because all bridging oxygens are protonated and repel the hydrogenoxalate hydrogen.

Since unbiased CMD simulations did not produce any configurations with inner-sphere adsorption, advanced MD simulations were utilized to force the system to explore these configurations. PMF energy profiles extracted from umbrella sampling simulations are shown in Figure 7. First, these

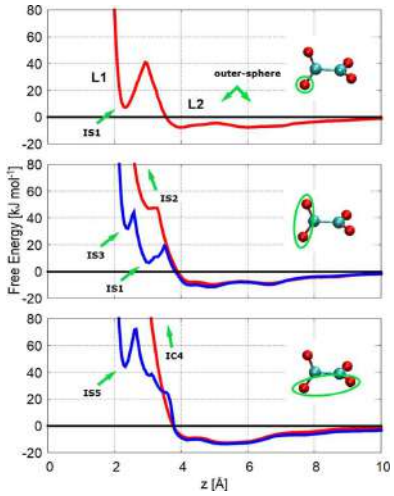

Figure 7. Potential of mean force (PMF) profiles of oxalate at the *nh* + 0.2 surface as a function of the height of a reference point (oxygen atom or the center of mass of two oxygens). Red lines represent chelate binding (with one Ti atom); blue lines represent bridging binding (with two Ti atoms). Zero energy corresponds to the position of a reference point in the bulk.

calculations point to large energy barriers between L1 and L2 regions along the *z*-coordinate. These barriers were also confirmed by our metadynamics calculations (not presented here) and previous ab initio MD calculations[100] describing CO_2 adsorption on (110) rutile. Second, all inner-sphere structures were found to be less energetically favorable than outer-sphere complexes. In fact, only the monodentate (IS1) and bidentate bridging (IS3 and IS5) structures have a well-defined energy minimum, though the energy difference between them and outer-sphere complexes is quite large (about 15, 40, and 50 kJ/mol, respectively). Chelating

DOI: 10.1021/acs.langmuir.8b03984
Langmuir 2019, 35, 7617−7630

structures are highly unlikely when compared with other inner-sphere and outer-sphere complexes. Note that energy minima (or even an energy plateau) in the region between L1 and L2 (middle and bottom panels of Figure 7) correspond to a transition state between outer-sphere and bidentate inner-sphere structures when one oxygen penetrates through the energy barrier between the L1 and L2 regions, whereas the other oxygen is still outer-sphere. Some of these configurations greatly resemble (in terms of geometry and the energy difference) the stable monodentate structure (IS1) identified from the independent series of simulations for the exclusive modeling of monodentate complexation.

Our quantum chemical calculations also reveal that outer-sphere adsorption is more favorable compared with the inner-sphere one. Several initial structures with inner-sphere and outer-sphere adsorbed oxalate were prepared and then optimized in the manner described in the Ab Initio Calculations section. The structures with bidentate inner-sphere complexes (IS2−IS4) were unstable and converged into either the monodentate inner-sphere structure (IS1), the outer-sphere (OS1) complex, or led to unrealistic binding at the edges of our rutile clusters. The IS5 structure was the only inner-sphere bidentate structure more stable than IS1 in our quantum calculations, though still less stable than OS1 by about 5 kJ/mol. The relative instability of inner-sphere complexes supports our PMF calculations, where bidentate complexes were also strongly unfavorable, particularly the chelating complexes IS2 and IS4. In agreement with our PMF calculations, IS1 and IS5 complexes were stable in our ab initio calculations, whereas the ab initio calculations initiated from the IS3 complex ended in the outer-sphere. For further comparison, the energies of the ab initio optimized structures, which finished in the IS1 structure, were extracted and averaged to single adsorption energy (E_{ads}) for the IS1 complex. In a similar way, the adsorption energy of the outer-sphere (OS1) complex was calculated. Given that most initial configurations converged to stable IS1 or OS1 structures, the average adsorption energy of only these structures was compared (Figure 8). As a result, the energy difference between inner-sphere and outer-sphere adsorption in our ab initio calculations is in near-perfect agreement with that from MD simulations (13 kJ/mol from ab initio vs 15 kJ/mol from PMF). Such a comparison of relative DFT electronic energies and MD Helmholtz free energies is adequate since the configurational freedom of inner- and outer-sphere complexes would be more or less similar. Thus, in relative Helmholtz free energies, the energy contribution would be dominant, whereas the entropy effect is minor.

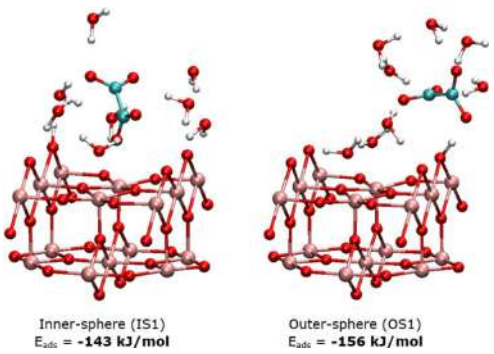

Figure 8. Optimized structures of adsorbed oxalate from ab initio calculations with a rutile cluster. Average adsorption energies (E_{ads}) of surface complexes are given below the structures.

CONCLUSIONS

Oxalic acid and its ions are unique in that a direct bond exists between two carboxyl carbons. Consequently, the single and double deprotonated oxalic acid ions form strongly interacting organic ions with high charge densities. These properties, together with the natural occurrence and importance of this acid, make the molecule an interesting and surprisingly challenging system to explore computationally, considering that it consists of only six to eight atoms. The high symmetry of the molecules, particularly oxalate, sometimes simplifies the analysis. At the same time, the small size of the compound and the capacity of both "ends" of the molecules to strongly participate in interactions with surfaces (even at the same time) lead to strong interactions and large energy barriers between different adsorption configurations.

Our results, including data from molecular dynamics simulations and ab initio calculations, indicate that oxalic acid is mainly an outer-sphere adsorbate at the rutile (110) perfect surface at ambient conditions. We show that outer-sphere adsorption of the molecule offers several donating oxygen atoms strongly interacting with hydrogen atoms of surface hydroxyls and strongly physisorbed L1 water. Consequently, the outer-sphere complexes are energetically more favorable than inner-sphere complexes featuring favorable Ti−O interaction(s) but limited hydrogen bonding. We suggest that this finding may apply more generally to other molecules with significant hydrogen-bonding capability.

The adsorption of oxalic acid ions, although outer-sphere, is extremely strong—in terms of the number of hydrogen bonds formed, their length (often shorter than in bulk water, as summarized in Table S2), the negative adsorption energy, and because most of the oxalate ions present in our systems were adsorbed, with only a few ions remaining in the solution. Another manifestation that (hydrogen)oxalate ions are very strong adsorbates is that while we had a significant concentration of background NaCl electrolyte in our simulations, Cl^- rarely adsorbed on the positively charged surfaces; see Figure S2 in the Supporting Information (SI). The surface charge was readily compensated by oxalic acid ions. Finally, oxalic acid ions adsorb in a non-negligible amount even at neutral surfaces (and in the experiments, adsorption even commences above the point of zero charge, which is at pH 5.4 in oxalate's absence[65]); this further demonstrates the role of strong hydrogen bonding even in cases when electrostatic interactions are weak or even repulsive. To a much smaller extent, we have observed similar behavior in our previous studies of cation adsorption on negatively to positively charged rutile surfaces, where strongly interacting Na^+ and Sr^{2+} ions adsorb on neutral surfaces.[25,27] For cations, it was the ability of the overall neutral surface groups, but with bare partial negative charges, to orient and offer convenient atomic interactions to the adsorbing ions. A similar phenomenon likely plays a role in the adsorption of oxalic acid ions, though it is of minor importance compared with strong hydrogen bonding.

The amount of adsorbed oxalic acid from our molecular dynamics simulations is close to that measured in macroscopic

DOI: 10.1021/acs.langmuir.8b03984
Langmuir 2019, 35, 7617−7630

adsorption experiments and predicted using CD-MUSIC modeling. The CD-MUSIC modeling was based on a somewhat simplified version of our simulation results.[75] Although an alternative CD-MUSIC model assuming monodentate inner-sphere adsorption led to equally accurate predictions of the adsorption data, CD-MUSIC models assuming inner-sphere bidentate/chelating structures were not able to fit the adsorption data successfully.

Addressing the role of computer simulations to molecularly interpret the experimental data, we refrain from the ad hoc assumption that the strong adsorption observed experimentally is an indication of inner-sphere coordination. For example, Figure 4 shows that our computer simulation data, based exclusively on outer-sphere adsorption detailed in Table 4 and Figure 5, nicely mimic experimental adsorption data. Furthermore, our results should encourage further study of the adsorption of organic molecules, particularly those containing carboxyl groups.

To address the discrepancy between our results and those concluding that oxalic acid adsorbs primarily as an inner-sphere complex, we highlight two of our findings. First, we have very carefully analyzed numerous inner-sphere and outer-sphere complexes and compared their energies by classical molecular dynamics augmented by potential of mean force calculations and ab initio calculations. The energy differences of about 13−15 kJ/mol between the energetically most favorable monodentate inner-sphere complex and the most favorable outer-sphere complexes were consistently determined by both computational techniques. Second, some of the previously suggested most likely adsorption complexes, namely, inner-sphere bidentate complexes (particularly chelating), were found to be extremely energetically unfavorable by our PMF calculations and unstable by our ab initio calculations (quickly transforming to the monodentate inner-sphere complex or outer-sphere complexes). This is in accord with the trends in adsorption energies[50] of oxalate from vacuum to a monolayer water coverage of (110) rutile, which (when corrected by 23 kJ/mol energy required to form an associated water molecule from its dissociated form upon inner-sphere adsorption of oxalate) make the adsorption energies of the monodentate inner-sphere complex −69 kJ/mol and those of the two bidentate complexes −51 and +29 kJ/mol. While already values with a monolayer water coverage of the surface make the monodentate inner-sphere complex preferable to bidentate complexes, incorporation of further water layers further enhances the preference of more exposed outer-sphere complexes compared with monodentate and even more buried bidentate inner-sphere complexes. Our estimate of the oxalate hydration energy, about 240 kJ/mol lower compared with a water molecule, is comparable to inner-sphere oxalate adsorption energies,[50] making outer-sphere adsorption energetically competitive with inner-sphere adsorption.

Moreover, some conclusions about the preference of inner-sphere complexes were made by detailed comparison of experimental IR spectra of adsorbed oxalic acid with computationally predicted IR spectra of selected inner-sphere complexes.[50] While the similarity of the spectra of some structures is indeed encouraging, no comparison with spectra of hydrogen-bonded outer-sphere complexes was carried out. Hydrogen-bonded outer-sphere complexes were not considered in this study because only a monolayer of water was included, not allowing full hydration of even inner-sphere adsorbed oxalate. It would be very interesting as a follow-up study to computationally determine the IR spectra of the outer-sphere complexes identified by us and compare them with experimental spectra. Finally, when comparing the simulation data to experimental results, special attention should also be devoted to the impact of surface defects, which are invariably present in reality, on adsorption. That was not investigated in this study but is among our future goals.

■ ASSOCIATED CONTENT

Supporting Information

The Supporting Information is available free of charge on the ACS Publications website at DOI: 10.1021/acs.langmuir.8b03984.

Additional axial density profiles, more information about the determined outer-sphere surface complexes (OS1−OS6), determining the amount of adsorbate, and details about the hydroxylation of the surfaces (PDF)

■ AUTHOR INFORMATION

Corresponding Authors

*E-mail: dbiriukov@prf.jcu.cz (D.B.).
*E-mail: predota@prf.jcu.cz. Tel: +420 387776258 (M.P.).

ORCID

Denys Biriukov: 0000-0003-1007-2203
Ondřej Kroutil: 0000-0001-8893-2969
Moira K. Ridley: 0000-0001-7325-9169
Michael L. Machesky: 0000-0002-8212-3922
Milan Předota: 0000-0003-3902-0992

Notes

The authors declare no competing financial interest.

■ ACKNOWLEDGMENTS

D.B., O.K., M.K., and M.P. acknowledge support from the Ministry of Education, Youth, and Sports of the Czech Republic (project LTAUSA17163). Computational resources were provided by the CESNET LM2015042 and the CERIT Scientific Cloud LM2015085, provided under the program "Projects of Large Research, Development, and Innovations Infrastructures". M.K.R. acknowledges support from the National Science Foundation (CHE-1308726 and EAR-0842526). M.L.M. was supported by the U.S. Department of Energy, Office of Science, Office of Basic Energy Sciences, Chemical Sciences, Geosciences, and Biosciences Division.

■ REFERENCES

(1) Chen, X.; Selloni, A. Introduction: Titanium Dioxide (TiO_2) Nanomaterials. *Chem. Rev.* **2014**, *114*, 9281−9282.
(2) Yin, Z. F.; Wu, L.; Yang, H. G.; Su, Y. H. Recent progress in biomedical applications of titanium dioxide. *Phys. Chem. Chem. Phys.* **2013**, *15*, 4844−4858.
(3) Rehman, F. U.; Zhao, C.; Jiang, H.; Wang, X. Biomedical applications of nano-titania in theranostics and photodynamic therapy. *Biomater. Sci.* **2016**, *4*, 40−54.
(4) Wu, S.; Weng, Z.; Liu, X.; Yeung, K. W. K.; Chu, P. K. Functionalized TiO_2 Based Nanomaterials for Biomedical Applications. *Adv. Funct. Mater.* **2014**, *24*, 5464−5481.
(5) Bai, J.; Zhou, B. Titanium Dioxide Nanomaterials for Sensor Applications. *Chem. Rev.* **2014**, *114*, 10131−10176.
(6) Shiba, K. Exploitation of peptide motif sequences and their use in nanobiotechnology. *Curr. Opin. Biotechnol.* **2010**, *21*, 412−425.
(7) Fujishima, A.; Honda, K. Electrochemical Photolysis of Water at a Semiconductor Electrode. *Nature* **1972**, *238*, 37−38.

DOI: 10.1021/acs.langmuir.8b03984
Langmuir 2019, 35, 7617−7630

(8) Wold, A. Photocatalytic Properties of TiO_2. *Chem. Mater.* **1993**, *5*, 280−283.
(9) Bai, Y.; Mora-Seró, I.; Angelis, F. D.; Bisquert, J.; Wang, P. Titanium Dioxide Nanomaterials for Photovoltaic Applications. *Chem. Rev.* **2014**, *114*, 10095−10130.
(10) Yang, C.; Yu, Y.; Linden, B.; Wu, J. C. S.; Mul, G. Artificial Photosynthesis over Crystalline TiO_2-Based Catalysts: Fact or Fiction? *J. Am. Chem. Soc.* **2010**, *132*, 8398−8406.
(11) Chen, H.; Nanayakkara, C. E.; Grassian, V. H. Titanium Dioxide Photocatalysis in Atmospheric Chemistry. *Chem. Rev.* **2012**, *112*, 5919−5948.
(12) Diebold, U. The Surface Science of Titanium Dioxide. *Surf. Sci. Rep.* **2003**, *48*, 53−229.
(13) Ohno, T.; Sarukawa, K.; Matsumura, M. Crystal faces of rutile and anatase TiO_2 particles and their roles in photocatalytic reactions. *New J. Chem.* **2002**, *26*, 1167−1170.
(14) Graham, J.; Rudham, R.; Rochester, C. H. Infrared Study of the Adsorption of Triethylamine at the Rutile/Vapour and Rutile/Heptane Interfaces. *J. Chem. Soc., Faraday Trans. 1* **1983**, *79*, 2991−2996.
(15) Rochester, C. H. Infrared studies of adsorbed species on rutile at the solid−vapour and solid−liquid interfaces. *Colloids Surf.* **1986**, *21*, 205−217.
(16) Zhang, Z.; Fenter, P.; Cheng, L.; Sturchio, N. C.; Bedzyk, M. J.; Předota, M.; Bandura, A.; Kubicki, J. D.; Lvov, S. N.; Cummings, P. T.; Chialvo, A. A.; Ridley, M. K.; Bénézeth, P.; Anovitz, L.; Palmer, D. A.; Machesky, M. L.; Wesolowski, D. J. Ion Adsorption at the Rutile-Water Interface: Linking Molecular and Macroscopic Properties. *Langmuir* **2004**, *20*, 4954−4969.
(17) Hawkins, T.; Allen, N.; Machesky, M. L.; Wesolowski, D. J.; Kabengi, N. Ion Exchange Thermodynamics at the Rutile−Water Interface: Flow Microcalorimetric Measurements and Surface Complexation Modeling of Na−K−Rb−Cl−NO_3 Adsorption. *Langmuir* **2017**, *33*, 4934−4941.
(18) Cheng, J.; Sprik, M. The electric double layer at a rutile TiO_2 water interface modelled using density functional theory based molecular dynamics simulation. *J. Phys.: Condens. Matter* **2014**, *26*, No. 244108.
(19) Machesky, M. L.; Předota, M.; Ridley, M. K.; Wesolowski, D. J. Constrained Surface Complexation Modeling: Rutile in RbCl, NaCl, and $NaCF_3SO_3$ Media to 250 °C. *J. Phys. Chem. C* **2015**, *119*, 15204−15215.
(20) Luber, S. Sum Frequency Generation of Acetonitrile on a Rutile (110) Surface from Density Functional Theory-Based Molecular Dynamics. *J. Phys. Chem. Lett.* **2016**, *7*, 5183−5187.
(21) Předota, M.; Bandura, A. V.; Cummings, P. T.; Kubicki, J. D.; Wesolowski, D. J.; Chialvo, A. A.; Machesky, M. L. Electric Double Layer at the Rutile (110) Surface. 1. Structure of Surfaces and Interfacial Water from Molecular Dynamics by Use of ab Initio Potentials. *J. Phys. Chem. B* **2004**, *108*, 12049−12060.
(22) Předota, M.; Zhang, Z.; Fenter, P.; Wesolowski, D. J.; Cummings, P. T. Electric Double Layer at the Rutile (110) Surface. 2. Adsorption of Ions from Molecular Dynamics and X-ray Experiments. *J. Phys. Chem. B* **2004**, *108*, 12061−12072.
(23) Předota, M.; Vlček, L. Comment on Parts 1 and 2 of the Series "Electric Double Layer at the Rutile (110) Surface". *J. Phys. Chem. B* **2007**, *111*, 1245−1247.
(24) Předota, M.; Cummings, P. T.; Wesolowski, D. J. Electric Double Layer at the Rutile (110) Surface. 3. Inhomogeneous Viscosity and Diffusivity Measurement by Computer Simulations. *J. Phys. Chem. C* **2007**, *111*, 3071−3079.
(25) Předota, M.; Machesky, M. L.; Wesolowski, D. J.; Cummings, P. T. Electric Double Layer at the Rutile (110) Surface. 4. Effect of Temperature and pH on the Adsorption and Dynamics of Ions. *J. Phys. Chem. C* **2013**, *117*, 22852−22866.
(26) Předota, M.; Machesky, M. L.; Wesolowski, D. J. Molecular Origins of the Zeta Potential. *Langmuir* **2016**, *32*, 10189−10198.
(27) Biriukov, D.; Kroutil, O.; Předota, M. Modeling of solid-liquid interfaces using scaled charges: rutile (110) surfaces. *Phys. Chem. Chem. Phys.* **2018**, *20*, 23954−23966.
(28) Leontyev, I.; Stuchebrukhov, A. Accounting for Electronic Polarization in Non-Polarizable Force Fields. *Phys. Chem. Chem. Phys.* **2011**, *13*, 2613−2626.
(29) Leontyev, I. V.; Stuchebrukhov, A. A. Electronic continuum model for molecular dynamics simulations of biological molecules. *J. Chem. Theory Comput.* **2010**, *6*, 1498−1508.
(30) Stumm, W.; Morgan, J. J. *Aquatic Chemistry: Chemical Equilibria and Rates in Natural Waters*; John Wiley & Sons Inc.: New York, 1996.
(31) Apelblat, A.; Manzurola, E. Solubility of oxalic, malonic, succinic, adipic, maleic, malic, citric, and tartaric acids in water from 278.15 to 338.15 K. *J. Chem. Thermodyn.* **1987**, *19*, 317−320.
(32) Kettler, R. M.; Wesolowski, D. J.; Palmer, D. A. Dissociation Constants of Oxalic Acid in Aqueous Sodium Chloride and Sodium Trifluoromethanesulfonate Media to 175 °C. *J. Chem. Eng. Data* **1998**, *43*, 337−350.
(33) Weber, K. H.; Morales, F. J.; Tao, F.-M. Theoretical Study on the Structure and Stabilities of Molecular Clusters of Oxalic Acid with Water. *J. Phys. Chem. A* **2012**, *116*, 11601−11617.
(34) Kroutil, O.; Minofar, B.; Kabeláč, M. Structure and dynamics of solvated hydrogenoxalate and oxalate anions: a theoretical study. *J. Mol. Model.* **2016**, *22*, 210.
(35) Buttke, L. G.; Schueller, J. R.; Pearson, C. S.; Beyer, K. D. Solubility of the Sodium and Ammonium Salts of Oxalic Acid in Water with Ammonium Sulfate. *J. Phys. Chem. A* **2016**, *120*, 6424−6433.
(36) Dean, P. A. W. The Oxalate Dianion, $C_2O_4^{2-}$: Planar or Nonplanar? *J. Chem. Educ.* **2012**, *89*, 417−418.
(37) Mohajeri, A.; Shakerin, N. The gas-phase acidity and intramolecular hydrogen bonding in oxalic acid. *J. Mol. Struct.: THEOCHEM* **2004**, *711*, 167−172.
(38) Kroutil, O.; Předota, M.; Kabeláč, M. Force Field Parametrization of Hydrogenoxalate and Oxalate Anions with Scaled Charges. *J. Mol. Model.* **2017**, *23*, 327.
(39) Schneider, J.; Matsuoka, M.; Takeuchi, M.; Zhang, J.; Horiuchi, Y.; Anpo, M.; Bahnemann, D. W. Understanding TiO_2 Photocatalysis: Mechanisms and Materials. *Chem. Rev.* **2014**, *114*, 9919−9986.
(40) Li, Y.; Wasgestian, F. Photocatalytic reduction of nitrate ions on TiO_2 by oxalic acid. *J. Photochem. Photobiol., A* **1998**, *112*, 255−259.
(41) Wang, Y.; Zhang, P. Photocatalytic decomposition of perfluorooctanoic acid (PFOA) by TiO_2 in the presence of oxalic acid. *J. Hazard. Mater.* **2011**, *192*, 1869−1875.
(42) Fahmi, A.; Minot, C.; Fourre, P.; Nortier, P. A theoretical study of the adsorption of oxalic acid on TiO_2. *Surf. Sci.* **1995**, *343*, 261−272.
(43) Hug, S. J.; Bahnemann, D. Infrared spectra of oxalate, malonate and succinate adsorbed on the aqueous surface of rutile, anatase and lepidocrocite measured with in situ ATR-FTIR. *J. Electron Spectrosc. Relat. Phenom.* **2006**, *150*, 208−219.
(44) Hug, S. J.; Sulzberger, B. In Situ Fourier Transform Infrared Spectroscopic Evidence for the Formation of Several Different Surface Complexes of Oxalate on TiO_2 in the Aqueous Phase. *Langmuir* **1994**, *10*, 3587−3597.
(45) Weisz, A. D.; Rodenas, L. G.; Morando, P. J.; Regazzoni, A. E.; Blesa, M. A. FTIR study of the adsorption of single pollutants and mixtures of pollutants onto titanium dioxide in water: oxalic and salicylic acids. *Catal. Today* **2002**, *76*, 103−112.
(46) Rotzinger, F. P.; Kesselman-Truttmann, J. M.; Hug, S. J.; Shklover, V.; Grätzel, M. Structure and Vibrational Spectrum of Formate and Acetate Adsorbed from Aqueous Solution onto the TiO_2 Rutile (110) Surface. *J. Phys. Chem. B* **2004**, *108*, 5004−5017.
(47) Mendive, C. B.; Bahnemann, D. W.; Blesa, M. A. Microscopic characterization of the photocatalytic oxidation of oxalic acid adsorbed onto TiO_2 by FTIR-ATR. *Catal. Today* **2005**, *101*, 237−244.

DOI: 10.1021/acs.langmuir.8b03984
Langmuir 2019, 35, 7617−7630

(48) Mendive, C. B.; Bredow, T.; Blesa, M. A.; Bahnemann, D. W. ATR-FTIR measurements and quantum chemical calculations concerning the adsorption and photoreaction of oxalic acid on TiO_2. *Phys. Chem. Chem. Phys.* **2006**, *8*, 3232−3247.
(49) Mendive, C. B.; Blesa, M. A.; Bahnemann, D. W. The adsorption and photodegradation of oxalic acid at the TiO_2 surface. *Water Sci. Technol.* **2007**, *55*, 139−145.
(50) Mendive, C. B.; Bredow, T.; Feldhoff, A.; Blesa, M. A.; Bahnemann, D. W. Adsorption of oxalate on rutile particles in aqueous solutions: a spectroscopic, electron-microscopic and theoretical study. *Phys. Chem. Chem. Phys.* **2008**, *10*, 1960−1974.
(51) Mendive, C. B.; Bredow, T.; Feldhoff, A.; Blesa, M. A.; Bahnemann, D. W. Adsorption of oxalate on anatase (100) and rutile (110) surfaces in aqueous systems: experimental results vs. theoretical predictions. *Phys. Chem. Chem. Phys.* **2009**, *11*, 1794−1808.
(52) Singh, J.; Gusain, A.; Saxena, V.; Chauhan, A. K.; Veerender, P.; Koiry, S. P.; Jha, P.; Jain, A.; Aswal, D. K.; Gupta, S. K. XPS, UV−Vis, FTIR, and EXAFS Studies to Investigate the Binding Mechanism of N719 Dye onto Oxalic Acid Treated TiO_2 and Its Implication on Photovoltaic Properties. *J. Phys. Chem. C* **2013**, *117*, 21096−21104.
(53) Young, A. G.; McQuillan, A. J. Adsorption/Desorption Kinetics from ATR-IR Spectroscopy. Aqueous Oxalic Acid on Anatase TiO_2. *Langmuir* **2009**, *25*, 3538−3548.
(54) Johnson, S. B.; Yoon, T. H.; Slowey, A. J.; Brown, G. E. Adsorption of Organic Matter at Mineral/Water Interfaces: 3. Implications of Surface Dissolution for Adsorption of Oxalate. *Langmuir* **2004**, *20*, 11480−11492.
(55) Borowski, S. C.; Biswakarma, J.; Kang, K.; Schenkeveld, W. D. C.; Hering, J. G.; Kubicki, J. D.; Kraemer, S. M.; Hug, S. J. Structure and reactivity of oxalate surface complexes on lepidocrocite derived from infrared spectroscopy, DFT-calculations, adsorption, dissolution and photochemical experiments. *Geochim. Cosmochim. Acta* **2018**, *226*, 244−262.
(56) Parikh, S. J.; Kubicki, J. D.; Jonsson, C. M.; Jonsson, C. L.; Hazen, R. M.; Sverjensky, D. A.; Sparks, D. L. Evaluating Glutamate and Aspartate Binding Mechanisms to Rutile (α-TiO_2) via ATR-FTIR Spectroscopy and Quantum Chemical Calculations. *Langmuir* **2011**, *27*, 1778−1787.
(57) Feng, H.; Liu, L.; Dong, S.; Cui, X.; Zhao, J.; Wang, B. Dynamic Processes of Formaldehyde at Terminal Ti Sites on the Rutile TiO_2(110) Surface. *J. Phys. Chem. C* **2016**, *120*, 24287−24293.
(58) Savory, D. M.; Warren, D. S.; McQuillan, A. J. Shallow Electron Trap, Interfacial Water, and Outer-Sphere Adsorbed Oxalate IR Absorptions Correlate during UV Irradiation of Photocatalytic TiO_2 Films in Aqueous Solution. *J. Phys. Chem. C* **2011**, *115*, 902−907.
(59) Livi, K. J. T.; Schaffer, B.; Azzolini, D.; Seabourne, C. R.; Hardcastle, T. P.; Scott, A. J.; Hazen, R. M.; Erlebacher, J. D.; Brydson, R.; Sverjensky, D. A. Atomic-Scale Surface Roughness of Rutile and Implications for Organic Molecule Adsorption. *Langmuir* **2013**, *29*, 6876−6883.
(60) Ridley, M. K.; Machesky, M. L.; Wesolowski, D. J.; Palmer, D. A. Surface complexation of neodymium at the rutile-water interface: A potentiometric and modeling study in NaCl media to 250 °C. *Geochem. Cosmochim. Acta* **2005**, *69*, 63−81.
(61) Ridley, M. K.; Machesky, M. L.; Palmer, D. A.; Wesolowski, D. J. Potentiometric studies of the rutile-water interface: hydrogen-electrode concentration-cell versus glass-electrode titrations. *Colloids Surf., A* **2002**, *204*, 295−308.
(62) Ridley, M. K.; Hackley, V. A.; Machesky, M. L. Characterization and Surface-Reactivity of Nanocrystalline Anatase in Aqueous Solutions. *Langmuir* **2006**, *22*, 10972−10982.
(63) Ridley, M. K.; Hiemstra, T.; van Riemsdijk, W. H.; Machesky, M. L. Inner-sphere complexation of cations at the rutile−water interface: A concise surface structural interpretation with the CD and MUSIC model. *Geochem. Cosmochim. Acta* **2009**, *73*, 1841−1856.
(64) Machesky, M. L.; Wesolowski, D. J.; Palmer, D. A.; Ridley, M. K.; Bénézeth, P.; Lvov, S. N.; Fedkin, M. V. Chapter 12 - Ion Adsorption into the Hydrothermal Regime: Experimental and Modeling Approaches. In *Interface Science and Technology*; Lützenkirchen, J., Ed.; Elsevier, 2006; pp 324−358.
(65) Machesky, M. L.; Wesolowski, D. J.; Palmer, D. A.; Ichiro-Hayashi, K. Potentiometric Titrations of Rutile Suspensions to 250 °C. *J. Colloid Interface Sci.* **1998**, *200*, 298−309.
(66) Kohagen, M.; Lepsik, M.; Jungwirth, P. Calcium Binding to Calmodulin by Molecular Dynamics with Effective Polarization. *J. Phys. Chem. Lett.* **2014**, *5*, 3464−3469.
(67) Duboué-Dijon, E.; Mason, P. E.; Fischer, H. E.; Jungwirth, P. Changes in the Hydration Structure of Imidazole upon Protonation: Neutron Scattering and Molecular Simulations. *J. Chem. Phys.* **2017**, *146*, No. 185102.
(68) Duboué-Dijon, E.; Delcroix, P.; Martinez-Seara, H.; Hladílková, J.; Coufal, P.; Křížek, T.; Jungwirth, P. Binding of Divalent Cations to Insulin: Capillary Electrophoresis and Molecular Simulations. *J. Phys. Chem. B* **2018**, *122*, 5640−5648.
(69) Berendsen, H. J. C.; Grigera, J. R.; Straatsma, T. P. The Missing Term in Effective Pair Potentials. *J. Phys. Chem.* **1987**, *91*, 6269−6271.
(70) Kohagen, M.; Mason, P. E.; Jungwirth, P. Accounting for Electronic Polarization Effects in Aqueous Sodium Chloride via Molecular Dynamics Aided by Neutron Scattering. *J. Phys. Chem. B* **2016**, *120*, 1454−1460.
(71) Van der Spoel, D.; Lindahl, E.; Hess, B.; Groenhof, G.; Mark, A. E.; Berendsen, H. J. C. GROMACS: Fast, Flexible, and Free. *J. Comput. Chem.* **2005**, *26*, 1701−1718.
(72) Matsui, M.; Akaogi, M. Molecular Dynamics Simulation of the Structural and Physical Properties of the Four Polymorphs of TiO_2. *Mol. Simul.* **1991**, *6*, 239−244.
(73) Brandt, E. G.; Lyubartsev, A. P. Systematic Optimization of a Force Field for Classical Simulations of TiO_2−Water Interfaces. *J. Phys. Chem. C* **2015**, *119*, 18110−18125.
(74) Parez, S.; Předota, M.; Machesky, M. L. Dielectric Properties of Water at Rutile and Graphite Surfaces: Effect of Molecular Structure. *J. Phys. Chem. C* **2014**, *118*, 4818−4834.
(75) Machesky, M. L.; Ridley, M. K.; Biriukov, D.; Kroutil, O.; Předota, M. Oxalic Acid Adsorption on Rutile: Experiments and Surface Complexation Modeling to 150 °C. *Langmuir* **2019**, DOI: 10.1021/acs.langmuir.8b03982.
(76) Kroutil, O.; Chval, Z.; Skelton, A. A.; Předota, M. Computer simulations of quartz (101) − water interface over a range of pH values. *J. Phys. Chem. C* **2015**, *119*, 9274−9286.
(77) Vlcek, L.; Zhang, Z.; Machesky, M. L.; Fenter, P.; Rosenqvist, J.; Wesolowski, D. J.; Anovitz, L. M.; Předota, M.; Cummings, P. T. Electric Double Layer at Metal Oxide Surfaces: Static Properties of the Cassiterite−Water Interface. *Langmuir* **2007**, *23*, 4925−4937.
(78) Kettler, R. M.; Palmer, D. A.; Wesolowski, D. J. Dissociation quotients of oxalic acid in aqueous sodium chloride media to 175 °C. *J. Solution Chem.* **1991**, *20*, 905−927.
(79) Essmann, U.; Perera, L.; Berkowitz, M. L.; Darden, T.; Lee, H.; Pedersen, L. G. A Smooth Particle Mesh Ewald Method. *J. Chem. Phys.* **1995**, *103*, 8577−8593.
(80) Yeh, I.-C.; Berkowitz, M. L. Ewald Summation for Systems with Slab Geometry. *J. Chem. Phys.* **1999**, *111*, 3155−3162.
(81) Hoover, W. G. Canonical dynamics: Equilibrium phase-space distributions. *Phys. Rev. A* **1985**, *31*, 1695.
(82) Hess, B.; Bekker, H.; Berendsen, H. J. C.; Fraaije, J. G. E. M. LINCS: A Linear Constraint Solver for Molecular Simulations. *J. Comput. Chem.* **1997**, *18*, 1463−1472.
(83) Hub, J. S.; de Groot, B. L.; van der Spoel, D. g_wham—A Free Weighted Histogram Analysis Implementation Including Robust Error and Autocorrelation Estimates. *J. Chem. Theory Comput.* **2010**, *6*, 3713−3720.
(84) Laio, A.; Parrinello, M. Escaping Free-Energy Minima. *Proc. Natl. Acad. Sci. U.S.A.* **2002**, *99*, 12562−15566.
(85) Monti, S.; Walsh, T. R. Free Energy Calculations of the Adsorption of Amino Acid Analogues at the Aqueous Titania Interface. *J. Phys. Chem. C* **2010**, *114*, 22197−22206.

DOI: 10.1021/acs.langmuir.8b03984
Langmuir 2019, 35, 7617−7630

(86) Mori, T.; Hamers, R. J.; Pedersen, J. A.; Cui, Q. An Explicit Consideration of Desolvation is Critical to Binding Free Energy Calculations of Charged Molecules at Ionic Surfaces. *J. Chem. Theory Comput.* **2013**, *9*, 5059−5069.
(87) YazdanYar, A.; Aschauer, U.; Bowen, P. Adsorption Free Energy of Single Amino Acids at the Rutile (110)/Water Interface Studied by Well-Tempered Metadynamics. *J. Phys. Chem. C* **2018**, *122*, 11355−11363.
(88) Sultan, A. M.; Hughes, Z. E.; Walsh, T. R. Binding Affinities of Amino Acid Analogues at the Charged Aqueous Titania Interface: Implications for Titania-Binding Peptides. *Langmuir* **2014**, *30*, 13321−13329.
(89) Haldar, S.; Spiwok, V.; Hobza, P. On the Association of the Base Pairs on the Silica Surface Based on Free Energy Biased Molecular Dynamics Simulation and Quantum Mechanical Calculations. *J. Phys. Chem. C* **2013**, *117*, 11066−11075.
(90) Wright, L. B.; Walsh, T. R. Facet Selectivity of Binding on Quartz Surfaces: Free Energy Calculations of Amino-Acid Analogue Adsorption. *J. Phys. Chem. C* **2012**, *116*, 2933−2945.
(91) Kerisit, S.; Parker, S. C. Free Energy of Adsorption of Water and Metal Ions on the {10$\bar{1}$4} Calcite Surface. *J. Am. Chem. Soc.* **2004**, *126*, 10152−10161.
(92) Frisch, M. J.; Trucks, G. W.; Schlegel, H. B.; Scuseria, G. E.; Robb, M. A.; Cheeseman, J. R.; Scalmani, G.; Barone, V.; Petersson, G. A.; Nakatsuji, H.; et al. *Gaussian 16*, revision B.01; Gaussian Inc.: Wallingford, CT, 2016.
(93) Kevorkyants, R.; Rudakova, A. V.; Chizhov, Y. V.; Bulanin, K. M. The origin of 1560 cm^{-1} band in experimental IR spectra of water adsorbed on TiO_2 surface: Ab initio assessment. *Chem. Phys. Lett.* **2016**, *662*, 97−101.
(94) Grimme, S.; Ehrlich, A. S.; Krieg, H. A consistent and accurate *ab initio* parametrization of density functional dispersion correction (DFT-D) for the 94 elements H-Pu. *J. Chem. Phys.* **2010**, *132*, No. 154104.
(95) Scalmani, G.; Frisch, M. J. Continuous surface charge polarizable continuum models of solvation. I. General formalism. *J. Chem. Phys.* **2010**, *132*, No. 114110.
(96) Boys, S. F.; Bernardi, F. The calculation of small molecular interactions by the differences of separate total energies. Some procedures with reduced errors. *Mol. Phys.* **1970**, *19*, 553−566.
(97) Humphrey, W.; Dalke, A.; Schulten, K. VMD − Visual Molecular Dynamics. *J. Mol. Graphics* **1996**, *14*, 33−38.
(98) Diebold, U. Perspective: A controversial benchmark system for water-oxide interfaces: $H_2O/TiO_2(110)$. *J. Chem. Phys.* **2017**, *147*, No. 040901.
(99) Hussain, H.; Tocci, G.; Woolcot, T.; Torrelles, X.; Pang, C. L.; Humphrey, D. S.; Yim, C. M.; Grinter, D. C.; Cabailh, G.; Bikondoa, O.; Lindsay, R.; Zegenhagen, J.; Michaelides, A.; Thornton, G. Structure of a model TiO_2 photocatalytic interface. *Nat. Mater.* **2017**, *16*, 461−466.
(100) Klyukin, K.; Alexandrov, V. CO_2 Adsorption and Reactivity on Rutile $TiO_2(110)$ in Water: An *Ab Initio* Molecular Dynamics Study. *J. Phys. Chem. C* **2017**, *121*, 10476−10483.

DOI: 10.1021/acs.langmuir.8b03984
Langmuir 2019, 35, 7617−7630

Article DB3

Machesky, M. L.; Ridley, M. K.; **Biriukov, D.**; Kroutil, O.; Předota, M.

Oxalic Acid Adsorption on Rutile: Experiments and Surface Complexation Modeling to 150 °C

Langmuir **2019**, *35* (24), 7631–7640;
IF (2018) = 3.638

Participation of Denys Biriukov:

DB performed all the molecular simulations, analyzed the results using pre-implemented and self-written utilities, provided the data for surface complexation modeling, and participated in the paper writing.

DOI: 10.1021/acs.langmuir.8b03982;

LANGMUIR
Cite This: *Langmuir* 2019, 35, 7631−7640
Article
pubs.acs.org/Langmuir

Oxalic Acid Adsorption on Rutile: Experiments and Surface Complexation Modeling to 150 °C

Michael L. Machesky,*[,†] Moira K. Ridley,[‡] Denys Biriukov,[§] Ondřej Kroutil,[§,∥] and Milan Předota[§]

[†]University of Illinois, Illinois State Water Survey, 1506 Coral Cove Drive, Champaign, Illinois 61821, United States
[‡]Department of Geosciences, Texas Tech University, Lubbock, Texas 79409-1053, United States
[§]Institute of Physics, Faculty of Science, University of South Bohemia, Branišovská 1760, 370 05 České Budějovice, Czech Republic
[∥]Faculty of Chemistry, Materials Research Centre, Brno University of Technology, Purkyňova 118, 612 00 Brno, Czech Republic

Supporting Information

ABSTRACT: Here, we characterize oxalate adsorption by rutile in NaCl media (0.03 and 0.30 *m*) and between pH 3 and 10 over a wide temperature range which includes the near hydrothermal regime (10−150 °C). Oxalate adsorption increases with decreasing pH (as is typical for anion binding by metal oxides), but systematic trends with respect to ionic strength or temperature are absent. Surface complexation modeling (SCM) following the CD-MUSIC formalism, and as constrained by molecular modeling simulations and IR spectroscopic results from the literature, is used to interpret the adsorption data. The molecular modeling simulations, which include molecular dynamics simulations supported by free-energy and ab initio calculations, reveal that oxalate binding is outer-sphere, albeit via strong hydrogen bonds. Conversely, previous IR spectroscopic results conclude that various types of inner-sphere complexes often predominate. SCMs constrained by both the molecular modeling results and the IR spectroscopic data were developed, and both fit the adsorption data equally well. We conjecture that the discrepancy between the molecular simulation and IR spectroscopic results is due to the nature of the rutile surfaces investigated, that is, the perfect (110) crystal faces for the molecular simulations and various rutile powders for the IR spectroscopy studies. Although the (110) surface plane is most often dominant for rutile powders, a variety of steps, kinks, and other types of surface defects are also invariably present. Hence, we speculate that surface defect sites may be primarily responsible for inner-sphere oxalate adsorption, although further study is necessary to prove or disprove this hypothesis.

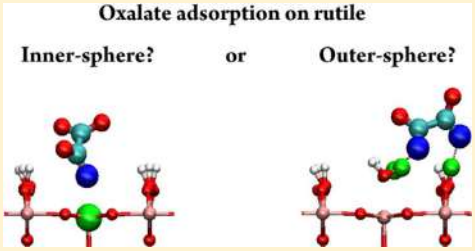

INTRODUCTION

Oxalate is abundant in natural environments and is also industrially important. It is secreted by fungi and roots to help sequester essential nutrients from soils and to detoxify, via complexation, metals such as aluminum.[1] Oxalates' metal complexing ability is also utilized in various industrial applications such as removing iron and other impurities from silica sand.[2] Moreover, its metal complexing ability also means that it can strongly adsorb to metal oxide surfaces, especially at pH values where such surfaces are positively charged [pH < pH_{zpc} (point of zero charge pH)] and oxalate is predominately unprotonated (pK_{a2} = 4.275 at 25 °C[3]).

Parfitt et al.[4,5] were among the first to systematically study oxalate adsorption by metal oxides. They utilized both batch adsorption studies and IR spectroscopy to probe oxalate adsorption by goethite[4] and gibbsite.[5] Adsorption increased between pH 8 and 3.4, and bidentate inner-sphere adsorption via ligand exchange with surface OH groups dominated adsorption on both surfaces, with a monodentate inner-sphere complex also observed on goethite at higher surface coverages.

Subsequent studies have confirmed and refined these results for a wider variety of metal oxide surfaces. In particular, attenuated total reflection−Fourier transform infrared (ATR−FTIR) spectroscopic results have revealed various inner-sphere bidentate, chelate, and monodentate structures formed via ligand exchange of surface OH groups singly coordinated to underlying metal cations is a dominant oxalate adsorption mechanism.[6−8] However, various outer-sphere complexes also exist under certain pH and surface coverage conditions.[8,9] Given this multitude of inferred pH and surface coverage-dependent surface species, assigning IR adsorption peaks to a particular surface species can be somewhat uncertain.[10] However, increasingly sophisticated and realistic molecular modeling techniques are helping to reduce this uncertainty through comparison of calculated and measured spectra.[9]

Received: November 28, 2018
Revised: January 23, 2019
Published: March 10, 2019

DOI: 10.1021/acs.langmuir.8b03982
Langmuir 2019, 35, 7631−7640

ATR−FTIR spectroscopy and molecular modeling have also been used to investigate oxalate adsorption by TiO_2, with most studies involving anatase or mixed anatase and rutile phases. Hug and Sulzberger[11] utilized ATR−FTIR to study oxalate adsorption on Degussa-P25, a mixed TiO_2 phase consisting of about 2/3 anatase and 1/3 rutile. Several inner-sphere bidentate complexes were formed depending on pH (2.9−8.6) and oxalate concentration (1−1000 μM). Young and McQuillan[12] investigated the adsorption/desorption kinetics of oxalate (100 μM) by anatase at pH 4 with ATR−IR spectroscopy. Three distinct desorption half-lives were observed (300, 14, and 2 min), suggesting the presence of 3 distinct surface species, with the slowest desorbing species likely being a bidentate inner-sphere complex and the fastest desorbing an outer-sphere complex. Hug and Bahnemann[10] compared oxalate (200 μM) adsorption by rutile, anatase, and lepidocrocite with ATR−FTIR spectroscopy between pH 3 and 9. Adsorption was predominately inner-sphere bidentate on all three surfaces, but observed spectral changes with pH were acknowledged to be incompletely understood. Mendive et al.[13] combined ATR−FTIR spectroscopy (pH 3.7, 2000 μM oxalate), electron microscopy [high-resolution transmission electron microscopy (HRTEM)], and semiempirical molecular modeling (MSINDO) to study oxalate adsorption by rutile. The MSINDO calculations utilized the (110) surface of rutile, which was the dominant crystal face (∼85%) of the rutile powder used for the IR experiments. Surface hydration was mimicked by including one monolayer of water. The combined results indicated three main surface species, two of which were inner-sphere bidentate (one protonated and one not) and the third being inner-sphere monodentate and protonated.

Temperature can greatly influence ion adsorption, and our group has documented that cation adsorption by rutile is greatly enhanced as the temperature increases from ambient into the hydrothermal regime, especially for multivalent cations.[14−16] However, the influence of temperature on anion adsorption has been far less studied under any conditions, and trends remain less certain. Machesky[17] hypothesized that anion adsorption should generally decrease with increasing temperature. This was based on calorimetrically determined adsorption enthalpies for several anions (fluoride, phosphate, salicylate, and iodate) at low to moderate surface coverages on goethite at pH 4 being exothermic at 25 °C,[18] and a few published batch adsorption studies. However, even their own batch adsorption results did not always decrease as the temperature increased from 10 and 40 °C. Of the relatively few batch anion adsorption results between about 10 and 70 °C available for anions, most have observed adsorption decreases with increasing temperature.[19−22] However, Fein and Brady[23] found that oxalate adsorption by alumina was unchanged between 25 and 60 °C. However, for both oxalic acid adsorbed on kaolinite[24] and mellitic acid on goethite[25] and kaolinite,[26] adsorption decreased with increasing temperature at lower pH, but increased with temperature at high pH.

Here, we investigate oxalate adsorption by rutile to 150 °C via a combined batch adsorption and molecular modeling approach and interpret these combined results with constrained surface complexation models (SCMs), following our approach for interpreting cation adsorption data.[27,28] We are aware of no other systematic study of anion adsorption that extends into the hydrothermal realm. Moreover, our molecular modeling results indicate that oxalate adsorbs on the perfect (110) surface of rutile as hydrogen-bonded outer-sphere complexes, which is at odds with IR spectroscopic data (summarized above), indicating that inner-sphere adsorption predominates. Finally, we offer a plausible explanation for this difference with the hope that additional spectroscopic and molecular modeling experiments will resolve the discrepancy.

EXPERIMENTAL SECTION

Oxalate Adsorption Experiments. The present study used two potentiometric experimental titration approaches. At low temperatures, 10−50 °C (±0.1 °C), potentiometric titrations utilized a Ross Semimicro combination glass electrode and Mettler DL70 autotitrator, whereas titrations from 50 to 150 °C used a hydrogen-electrode concentration cell (HECC). At 50 °C, titrations were performed using both experimental approaches. The general titration procedures used in this study have been described in detail previously.[16,29−32] For completeness, an overview of key aspects of the titration procedures is presented here.

All experimental solutions were prepared from reagent-grade chemicals and deionized water. Solutions were prepared in NaCl media, with sufficient electrolyte to give ionic strengths of 0.03 or 0.3 *m*. The adsorption of oxalate onto the rutile surface was determined with test solutions comprising 0.001 *m* $C_2O_4^{2-}$. The rutile powder used in all titrations came from Tioxide Corporation; this rutile has a distinct and dominant (110) crystal face. Prior to use, the rutile was hydrothermally pretreated following Machesky et al.[33]

The standard experimental procedure for titrations performed using a Ross glass electrode and autotitrator was to first calibrate the electrode. The electrode was calibrated using an initial acid solution comprising 5×10^{-3} *m* H^+, to which a base calibration solution was added giving a second calibration point close to 1×10^{-3} *m* OH^-. The oxalate adsorption titrations were performed by suspending 1 g of rutile in 44 g of test solution. The rutile used for all electrode−autotitrator experiments had a specific N_2-BET surface are of 15.65 ± 0.1 m^2/g. The titration cell was immersed in a water bath at the desired temperature, the headspace was purged with purified argon to prevent CO_2 contamination, and the solution was stirred mechanically throughout the experiment. During each titration, 30−40 aliquots of acid titrant were added, over a pH_m range of 6−7 units (where pH_m is the molar H^+ concentration).

In each HECC potentiometric titration, approximately 1.5 g of rutile was suspended in 45 g of base test solution. Titrations performed at 0.03 *m* ionic strength used the same batch of rutile as for the electrode−autotitrator experiments (i.e., surface area = 15.65 ± 0.1 m^2/g). The rutile used for titration at 0.3 *m* ionic strength had a slightly higher surface area of 16.75 ± 0.1 m^2/g. The titration cell was equilibrated overnight at temperature and was stirred magnetically throughout. Approximately 15 aliquots of acid titrant were added to the titration cell, with titrations performed over 5−6 pH_m units.

Two independent sets of titrations were completed for both HECC and glass electrode−autotitrator procedures. In the first, the excess or deficit of protons in solution were calculated at each point in the titration and expressed as a function of m^2 of rutile surface area. In the second set of titrations, samples were periodically withdrawn from the test solution; these titrations are referred to as adsorption "pH-edge" experiments.[34] The withdrawn samples were filtered through 0.2 μm filters; later, the total dissolved oxalate concentration was analyzed by ion chromatography and the amount adsorbed determined by difference. All data reduction followed standard procedures detailed in Ridley et al.[16,30] and Palmer and Wesolowski.[35]

Molecular Modeling Methods. Our custom simulation code used in previous work[28,36] was modified to include electronic continuum theory[37] and was transferred to the Gromacs software package[38] as detailed in our recent study of ion adsorption on rutile (110) surfaces.[39] Briefly, we constructed two rutile (110) non-hydroxylated surfaces with a lateral size of 38.981 × 35.508 Å separated by an ∼50 Å wide aqueous solution containing oxalic acid anions at a bulk concentration of about 0.05 M in an NaCl background of about 0.3−0.4 M. A combination of optimized

DOI: 10.1021/acs.langmuir.8b03982
Langmuir 2019, 35, 7631−7640

Table 1. Predominant H-Bonded Oxalate Surface Complexes (% Relative Distribution within Adsorbed Complexes) at +0.104 and +0.208 C/m^2 Surface Charge Density, and 25 and 100 °C[a]

name	complex	+0.104 C/m^2, 25°C	+0.208 C/m^2, 25°C	+0.104C/m^2, 100°C	+0.208 C/m^2, 100°C
OS1 $1H_b$ $1H_t$	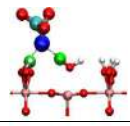	20%	26 %	18%	21 %
OS2 $1H_b$ $2H_t$	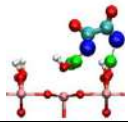	18%	23 %	19%	23 %
OS3 $1H_t$	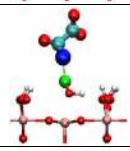	15%	11 %	14%	9 %
OS4 $2H_t$	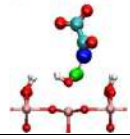	16 %	12 %	13 %	10 %

[a]H-bonds between oxalate oxygens (blue spheres) and surface hydrogens (green spheres) are shown as black dashed lines, with the type and number of H atoms involved (H_b, to bridging oxygen atoms, and/or H_t, to terminal oxygen atoms) given in the first column.

Lennard-Jones potentials for TiO_2–water interactions[40] and a recently developed force field for oxalate and hydrogenoxalate anions[41] was used to model rutile–electrolyte interactions in explicit SPC/E water. The neutral hydrated (110) surface was generated by populating the fivefold coordinated surface Ti atoms, which define zero height of the (110) rutile face, with water molecules. We term this our nonhydroxylated surface, which best mimics that terminal Ti groups are more basic than bridging oxygen atoms.[28] To generate positive surface charge densities of +0.104 and +0.208 C/m^2, 18 and 36 bridging oxygens, respectively, were protonated to form bridging hydroxyls. These surface charge densities correspond to pH values near 4.6 and 3.7 in 0.30 *m* NaCl oxalate containing solutions (Figure 2, below).

The numbers of oxalate and hydrogenoxalate anions in the bulk region of the simulation system were set to reproduce ratios in accord with pK_a values of oxalic acid. Simulations were conducted at 25 and 100 °C with the correct bulk water densities (996 and 958 kg/m^3, respectively). The analysis of these classical unbiased simulations revealed no inner-sphere adsorption but strong outer-sphere adsorption with the dominant structures summarized in Table 1. These adsorption structures were also prevalent for hydrogenoxalate, although hydrogenoxalate was less strongly adsorbed than oxalate.

Free-energy profiles comparing inner- and outer-sphere adsorption were obtained using potential of mean force (PMF) methods. These profiles indicated that monodentate inner-sphere adsorption was considerably more energetically favorable than bidentate inner-sphere adsorption.[42] Consequently, the PMF calculations presented here only compare monodentate inner-sphere adsorption with outer-sphere adsorption and were performed as follows. The reaction coordinate, the *z*-separation between a surface terminal Ti atom and one oxygen of an oxalate molecule, was divided into 37 windows of 0.1–0.3 Å width in the inner-sphere and outer-sphere adsorption regions and 0.5 Å width in the bulk region, thereby generating in all cases a sufficient sampling with overlapping distributions. An independent simulation for each window was carried out with a harmonic *z*-constraint to keep the reference oxygen atom of the oxalic ion at a defined distance. The total free-energy profile up to 10 Å above the rutile surface was calculated using the WHAM algorithm.[43] These energy calculations were performed only at +0.208 C/m^2 surface charge given that inner-sphere adsorption should be more favorable at higher positive surface charge (i.e., lower pH values).

Further computational details of the studied systems and applied methods can be found in a paper focused on the detailed computational results of oxalate adsorption by rutile.[42]

RESULTS AND DISCUSSION

Oxalate adsorption pH edge results in 0.03 *m* NaCl and proton charge data in 0.30 *m* NaCl are presented in Figures 1 and 2, respectively, and the complete set of data collected are provided in the Supporting Information. The data are plotted against the pH corrected for the pH of zero net proton charge (pH_{znpc}) change with temperature (pH_{znpc} − pH). The pH_{znpc} decreases from 5.7 at 10 °C to 4.4 at 150 °C.[29] Adsorption pH edge data are a direct measure of oxalate adsorption. Proton charge, however, indicates the excess or deficit of protons during a titration expressed in terms of surface area and charge (mol/m^2 surface excess or deficit H^+ × Faradays constant). Consequently, any reaction that generates or consumes protons contributes to the proton charge. These reactions include surface protonation/deprotonation with and without Na^+ and Cl^- binding, and protonation/deprotonation of oxalate in solution, in addition to proton consuming/generating reactions resulting from oxalate adsorption. A primary advantage of proton charge experiments is that they are inherently more accurate because withdrawing, filtering, and analyzing for the adsorbate of interest are not necessary.

DOI: 10.1021/acs.langmuir.8b03982
Langmuir 2019, 35, 7631–7640

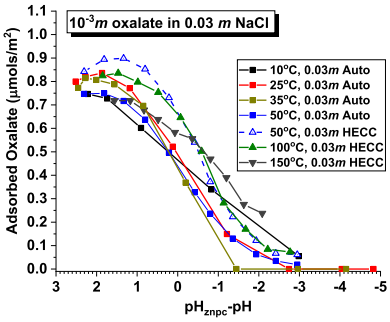

Figure 1. Adsorption pH edge data for oxalate on rutile corrected for the pH_{znpc} change with temperature. Within the legend, Auto and HECC refer to experiments performed in an autotitrator and HECC, respectively. The lines are included to guide the eye.

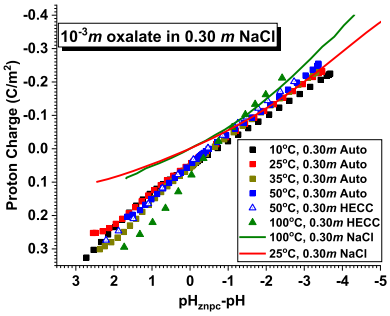

Figure 2. Surface charge data for oxalate on rutile corrected for the pH_{znpc} change with temperature. The lines depict surface charge data at 25 °C (red) and 100 °C (green) for 0.30 *m* NaCl without added oxalate.

Moreover, fitting both adsorption pH edge and proton charge data increases confidence in SCM results.

Experiments were conducted to 150 °C in 0.03 *m* NaCl, but only to 100 °C in 0.30 *m* NaCl because above these ionic strength−temperature combinations, oxalate is thermally decomposed.[3] Also, the 50 °C data were collected in both a HECC and glass electrode autotitrator (Auto), and those results are quite different for the adsorption pH edge data, which we attribute to unknown experimental factors. Proton charge data for 0.30 *m* NaCl alone at 25 and 100 °C are also presented in Figure 2.

Oxalate adsorption commences 1−2 pH units above the pH_{znpc} (Figure 1) where the net proton charge is negative ($pH_{znpc} - pH < 0$, Figure 2). However, the adsorption pH edge data show no systematic temperature dependence. This contrasts with our cation adsorption pH edge data, which steadily shift to more positive $pH_{znpc} - pH$ values over the same increasing temperature range and ionic strength conditions.[15] However, as summarized above, temperature trends for anion adsorption available in the literature are also not consistent, albeit over a narrower temperature range than investigated in this study.

The proton charge curves attain significantly more positive values in the presence of 10^{-3} *m* oxalate than in NaCl media alone (Figure 2). In addition, the 100 °C proton charge data are distinctly more positive below the pH_{znpc} than at lower temperatures, and this increase is even greater at 150 °C for the 0.03 *m* NaCl data tabulated in the Supporting Information. Our SCM results (discussed below) suggest that this increase is related to oxalate adsorption but only indirectly, which helps explain why the adsorption pH edge data do not also increase at higher temperatures.

Molecular Modeling. Our classical molecular dynamics (CMD) simulations revealed only outer-sphere oxalate adsorption on the rutile (110) surface. A variety of H-bonded complexes are formed, the most predominant of which at 2 charge states and temperatures are given in Table 1. The adsorbed complexes are anchored by 1 (OS3), 2 (OS1, OS4), or 3 H-bonds (OS2) between oxalate oxygen atoms and protons bound to terminal water or bridging oxygen groups, and the lengths of the H-bonds are generally less than or similar to H-bonds in bulk water (Tables S1 and S2 in the Supporting Information). Also, surface charge and temperature only slightly affect adsorbed complex distribution.

Representative PMF free-energy profiles at 25 and 100 °C, as obtained by bringing an oxalate molecule aligned for monodentate inner-sphere coordination toward the +0.208 C/m^2 rutile surface, are shown in Figure 3. There is a well-defined

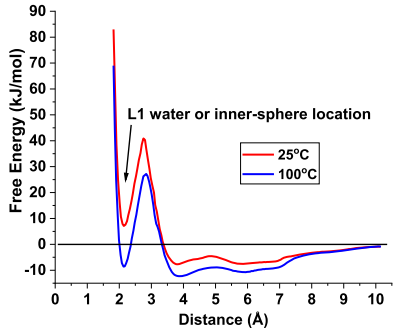

Figure 3. PMF free-energy profiles for the adsorption of an oxalate oxygen approaching monodentate inner-sphere coordination at the +0.208 C/m^2 surface obtained from the umbrella sampling at 25 and 100 °C. Zero energy (black horizontal line) corresponds to the energy in the bulk. The horizontal coordinate is the height of sampled oxygen of oxalate above the projected face of unrelaxed surface Ti atoms.

energy minimum for monodentate inner-sphere coordination at about 2.1 Å above the (110) surface face at both 25 and 100 °C. At 25 °C that minimum is separated by a 35 kJ/mol energy barrier from the more stable (by about 15 kJ/mol) outer-sphere H-bonded complexes at about 3.8 Å (and higher) above the surface, whereas at 100 °C, the energy barrier is slightly lower (~30 kJ/mol) but outer-sphere complexes are only about 4 kJ/mol more stable than the inner-sphere monodentate complex. Additional PMF calculations[42] demonstrated that monodentate inner-sphere coordination was more stable than bidentate or chelate inner-sphere configurations, supporting our CMD results that oxalate binding is predominately outer-sphere, at least at temperatures below 100 °C where oxalate is thermally stable.

Constrained Surface Complexation Modeling. Our oxalate SCM utilizes some of our previous experimental and modeling results and in particular proton charge titration data and a molecularly constrained Basic Stern SCM describing

DOI: 10.1021/acs.langmuir.8b03982
Langmuir 2019, 35, 7631−7640

surface protonation and Na^+ and Cl^- binding in 0.03 and 0.30 *m* NaCl media to 250 °C.[28] Relevant model parameters for the NaCl only data to 150 °C are given in the Supporting Information, and those parameters were held constant when fitting our oxalate adsorption data.

Our CMD results indicate that there are 4 predominant H-bonded oxalate complexes at the rutile (110) surface (Table 1, above). Although it would have been possible to incorporate these 4 complexes into our SCM separately, we chose to develop a simpler H-bond SCM with only 2 H-bonded complexes. To do so, complexes OS1 and OS2, which are bound by 2 and 3 H-bonds, respectively, to both terminal water hydrogens (H_t) and protonated bridging oxygen hydrogens (H_b) were combined, as were OS3 and OS4 which are bound by 1 and 2 H-bonds, respectively, to H_t atoms. The OS1 and OS2 hybrids are taken to have 2.5 H-bonds, of which 1.5 are formed between H_t atoms and an oxalate O atom and 1 is formed between a H_b atom and oxalate O atom. The OS3 and OS4 hybrids are taken to form 1.5 H-bonds between H_t atoms and oxalate oxygens. At 25 °C, H-bond lengths to H_b atoms are about 1.7 Å, whereas those to H_t atoms are about 1.90 Å for OS1 and OS2 complexes and 1.95 Å for the OS3 and OS4 complexes, and these lengths increase by about 0.03 Å at 100 °C (Supporting Information, Tables 1 and 2).

The H-bond lengths were converted to bond valence (BV) units with the following equation from Machesky et al.,[44] which was fit to the H-bond length versus H-bond BV data tabulated by Brown[45]

$$\text{H-bond (BV units)} = 1.55 - (\text{H-bond length (Å)} \times 1.06) + ((\text{H-bond length(Å)})^2 \times 0.186) \quad (1)$$

The calculated BV values were then multiplied by the number of H-bonds involved for each hybrid complex, which resulted in total H-bond CD values of 0.60 BV units for the combined OS1 and OS2 complexes, and 0.28 BV units for the combined OS3 and OS4 complexes at all temperatures. Recently, Hiemstra et al.[46] developed a similar approach to help describe silicate binding by ferrihydrite. Because their approach also relied primarily on the H-bond length versus H-bond BV data tabulated by Brown, the translation of H-bond length to BV units results in BV values nearly identical to ours. For example, a H-bond length of 1.83 Å yields 0.23 BV units via eq 1, and 0.22 BV units with the Hiemstra et al. approach.

For comparative purposes, we also developed an inner-sphere SCM. Of the bidentate, chelate, and monodentate complexes considered, both unprotonated and monoprotonated, the unprotonated−monodentate complex provided the most satisfactory fit to the pH edge and proton charge data (Figure S1 in the Supporting Information demonstrates this for our 25 °C data). The CD value for the monodentate complex was fixed at −0.5 BV units, which assumes that the carboxyl oxygens are resonance stabilized, and that the entire charge of one of the 4 oxygens is assigned to the rutile surface. This follows previous CD-MUSIC model descriptions of inner-sphere carboxylic acid binding by oxide surfaces.[47] It was somewhat surprising that none of the bidentate and/or chelate complexes identified in previous IR spectroscopic studies (summarized in the Introduction section) fit our data well. Perhaps our experimental data do not span a wide enough range of surface coverages, or possibly our modeling approach is deficient. It is also possible that some of the IR spectroscopic results have been misinterpreted. Nonetheless, our PMF free-energy calculations also indicated that monodentate binding was the preferred inner-sphere adsorption configuration.

Both SCMs followed the combined charge distribution (CD[48]) and multisite complexation (MUSIC[49]) approaches of Hiemstra et al. (CD-MUSIC) and were optimized with the aid of custom Mathematica notebooks, with only the oxalate binding constants as variable parameters. The final set of SCM equations and equilibrium constant designations is given in Table 2. Included are protonation and Na^+ and Cl^- binding reactions that are fully described elsewhere (values provided in the Supporting Information),[28] as well as the H-bonded (HB) and inner-sphere (IS) oxalate binding reactions. Table 3 contains the optimized oxalate binding parameters and associated CD values, as well as ancillary values including error bounds (±1 SD) for oxalate binding parameters, model selection criterion (MSC) values as a goodness of fit measure (larger is better), and aqueous oxalate protonation constants.

Representative SCM fits to the 25 and 150 °C oxalate pH adsorption edge and proton charge data are presented in Figures 4 and 5, respectively. The entire set of adsorption data and model fits for both the H-bonded and inner-sphere SCMs are provided in the Supporting Information. MSC values are somewhat greater at 25 and 35 °C for the inner-sphere SCM signifying a better overall fit, but H-bond and inner-sphere SCM MSC values are virtually identical at the other temperatures studied (Table 3). The MSC values also indicate that the fits to the 100 and 150 °C data are less precise than

Table 2. Protonation, Oxalate, Na^+, and Cl^- Surface Complexation Reactions, Stoichiometry, and Equilibrium Constant Designations[a]

	equil. const.
Surface Protonation	
$\equiv TiOH^{-0.434} + H^+ \rightarrow \equiv TiOH_2^{+0.566}$	K_{H1}
$\equiv Ti_2O^{-0.555} + H^+ \rightarrow \equiv Ti_2OH^{+0.445}$	K_{H2}
OS1 + OS2 H-Bonded Oxalate^{2-}	
$1.5\equiv TiOH^{-0.434} + 1\equiv Ti_2O^{-0.555} + Ox^{2-} + 2.5H^+ \rightarrow [(1.5\equiv TiOH_2^{+0.566})(1\equiv Ti_2OH^{+0.445})]\cdots Ox^{2-}$	K_{Ox1} (OS1 + OS2)
OS3 + OS4 H-Bonded Oxalate^{2-}	
$1.5\equiv TiOH^{-0.434} + Ox^{2-} + 1.5H^+ \rightarrow [(1.5\equiv TiOH_2^{+0.566})]\cdots Ox^{2-}$	K_{Ox2} (OS3 + OS4)
Inner-Sphere Oxalate^{2-}	
$1\equiv TiOH^{-0.434} + Ox^{2-} + 1H^+ \rightarrow [(1\equiv Ti{-}Ox)] + H_2O$	K_{OxIS} (IS)
Inner-Sphere Na^+	
$2\equiv TiOH^{-0.434} + 2\equiv Ti_2O^{-0.555} + Na^+ + xH^+ \rightarrow [(\equiv(2-x)TiOH^{-0.434})(\equiv xTiOH_2^{+0.566})(\equiv Ti_2O^{-0.555})_2]{-}Na^+$	K_{Na} (TD)
$\equiv TiOH^{-0.434} + \equiv Ti_2O^{-0.555} + Na^+ + yH^+ \rightarrow [(\equiv(1-y)TiOH^{-0.434})(\equiv yTiOH_2^{+0.566})(\equiv Ti_2O^{-0.555})]{-}Na^+$	K_{Na} (BOTO)
$2\equiv TiOH^{-0.434} + Na^+ + zH^+ \rightarrow [(\equiv(2-z)TiOH^{-0.434})(\equiv zTiOH_2^{+0.566})]{-}Na^+$	K_{Na} (TOTO)
Outer-Sphere Na^+	
$\equiv TiOH^{-0.434} + Na^+ \rightarrow (\equiv TiOH^{-0.434}){-}Na^+$	K_{Na} (OS)
$\equiv Ti_2O^{-0.555} + Na^+ \rightarrow (\equiv Ti_2O^{-0.555}){-}Na^+$	K_{Na} (OS)
Inner-Sphere BOH Cl^-	
$\equiv Ti_2O^{-0.555} + H^+ + Cl^- \rightarrow (\equiv Ti_2OH^{+0.445}){-}Cl^-$	K_{Cl} (BOH)

[a]The corresponding equilibrium constant values (log units) are given in Table 3 and the Supporting Information. The variables *x*, *y*, and *z* represent the number of $TiOH_2^{+0.566}$ groups participating in the various inner-sphere Na^+ complexes modeled as given in the Supporting Information.

DOI: 10.1021/acs.langmuir.8b03982
Langmuir 2019, 35, 7631−7640

Table 3. Oxalate Associated SCM Parameters for the H-Bond Model (Left) and Inner-Sphere Model (Rightmost 4 Columns)[a]

			H-bond model (HB)							inner-sphere model (IS)			
temp (°C)	log K_2 (sol)	log K_1 (sol)	log K_{ox1}	SD	CD	log K_{ox2}	SD	CD	MSC	log K_{oxIS}	SD	CD	MSC
10	4.265	1.260	3.40	0.24	−0.60	3.70	0.25	−0.28	4.75	9.70	0.10	−0.50	4.69
25	4.275	1.277	3.30	0.22	−0.60	3.50	0.24	−0.28	4.88	9.30	0.07	−0.50	5.17
35	4.335	1.310	3.40	0.22	−0.60	3.50	0.24	−0.28	5.08	9.20	0.06	−0.50	5.49
50	4.408	1.358	3.60	0.28	−0.60	3.70	0.29	−0.28	4.16	9.30	0.09	−0.50	4.20
100	4.792	1.581	4.30	0.55	−0.60	4.20	0.64	−0.28	3.63	9.40	0.15	−0.50	3.64
150	5.264	1.830	4.40	0.97	−0.60	4.30	1.01	−0.28	3.13	9.30	0.22	−0.50	3.17

[a]Note that the CD values refer to the charge of the adsorbed oxalate oxygens (total oxalate charge = −2) that is assigned to the surface plane.

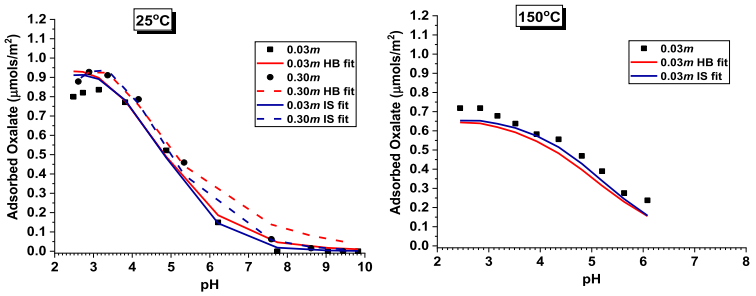

Figure 4. H-bond (HB, red lines) and inner-sphere (IS, blue lines) SCM fits to the 25 °C (left) and 150 °C (right) adsorption pH edge data (closed black symbols).

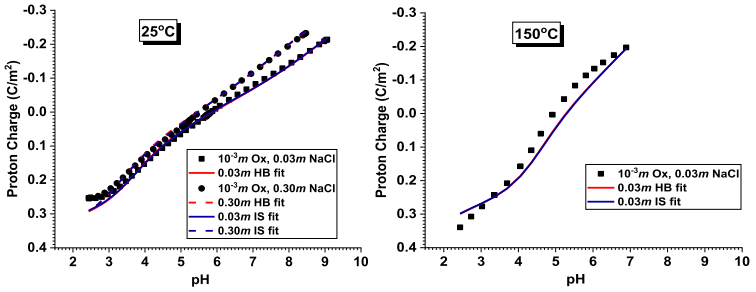

Figure 5. H-bond (HB, red lines) and inner-sphere (IS, blue lines) SCM fits to the 25 °C (left) and 150 °C (right) proton charge data (closed black symbols).

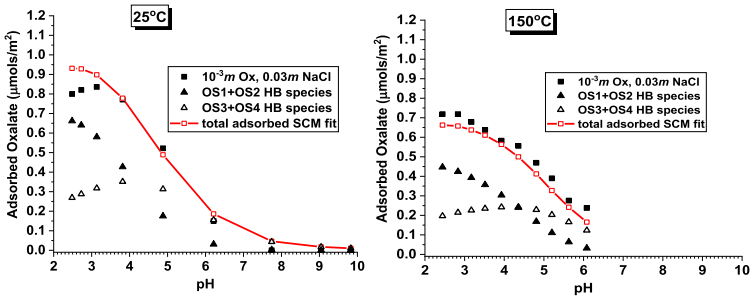

Figure 6. H-bonded species distribution vs pH for the 0.03 *m* NaCl adsorption pH edge data at 25 °C (left) and 150 °C (right).

that at lower temperatures, as can also be seen in comparing the left and right plots in Figures 4 and 5.

The concentrations of the two H-bonded species at 25 and 150 °C for the pH adsorption edge data in 0.03 *m* NaCl for our H-bond SCM are presented in Figure 6. The OS1 + OS2 H-bonded species increasingly dominates as pH decreases. This agrees with the CMD results where the OS1 and OS2 complexes are more dominant at +0.208 than that at +0.104

DOI: 10.1021/acs.langmuir.8b03982
Langmuir 2019, 35, 7631−7640

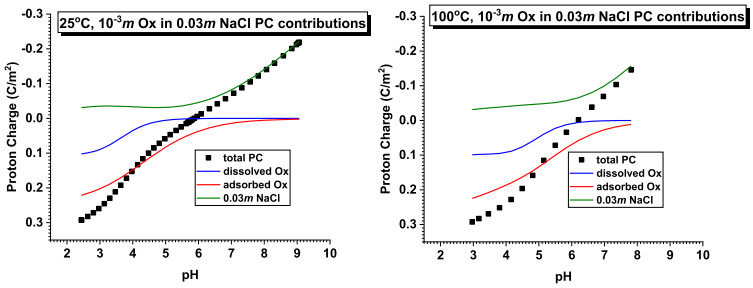

Figure 7. Species contributing to the total proton charge (PC) over the titration pH range according to the H-bond SCM.

C/m^2 charge (Table 1). Maximum adsorption densities for the OS3 + OS4 H-bonded species are only 0.25−0.4 $\mu mol/m^2$ and occur at pH 4−5. In fact, from the perspective of SCM fitting only, fits are nearly as good when the OS3 + OS4 H-bonded species is omitted. However, its inclusion results in a more robust SCM, given that the relative proportions of the 2 H-bonded species including their pH dependence closely mirrors the CMD results. The CMD (OS1 + OS2/OS3 + OS4) ratio at +0.208 C/m^2 is about 2:1 at 25 °C (Table 1), which is very similar to the corresponding SCM fit ratio of 1.8:1 at the equivalent pH of about 3.6 (Figure 6).

The distribution of proton charge for our H-bond SCM at 25 and 100 °C in 0.03 *m* NaCl is presented in Figure 7. Three processes contribute to the total proton charge, and these are conveniently discussed from the viewpoint of a high to low pH titration where a net consumption of protons occurs. The individual surface reactions contributing to proton consumption are given in Table 2. Charging in NaCl media (green curves) is due to protonation of the terminal and bridging oxygens on the rutile (110) surface, including protons accompanying Na^+ and Cl^- binding. That contribution, in the presence of 10^{-3} *m* oxalate, dominates the total proton charge only at the highest pH values studied, especially at 100 °C. A second contribution results from the protonation of dissolved oxalate in solution (blue curves). This contribution becomes important near the second pK_a of oxalic acid when oxalate is protonated to hydrogenoxalate and contributes about 25% of the total proton charge at the lowest pH values. The third contribution is the protons that adsorb during oxalate binding (red curves). This contribution dominates at all pH values where oxalate adsorbs and contributes about 70% of the total proton charge at the lowest pH values. A closer inspection of the 100 °C proton charge contributions reveals that the adsorbed oxalate contribution is primarily responsible for the increased positive charge relative to the lower temperature results (Figure 2, above).

Our CMD and PMF free-energy results indicate that inner-sphere binding of oxalate on the (110) surface of rutile is very energetically unfavorable at 25 °C and slightly unfavorable at 100 °C, but that adsorption is still strong albeit in the form of outer-sphere H-bond interactions. Conversely, a large body of spectroscopic evidence indicates that oxalate binds in various kinds of inner-sphere configurations. We have developed SCMs that accommodate both scenarios but that does not address the discrepancy directly.

Our CMD simulations involve the perfect (110) surface of rutile. However, all of the available IR spectroscopic studies utilized powdered rutile samples, as did our oxalate adsorption experiments. As is the case for our Tioxide rutile powder, the (110) surface often dominates the external surface area of rutile powders. However, that surface can be far from perfect, with steps, kinks, and other imperfections also being present. Livi et al.[50] examined the same Tioxide rutile sample utilized in our oxalate adsorption studies via atomic-resolution scanning transmission spectroscopy and found that the dominant (110) face is heavily stepped, at up to 33% of the face area. Mendive et al.[13] also noted the presence of steps on the dominant (110) face of their powdered rutile sample (with HRTEM) used to investigate oxalate adsorption via FTIR spectroscopy. Zheng et al.[51] have also shown that the adsorption energy of a water molecule on a fivefold coordinated Ti site on the perfect (110) rutile face is greater (−1.23 eV or equivalently −119 kJ/mol) than that on fivefold coordinated Ti sites on (110) face steps (−0.77 to −0.96 eV or equivalently −74 to −93 kJ/mol). Because inner-sphere adsorption would require removal of these water molecules, energy barriers to do so would be about 20−40 kJ/mol lower at such defect sites. This should facilitate inner-sphere adsorption and could result in PMF profiles (e.g., Figure 3) where inner-sphere complexes are favored.

The (110) face step densities reported by Livi et al.[50] would also contain sufficient sites to completely bind up to the maximum oxalate adsorption densities observed in this study (~0.9 $\mu mol/m^2$). More probably, however, if both our CMD results (for the perfect (110) face) and the IR spectroscopic results (for rutile powders) are correct, then a combination of outer-sphere H-bonded and inner-sphere adsorbed oxalate species exists together. Moreover, the types of surface groups which bind oxalate would be different on steps or other surface imperfections than those on the ideal (110) surface, as has already been suggested by Jonsson et al.[52] in their study of L-glutamate binding by rutile.

Resolving this dilemma will require additional IR spectroscopic and molecular modeling studies. Spectroscopic studies should be conducted on single-crystal rutile samples with the (110) face exposed, which might reveal that outer-sphere adsorption is predominant. These samples are commercially available, and our group has used them extensively in both X-ray synchrotron[15] and SHG[53] investigations. Hug and Bahnemann[10] have also called for the use of oxides with well-defined crystal terminations to reduce IR spectra ambiguity. IR spectra must also be more carefully analyzed to better discern between inner- and outer-sphere binding, and molecular calculations can aid this endeavor. Mendive et al.[13] used semiempirical quantum chemical modeling to help interpret their ATR−FTIR spectra of oxalate binding by rutile, which appears to be the only other study involving molecular

DOI: 10.1021/acs.langmuir.8b03982
Langmuir 2019, 35, 7631−7640

modeling besides our own. Those simulations suggested that oxalate could adsorb inner-spherically, which supported their spectroscopic interpretations. However, the simulations were extremely sensitive to the arrangement of water molecules above the surface, and because only a monolayer of water was included, the simulation results are not definitive. Therefore, additional simulation studies are needed, including those incorporating various types of surface defects. A few such studies already exist,[54] and they should be coupled with careful microscopic characterization to focus the computations on the kinds of surface imperfections that actually exist.

SUMMARY AND CONCLUSIONS

The adsorption of oxalate by rutile into the near hydrothermal regime was experimentally determined for the first time. Over the broad temperature range investigated (10−150 °C), systematic temperature trends were absent, in contrast to our previous studies of cation adsorption by rutile where adsorption is enhanced with increasing temperature. Additional anion adsorption studies into the hydrothermal region would be necessary to determine whether the absence of a systematic trend in adsorption with temperature is a specific or general characteristic.

Surface complexation modeling was utilized to rationalize the macroscopic adsorption data. Molecular level information, from molecular modeling calculations as well as previously conducted IR spectroscopic studies, was used to constrain the SCM efforts. The molecular modeling simulations, which included molecular dynamic simulations supported by free-energy and ab initio calculations, revealed that oxalate binding was predominately outer-sphere albeit through strong H-bonds between oxalate oxygens and surface hydroxyl group protons. Conversely, IR spectroscopic studies have concluded that oxalate binding on rutile involves a variety of inner-sphere complexes in addition to outer-sphere associations. Both the SCM constrained by the molecular simulation results, and the SCM containing inner-sphere binding, were able to fit the macroscopic adsorption data well, although the inner-sphere SCM fits were considerably better for monodentate binding than for bidentate or chelate binding. Our PMF and ab initio calculations[42] also indicated that monodentate inner-sphere binding was much more energetically favorable than bidentate or chelate binding.

Finally, we proposed that the discrepancy between the molecular simulation and IR spectroscopic results may stem from the nature of the rutile surfaces investigated. That is, for the molecular simulations, the perfect (110) surface face, and for all previous IR spectroscopic studies (and our adsorption experiments), various powdered rutile samples. Although the (110) surface face dominates many powdered rutile samples, including the Tioxide rutile used in our adsorption studies, that face is invariably punctuated by steps, kinks, and various other surface defects. Thus, we hypothesized that inner-sphere oxalate adsorption occurs predominately at defect sites, as has previously been suggested to govern amino acid adsorption to the same Tioxide rutile used in our studies. Further study, including IR spectroscopy on well-defined rutile specimens and molecular simulations on defective rutile surfaces, is required to prove or disprove this conjecture.

ASSOCIATED CONTENT

Supporting Information

The Supporting Information is available free of charge on the ACS Publications website at DOI: 10.1021/acs.langmuir.8b03982.

H-bond lengths for the adsorbed H-bonded oxalate complexes and plots of the 25 °C proton charge and adsorption pH edge data as best-fit with inner-sphere monodentate, bidentate, and chelate adsorbed oxalate complexes (PDF)

First sheet contains SCM parameters for the surface charge titrations conducted in NaCl only media; the second sheet contains all the oxalate adsorption data modeled in this study as well as the model fits; and the third sheet contains expanded definitions of the row designations appearing in the first column of the second sheet (XLSX)

AUTHOR INFORMATION

Corresponding Author

*E-mail: machesky@illinois.edu. Phone: 217-722-0927.

ORCID

Michael L. Machesky: 0000-0002-8212-3922
Denys Biriukov: 0000-0003-1007-2203
Ondřej Kroutil: 0000-0001-8893-2969
Milan Předota: 0000-0003-3902-0992

Notes

The authors declare no competing financial interest.

ACKNOWLEDGMENTS

M.L.M. was supported by the U.S. Department of Energy, Office of Science, Office of Basic Energy Sciences, Chemical Sciences, Geosciences, and Biosciences Division. M.K.R. acknowledges support from the National Science Foundation (CHE-1308726 and EAR-0842526). D.B., O.K., and M.P. acknowledge support from the Ministry of Education, Youth, and Sports of the Czech Republic (project LTAUSA17163). Computational resources were provided by the CESNET LM2015042 and the CERIT Scientific Cloud LM2015085, under the program "Projects of Large Research, Development, and Innovations Infrastructures". The comments of two anonymous reviewers were greatly appreciated.

REFERENCES

(1) Jones, D. L. Organic acids in the rhizosphere − a critical review. *Plant Soil* **1998**, *205*, 25−44.
(2) Taxiarchou, M.; Panias, D.; Douni, I.; Paspaliaris, I.; Kontopoulos, A. Removal of iron from silica sand by leaching with oxalic acid. *Hydrometallurgy* **1997**, *46*, 215−227.
(3) Kettler, R. M.; Palmer, D. A.; Wesolowski, D. J. Dissociation quotients of oxalic acid in aqueous sodium chloride media to 175°C. *J. Sol. Chem.* **1991**, *20*, 905−927.
(4) Parfitt, R. L.; Farmer, V. C.; Russell, J. D. Adsorption on hydrous oxides I. Oxalate and benzoate on goethite. *J. Soil Sci.* **1977**, *28*, 29−39.
(5) Parfitt, R. L.; Fraser, A. R.; Russell, J. D.; Farmer, V. C. Adsorption on hydrous oxides: II. Oxalate, Benzoate and phosphate on gibbsite. *J. Soil Sci.* **1977**, *28*, 40−47.
(6) Degenhardt, J.; McQuillan, A. J. Mechanism of oxalate ion adsorption on chromium oxide-hydroxide from pH dependence and time evolution of ATR-IR spectra. *Chem. Phys. Lett.* **1999**, *311*, 179−184.

DOI: 10.1021/acs.langmuir.8b03982
Langmuir 2019, 35, 7631−7640

(7) Yoon, T. H.; Johnson, S. B.; Musgrave, C. B.; Brown, G. E., Jr Adsorption of organic matter at mineral/water interfaces: I. ATR-FTIR spectroscopic and quantum chemical study of oxalate adsorbed at boehmite/water and corundum/water interfaces. *Geochem. Cosmochim. Acta* **2004**, *68*, 4505.
(8) Persson, P.; Axe, K. Adsorption of oxalate and malonate at the water-goethite interface: Molecular surface speciation from IR spectroscopy. *Geochem. Cosmochim. Acta* **2005**, *69*, 541−552.
(9) Borowski, S. C.; Biswakarma, J.; Kang, K.; Schenkeveld, W. D. C.; Hering, J. G.; Kubicki, J. D.; Kraemer, S. M.; Hug, S. J. Structure and reactivity of oxalate surface complexes on lepidocrocite derived from infrared spectroscopy, DFT-calculations, adsorption, dissolution and photochemical experiments. *Geochem. Cosmochim. Acta* **2018**, *226*, 244−262.
(10) Hug, S. J.; Bahnemann, D. Infrared spectra of oxalate, malonate and succinate adsorbed on the aqueous surface of rutile, anatase and lepidocrocite measured with in situ ATR-FTIR. *J. Electron Spectrosc. Relat. Phenom.* **2006**, *150*, 208−219.
(11) Hug, S. J.; Sulzberger, B. In situ Fourier Transform Infrared Spectroscopic Evidence for the Formation of Several Different Surface Complexes of Oxalate on TiO2 in the Aqueous Phase. *Langmuir* **1994**, *10*, 3587−3597.
(12) Young, A. G.; McQuillan, A. J. Adsorption/Desorption Kinetics from ATR-IR Spectroscopy. Aqueous Oxalic Acid on Anatase TiO2. *Langmuir* **2009**, *25*, 3538−3548.
(13) Mendive, C. B.; Bredow, T.; Feldhoff, A.; Blesa, M.; Bahnemann, D. Adsorption of oxalate on rutile particles in aqueous solutions: a spectroscopic, electron-microscopic and theoretical study. *Phys. Chem. Chem. Phys.* **2008**, *10*, 1960−1974.
(14) Ridley, M. K.; Machesky, M. L.; Wesolowski, D. J.; Palmer, D. A. Calcium adsorption at the rutile-water interface: a potentiometric study in NaCl media to 250°C. *Geochem. Cosmochim. Acta* **1999**, *63*, 3087−3096.
(15) Zhang, Z.; Fenter, P.; Cheng, L.; Sturchio, N. C.; Bedzyk, M. J.; Předota, M.; Bandura, A.; Kubicki, J. D.; Lvov, S. N.; Cummings, P. T.; Chialvo, A. A.; Ridley, M. K.; Bénézeth, P.; Anovitz, L.; Palmer, D. A.; Machesky, M. L.; Wesolowski, D. J. Ion Adsorption at the Rutile−Water Interface: Linking Molecular and Macroscopic Properties. *Langmuir* **2004**, *20*, 4954−4969.
(16) Ridley, M. K.; Machesky, M. L.; Wesolowski, D. J.; Palmer, D. A. Surface complexation of neodymium at the rutile-water interface: A potentiometric and modeling study in NaCl media to 250°C. *Geochem. Cosmochim. Acta* **2005**, *69*, 63−81.
(17) Machesky, M. L. Influence of temperature on ion adsorption by hydrous metal oxides. *ACS Symp. Ser.* **1990**, *416*, 282−292.
(18) Machesky, M. L.; Bischoff, B. L.; Anderson, M. A. Calorimetric investigation of anion adsorption onto goethite. *Environ. Sci. Technol.* **1989**, *23*, 580−587.
(19) Barrow, N. J.; Shaw, T. C. The Slow Reactions between Soil and Anions. *Soil Sci.* **1975**, *119*, 167−177.
(20) Balistrieri, L. S.; Chao, T. T. Selenium Adsorption by Goethite1. *Soil Sci. Soc. Am. J.* **1987**, *51*, 1145−1151.
(21) Goldberg, S.; Forster, H. S.; Heick, E. L. Temperature effects on boron adsorption by reference minerals and soils. *Soil Sci.* **1993**, *156*, 316−321.
(22) López Valdivieso, A.; Reyes Bahena, J. L.; Song, S.; Herrera Urbina, R. Temperature effect on the zeta potential and fluoride adsorption at the α-Al2O3/aqueous solution interface. *J. Colloid Interface Sci.* **2006**, *298*, 1−5.
(23) Fein, J. B.; Brady, P. V. Mineral surface controls on the diagenetic transport of oxalate and aluminum. *Chem. Geol.* **1995**, *121*, 11−18.
(24) Ward, D. B.; Brady, P. V. Effect of Al and organic acids on the surface chemistry of kaolinite. *Clays Clay Miner.* **1998**, *46*, 453−465.
(25) Angove, M. J.; Wells, J. D.; Johnson, B. B. The influence of temperature on the adsorption of mellitic acid onto goethite. *J. Colloid Interface Sci.* **2006**, *296*, 30−40.
(26) Angove, M. J.; Wells, J. D.; Johnson, B. B. Influence of Temperature on the Adsorption of Mellitic Acid onto Kaolinite. *Langmuir* **2006**, *22*, 4208−4214.
(27) Ridley, M. K.; Hiemstra, T.; Machesky, M. L.; Wesolowski, D. J.; van Riemsdijk, W. H. Surface speciation of yttrium and neodymium sorbed on rutile: Interpretations using the charge distribution model. *Geochem. Cosmochim. Acta* **2012**, *95*, 227−240.
(28) Machesky, M. L.; Předota, M.; Ridley, M. K.; Wesolowski, D. J. Constrained Surface Complexation Modeling: Rutile in RbCl, NaCl, and $NaCF_3SO_3$ Media to 250 °C. *J. Phys. Chem. C* **2015**, *119*, 15204−15215.
(29) Ridley, M. K.; Machesky, M. L.; Palmer, D. A.; Wesolowski, D. J. Potentiometric studies of the rutile-water interface: hydrogen-electrode concentration-cell versus glass-electrode titrations. *Colloids Surf., A* **2002**, *204*, 295−308.
(30) Ridley, M. K.; Hackley, V. A.; Machesky, M. L. Characterization and Surface-Reactivity of Nanocrystalline Anatase in Aqueous Solutions. *Langmuir* **2006**, *22*, 10972−10982.
(31) Ridley, M. K.; Hiemstra, T.; van Riemsdijk, W. H.; Machesky, M. L. Inner-sphere complexation of cations at the rutile-water interface: A concise surface structural interpretation with the CD and MUSIC model. *Geochem. Cosmochim. Acta* **2009**, *73*, 1841−1856.
(32) Machesky, M. L.; Wesolowski, D. J.; Palmer, D. A.; Ridley, M. K.; Bénézeth, P.; Lvov, S. N.; Fedkin, M. V. Ion Adsorption into the Hydrothermal Regime: Experimental and Modeling Approaches. In *Interface Science and Technology*; Lützenkirchen, J., Ed.; Elsevier, 2006; Chapter 12, pp 324−358.
(33) Machesky, M. L.; Wesolowski, D. J.; Palmer, D. A.; Ichiro-Hayashi, K. Potentiometric Titrations of Rutile Suspensions to 250°C. *J. Colloid Interface Sci.* **1998**, *200*, 298−309.
(34) Dzombak, D. A. *Surface Complexation Modeling: Hydrous Ferric Oxide*; John Wiley & Sons, 1990.
(35) Palmer, D. A.; Wesolowski, D. J. Aluminum speciation and equilibria in aqueous solution: III. Potentiometric determination of the first hydrolysis constant of aluminum(III) in sodium chloride solutions to 125°C. *Geochem. Cosmochim. Acta* **1993**, *57*, 2929−2938.
(36) Předota, M.; Machesky, M. L.; Wesolowski, D. J.; Cummings, P. T. Electric Double Layer at the Rutile (110) Surface. 4. Effect of Temperature and pH on the Adsorption and Dynamics of Ions. *J. Phys. Chem. C* **2013**, *117*, 22852−22866.
(37) Leontyev, I.; Stuchebrukhov, A. Accounting for electronic polarization in non-polarizable force fields. *Phys. Chem. Chem. Phys.* **2011**, *13*, 2613.
(38) Van Der Spoel, D.; Lindahl, E.; Hess, B.; Groenhof, G.; Mark, A. E.; Berendsen, H. J. C. GROMACS: fast, flexible, and free. *J. Comput. Chem.* **2005**, *26*, 1701−1718.
(39) Biriukov, D.; Kroutil, O.; Předota, M. Modeling of solid-liquid interfaces using scaled charges: rutile (110) surfaces. *Phys. Chem. Chem. Phys.* **2018**, *20*, 23954−23966.
(40) Brandt, E. G.; Lyubartsev, A. P. Systematic Optimization of a Force Field for Classical Simulations of TiO2-Water Interfaces. *J. Phys. Chem. C* **2015**, *119*, 18110−18125.
(41) Kroutil, O.; Předota, M.; Kabeláč, M. Force field parametrization of hydrogenoxalate and oxalate anions with scaled charges. *J. Mol. Modeling* **2017**, *23*, 327.
(42) Biriukov, D.; Kroutil, O.; Kabeláč, M.; Ridley, M. K.; Machesky, M. L.; Předota, M. Molecular Description of Oxalic Acid Adsorption on Rutile: Molecular Dynamics and Ab Initio Calculations. *Langmuir* **2019**, DOI: 10.1021/acs.langmuir.8b03984.
(43) Hub, J. S.; de Groot, B. L.; van der Spoel, D. g_wham-A Free Weighted Histogram Analysis Implementation Including Robust Error and Autocorrelation Estimates. *J. Chem. Theory Comp.* **2010**, *6*, 3713−3720.
(44) Machesky, M. L.; Predota, M.; Wesolowski, D. J.; Vlcek, L.; Cummings, P. T.; Rosenqvist, J.; Ridley, M. K.; Kubicki, J. D.; Bandura, A. V.; Kumar, N.; Sofo, J. O. Surface Protonation at the Rutile (110) Interface: Explicit Incorporation of Solvation Structure within the Refined MUSIC Model Framework. *Langmuir* **2008**, *24*, 12331−12339.

DOI: 10.1021/acs.langmuir.8b03982
Langmuir 2019, 35, 7631−7640

(45) Brown, I. D. *The Chemical Bond in Inorganic Chemistry: The Bond Valence Model*; Oxford University Press: New York, 2002; p 288.
(46) Hiemstra, T. Ferrihydrite interaction with silicate and competing oxyanions: Geometry and Hydrogen bonding of surface species. *Geochem. Cosmochim. Acta* **2018**, *238*, 453−476.
(47) Filius, J. D.; Hiemstra, T.; Van Riemsdijk, W. H. Adsorption of Small Weak Organic Acids on Goethite: Modeling of Mechanisms. *J. Colloid Interface Sci.* **1997**, *195*, 368−380.
(48) Hiemstra, T.; Venema, P.; Riemsdijk, W. H. V. Intrinsic proton affinity of reactive surface groups of metal (hydr)oxides: The bond valence principle. *J. Colloid Interface Sci.* **1996**, *184*, 680−692.
(49) Hiemstra, T.; Van Riemsdijk, W. H. A surface structural approach to ion adsorption: The charge distribution (CD) model. *J. Colloid Interface Sci.* **1996**, *179*, 488−508.
(50) Livi, K. J. T.; Schaffer, B.; Azzolini, D.; Seabourne, C. R.; Hardcastle, T. P.; Scott, A. J.; Hazen, R. M.; Erlebacher, J. D.; Brydson, R.; Sverjensky, D. A. Atomic-Scale Surface Roughness of Rutile and Implications for Organic Molecule Adsorption. *Langmuir* **2013**, *29*, 6876−6883.
(51) Zheng, T.; Wu, C.; Chen, M.; Zhang, Y.; Cummings, P. T. A DFT study of water adsorption on rutile TiO2 (110) surface: The effects of surface steps. *J. Chem. Phys.* **2016**, *145*, 044702.
(52) Jonsson, C. M.; Jonsson, C. L.; Sverjensky, D. A.; Cleaves, H. J.; Hazen, R. M. Attachment ofl-Glutamate to Rutile (α-TiO2): A Potentiometric, Adsorption, and Surface Complexation Study. *Langmuir* **2009**, *25*, 12127−12135.
(53) Fitts, J. P.; Machesky, M. L.; Wesolowski, D. J.; Shang, X.; Kubicki, J. D.; Flynn, G. W.; Heinz, T. F.; Eisenthal, K. B. Second-harmonic generation and theoretical studies of protonation at the water/α-TiO2 (110) interface. *Chem. Phys. Lett.* **2005**, *411*, 399−403.
(54) Parikh, S. J.; Kubicki, J. D.; Jonsson, C. M.; Jonsson, C. L.; Hazen, R. M.; Sverjensky, D. A.; Sparks, D. L. Evaluating Glutamate and Aspartate Binding Mechanisms to Rutile (α-TiO2) via ATR-FTIR Spectroscopy and Quantum Chemical Calculations. *Langmuir* **2011**, *27*, 1778−1787.

DOI: 10.1021/acs.langmuir.8b03982
Langmuir 2019, 35, 7631−7640

Article DB4

Marchioro, A.; Bischoff, M.; Lütgebaucks, C.; **Biriukov, D.**; Předota, M.; Roke, S.

Surface Characterization of Colloidal Silica Nanoparticles by Second Harmonic Scattering: Quantifying the Surface Potential and Interfacial Water Order

Journal of Physical Chemistry C **2019**, *123* (33), 20393–20404;
IF (2018) = 4.309

Participation of Denys Biriukov:

DB performed all the molecular simulations, analyzed the results, and participated in the paper writing.

DOI: 10.1021/acs.jpcc.9b05482;

THE JOURNAL OF PHYSICAL CHEMISTRY C

Article

Cite This: J. Phys. Chem. C 2019, 123, 20393−20404

pubs.acs.org/JPCC

Surface Characterization of Colloidal Silica Nanoparticles by Second Harmonic Scattering: Quantifying the Surface Potential and Interfacial Water Order

Published as part of The Journal of Physical Chemistry virtual special issue "Hai-Lung Dai Festschrift".

Arianna Marchioro,[†] Marie Bischoff,[†] Cornelis Lütgebaucks,[†] Denys Biriukov,[‡] Milan Předota,[‡] and Sylvie Roke*[,†]

[†]Laboratory for Fundamental BioPhotonics (LBP), Institute of Bioengineering (IBI), and Institute of Materials Science (IMX), School of Engineering (STI), Ecole Polytechnique Fédérale de Lausanne (EPFL), CH-1015 Lausanne, Switzerland

[‡]Institute of Physics, Faculty of Science, University of South Bohemia, 370 05 České Budějovice, Czech Republic

Supporting Information

ABSTRACT: The microscopic description of the interface of colloidal particles in solution is essential to understand and predict the stability of these systems, as well as their chemical and electrochemical reactivity. However, this description often relies on the use of simplified electrostatic mean field models for the structure of the interface, which give only theoretical estimates of surface potential values and do not provide properties related to the local microscopic structure, such as the orientation of interfacial water molecules. Here we apply polarimetric angle-resolved second harmonic scattering (AR-SHS) to 300 nm diameter SiO_2 colloidal suspensions to experimentally determine both surface potential and interfacial water orientation as a function of pH and NaCl concentration. The surface potential values and interfacial water orientation change significantly over the studied pH and salt concentration range, whereas zeta-potential (ζ) values remain constant. By comparing the surface and ζ-potentials, we find a layer of hydrated condensed ions present in the high pH case, and for NaCl concentrations $\geq$1 mM. For milder pH ranges (pH < 11), as well as for salt concentrations <1 mM, no charge condensation layer is observed. These findings are used to compute the surface charge densities using the Gouy−Chapman and Gouy−Chapman−Stern models. Furthermore, by using the AR-SHS data, we are able to determine the preferred water orientation in the layer directly in contact with the silica interface. Molecular dynamics simulations confirm the experimental trends and allow deciphering of the contributions of water layers to the total response.

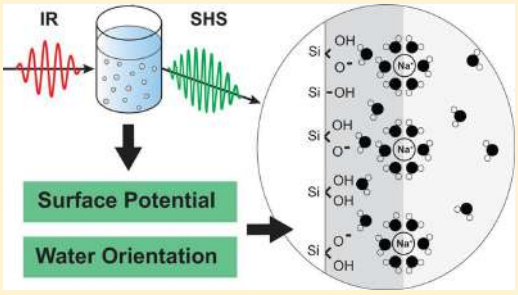

INTRODUCTION

The surface chemistry of silica is key to a large number of applications, both in research and in industrial processes. In the past few decades, colloidal suspensions of SiO_2 particles have been extensively used for separation, heterogeneous catalysis, and as major components of ceramics and coatings. Colloidal silica is also widely used in the food, health care and pharmaceutical industries, as well as in the production of microelectronics components.[1] The microscopic characterization of colloidal particle interfaces with liquids is of fundamental interest to understand the stability of these systems and their chemical and electrochemical reactivity. In contact with water or another fluid, a solid surface usually develops a charged layer at its surface that is compensated by a distribution of counterions in the surrounding solution. This so-called "electrical double layer" (EDL) has been first put forth by Helmholtz in the 1850s and since then, many different mean field models have been proposed to describe the structure of a solid/electrolyte interface. In such models, the often complex chemical nature of the interface with its different structures and nonuniformity is reduced to a uniformly charged interface, the aqueous phase is represented by a uniform dielectric, and the ions are represented as point charges. The most frequently used model was originally proposed by Gouy and Chapman. In their model a charged interface is in contact with an aqueous solution in which the counterion distribution decays exponentially along the surface normal. This layer is usually referred to as the diffuse double layer (DDL). Stern suggested a modification for high charge densities, comprised of the formation of a condensed layer, or

Received: June 9, 2019
Revised: July 25, 2019
Published: July 26, 2019

DOI: 10.1021/acs.jpcc.9b05482
J. Phys. Chem. C 2019, 123, 20393−20404

Stern layer, of potentially hydrated counterions close to the surface.[2−4] However, in reality, the structure and chemistry of this electrical double layer is more complex and the electrostatic environment will depend on the local chemical nature of the surface, of the type of ions, their solvation shells and the solvent in the first few atomic dimensions adjacent to the interface.[4−9] As many of the mentioned ingredients are challenging to determine experimentally, the microscopic description of a relatively simple interface such as SiO_2/aqueous solution remains elusive.

When considering a colloidal suspension, two parameters are most often reported, as they give an information on the stability of the suspension. These quantities, namely surface charge density and ζ-potential, can be measured with relatively simple experimental techniques. The first quantity is usually determined by potentiometric titrations,[10] assuming that all the charges in the system are confined to an outer smooth surface of the particle, which means such a measurement gives, at best, an upper limit for the surface charge. The second one is obtained by measuring the electrophoretic mobility. The ζ-potential is then calculated from the mobility, assuming a sufficiently thin double layer, and it is defined as the potential at the plane of shear, where the liquid velocity is zero. This plane is likely at some distance outside the particle and includes both the particle plus a 0.3−1 nm thick layer of stationary solvent and ions that can move with the particle in an electric field.[11−14] However, the ζ-potential only provides an empirical indication of the stability of colloidal suspensions. Direct information on the surface electrostatics is obtained via the surface potential, which in contrast to the ζ-potential, is not a trivial quantity to access experimentally.[15] The surface potential can be computed from applying the constant capacitor model (CC), the Gouy−Chapman (GC) or the Gouy−Chapman−Stern (GCS) models to titration and ζ-potential data[16] or to nonlinear optics data. Indeed, for planar SiO_2/water interfaces, surface-sensitive techniques such as SHG and sum frequency generation (SFG) have shown to provide insight into the structure of the SiO_2 double layer and water orientation at the interface,[9,17−24] as well as values for surface potential as developed by Eisenthal and co-workers.[25−30] For colloidal solutions, the so-called "Eisenthal-chi3 method" can be used to estimate values for surface potential;[18,31] however, this method is bound to the use of a model such as the CC, GC, or the GCS one, and does not provide a unique solution for the surface potential, as the number of unknowns in the expression exceeds the number of independently available observables. Information about the potential drop in the EDL can be obtained by X-ray photoelectron spectroscopy (XPS).[32] Brown et al. have shown that surface potential values of colloidal SiO_2 particles can be obtained through XPS of a liquid microjet,[33−35] using the charge divided energy difference between the binding energy of the Si 2p photoelectrons in the presence of salt and the extrapolated binding energy of the Si 2p photoelectrons at the point of zero charge. However, this measurement requires the use of synchrotron facilities and has some intrinsic limitations due to the relatively low signal-to-noise level. The colloid size needs to be small (ca. 10 nm diameter), and the salt concentration high, ~>50 mM.

Our laboratory has recently reported an alternative way to determine the average surface potential of colloidal particles in solution using polarimetric angle-resolved nonresonant second harmonic scattering (AR-SHS) measurements.[36−39] AR-SHS does not require any information on the specific structure of the interface, and only assumes exponential decay of the electrostatic potential several nanometers away from the interface. In this all-optical approach taking advantage of nonlinear light scattering theory, the nonresonantly scattered second harmonic (SH) light that is emitted from the particle interface and the EDL contains enough information to determine the surface potential quantitatively. Additionally, because of the symmetry properties of second harmonic experiments, AR-SHS also provides another essential parameter of interfaces: molecular orientation of water molecules at the interface. These two elements together greatly contribute to the microscopic description of colloid/solvent interfaces.

Here, we apply polarimetric AR-SHS to 300 nm diameter SiO_2 colloids suspended in aqueous solution and extract both surface potential and interfacial molecular orientation. Polarimetric AR-SHS experiments are performed as a function of pH and NaCl concentration. The surface potential values, as well as the interfacial water orientation, vary drastically over the studied pH and salt concentration range, in contrast to the ζ-potential values, which do not change much in magnitude. Comparing the surface and ζ-potentials, we find that for high pH cases, as well as for salt concentrations $\geq$1 mM, there is a (Stern) layer of condensed charges, forming a capacitor with respect to the surface and causing preferential orientation of interfacial water molecules with their hydrogens facing the particle surface. On the other hand, for pH values below 11, as well as below 1 mM salt concentration, there is no such layer, and the interfacial water is preferentially oriented with the oxygen atom facing the particle surface. These findings are compared to results from molecular dynamics (MD) simulations that consider the orientation of water on a single crystalline quartz surface and agree with the experimental results.

MATERIALS AND METHODS

A. Chemicals. Sodium hydroxide (NaOH, > 99.99% trace metals basis, Sigma-Aldrich) and sodium chloride (NaCl, > 99.999%, Sigma-Aldrich) were used as received. SiO_2 colloids (300 nm diameter) were purchased in powder form from Bangs Laboratories, Inc. Colloidal particles were washed as described in the sample preparation section.

B. Sample Preparation. All procedures described hereafter used ultrapure water (Milli Q, Millipore, Inc., electrical resistance of 18.2 MΩ × cm). First, 50 mg of SiO_2 colloidal particles were dispersed in 1 mL of ultrapure water, sonicated for 10 min, and then diluted to 10 mL with ultrapure water and sonicated again for 3 min. The solution was then centrifuged for 10 min at 7800 rpm (5430R, Eppendorf) in order to precipitate the colloidal particles. Then 9 mL of the supernatant were removed, and the pellet was resuspended in the same volume of Milli Q water by vortexing, followed by ultrasonication (35 kHz, 400 W, Bandelin) for 3−5 min. This procedure was repeated twice to ensure proper washing of the SiO_2 particles and removal of any additional ions in solution coming from the synthetic procedure. The conductivity of the washed particles was measured as described in section C to ensure that the initial ionic strength of the particle solution was as low as possible (below 2 μS/cm for a sample in ultrapure water and in equilibrium with atmospheric CO_2). Particles were further diluted to 0.1% wt. solutions (corresponding to ca. 3.5×10^{10} particles/mL). The pH and/or ionic strength of the solution were adjusted using 0.1 or 0.01 M stock solutions

DOI: 10.1021/acs.jpcc.9b05482
J. Phys. Chem. C 2019, 123, 20393−20404

of NaOH and NaCl. The solutions were used without further filtering and measured on the same day. Corresponding water references at the same pH/ionic strength where prepared for each SiO_2 sample. All preparation steps and measurements were performed at room temperature, 23 °C.

C. Sample Characterization. The particle size distribution was determined by dynamic light scattering (DLS) and the ζ-potential was measured by electrophoretic measurements (Zetasizer Nano ZS, Malvern). The SiO_2 colloids had a mean hydrodynamic diameter of ∼300 nm with a narrow distribution (for most samples, polydispersity index (PDI) < 0.1). Average radii and ζ-potentials are tabulated in parts D of Figures 1 and 2. Values for size and ζ-potential are averages of 3 measurements. pH was measured using a pH-meter (HI 5522 pH/ISE/EC bench meter and HI 1330 pH electrode, Hanna Instruments) calibrated with the appropriate buffer solutions. Conductivity values were measured to ensure that the proper amount of salt had been added to the sample. Conductivity values were obtained by two different means: using a conductivity meter (HI 5522 pH/ISE/EC bench meter and HI 76312 conductivity electrode, Hanna Instruments) calibrated with the appropriate buffer solutions, as well as from the ζ- potential measurements (Zetasizer Nano ZS, Malvern). Average ionic strengths in solution were calculated by the following formula:

$$c = \frac{\kappa}{\Lambda_m} = \frac{\kappa}{\sum_i \upsilon_i \lambda_i}$$

where c is the concentration of ions in solution, κ is the specific conductance, Λ_m is the equivalent (molar) ionic conductivity, λ_i is the equivalent ionic conductivities of the cations and anions, and υ_i refers to the number of moles of cations and anions.

Below theoretical concentrations of 0.1 mM, the ionic molar conductivity at infinite dilution was used, whereas for higher theoretical concentrations the ionic molar conductivity, obtained through the Debye−Hückel−Onsager equation, was used. For samples diluted in ultrapure water (no added ionic strength), average conductivity was assumed to be due solely to protons and bicarbonate ions coming from the dissociation of carbonic acid in water, as the volumes of solution were small enough to always be in equilibrium with atmospheric CO_2 (confirmed by pH measurements, pH 5.7). The measured conductivity values were in agreement with the pH of a water solution fully saturated with carbonic acid. This measurement was used in order to determine the value of the ionic strength to be used in the fitting procedure for the sample in ultrapure water.

D. AR-SHS Measurements. Second harmonic scattering measurements were performed on the same SHS setup as described in ref 38. Briefly, 190 fs laser pulses at a center wavelength of 1028 nm with a repetition rate of 200 kHz and average power of 60 mW were focused into a cylindrical glass sample cell (4.2 mm inner diameter, high precision cylindrical glass cuvettes, LS instruments). The input- (output-) polarization was controlled by a Glan Taylor polarizer (GT10-B, Thorlabs) and a zero-order half wave plate (WPH05M-1030), and another Glan Taylor polarizer (GT10-A, Thorlabs), respectively. The beam waist was about $2w_0 \sim 36$ μm; the corresponding Rayleigh length was ∼0.94 mm. The scattered SH light was collected, collimated with a plano-convex lens (f = 5 cm), polarization analyzed, and filtered (ET525/50, Chroma) before being focused into a gated photomultiplier tube (H7421−40, Hamamatsu). The acceptance angle was set to 2.4° for scattering patterns. Patterns were obtained in steps of 5° from $\theta = -90°$ to $\theta = 90°$ with 0° being the forward direction of the fundamental. Data points were acquired using 30 × 1 s acquisition time with a gate width of 10 ns. To correct for incoherent hyper-Rayleigh scattering (HRS) from the solvent phase, both the SHS response from the sample solution and the HRS response from a solution of identical ionic strength but without nanoparticles are collected. The measured data, which is a relative quantity, needs to be related to absolute quantities for the parameters required in these expressions: the second order hyperpolarizability $\beta^{(2)}$, the third order hyperpolarizability $\beta^{(3)}$, number of contributing molecules, ionic strength, radius of the particle, temperature, and refractive indices. Indeed, the detector counts in a certain polarization combination cannot be linked directly to an absolute magnitude of the $\beta^{(2)}$ component. We thus employ a normalization scheme that uses water as a reference, which has the advantage that the $\beta^{(2)}$ and $\beta^{(3)}$ values for uncorrelated water are known, so that the calibrated SSS response of water can be used to correct for differences in the beam profile on a day-to-day basis. The HRS is subtracted from the SHS and the obtained difference is then normalized to the isotropic SSS intensity of pure water:

$$I_{PPP}^{Norm}(\theta) = \left[\frac{I(\theta)_{SHS,sample,PPP} - I(\theta)_{HRS,solution,PPP}}{I(\theta)_{HRS,water,SSS}}\right]$$

This normalization does not affect the value of $\chi_{S,2}^{(2)}$ or Φ_0. The fitting procedure is described in details elsewhere.[37,38] We note here that the errors we report for surface potential and surface susceptibility are the numerical errors on the fitting procedure. The total error may include other sources, such as the variations in the experimentally determined parameters (the radius, the number density, in some cases the ionic strength) and an estimation for such error on the values of surface potential and surface susceptibility for samples of oil droplets in water is given in ref 38.

E. Molecular Dynamics. To support findings obtained by AR-SHS measurements, we also carried out realistic all-atom molecular dynamics simulations. Investigating the water orientation at SiO_2/water interface, we prepared a simulation setup consisting of two SiO_2 slabs (55 Å × 39.82 Å) modeled as quartz surfaces with (101) crystal face that were separated by a ∼55 Å thick aqueous NaCl solution. The obtained results are averaged over both identical solid/liquid interfaces present in the system.

The recently developed force field for quartz (101) surfaces[40] allowing simulations over the wide range of pH values (at pH equal to the point of zero charge (∼2.5−4) and higher) has been applied and improved to adopt the electronic continuum correction, ECC (also known as model with scaled charges to 75% of their nominal values).[41] The latter accounts for usually missed solvent polarization effects in nonpolarizable force fields, which can significantly influence interactions of charged species including charged surfaces. A general approach how to apply ECC to the modeling of solid/liquid interfaces has been described previously for TiO_2 systems,[42] while a study dedicated to "ECC-quartz" force field is currently under preparation. Note that the only modifications to the original force field[40] are modified partial charges of surface atoms, while all other parameters remain the same. Compatible ECC models were also used for Na^+ and Cl^- ions,[43] while the rigid

DOI: 10.1021/acs.jpcc.9b05482
J. Phys. Chem. C 2019, 123, 20393−20404

SPC/E model of water was employed as the solvent.[44] The charge scaling introduced by ECC significantly improves the interactions of multivalent ions (divalent, trivalent, ...) while its effect on monovalent ions is minor. We confirmed that the results presented here with ECC for NaCl are very similar to those we obtained with the original force field for quartz (101).[40] Number of surface atoms (apart from removed silanol hydrogens to design a surface charge) and water molecules was the same in all simulations, and only number of Na^+ and Cl^- ions was varied to compensate a negative surface charge and yield a specific bulk ionic concentration. All the simulations were 50 ns long after 5 ns equilibration of prepared structures. Other simulations settings were similar to those used in our previous studies.[40,42]

To probe the pH and ionic concentration effects on the water orientation at the interface, we performed two sets of simulations. In the first set, we varied a surface charge of quartz (101) surfaces via the deprotonation of selected surface silanols as described previously.[40] The bulk ionic concentration in these simulations was approximately constant (0.1−0.15 M). In the second set, we compared four different ionic concentrations ranging from 0.05 to 0.31 M at the one selected surface charge density (−0.06 C/m^2). While experiments could be performed only up to 1 mM NaCl concentration, computer simulations of a limited sample of 3745 water molecules and dozens of ions face the opposite limitations—already just one ion pair in the bulk region of our box generates a concentration ∼0.02 M, and we are therefore restricted to higher bulk concentrations. We were however able to approach the ultimate limit of low bulk concentration of the salt by modeling a system with just the number of Na^+ counterions needed to compensate the negative surface charge and no Cl^- in the system. Such a system mimics the effect of added NaOH to pure water, with all the OH^- groups attached to the surface. We admit that this setup is a bit unrealistic, as any Na^+ outside of the interfacial region makes the interfacial charge unbalanced, but it represents successfully the salt solution close to infinite dilution.

EXPERIMENTAL RESULTS

Before describing the results, we briefly summarize some of the important aspects of the AR-SHS model; more details can be found elsewhere.[36,37] In a nonresonant AR-SHS experiment, the fundamental frequency of a laser beam interacts with a liquid dispersion containing particles. In regions where the centrosymmetry of the material is broken—typically at the interface between the particles and the liquid—SH photons at half the wavelength of the fundamental beam will be generated. These photons are then collected as a function of the scattering angle (θ), defined as the angle between the sum of the incoming **k**-vectors of the fundamental beam and the **k**-vector of the scattered SH light. Under nonresonant conditions, the second-order polarization depends on the electron density in the medium,[45] which implies that the SH response is of the same order of magnitude for every noncentrosymmetric molecule in the sample. However, since the SH intensity scales quadratically with the number density, in most cases the majority of the SH signal intensity is due to water molecules at the interface, as the number of noncentrosymmetrically distributed surface groups is much smaller than the number of noncentrosymmetrically distributed water molecules.[26] In an aqueous solution, the nonresonant SHS signal then arises from the net orientational order of water molecules along the surface normal. Two types of interactions will contribute to this orientational order of water: The orientational order induced by electrostatic field interactions, either at the surface or in the bulk (present in the effective third order particle susceptibility, denoted as $\Gamma^{(3)'}$), and the orientational order induced by all other (chemical) interactions confined to the particle surface plane (represented by the second-order particle surface susceptibility $\Gamma^{(2)}$ that contains the surface susceptibility $\chi_S^{(2)}$). A third type of effect could be in principle considered, such as a reactant/product gradient along the surface normal; however, such an effect would be mostly noticeable outside of equilibrium conditions and/or during a chemical reaction, which is outside the scope of the present paper. The scattered intensity of the second harmonic can thus be given as

$$I_{2\omega} \propto \left|\Gamma^{(2)}(R, \chi_S^{(2)}, \theta) + \Gamma^{(3)\prime}(R, \chi^{(3)\prime}, \theta)\Phi_0\right|^2 \tag{1}$$

where is R the particle radius, θ is the scattering angle, and Φ_0 is the surface potential. $\chi^{(3)\prime}$ is the effective third order surface susceptibility, which includes the contributions of the water molecules oriented by the electric field as well as the water bulk susceptibility. The scattered intensity for the two independent polarization combinations PPP and PSS (the first letter refers to the polarization state of the SH beam and the second and third letter refer to that of the fundamental beam; P is parallel to the detector plane[38]) can be expressed as

$$\frac{I_{PPP}(\omega)}{I_{SSS}(\omega)} = \frac{\left(E_P(\omega)^2\left[\cos\left(\frac{\theta}{2}\right)^3(\Gamma_1^{(2)}) + \cos\left(\frac{\theta}{2}\right)(\Gamma_2^{(2)} + \Gamma_2^{(3)\prime})(2\cos(\theta) + 1)\right]\right)^2}{\bar{\mu}^2 N_b/N_p} \tag{2}$$

$$\frac{I_{PSS}(\omega)}{I_{SSS}(\omega)} = \frac{\left(E_S(\omega)^2\left[\cos\left(\frac{\theta}{2}\right)(\Gamma_2^{(2)} + \Gamma_2^{(3)\prime})\right]\right)^2}{\bar{\mu}^2 N_b/N_p} \tag{3}$$

where $\bar{\mu} = \bar{\beta}_{H_2O}^{(2)} E(\omega)^2$, N_p is the density of particles, and N_b is the density of bulk water (3.34×10^{28} molecules/m^3). By definition, $\Gamma^{(3)'}$is directly related to the surface potential Φ_0, and $\chi_S^{(2)}$ contains information about interfacial oriented water, limited to the water molecules that experience an orientational change due to chemical interactions with the silica surface.[37] $\chi_S^{(2)}$ is a tensor element with 81 components, but in the case of a particle interface that can be considered isotropic in the lateral dimensions of the interface, this number reduces to four components, $\chi_{S,1}^{(2)}$, $\chi_{S,2}^{(2)}$, $\chi_{S,3}^{(2)}$, and $\chi_{S,4}^{(2)}$. Assuming nonresonant interactions and an orientationally broad water distribution[46] $\chi_{S,1}^{(2)}$ vanishes and $\chi_{S,2}^{(2)} = \chi_{S,3}^{(2)} = \chi_{S,4}^{(2)}$ (a definition for those terms is provided in Table S1).[37,47] By fitting polarimetric AR-SHS patterns in two different polarization combinations as described by eqs 2 and 3, and knowing the radius of the particle as well as the ionic strength of the solution, unique values for both Φ_0 and $\chi_{S,2}^{(2)}$ can be extracted (see ref 38 for more details). Note that all patterns are normalized with respect to the water SSS pattern, which does not influence the value of $\chi_{S,2}^{(2)}$ or Φ_0, as detailed in the Materials and Methods. This ensures a comparison to other samples and experiments, and it corrects for any change in the experimental geometry (such as small variations in beam alignment or sample position). We also note that the model assumes an exponential

DOI: 10.1021/acs.jpcc.9b05482
J. Phys. Chem. C 2019, 123, 20393−20404

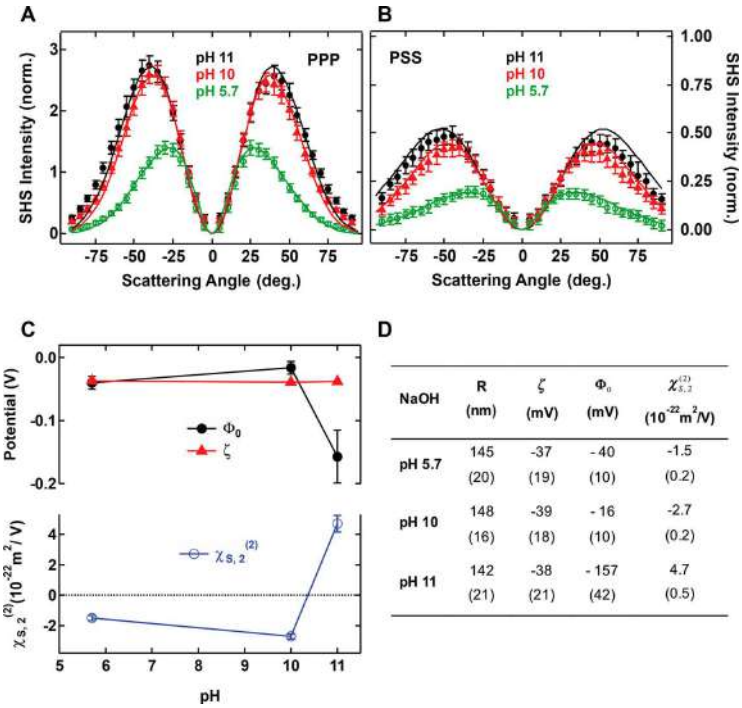

NaOH	R (nm)	ζ (mV)	Φ_0 (mV)	$\chi_{S,2}^{(2)}$ (10^{-22} m^2/V)
pH 5.7	145 (20)	-37 (19)	- 40 (10)	-1.5 (0.2)
pH 10	148 (16)	-39 (18)	- 16 (10)	-2.7 (0.2)
pH 11	142 (21)	-38 (21)	- 157 (42)	4.7 (0.5)

Figure 1. AR-SHS patterns for silica particles in aqueous solution. SH scattering patterns of 300 nm diameter SiO_2 particles as a function of pH in (A) PPP polarization combination and (B) PSS polarization combination. Black plain dots: pH 11. Red plain triangles: pH 10. Green open circles: pH 5.7. pH was adjusted through NaOH addition. The particle density was kept constant for each sample and equal to 3.5×10^{10} particles/mL. All measurements were performed at $T = 23$ °C. All the parameters used for the fits, including ionic concentrations, are summarized in Table S2. Error bars represent the standard deviation from 30 measurements. Solid lines represent the fit to the data points using the AR-SHS model. (C, top) Surface potential Φ_0 and zeta-potential ζ. (C, bottom) Surface susceptibility $\chi_{S,2}^{(2)}$ as a function of pH. The values are extracted from the fit of data of parts A and B, where error bars represent error on the values as estimated from fitting the data ± standard deviation. (D) Table summarizing the radius R, ζ-potential ζ, surface potential Φ_0 and the surface susceptibility $\chi_{S,2}^{(2)}$ for different pH conditions. Numbers in brackets pertain to measurement errors as detailed in the Materials and Methods.

decay in the diffuse double layer,[37] which is a common term for all models.[48] For the convention on the sign of $\chi_{S,2}^{(2)}$, we use the following: Negative for water molecules with O atoms pointing toward the surface (dipole moment pointing away from the surface) and positive for water molecules with H atoms toward the surface (dipole moment pointing toward the surface). This sign convention arises from a comparison to imaginary values obtained from SFG studies.[49]

Parts A and B of Figure 1 show AR-SHS scattering patterns obtained for solutions of 300 nm diameter SiO_2 particles at different pH values. The pH was adjusted through addition of NaOH and no additional salt was added to the solutions. Increasing pH promotes deprotonation of the silanol groups at the surface, leading to a larger negative surface charge density of the SiO_2 particles. The solid lines are fits to eqs 2 and 3, and the values for all experimental parameters used for the fits are summarized in the Supporting Information. The normalized SHS intensity directly relates to the number of oriented water molecules at the interface. Parts A and B of Figure 1 show an increasing normalized SHS intensity with increasing pH. The obtained values of both Φ_0 and $\chi_{S,2}^{(2)}$ from the fits of PPP and PSS patterns are plotted in Figure 1C as a function of pH. Figure 1C also shows ζ-potential values measured by electrophoretic light scattering from the same samples. All values are summarized in Figure 1D for easier comparison. The negative valued ζ-potentials are almost unchanged from pH 5.7 to 11 (~-38 mV). For these particles, the isoelectric point (ζ = 0 mV) is reached at pH = 3, as given by electrokinetic measurements. The surface potential has the same sign as the ζ-potential. However, contrarily to the ζ-potential, the obtained surface potential values vary as a function of pH showing two distinct behaviors: one where the ζ and Φ_0-potentials are very close in magnitude (pH 5.7 and 10) and one where they deviate significantly. This behavior is also shown in the obtained $\chi_{S,2}^{(2)}$ values: pH 11 shows positive values of $\chi_{S,2}^{(2)}$, corresponding to water hydrogen atoms oriented toward the surface, while milder pHs (5.7 and 10) show negative values of $\chi_{S,2}^{(2)}$, corresponding to water hydrogen atoms oriented away from the surface, and oxygen atoms facing the surface.

We also performed similar measurements at constant pH while varying the ionic strength. Parts A and B of Figure 2 show SHS scattering patterns for solutions of 300 nm diameter SiO_2 particles at pH 10, where different amounts of NaCl were added. In this case, the surface charge density is mainly expected to be set by the presence of NaOH and to a minor

DOI: 10.1021/acs.jpcc.9b05482
J. Phys. Chem. C 2019, 123, 20393−20404

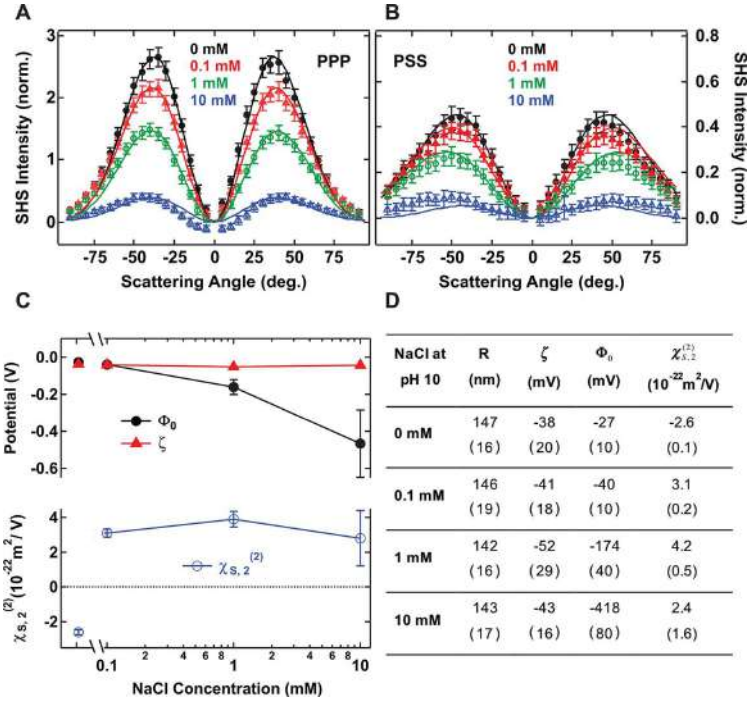

NaCl at pH 10	R (nm)	ζ (mV)	Φ_0 (mV)	$\chi^{(2)}_{S,2}$ (10^{-22} m^2/V)
0 mM	147 (16)	-38 (20)	-27 (10)	-2.6 (0.1)
0.1 mM	146 (19)	-41 (18)	-40 (10)	3.1 (0.2)
1 mM	142 (16)	-52 (29)	-174 (40)	4.2 (0.5)
10 mM	143 (17)	-43 (16)	-418 (80)	2.4 (1.6)

Figure 2. Scattering patterns of 300 nm diameter SiO_2 particles in a pH 10 solution as a function of NaCl concentration in (A) PPP polarization combination and (B) PSS polarization combination. Black plain dots: 0 mM NaCl. Red plain triangles: 0.1 mM NaCl. Green open circles: 1 mM NaCl. Blue open triangles: 10 mM NaCl. pH was adjusted through NaOH addition. The particle density was kept constant for each sample and equal to 3.5×10^{10} particles/ml. All measurements were performed at $T = 23$ °C. All the parameters used for the fits are summarized in Table S3. Error bars represent the standard deviation from 30 measurements. Solid lines represent the fit to the data points using the AR-SHS model. (C, top) Semilog plot of surface potential Φ_0 and ζ-potential ζ. (C, bottom) Surface susceptibility $\chi^{(2)}_{S,2}$ as a function of NaCl concentration for fixed pH = 10. The values are extracted from the fit of data in parts A and B. Error bars represent error on the values as estimated from fitting the data ± standard deviation. (D) Table summarizing the radius R, ζ-potential ζ, surface potential Φ_0, and the surface susceptibility $\chi^{(2)}_{S,2}$ for different salt conditions. Numbers in brackets pertain to measurement errors as detailed in the Materials and Methods.

extent by the additional Na^+ ions, which can facilitate the deprotonation of surface silanol groups through electrostatic screening and stabilization of the SiO^- group.[50] On the basis of values of surface charge densities measured for a fixed pH and different NaCl concentrations,[50] this latter effect can be estimated to ∼10% of the total deprotonation and will depend on the range of salt concentration and the size of the particles, as well as the nature of the cation.[30,51] It can be seen that the normalized SHS intensity decreases with increasing salt concentration, indicative of a decrease in the amount of ordered water molecules around the surface of the SiO_2 particles. Figure 2C shows the obtained fit values for the surface potential and the second-order susceptibility element representative of the molecular orientation of interfacial water. The measured ζ-potential values are also plotted. All values are summarized in Figure 2D. For the two lowest salt concentrations both potentials are similar in magnitude. For 1 and 10 mM NaCl, however, the magnitude of the surface potential becomes much higher than the ζ-potential. Another interesting observation is that the sign of $\chi^{(2)}_{S,2}$ changes when salt is added. In the case where no salt is added at a fixed pH of 10, a negative sign of $\chi^{(2)}_{S,2}$ indicates a situation where water molecules are mostly oriented with their hydrogen atoms away from the surface. With the addition of NaCl, and even for the smallest quantity (0.1 mM), the sign of this parameter is inverted and points to a shift in the water orientation, where the hydrogen atoms are oriented toward the surface.

Simulation Results. Computer simulations provide molecular details of the interface and help the experiment in deciphering the contribution of oriented water molecules at a given distance from the surface to the nonlinear optics signal (i.e., $\chi^{(2)}_{S,2}$ or Φ_0). Because a model of ∼300 nm diameter colloidal SiO_2 is not available, we utilized our model of the flat (101) quartz surface (see Materials and Methods). The flat geometry is well justified by the large size of the colloidal particles, and the terminations by silanol groups are similar in both cases,[52] though more defects must be expected for amorphous and spherical particles. The density of silanol groups for perfect (101) quartz (5.8 OH/nm^2 for neutral surface, 5.1 OH/nm^2 for −0.12 C/m^2 negative surface[40]) is close to the value 4.9 OH/nm^2 reported for amorphous silica.[53]

The signal of each layer is proportional to the "dipole concentration" given by a product of the number density of water molecules, water dipole orientation (the cosine of the angle between the water dipole vector and z-axis with positive

DOI: 10.1021/acs.jpcc.9b05482
J. Phys. Chem. C 2019, 123, 20393−20404

values indicating hydrogens facing the solid surface, i.e. as in the experiment), and the dipole moment of SPC/E water model, which equals 2.35 D (1 D = 3.336 × 10^{-30} Cm). The running integral of the dipole concentration provides an indicator for the buildup of the total SHS intensity. Indeed, the SHS intensity is by definition given as the square of the absolute value (magnitude) of the summed nonlinear second order and third order polarization (emitted at the second harmonic frequency). We then assume that the sum of the dipoles in a certain volume is proportional to the second order and third order polarization (emitted at the second harmonic frequency), and as such the SHS intensity is proportional to the square of the running integral of the dipole concentration.[54] The interfacial plane at z = 0 corresponds to the average position of surface silicon atoms. MD simulations were carried out for surface charge densities 0, −0.03, −0.06, and −0.12 C/m^2. Using surface titration experiments we can link these simulations to pH ∼ 4, 8.5, 9.4, and 10.1, respectively, which allows us to compare simulation and experimental data, though the simulation and experimental conditions cannot be matched exactly due to differences in surface geometry. A simulation of the quartz surface in pure water is also added for comparison.

The results obtained from the molecular dynamics simulations are summarized in Figure 3. The left-hand panels (A, B, C) display effects of changing surface charge density, while the right-hand panels (E, F) display effects of changing the ionic strength at fixed surface charge density. Figure 3A shows the axial density profile of water oxygens, i.e., the laterally averaged density of water as a function of distance from the quartz (101) surface. The axial density of water is nearly independent of the surface charge (shown in Figure 3A) and salt concentration (not shown). The positions of the first two clearly evident water layers are z ∼ 3.5 Å and z ∼ 6 Å, and are invariable. Figure 3B shows the dipole concentration as a function of distance for different surface charge densities. A positive value indicates water molecule with hydrogens facing the surface, while a negative value indicate a reversed molecular orientation with oxygens facing the surface. These features can thus be used to connect to the sign of $\chi^{(2)}_{S,2}$. It can be seen that the curves for low charge density are more negative, while increasing the charge density brings them up to positive values. Figure 3C shows the running integral of the dipole concentration, which reaches a plateau away from the interface, where the average orientation of water molecules is zero (isotropic). This plateau value is an indicator of the total SH intensity and increases with surface charge density. Figure 3E shows the ionic strength dependence of the interfacial dipole orientation for a fixed surface charge density of −0.06 C/m^2, and for the salt concentration range used in the simulations (0.05 to 0.31 M NaCl). The water orientation with hydrogens facing the surface is less pronounced at higher concentrations, leading also to decreasing plateau values of the running integral of the dipole concentration (Figure 3F) with salt concentration.

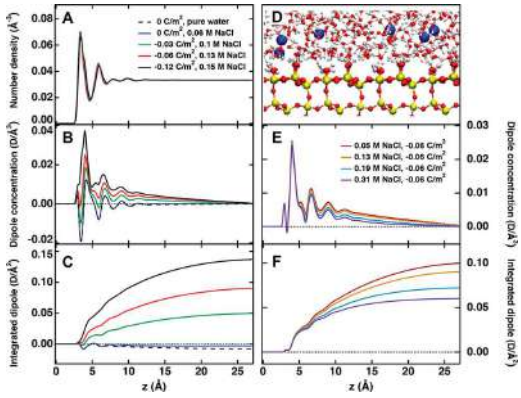

Figure 3. (A) Number density of water, (B) dipole concentration, and (C) integrated dipole as a function of distance z from the quartz (101) surface for different surface charge densities at similar bulk ionic concentration. (D) Snapshot of the quartz (101) surface at 0.34 M and −0.12 C/m^2. (E) Dipole concentration and (F) integrated dipole as a function of distance from the quartz (101) surface for different bulk ionic concentrations at the same surface charge density of −0.06 C/m^2.

DISCUSSION

Surface Potential and Water Orientation under Low Ionic Strength Conditions. In mild pH cases (5.7 and 10) and low ionic strength (<1 mM), the values of the surface potential are very close to the ζ-potential values. Negative values of the ζ-potential are found for colloidal SiO_2 surfaces[50,55,56] as expected from the negative surface charge densities.[10,57,58] As mentioned in the introduction, the slip plane where the ζ-potential is measured is considered to be located in the first few water layers away from the surface plane where the surface potential is measured. Therefore, with both values being very similar, it is highly unlikely that there is any buildup of counterions close to or at the surface. This means there is no charge condensation or Stern layer formed. By charge condensation layer, we refer to a packed layer of ions that is at some distance away from the interface, also known as an outer-sphere complex. We note here the specific case of direct counterion adsorption, also referred to as an inner-sphere complex, which would lead to (partial) surface charge neutralization. This surface charge neutralization effectively decreases the electric field extending in the solution and therefore results in a reduction of the surface potential. However, this effect is expected to be small for small concentrations of counterions in solution.

The negative values of $\chi^{(2)}_{S,2}$ are indicative of a net dipole moment pointing away from the surface, with water molecules mainly oriented with their oxygen atom toward the surface. This water orientation in low ionic strength conditions can be rationalized by considering the hydrogen bonding between the silanol groups and the oxygen atom of water. This is illustrated in Figure 4A.

Having established that there is no significant accumulation of counterions at the interface, for this particular case, the simplest model that describes the relation between surface charge and surface potential is given by the spherical Gouy–Chapman model. Ohshima derived an approximate analytical solution for the potential distribution around a sphere with arbitrary potential,[48] where the surface charge density is related to the surface potential by

DOI: 10.1021/acs.jpcc.9b05482
J. Phys. Chem. C 2019, 123, 20393−20404

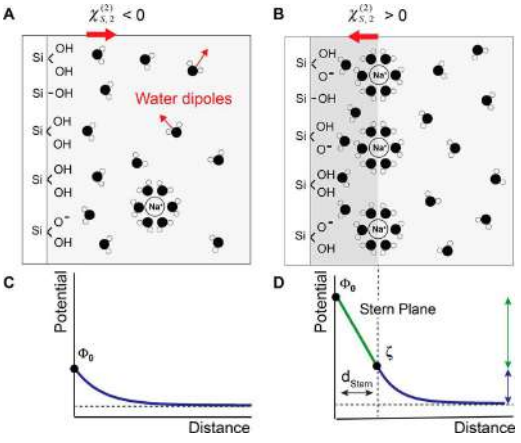

Figure 4. Schematic view of a SiO_2/water interface for (A) Low surface charge density and low Na^+ concentration and (B) High surface charge density and high concentration of Na^+ ions. In both cases the surface keeps a majority of silanol groups protonated and is overall negatively charged. (A) Water molecules are preferably oriented with their oxygen toward the surface. The net water dipole summed over all water molecules is then oriented away from the surface (red arrow). (B) Water molecules are preferably oriented with their hydrogens toward the surface. The net water dipole is oriented toward the surface (red arrow). The potential decay profile in the Gouy−Chapman (C) or Gouy−Chapman−Stern models (D). In the first case, the ionic strength in solution is low and the surface potential decays exponentially with distance. At higher ionic strengths, the GCS approximation is considered, where the potential decay profile integrates two components: a steep decay associated with the strong electric field in the charge condensation layer, known in the model as the Stern layer, and a more gradual one at larger distances from the interface. We approximate here the potential at the Stern plane to be equal to the ζ-potential.

$$\sigma_0^{GC} = \frac{2\varepsilon_r\varepsilon_0\kappa k_B T}{e}\sinh\left(\frac{ze\Phi_0}{2k_BT}\right) \times\left[1+\frac{1}{\kappa R}\frac{2}{\cosh(ze\Phi_0/4k_BT)^2} + \frac{1}{(\kappa R)^2}\frac{8\ln[\cosh(ze\Phi_0/4k_BT)]}{\sinh(ze\Phi_0/2k_BT)^2}\right]^{1/2} \quad (4)$$

where σ_0^{GC} is the surface charge density in the spherical Gouy−Chapman model, R the particle radius, ε_r the relative permittivity of the solvent (water), ε_0 the permittivity of vacuum, κ the Debye parameter, e the elementary electric charge, z the valence of ions, k_B the Boltzmann constant, and T the temperature. Knowing Φ_0, we can compute σ_0^{GC}, and the expected degree of deprotonation. Table 1 shows the values for σ_0^{GC} as a function of pH and NaCl concentration, as well as the corresponding percentage of surface deprotonation.

Table 1 shows that the surface charge densities for the low ionic strength regime range from −0.35 to +1.63 mC/m^2, which correspond approximately to 0.04−0.2% deprotonation, assuming a silanol density of 4.9 OH/nm^2 as reported by Zhuravlev,[53] who showed that this value is a constant for a fully hydroxylated amorphous surface and does not depend on the type of silica. These surface charge densities values are in the range of reported values in the literature for salt free and low salt dispersions[59,60] and agree with the notion that the majority of the silanol groups remain protonated.[61,62] Thus, in mild pH conditions and low ionic strength, only a very small fraction of the silanol groups are deprotonated, and the dominant orientation of water dipoles in the first layer away from the surface is due to hydrogen bonding between the protonated silanol groups and the oxygen atoms of water.

Surface Potential and Water Orientation in Higher Ionic Strength Conditions. In higher pH conditions (pH 11) and with increasing amounts of NaCl (≥1 mM), we observe a much higher magnitude for the surface potential than the ζ-potential. The distance between the slip plane and the surface plane is 1−3 water molecules.[12] The differences $\|\Phi_0 - \zeta\|$ of 119 mV (pH 11), 122 mV (1 mM NaCl), and 375 mV (10 mM NaCl) means that the electrostatic field in this thin layer must be on the order of 10^8−10^9 V/m. This large electrostatic field indicates the presence of a condensed layer of charges.[12]

This hypothesis is further supported by the fact that higher values of surface potential are found for both pH 11 and for pH 10 + 1 mM NaCl and above, which correspond to a similar concentration of sodium ions (respectively 1 mM and 1.1 mM Na^+). Such a charge condensation layer of positive counterions close to the negative surface influences water orientation. Positive values of $\chi^{(2)}_{S,2}$ here indicate a net dipole moment with the hydrogens pointing toward the surface, thus effectively interpreted as a net flip in the surface water orientation with respect to the low ionic strength situation (Figures 1C and 2C). This flip in water orientation is illustrated in Figure 4B and arises from the formation of a charge condensation layer composed of hydrated sodium ions. As the hydration shells of the Na^+ ions overlap with the surface hydration layer, the Na^+ ions disrupt the hydrogen bonding between the silanol groups and the water molecules and a water layer with a net dipole moment facing the surface results.

Having determined experimentally that here we are dealing with a Stern layer, we can compute the charge density on the slip plane, σ_d, assuming that the slip plane and the outer Stern layer coincide, using eq 4 and replacing Φ_0 by ζ and σ_0^{GC} by σ_d. Values for σ_d are shown in Table 2. Approximating the surface of the particle and the Stern layer as two plates of a spherical capacitor, it is also possible to use the equation describing a spherical capacitor to relate the potential drop in the Stern layer ($\Phi^{GCS}_{drop} = \Phi_0 - \zeta$) to the surface charge density at the surface, σ_0^{GCS}:

$$\Phi^{GCS}_{drop} = \frac{\sigma_0^{GCS}R^2}{\varepsilon_{SW}\varepsilon_0}\left(\frac{1}{R} - \frac{1}{R + d_{Stern}}\right) \quad (5)$$

Table 1. σ_0^{GC} and Percentage of Deprotonation as a Function of pH and Salt Concentration

NaOH	σ_0^{GC} (mC/m^2)	% deprotonation	[NaCl], pH = 10 (mM)	σ_0^{GC} (mC/m^2)	% deprotonation
pH 5.7	−0.35	0.04	0	−0.77	0.10
pH 10	−0.45	0.06	0.1	−1.63	0.21

DOI: 10.1021/acs.jpcc.9b05482
J. Phys. Chem. C 2019, 123, 20393−20404

Table 2. Table Showing σ_d, σ_0^{GCS} and % Deprotonation as a Function of pH and Salt Concentration

NaOH	σ_d (mC/m^2)	σ_0^{GCS} (mC/m^2)		% deprot.
pH 11	−3.2	d_{Stern}= 0.3 nm	−151	19.2
		d_{Stern}= 0.9 nm	−50.3	6.4
[NaCl], pH = 10	σ_d (mC/m^2)	σ_0^{GCS} (mC/m^2)		% deprot.
1 mM	−5.0	d_{Stern} = 0.3 nm	−155	19.7
		d_{Stern} = 0.9 nm	−51.6	6.6
10 mM	−11.5	d_{Stern} = 0.3 nm	−476	60.6
		d_{Stern} = 0.9 nm	−159	20.2

where σ_0^{GCS} is the surface charge density in the presence of a charge condensation layer, R is the radius of the particle, ε_0 is the vacuum permittivity, and d_{Stern} is the thickness of the capacitor. Contrary to the GC case, which assumes the permittivity of bulk water because of the small electric fields generated at the interface, in the GCS case the higher electric fields will orient the water dipoles and therefore change the dielectric constant of the first few layers adjacent to the interface. Therefore, we use here ε_{SW} as the dielectric constant at the silica/water interface (ε_{SW} = 43).[63] Assuming a Stern layer thickness range of 0.3 < d_{Stern} < 0.9 nm (between one and three water molecules) one obtains a range of values for σ_0^{GCS}, summarized in Table 2.

Table 2 shows that the computed surface charge densities range from −50 to −476 mC/m^2 depending on the choice of the Stern layer thickness. These values correspond to deprotonation degrees between 6 and 61%. While the deprotonation value for [NaCl] = 10 mM seems high for d_{Stern} = 0.3 nm (maximum 25% deprotonation is expected at pH 10 and 0.1 M NaCl),[50] all the other results are comparable to surface charge densities that have been measured by potentiometric titrations for SiO_2 particles in similar conditions,[10,35,57,64] keeping in mind that these values are strongly size-dependent below 30 nm diameter.[65,66] Interestingly, one can see that surface charge densities in both pH 11 case and the 1 mM NaCl case at pH 10 are very similar, which is a direct result of the similar surface potential values obtained by AR-SHS (Figures 1C,D and 2C,D). Considering nearly the same concentrations of ions at these two conditions (1 mM Na^+,OH^- at pH 11 vs 0.1 mM of Na^+,OH^- + 1 mM Na^+,Cl^- at pH 10), this indicates that the ionic strength and the interfacial presence of Na^+ ions, is here the main element in setting the magnitude of the surface potential.

While both base and salt treatment show a similar increase in the surface potential value, similar surface charge densities for a given value of d_{Stern} and similar orientation of the surface water molecules indicating the presence of a charge condensation layer, the SH intensity change as a function of the ionic strength does show some differences, which has implications on the thickness of this charge condensation layer. In the case of the basic treatment, the surface charge becomes increasingly more negative with increasing NaOH addition. This higher surface charge density is then compensated by screening by the Na^+ cations, which additionally participate in orienting the water molecules with their hydrogens facing the surface (Figure 4B). For a higher surface charge density, we can thus expect a larger number of water molecules to be oriented with their hydrogen facing the surface to counterbalance for the presence of deprotonated silanols. The increase in SH signal intensity as a function of pH (Figure 1A,B) thus reflects the electric-field induced polarization of the water molecules at the interface as previously described for flat surfaces.[25,67] In the case of salt addition at fixed pH, we observe a decrease in SH intensity (Figure 2A,B) that physically corresponds to a decrease in the number of the oriented water molecules. Such a decrease in ordered water is then indicative of more efficient screening of the surface charge by more concentrated salt solution and shrinking of the diffuse layer. This decrease in the amount of ordered water is already visible between 0 mM NaCl at pH 10 and 0.1 mM NaCl at pH 10, while it is not noticeable between pH 10 and 11 when no salt is added. This indicates that the thickness of the charge condensation layer will be dependent on the nature of the added compound (NaOH/NaCl), most likely because of modifications of the surface charge density. Additional information that can be extracted from the AR-SHS plots is the relative variation of the thickness of the charge condensation layer and of the surface charge density. From eq 5, a decrease in the thickness would directly result in a decrease of the magnitude of the surface potential. However, since we observe an effective increase in magnitude of surface potential with increasing salt concentration, this implies that, in this range of salt concentrations, the increase in magnitude of surface charge density must be larger than the decrease in the charge condensation thickness. Note that at higher salt concentration (>10 mM), the opposite behavior has been observed:[50] While the surface charge density still increases with increasing salt concentration, the decrease in the thickness of the charge condensation layer overall dominates, thus resulting in a decrease of the surface potential with increasing salt concentration. In our case, due to the limited range of stability of our colloidal suspensions, we could not explore salt concentration ranges above 10 mM. It is also important to note that Brown et al.[50] use particles below 10 nm diameter, and as the surface charge density is strongly size-dependent for particles below 30 nm diameter,[65,66] we can expect a different relative variation of the surface charge density and the charge condensation layer thickness for different sizes of particles, which could imply a different dependence of the surface potential on the salt concentration. Further measurements are thus needed to test the size dependence of the surface potential at various ionic strengths. Similarly, the surface charge density as well as the pK_a of different silanol groups is expected to change depending on the preparation of the surface prior to the experiment,[25,61,68] which could be additional factors playing a role in the observed trends for the surface potential.

One last observation that can be made on the basis of the AR-SHS results is that the transition between the low ionic strength regime, where $\|\Phi_0\| \approx \|\zeta\|$ and the high ionic strength regime, where $\|\Phi_0\| \gg \|\zeta\|$, occurs for electrolyte concentrations between 10^{-4} and 10^{-3} M, while it is generally considered for flat surfaces (as for example metal electrodes) that the GC model can be used up to electrolyte concentrations of 10^{-3}–10^{-2} M.[12,69,70]

Comparison of AR-SHS Experiment and MD Simulation. We turn now to the discussion of the results obtained through simulations. Despite the fact that simulation results for one selected crystal face of quartz surface are used when comparing to experimental data of spherical silica nanoparticles, the trends observed in simulations are in line with experimental findings. The lowest charge densities and salt concentrations studied experimentally are not reachable with the MD simulations (see Materials and Methods for details), but we still can discuss the experimental trends in the presence

DOI: 10.1021/acs.jpcc.9b05482
J. Phys. Chem. C 2019, 123, 20393−20404

of only NaOH or for very small salt concentrations with the help of the molecular picture of this model interface. Figure 3A shows that there is interface induced water layering as witnessed by the two peaks at ∼3.5 and 6 Å. The orientational first peak in Figure 3B can be easily connected to $\chi^{(2)}_{S,2}$, as by definition $\chi^{(2)}_{S,2}$ contains the orientational order induced by all chemical interactions confined to the particle surface plane. The first peak in Figure 3B for surface charge densities $\sigma = 0$ and -0.03 C/m^2 is negative, in agreement with negative $\chi^{(2)}_{S,2}$ observed experimentally at pH 5.7. The negative signal at low pH is further supported by simulations of neutral quartz surface ($\sigma = 0$ C/m^2), where even the integrated dipole is very slightly negative, both for 0.06 M NaCl solution (represented by only 4 ion pairs in the simulated system) and even more for pure water (which is the limiting case of low salt concentration for neutral surfaces). The first peak for $\sigma = -0.06$ C/m^2 is close to zero and does not predict the negative $\chi^{(2)}_{S,2}$ seen experimentally at pH 10 in absence of salt, but the concentration dependence of the second peak easily explains the positive $\chi^{(2)}_{S,2}$ at larger concentrations. Finally, based on the positive first peak at $\sigma = -0.12$ C/m^2, we predict that at very high pH values, even in the absence of salt, $\chi^{(2)}_{S,2}$ should be positive, in agreement with Figure 1C for pH 11. Figure 3C also agrees with the measured SH intensity shown in Figure 1A,B, where increasing pH (and thus more negative surface charge density) leads to an increase in the total SH intensity, indicative of a larger number of overall oriented molecules.

Parts E and F of Figure 3 capture, as much as possible using our MD setup, the experimental drop in overall SHS intensity with salt concentration (Figure 2A,B), indicative of more efficient charge screening and less overall oriented water. Figure 3E shows that for higher charge densities (pH) the magnitude and sign of the first peak for a given pH is insensitive to the salt concentration. The second peak (∼6 Å) and the water orientation further out displays however a decreasing magnitude with increasing salt concentration. This behavior is also shown in the curves in Figure 3F, which overlap in the first peak but start to deviate at the second peak and gain less signal at distances of ∼6−20 Å for higher salt concentrations. In this high concentration range (>10 mM), the weakening of the orientation with hydrogens facing the solid with increase in concentration also agrees with the drop in susceptibility measured experimentally from 1 to 10 mM (see Figure 2C,D). These effects were observed for all simulated ionic concentrations and surface charge densities.

Simulations evidence Na^+ (a strong sorbent) adsorbing as an inner-sphere complex at height ∼3.5 Å, i.e., in the location of the first water layer, and also as outer-sphere complex at distances around 5.5 Å, i.e., close to the position of the second water layer (not shown). With increasing pH and salt concentration, the surface attains more negative charge. While less negative surface charge can be easily compensated by a few Na^+ ions, at more negative surfaces the compensation of the surface charge is partly hindered by repulsion among numerous adsorbed Na^+ ions, leading to formation of the condensed layer further from the surface and more negative surface potential, as deduced from the SHS data.

CONCLUSIONS

Nonlinear light scattering theory can be used to derive expressions for surface potential of colloidal suspensions Φ_0 and interfacial water ordering in terms of the second-order susceptibility $\chi^{(2)}_{S,2}$. This system of two variables can be solved by nonresonant polarimetric AR-SHS measurements in two different polarization combinations. Φ_0 and $\chi^{(2)}_{S,2}$ are obtained from analytical expressions and therefore do not assume any model for the distribution of ions at the interface. In this work, we report AR-SHS patterns for 300 nm diameter SiO_2 colloidal suspensions as a function of pH and NaCl concentration, and we support these data by MD simulations of the crystal quartz (101) surface interacting with aqueous solutions. By combining the knowledge of the parameters $\chi^{(2)}_{S,2}$ and Φ_0 with ζ, which is obtained through electrokinetic measurements, we are able to establish a description of the interface that does not rely on a specific model for the charge distribution at the interface. Between pH values close to neutral and 10, as well as at low salt concentration (<1 mM), our data indicate the presence of a diffuse double layer where the surface potential is very close to the ζ-potential, and where the most favorable orientation for the interfacial water molecules is the one with the oxygen atom facing the silanol terminated surface. At higher pH or ionic strength (pH 11 or ≥1 mM salt), we observe an increase in surface potential, while the ζ-potential changes very little, indicative of the formation of a charge condensation layer. Furthermore, values of $\chi^{(2)}_{S,2}$ indicate that interfacial water adjusts its orientation following counterion adsorption, in this case favoring hydrogen atoms facing the surface. Surface charge densities estimated through the GC or GCS model using the measured surface potential values agree with reported values in the literature. This validates our experimental approach where the surface potential values can be extracted without assuming any model for the structure of the electrical double layer. The experimental trends are nicely supported by molecular simulations, which observe that the orientation of interfacial water increases with pH and decreases with NaCl concentration, in accord with the intensity of the AR-SHS signal. The flipping of the dipolar orientation of water molecules closest the surface from orientations away from the surface (prevailing orientation due to termination of the surface by protonated silanols) at low pH to orientation toward the surface at high pH (induced by negative surface charge and the presence of Na^+ counterions), can be directly linked to the trends observed for the pH dependence of the surface susceptibility.

ASSOCIATED CONTENT

Supporting Information

The Supporting Information is available free of charge on the ACS Publications website at DOI: 10.1021/acs.jpcc.9b05482.

Table of the shorthand notation for independent tensor components and tables of parameters used for the surface potential fittings (PDF)

AUTHOR INFORMATION

Corresponding Author

*(S.R.) E-mail: sylvie.roke@epfl.ch.

ORCID

Arianna Marchioro: 0000-0002-5838-8517
Denys Biriukov: 0000-0003-1007-2203
Milan Předota: 0000-0003-3902-0992
Sylvie Roke: 0000-0002-6062-7871

Notes

The authors declare no competing financial interest.

DOI: 10.1021/acs.jpcc.9b05482
J. Phys. Chem. C 2019, 123, 20393−20404

■ ACKNOWLEDGMENTS

This work was supported by the Julia Jacobi Foundation, and the Swiss National Science Foundation (Ambizione Grant Number PZ00P2_174146). D.B. and M.P. were supported by the Czech Science Foundation, project 17-10734S. Computational resources were provided by the CESNET LM2015042 and the CERIT Scientific Cloud LM2015085 projects. A.M. thanks Dr. Halil Okur for helpful discussions and M.P. thanks Prof. Moira Ridley for her surface titration data. The authors also thank the anonymous reviewers for stimulating comments.

■ REFERENCES

(1) *Colloidal Silica: Fundamentals and Applications*; Bergna, H. E., Roberts, W. O., Eds.; CRC Press, Boca Raton, 2005.
(2) Bard, A. J.; Faulkner, L. R.; *Electrochemical Methods: Fundamentals and Applications*; Wiley, New York, 2000.
(3) Hunter, R. J. *Foundations of Colloid Science*; Oxford University Press: New York, 2004.
(4) *Fundamentals of Interface and Colloid Science*; Lyklema, J., Ed.; Academic Press: London, 2005; Vol. 5.
(5) Liu, S. H. Microscopically Inhomogeneous Nature of the Stern Layer. *J. Electroanal. Chem. Interfacial Electrochem.* **1983**, *150*, 305−313.
(6) Halley, J. W.; Price, D. Quantum Theory of the Double Layer: Model Including Solvent Structure. *Phys. Rev. B: Condens. Matter Mater. Phys.* **1987**, *35* (17), 9095−9102.
(7) Weaver, M. J.; Wasileski, S. A. Influence of Double-Layer Solvation on Local Versus Macroscopic Surface Potentials on Ordered Platinum-Group Metals as Sensed by the Vibrational Stark Effect. *Langmuir* **2001**, *17* (10), 3039−3043.
(8) Wen, Y.-C.; Zha, S.; Liu, X.; Yang, S.; Guo, P.; Shi, G.; Fang, H.; Shen, Y. R.; Tian, C. Unveiling Microscopic Structures of Charged Water Interfaces by Surface-Specific Vibrational Spectroscopy. *Phys. Rev. Lett.* **2016**, *116* (1), 016101−016105.
(9) Lovering, K. A.; Bertram, A. K.; Chou, K. C. New Information on the Ion-Identity-Dependent Structure of Stern Layer Revealed by Sum Frequency Generation Vibrational Spectroscopy. *J. Phys. Chem. C* **2016**, *120* (32), 18099−18104.
(10) Kobayashi, M.; Juillerat, F.; Galletto, P.; Bowen, P.; Borkovec, M. Aggregation and Charging of Colloidal Silica Particles: Effect of Particle Size. *Langmuir* **2005**, *21* (13), 5761−5769.
(11) Hiemenz, P. C.; Rajagopalan, R. *Principles of Colloid and Surface Chemistry*; Marcel Dekker: New York, 1997.
(12) Hunter, R. J. *Zeta Potential in Colloid Science*; Academic Press: London, 1981.
(13) Lyklema, J. Molecular Interpretation of Electrokinetic Potentials. *Curr. Opin. Colloid Interface Sci.* **2010**, *15* (3), 125−130.
(14) Předota, M.; Machesky, M. L.; Wesolowski, D. J. Molecular Origins of the Zeta Potential. *Langmuir* **2016**, *32* (40), 10189−10198.
(15) Brkljača, Z.; Namjesnik, D.; Lützenkirchen, J.; Předota, M.; Preočanin, T. Quartz/Aqueous Electrolyte Solution Interface: Molecular Dynamic Simulation and Interfacial Potential Measurements. *J. Phys. Chem. C* **2018**, *122*, 24025−24036.
(16) Scales, P. J.; Grieser, F.; Healy, T. W.; White, L. R.; Chan, D. Y. C. Electrokinetics of the Silica-Solution Interface: a Flat Plate Streaming Potential Study. *Langmuir* **1992**, *8* (3), 965−974.
(17) Jena, K. C.; Hore, D. K. Variation of Ionic Strength Reveals the Interfacial Water Structure at a Charged Mineral Surface. *J. Phys. Chem. C* **2009**, *113* (34), 15364−15372.
(18) Campen, R. K.; Pymer, A. K.; Nihonyanagi, S.; Borguet, E. Linking Surface Potential and Deprotonation in Nanoporous Silica: Second Harmonic Generation and Acid/Base Titration. *J. Phys. Chem. C* **2010**, *114* (43), 18465−18473.
(19) Flores, S. C.; Kherb, J.; Konelick, N.; Chen, X.; Cremer, P. S. The Effects of Hofmeister Cations at Negatively Charged Hydrophilic Surfaces. *J. Phys. Chem. C* **2012**, *116* (9), 5730−5734.
(20) Dewan, S.; Yeganeh, M. S.; Borguet, E. Experimental Correlation Between Interfacial Water Structure and Mineral Reactivity. *J. Phys. Chem. Lett.* **2013**, *4* (11), 1977−1982.
(21) Covert, P. A.; Jena, K. C.; Hore, D. K. Throwing Salt Into the Mix: Altering Interfacial Water Structure by Electrolyte Addition. *J. Phys. Chem. Lett.* **2014**, *5* (1), 143−148.
(22) Darlington, A. M.; Jarisz, T. A.; DeWalt-Kerian, E. L.; Roy, S.; Kim, S.; Azam, M. S.; Hore, D. K.; Gibbs, J. M. Separating the pH-Dependent Behavior of Water in the Stern and Diffuse Layers with Varying Salt Concentration. *J. Phys. Chem. C* **2017**, *121* (37), 20229−20241.
(23) DeWalt-Kerian, E. L.; Kim, S.; Azam, M. S.; Zeng, H.; Liu, Q.; Gibbs, J. M. pH-Dependent Inversion of Hofmeister Trends in the Water Structure of the Electrical Double Layer. *J. Phys. Chem. Lett.* **2017**, *8* (13), 2855−2861.
(24) Boamah, M. D.; Ohno, P. E.; Geiger, F. M.; Eisenthal, K. B. Relative Permittivity in the Electrical Double Layer From Nonlinear Optics. *J. Chem. Phys.* **2018**, *148* (22), 222808−222808.
(25) Ong, S.; Zhao, X.; Eisenthal, K. B. Polarization of Water Molecules at a Charged Interface: Second Harmonic Studies of the Silica/Water Interface. *Chem. Phys. Lett.* **1992**, *191* (3−4), 327−335.
(26) Zhao, X.; Ong, S.; Eisenthal, K. B. Polarization of Water Molecules at a Charged Interface. Second Harmonic Studies of Charged Monolayers at the Air/Water Interface. *Chem. Phys. Lett.* **1993**, *202* (6), 513−520.
(27) Zhao, X.; Ong, S.; Wang, H.; Eisenthal, K. B. New Method for Determination of Surface pKa Using Second Harmonic Generation. *Chem. Phys. Lett.* **1993**, *214* (2), 203−207.
(28) Geiger, F. M. Second Harmonic Generation, Sum Frequency Generation, and X (3): Dissecting Environmental Interfaces with a Nonlinear Optical Swiss Army Knife. *Annu. Rev. Phys. Chem.* **2009**, *60* (1), 61−83.
(29) Malin, J. N.; Holland, J. G.; Geiger, F. M. Free Energy Relationships in the Electric Double Layer and Alkali Earth Speciation at the Fused Silica/Water Interface. *J. Phys. Chem. C* **2009**, *113* (41), 17795−17802.
(30) Azam, M. S.; Darlington, A.; Gibbs-Davis, J. M. The Influence of Concentration on Specific Ion Effects at the Silica/Water Interface. *J. Phys.: Condens. Matter* **2014**, *26* (24), 244107−244111.
(31) Yan, E. C. Y.; Liu, Y.; Eisenthal, K. B. New Method for Determination of Surface Potential of Microscopic Particles by Second Harmonic Generation. *J. Phys. Chem. B* **1998**, *102*, 6331.
(32) Favaro, M.; Jeong, B.; Ross, P. N.; Yano, J.; Hussain, Z.; Liu, Z.; Crumlin, E. J. Unravelling the Electrochemical Double Layer by Direct Probing of the Solid/Liquid Interface. *Nat. Commun.* **2016**, *7* (1), 12695.
(33) Brown, M. A.; Jordan, I.; Redondo, A. B.; Kleibert, A.; Wörner, H. J.; van Bokhoven, J. A. In Situ Photoelectron Spectroscopy at the Liquid/Nanoparticle Interface. *Surf. Sci.* **2013**, *610* (C), 1−6.
(34) Brown, M. A.; Beloqui Redondo, A.; Sterrer, M.; Winter, B.; Pacchioni, G.; Abbas, Z.; van Bokhoven, J. A. Measure of Surface Potential at the Aqueous−Oxide Nanoparticle Interface by XPS From a Liquid Microjet. *Nano Lett.* **2013**, *13* (11), 5403−5407.
(35) Brown, M. A.; Abbas, Z.; Kleibert, A.; Green, R. G.; Goel, A.; May, S.; Squires, T. M. Determination of Surface Potential and Electrical Double-Layer Structure at the Aqueous Electrolyte-Nanoparticle Interface. *Phys. Rev. X* **2016**, *6* (1), 011007−011012.
(36) de Beer, A. G. F.; Campen, R. K.; Roke, S. Separating Surface Structure and Surface Charge with Second-Harmonic and Sum-Frequency Scattering. *Phys. Rev. B: Condens. Matter Mater. Phys.* **2010**, *82* (23), 235431−235439.
(37) Gonella, G.; Lütgebaucks, C.; de Beer, A. G. F.; Roke, S. Second Harmonic and Sum-Frequency Generation From Aqueous Interfaces Is Modulated by Interference. *J. Phys. Chem. C* **2016**, *120* (17), 9165−9173.
(38) Lütgebaucks, C.; Gonella, G.; Roke, S. Optical Label-Free and Model-Free Probe of the Surface Potential of Nanoscale and Microscopic Objects in Aqueous Solution. *Phys. Rev. B: Condens. Matter Mater. Phys.* **2016**, *94* (19), 195410.

DOI: 10.1021/acs.jpcc.9b05482
J. Phys. Chem. C 2019, 123, 20393−20404

(39) Lütgebaucks, C.; Macias-Romero, C.; Roke, S. Characterization of the Interface of Binary Mixed DOPC:DOPS Liposomes in Water: the Impact of Charge Condensation. *J. Chem. Phys.* **2017**, *146* (4), 044701−044708.
(40) Kroutil, O.; Chval, Z.; Skelton, A. A.; Předota, M. Computer Simulations of Quartz (101)−Water Interface Over a Range of pH Values. *J. Phys. Chem. C* **2015**, *119* (17), 9274−9286.
(41) Leontyev, I.; Stuchebrukhov, A. Accounting for Electronic Polarization in Non-Polarizable Force Fields. *Phys. Chem. Chem. Phys.* **2011**, *13* (7), 2613−2626.
(42) Biriukov, D.; Kroutil, O.; Předota, M. Modeling of Solid−Liquid Interfaces Using Scaled Charges: Rutile (110) Surfaces. *Phys. Chem. Chem. Phys.* **2018**, *20*, 23954−23966.
(43) Kohagen, M.; Mason, P. E.; Jungwirth, P. Accounting for Electronic Polarization Effects in Aqueous Sodium Chloride via Molecular Dynamics Aided by Neutron Scattering. *J. Phys. Chem. B* **2016**, *120*, 1454−1469.
(44) Berendsen, H.; Grigera, J. R.; Straatsma, T. P. The Missing Term in Effective Pair Potentials. *J. Phys. Chem.* **1987**, *91*, 6269−6271.
(45) Boyd, R. W. *Nonlinear Opt.* **2008**, 1−619.
(46) de Beer, A. G. F.; Roke, S. What Interactions Can Distort the Orientational Distribution of Interfacial Water Molecules as Probed by Second Harmonic and Sum Frequency Generation? *J. Chem. Phys.* **2016**, *145* (4), 044705−044707.
(47) de Beer, A. G. F.; Roke, S. Nonlinear Mie Theory for Second-Harmonic and Sum-Frequency Scattering. *Phys. Rev. B: Condens. Matter Mater. Phys.* **2009**, *79* (15), 155420−155429.
(48) Ohshima, H. *Theory of Colloid and Interfacial Electric Phenomena*; Elsevier, **2006**; pp 1−491.
(49) Nihonyanagi, S.; Yamaguchi, S.; Tahara, T. Direct Evidence for Orientational Flip-Flop of Water Molecules at Charged Interfaces: a Heterodyne-Detected Vibrational Sum Frequency Generation Study. *J. Chem. Phys.* **2009**, *130* (20), 204704.
(50) Brown, M. A.; Goel, A.; Abbas, Z. Effect of Electrolyte Concentration on the Stern Layer Thickness at a Charged Interface. *Angew. Chem., Int. Ed.* **2016**, *55* (11), 3790−3794.
(51) Abbas, Z.; Labbez, C.; Nordholm, S.; Ahlberg, E. Size-Dependent Surface Charging of Nanoparticles. *J. Phys. Chem. C* **2008**, *112* (15), 5715−5723.
(52) Hassanali, A. A.; Singer, S. J. Model for the Water−Amorphous Silica Interface: the Undissociated Surface. *J. Phys. Chem. B* **2007**, *111* (38), 11181−11193.
(53) Zhuravlev, L. T. Concentration of Hydroxyl Groups on the Surface of Amorphous Silicas. *Langmuir* **1987**, *3* (3), 316−318.
(54) Roke, S.; Gonella, G. Nonlinear Light Scattering and Spectroscopy of Particles and Droplets in Liquids. *Annu. Rev. Phys. Chem.* **2012**, *63* (1), 353−378.
(55) Kosmulski, M. Positive Electrokinetic Charge of Silica in the Presence of Chlorides. *J. Colloid Interface Sci.* **1998**, *208*, 543−545.
(56) Leroy, P.; Devau, N.; Revil, A.; Bizi, M. Influence of Surface Conductivity on the Apparent Zeta Potential of Amorphous Silica Nanoparticles. *J. Colloid Interface Sci.* **2013**, *410* (C), 81−93.
(57) Bolt, G. H. Determination of the Charge Density of Silica Sols. *J. Phys. Chem.* **1957**, *61* (9), 1166−1169.
(58) Behrens, S. H.; Grier, D. G. The Charge of Glass and Silica Surfaces. *J. Chem. Phys.* **2001**, *115* (14), 6716−6721.
(59) Yamanaka, J.; Hayashi, Y.; Ise, N.; Yamaguchi, T. Control of the Surface Charge Density of Colloidal Silica by Sodium Hydroxide in Salt-Free and Low-Salt Dispersions. *Phys. Rev. E: Stat. Phys., Plasmas, Fluids, Relat. Interdiscip. Top.* **1997**, *55* (3), 3028−3036.
(60) Dunstan, D. E. Temperature Dependence of the Electrokinetic Properties of Two Disparate Surfaces. *J. Colloid Interface Sci.* **1994**, *166*, 472−475.
(61) Darlington, A. M.; Gibbs-Davis, J. M. Bimodal or Trimodal? the Influence of Starting pH on Site Identity and Distribution at the Low Salt Aqueous/Silica Interface. *J. Phys. Chem. C* **2015**, *119* (29), 16560−16567.
(62) Brown, M. A.; Bossa, G. V.; May, S. Emergence of a Stern Layer From the Incorporation of Hydration Interactions Into the Gouy−Chapman Model of the Electrical Double Layer. *Langmuir* **2015**, *31* (42), 11477−11483.
(63) Sverjensky, D. A. Prediction of Surface Charge on Oxides in Salt Solutions: Revisions for 1:1 (M+L−) Electrolytes. *Geochim. Cosmochim. Acta* **2005**, *69* (2), 225−257.
(64) Sonnefeld, J. Determination of Surface Charge Density Constants for Spherical Silica Particles Using a Linear Transformation. *J. Colloid Interface Sci.* **1996**, *183*, 597−599.
(65) Barisik, M.; Atalay, S.; Beskok, A.; Qian, S. Size Dependent Surface Charge Properties of Silica Nanoparticles. *J. Phys. Chem. C* **2014**, *118* (4), 1836−1842.
(66) Shi, Y.-R.; Ye, M.-P.; Du, L.-C.; Weng, Y.-X. Experimental Determination of Particle Size-Dependent Surface Charge Density for Silica Nanospheres. *J. Phys. Chem. C* **2018**, *122* (41), 23764−23771.
(67) Vance, F. W.; Lemon, B. I.; Ekhoff, J. A.; Hupp, J. T. Interrogation of Nanoscale Silicon Dioxide/Water Interfaces via Hyper-Rayleigh Scattering. *J. Phys. Chem. B* **1998**, *102* (11), 1845−1848.
(68) Sulpizi, M.; Gaigeot, M.-P.; Sprik, M. The Silica−Water Interface: How the Silanols Determine the Surface Acidity and Modulate the Water Properties. *J. Chem. Theory Comput.* **2012**, *8* (3), 1037−1047.
(69) Schmickler, W., Santos, E. *Interfacial Electrochemistry*; Springer: New York, 2010.
(70) Gongadze, E.; Petersen, S.; Beck, U.; van Rienen, U.; Classical Models of the Interface Between an Electrode and an Electrolyte. *Proceedings of the COMSOL conference*; Milan, Italy, 2009.

DOI: 10.1021/acs.jpcc.9b05482
J. Phys. Chem. C 2019, 123, 20393−20404

Article DB5

Biriukov, D.; Fibich, P.; Předota, M.

Zeta Potential Determination from Molecular Simulations

Journal of Physical Chemistry C **2020**, 124 (4), 3159–3170;
IF (2018) = 4.309

Participation of Denys Biriukov:

DB integrated the method of prediction the zeta potential from nonequilibrium molecular dynamics simulations into LAMMPS software, prepared all the computational models, performed all the molecular simulations, analyzed the results using pre-implemented and self-written utilities, and was the key person in the paper writing.

DOI: 10.1021/acs.jpcc.9b11371;

THE JOURNAL OF PHYSICAL CHEMISTRY C

pubs.acs.org/JPCC Article

Zeta Potential Determination from Molecular Simulations

Denys Biriukov, Pavel Fibich, and Milan Předota*

Cite This: J. Phys. Chem. C 2020, 124, 3159−3170 Read Online

ACCESS | Metrics & More | Article Recommendations | Supporting Information

ABSTRACT: ζ-Potential (ZP) is among key physical properties characterizing the behavior of nanoparticles in colloidal solutions. Despite many attempts to calculate and neatly interpret the ZP, a full understanding of various factors influencing its values has not been achieved yet, even for standard metal oxides, particularly when considering high ionic concentrations and the effect of temperature. This contribution extends our recent work [Předota, M. et al. *Langmuir* **2016**, *32*, 10189−10198], where we suggested a direct approach to calculate the ZP from nonequilibrium molecular dynamics (NEMD) simulations. Here, we investigate NaCl, RbCl, $CaCl_2$, $SrCl_2$, and $Na_2C_2O_4$ aqueous solutions interacting with TiO_2 and SiO_2 surfaces and show contrasting ZP behaviors of these metal oxides, elucidated by theoretical insights gained by molecular simulations. We show that both surface-specific and ion-specific properties play a key role in the observed electrokinetics. Additionally, we explore the concentration and temperature influence on the ZP of selected systems and discuss the measurement of the ZP of systems with surfaces and ions modeled using scaled partial charges. Our results agree well with available experimental data and capture all key ZP features predicted by theory or revealed by experiments and advance the microscopic description of solid/liquid interfaces, promoting further applications of the suggested NEMD approach.

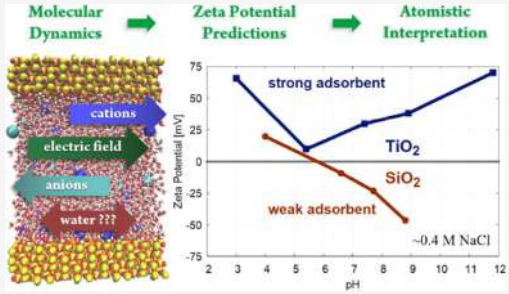

1. INTRODUCTION

ζ-Potential (ZP) is an important macroscopic measure of tremendous practical and scientific interest in the field of nanoparticles (NPs). In classical interpretation, the ZP is associated with the electrostatic potential that develops at an ill-defined boundary between a NP (including an immobile layer containing strongly adsorbed species, which moves together with the NP) and the surrounding fluid (usually aqueous solution). A surface charge, formed when the solid surface is exposed to an aqueous solution or another liquid, is compensated by counterions present in the solution. These oppositely charged layers form the so-called electric double layer (EDL),[1] giving rise (among other interfacial phenomena) to the ZP. By electrostatics, the ZP dictates the physical stability of NPs in colloidal solutions, particularly their aggregation, sedimentation, and complexation with other species. With the increasing use of NPs in nanomedicine, the ability to measure, predict, and control the ZP can significantly help in grasping the interactions of NPs with cells and biomolecules.[2,3] Since the ZP also reflects a response of NPs to an applied electric field, a detailed understanding of the ZP origin could provide stimulating ideas of advancing, e.g., water purification technologies.[4,5] Moreover, ZP measurements can be applied to track the coating of NPs, which is of vital importance in materials science, industries, and medicine.[6]

Experimental measurements of the ZP are commonly available in the literature of the last few decades. These studies employ various methods for measuring the ZP, e.g., tunable resistive pulse sensing, electroacoustics, ζ-particle tracking analysis, and electrophoretic light scattering.[7−11] The latter is usually coupled with dynamic light scattering, which determines the size of NPs.[12] The most common way of determining the ZP is via conversion of the electrophoretic mobility into the ZP using the Helmholtz−Smoluchowski (H−S) equation.[13,14] Although this simple formula ignores the surface conductivity, and it was shown that this approximation usually leads to a slightly smaller amplitude of ZP values, particularly for TiO_2 and SiO_2,[15,16] this equation is widely used in both experimental and theoretical ZP conversions due to its clarity and reasonable accuracy.

Other theoretical methods include the prediction of the ZP through simplified models of EDL like the Poisson−Boltzmann equation, Debye−Hückel theory, and the Karhunen−Loève Galerkin procedure.[17−20] Another recent work suggests that the ZP can be estimated from the size of a NP and the energy of the highest occupied molecular orbital per metal atom of the NP.[21] While the energy calculations require accurate and computationally expensive ab initio simulations, the size

Received: December 8, 2019
Revised: December 31, 2019
Published: January 8, 2020

https://dx.doi.org/10.1021/acs.jpcc.9b11371
J. Phys. Chem. C 2020, 124, 3159−3170

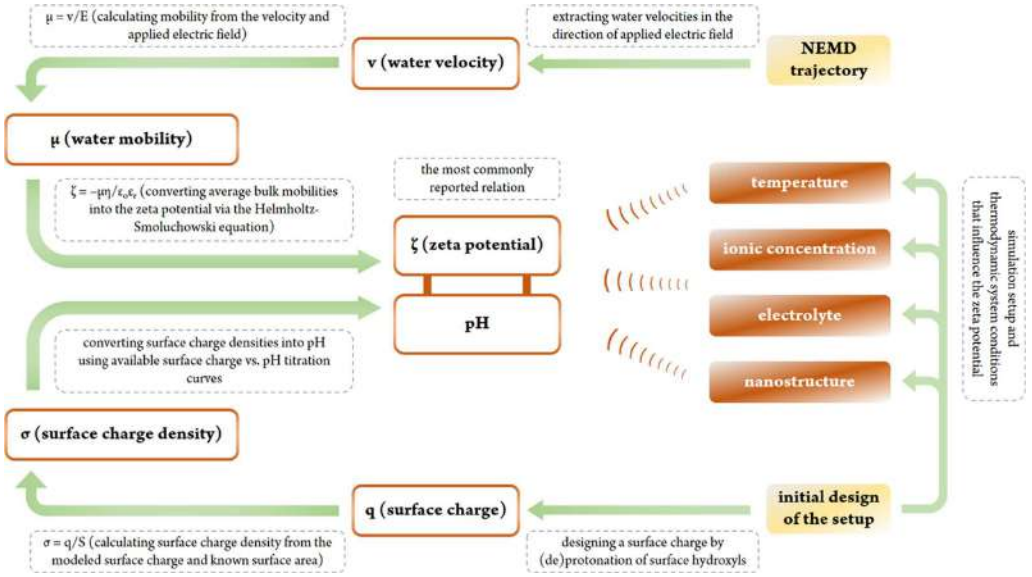

Figure 1. Schematic of the method.

should be measured experimentally. In principle, combining (pseudo)experimental and theoretical methods is common in interpretation of the ZP,[22] particularly involving molecular dynamics (MD) simulations.[23,24]

Despite huge attention to the ZP and its underlying molecular origin, the full microscopic description of the ZP is not complete yet. Eventually, even to some extent, a basic knowledge of where exactly the position of the ZP plane is defined at the interface has been intensively discussed until recently,[25,26] and the interpretation of the inner surface potential, another important interfacial measure, remains elusive.[27] Most experimental studies report the pH dependence of the ZP of a selected NP, often together with the effect of a salt (its composition and concentration) and particle size and occasionally including the effect of temperature.[28−32] Since all of these conditions can significantly influence the ZP,[33,34] it is sometimes tricky to clarify the contribution of each factor separately.[35]

Even for a widely studied metal oxide like TiO_2, measured ZP values range remarkably when using different experimental techniques.[36] This highlights the complexity of NP/aqueous interfaces and the importance of developing efficient, yet simple methods that would not only enable the measurement of the ZP but also reveal underlying interfacial phenomena. Molecular simulations have proved to be a powerful tool in providing details of atomistic resolution,[37] and obviously, they have been actively used to investigate electrokinetic phenomena at solid/liquid interfaces.[38] Following this strategy, one can link experimentally measured ZP with molecular details obtained from MD simulations if the latter gives similar trends or even similar values of the ZP over a wide range of conditions, e.g., pH, salt concentration, and temperature.

Recently, we proposed a simple method to calculate the ZP using nonequilibrium molecular dynamics (NEMD) simulations mimicking electro-osmosis.[25] The idea of the method is based on applying an electric field along the surface to obtain the streaming mobility of the fluid interacting with the surface. This mobility can be converted into the ZP, e.g., through the Helmholtz−Smoluchowski equation

$$\zeta = -\frac{\mu\eta}{\varepsilon_r\varepsilon_0} \tag{1}$$

where ζ is the ζ-potential; μ is the measured mobility of the bulk fluid relative to the surface; ε_0 is the vacuum permittivity; and ε_r and η are the relative permittivity and dynamic viscosity of the fluid, respectively.

In our in silico experiments of electro-osmosis, the planar solid surfaces are immobile and the electric field acts on the solution, generating its streaming motion along the surface. The negative sign in eq 1 reflects this difference from the H−S formula for electrophoresis. This pseudoexperiment enables the direct extraction of all molecular details of the modeled interface. For example, modeling the electro-osmosis, Siboulet et al. successfully characterized the silica/water interface in the presence of a CsCl solution.[39] English and Long[40] modeled electrophoresis by applying an electric field to TiO_2 particles of different radii and charges and estimated the ZP of these NPs in aqueous solution.

The NEMD method by Předota et al.[25] determines the ZP from the electro-osmotic flow of any solution in contact with any macroscopically planar (but atomistically structured) surface only within the limits of the accuracy of molecular models. The choice of planar surfaces is convenient in terms of statistics and periodic boundary conditions, but the results are relevant for any (nearly) planar surfaces of solid particles, including electrophoresis of spherical particles larger than few micrometers. The measurement of the ZP from simulations of electro-osmosis (averaging the streaming motion of thousands of liquid molecules relative to immobile surfaces) is much more accurate than the measurement of the streaming motion of few solid particles in corresponding simulations of electrophoresis. Another huge advantage of using molecular

https://dx.doi.org/10.1021/acs.jpcc.9b11371
J. Phys. Chem. C 2020, 124, 3159−3170

simulations is that one can carefully control system conditions, like the ionic concentration or pH (the latter, in our case, via the preset surface charge), or model extreme cases, e.g., high temperatures, which is sometimes technically difficult or impossible in experiments due to sedimentation.

The previously published data[25] were obtained using our self-written simulation code, which included both the molecular dynamics engine and on-the-fly analysis of the streaming velocities. Its main limitation was uneasy modifications for modeling other surfaces and solutions. Particularly, the code allowed only rigid solvents and monoatomic solute (ions) molecules. In this work, we utilize popular and freely available molecular software packages, namely, Gromacs[41] and large-scale atomic/molecular massively parallel simulator (LAMMPS).[42] This allows us to significantly extend the number of studied systems and generalize our method[25] and make it easily applicable by the large scientific community if input specifications and postprocessing codes are provided. The latter will be a subject of a more technically oriented paper, while, here, we focus on applications to new systems.

The two main goals of this study are (1) to describe in detail how to run NEMD simulations providing the ZP, following the scheme shown in Figure 1, and (2) present the new data that demonstrate high potential of the method. Regarding the second part, we tested modeling of (i) two metal oxide surfaces, namely, (110) rutile (TiO_2) and (101) quartz (SiO_2); (ii) monoatomic ions (Na^+, Rb^+, Ca^{2+}, Sr^{2+}, and Cl^-), similar to the original work,[25] where NaCl, RbCl, and $SrCl_2$ solutions interacting with rutile (110) surfaces were studied; (iii) adsorption of molecular anions, namely, oxalic acid ions, by rutile (110) surfaces; and (iv) pH, concentration, and temperature effects. Along with this, we carefully described the effect of a chosen MD thermostat and the strength of an applied electric field on our results.

TiO_2 and SiO_2 are treated as standard metal oxides, and they are ubiquitously present in nature, science, and technology. Therefore, both have been heavily studied and their ZPs have been frequently measured under various conditions. For example, Kosmulski has been very active in the development of theoretical models for calculating not only the ZP but also surface charge densities (SCD) using activity coefficients of surface hydroxyls of various NPs, including TiO_2 and SiO_2.[43] Particularly, he has been interested in the effect of high ionic concentration on electrokinetic properties,[44−47] which is important in the light of our simulation work. The general conclusions were that with the increasing ionic concentration (i) there is a shift of the point of zero charge (pH_{zpc}) and isoelectric point (pH_{iep}) to a larger pH; (ii) absolute values of the ZP decrease; and (iii) consequently, the ZP curves become flatter, which sometimes leads to the disappearance of pH_{iep}. These phenomena were observed already in our seminal simulation study.[25]

This work is not focused on the idea of completely reproducing the experimental data by tuning available force fields. First of all, experimental data are sensitive to many factors including those that cannot be captured in simulations of flat surfaces, e.g., the size and concentration of nanoparticles.[48−50] Therefore, even available experimental data vary in absolute ZP values, though consistent in e.g., pH and concentration trends. The force fields used in this study have been fairly verified against experimental data previously, and they perform well in predicting interfacial properties.[51−57] The only force field consideration in this work is about using scaled charges, i.e., the electronic continuum correction (ECC) theory.[58] The theory states that partial charges of charged species in aqueous solutions should be scaled down to reflect the electronic screening effects absent in nonpolarizable MD simulations. This approach has been proven successful in a more accurate description of solvated structures, primarily using 75 or 85% charge scaling (see, e.g., refs 59, 60 and references therein). We have shown that full charge models of oxalic acid anions, which were also studied in this work, fail to reproduce even basic structural properties of these ions in bulk water, and the reasonable models could have been developed only with scaled charges.[61] Having established the strategy for dealing with ECC when modeling solid/liquid interfaces,[54] we described in detail the adsorption of oxalic acid anions on rutile (110), applying the ECC approach for both the surfaces and ions.[56,57] Even in the case of atomic cations, we observed an improvement in the prediction of adsorption properties when using ECC, though with some shortcomings, e.g., ionic diffusivities can be higher compared to the experimental values if the scaling factor is too low.[54] Relying on summarized findings and the performance of the developed models, all of the data presented here were obtained using the force fields with 75% scaling (hereafter, denoted ECC), mostly due to the availability of compatible ECC models, motivated by justification of the 75% scaling factor as $1/\sqrt{\varepsilon_{el}}$, where ε_{el} is the electronic (also denoted high-frequency, ε_∞, or optical) part of the permittivity,[62] equal to the square of the refraction index of the medium, $\varepsilon_{el} = n^2$.[63] The only two sets of simulations with full charges are included for systems with a NaCl solution at rutile (110) surfaces [with ionic Lennard-Jones (LJ) parameters from the original ZP work[25]] and quartz (101) surfaces (with LJ parameters used in our previous simulation study of this metal oxide[53]) to check the effect of ECC on ZP calculations, which has not been examined before.

2. METHODS AND COMPUTATIONAL DETAILS

2.1. Molecular Dynamics Simulations. We modeled surface/water interactions in the same way as in our previous works.[53,54,56] Briefly, each simulation box was constructed from two identically charged surfaces, rutile (110) or quartz (101), with an aqueous solution in between. All of the results were averaged over the two equivalent solid/liquid interfaces. Since we were mostly interested in the pH dependence of measured properties, we prepared several surfaces of different surface charge densities (SCDs) by a preset ratio of (de)protonated surface hydroxyls. The SCD corresponds to a single pH value and is constant within one particular simulation due to the nondissociative nature of our force fields. The link between pH and SCD is often available from titration experiments.[52,57,64] Table 1 provides the list of modeled SCDs and corresponding pH values under simulated conditions.

To model rutile (110) surfaces, we used the recently developed ECC force field or its full charge analogue.[54] To reduce the number of modeled systems, we adopted only the nonhydroxylated type of the surface,[51] bearing in mind that hydroxylated rutile surfaces were investigated in the original study.[25] ECC models of quartz (101) surfaces were developed in the same way as for rutile (110). Water was modeled as rigid SPC/E,[65] whereas ionic LJ parameters were taken from the available literature or developed by us previously;[54,61,66−70] see Table S1 in the Supporting Information (SI).

https://dx.doi.org/10.1021/acs.jpcc.9b11371
J. Phys. Chem. C 2020, 124, 3159−3170

Table 1. Estimated Relation between the Surface Charge Density (SCD) and pH for Different Combinations of Surfaces and Ionic Solutions

	pH		
	rutile (110)		
SCD (C/m^2)	NaCl, 25 °C[52]	oxalic acid salts, 25 °C[57]	
+0.208	[a]	3.7	
+0.104	3	4.6	
0	5.4	6	
−0.104	7.4	7.7	
−0.208	8.9	[a]	
−0.416	11.8	[a]	
	quartz (101)		
SCD (C/m^2)	NaCl, RbCl, 25 °C[b]	$CaCl_2$, $SrCl_2$ 25 °C[64]	NaCl 100 °C[b,c]
0	4	4	4
−0.03	6.6	6	6.4
−0.06	7.7	7.2	7.1
−0.12	8.8	8.5	7.6

[a]Not modeled in this work. [b]Personal communication with Moira K. Ridley. [c]pH was roughly estimated from the extrapolation of temperature-dependent surface charge data that are available only up to 50 °C due to quartz dissolution at higher temperatures.

MD simulations were carried out in two molecular software packages, namely, Gromacs and LAMMPS. The original reason to start using more than one molecular package was that Gromacs does not offer a possibility to run simulations with thermostatting only selected components of atomic velocities (important when the average streaming velocity is nonzero). LAMMPS is more flexible and offers that option, but the speed of running simulations is significantly lower compared to that of Gromacs. However, employing Gromacs and LAMMPS simultaneously and taking the advantages of both packages helped in finding an adequate balance between functionality and speed performance. Each prepared system was initially equilibrated without applying an electric field for at least 60 ns (usually around 50 ns in Gromacs and 10 ns in LAMMPS). Then, the equilibrated structure was adopted for a NEMD simulation (in LAMMPS), with at least a 1 ns equilibration stage followed by not less than a 15 ns production run (when streaming velocities were stored or averaged on the fly and positions were stored in a trajectory). Favorable comparison of the results from equilibrium MD simulations in Gromacs with those from LAMMPS for selected systems is given in SI (Figures S1−S4).

In most of the figures, we present the ZP curve as a function of pH, combined from a collection of several simulations with different SCDs and similar bulk ionic concentrations. Only the average of these concentrations is given in the legend or caption of a figure. The full information about bulk ionic concentrations and the number of ions in studied systems can be found in SI, Table S3. Bulk pure water density in the center of the simulation box was always around the experimental value (±3 kg/m^3) of that at simulated temperature and normal pressure (997 and 958 kg/m^3 at 298.15 and 373.15 K, respectively). In all density and mobility profiles, the zero height corresponds to the zero planes of the surfaces; for rutile (110), it is the last row of Ti atoms if they were unrelaxed, whereas for quartz (101), it is the average position of surface top-layer silicon atoms. Additional technical details can be found in SI, below, or elsewhere.[53,54,56] Also, in SI, we provide example Gromacs and LAMMPS input files for MD simulations of investigated systems.

2.2. Applied Electric Field. In our study, the x and y axes are oriented along the surface, while the z axis is perpendicular to the surface. The directly observed properties in NEMD simulations are the streaming velocities $v_x(z)$ of water and ions along the surface, in the direction of the applied electric field (E_x) acting on water molecules, ions, and all mobile surface atoms. For the ZP to be predicted, only the average mobility of water away from the interface (bulklike water) is needed [though it is possible to calculate the center-of-mass (COM) mobility knowing the concentration of ions in each layer], since we explained earlier[25] that the COM mobility of a bulk layer is almost the same as that of water. Even though most of the noise cancels out by averaging v_x over all bulk water molecules (which is a significant advantage of our method) and time, we must use huge fields compared to real experiments (related to the fact that we use a tiny number of molecules compared to real experiments).

The chosen electric field should be relatively weak to preserve the equilibrium interfacial structure but strong enough to provide an acceptable signal-to-noise ratio. According to our tests with few systems, including the one shown in Figure 2, we have chosen 0.7 × 10^8 V/m as the default value, which provides satisfactory results for all studied systems. For testing purposes, we have obtained selected results with stronger fields of up to 2.1 × 10^8 V/m. Although all of these electric fields are many orders of magnitude larger than in real experiments, the relation between the streaming velocity and streaming mobility is still very close to linear, as has been proven in other simulation studies[24,25] and also verified in this work (Figure S5). The interfacial structure of

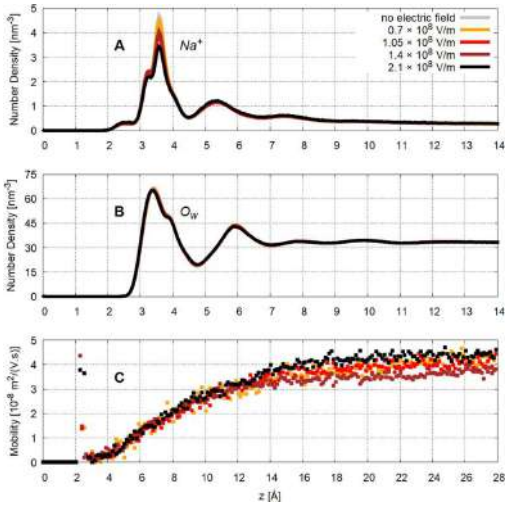

Figure 2. Effect of an applied electric field on the axial number density of (A) sodium and (B) water oxygen, and (C) mobility of water for the system with a 0.33 M NaCl solution at the most negatively charged (−0.12 C/m^2) quartz (101) surface. Note different horizontal and vertical scales. Density profiles from simulations without an applied electric field are given as a benchmark.

https://dx.doi.org/10.1021/acs.jpcc.9b11371
J. Phys. Chem. C 2020, 124, 3159−3170

ions and water should not be disturbed from simulations without an applied electric field to be in the linear response regime when modeling electro-osmosis (Figure 2A,B). While Figure 2B demonstrates that the interfacial water structure is unaffected even under the strongest electric field tested, one can see that increasing the electric field beyond 0.7×10^8 V/m gradually starts to modify the ionic interfacial structure (Figure 2A), washing away ions from the equilibrium adsorption sites, which impacts accordingly the streaming mobility of the whole liquid, including bulk water. Therefore, the field 0.7×10^8 V/m can be treated as a value approaching an upper limit of the linear regime applicable for calculations of streaming mobilities in simulated systems.

2.3. Applied Thermostat. When running NEMD simulations and having the streaming velocity as a target property to measure, one should also assess the influence of an applied thermostat. A standard MD thermostat (in this work, we have used a Nosé−Hoover thermostat[71]) is based on adjusting velocities to a desired kinetic energy (E_k) and consequently temperature. Since we are immensely interested in atomic velocities along the direction of the applied electric field (in our case, it is the x axis), we should exclude that velocity component from the calculation of temperature. In both this and original works,[25] most of the data were obtained using the so-called "YZ thermostat", which excludes the x direction from both E_k calculation and thermostatting, i.e., only y and z components of atomic velocities are subject to thermostatting. Additionally, we tested other thermostats offered in LAMMPS, Figure S6, including the default "XYZ thermostat", which acts on all components of velocity. All of the tested thermostats perform satisfactorily in terms of keeping the temperature at the selected value of 298.15 K. Surprisingly, even the calculated mobility of water, Figure 3, is

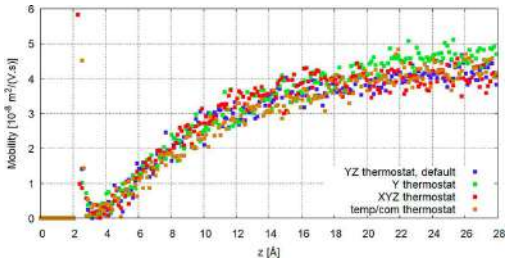

Figure 3. Mobility profiles of water of a 0.33 M NaCl solution at the most negatively charged (−0.12 C/m^2) quartz (101) surface, calculated from simulations with different types of thermostats.

very similar, regardless of the applied thermostat. The deviations in the obtained data are relatively small and within statistical uncertainties, so, in principle, to obtain quick and estimative data, one can use any of the proposed thermostats, including "XYZ thermostat", which is conceptually wrong because of the inclusion of the average streaming velocity. However, we argue that for accurate measurements of streaming velocities, the velocity component in the direction of the field should be excluded from both energy and temperature calculations.

2.4. ζ-Potential Predictions. Finally, after choosing the type of thermostat and the strength of the applied electric field, we can collect the streaming velocities. The first approach is to extract and average these velocities on the fly, directly during simulations; this is possible only if simulations are run in LAMMPS, but not Gromacs, unless the source code is modified. The second approach is to postprocess a trajectory (usually a binary file containing positions and optionally velocities of atoms). In this study, we tried both approaches (a representative comparison of data obtained by LAMMPS with on-the-fly analysis and source-code-modified Gromacs with postprocessing is given in SI, Figure S7), and as a byproduct of this work, we developed a rather general postprocessing code, which we call g_mu. g_mu (the name was chosen to follow the old-style naming of Gromacs tools) is a self-written FORTRAN code that allows a user to calculate the streaming velocity, mobility (if the electric field and charge scaling factor are provided), and temperature in the system from the text version (.gro format) of the trajectory file (generalization for reading .xtc files is in development). In fact, temperature calculations in Figure S6 were obtained using g_mu, while all of the ZP data presented here were collected using the on-the-fly analysis in LAMMPS.

We obtained distance-dependent velocities in the same way as in the original work,[25] i.e., the box was divided into 0.125 Å narrow bins parallel to the surfaces and streaming atomic velocities were averaged in each bin over the production simulation time. For the determination of ZP, we are interested only in the average mobility of liquid layers that are sufficiently far from the surface, where bulk properties are established.

When nominal charges of ions are used, the streaming mobility of water is calculated as a ratio of the streaming velocity of water and the applied electric field

$$\mu_x = \frac{v_x}{E_x} \tag{2}$$

However, this formula must be reconsidered if using ECC force fields. The force acting on a charged ion (F_x) equals to the product of an applied electric field and atomic/molecular charge (q)

$$F_x = E_x q \tag{3}$$

The charge of any ion in ECC simulations is only 75% of its nominal value [+0.75 for Na^+, +1.5 for Ca^{2+}, −0.75 for Cl^- and hydrogenoxalate $H^+(COO^-)_2$, −1.5 for oxalate $(COO^-)_2$, etc.] to effectively incorporate the electronic polarizability and weaken electrostatic interactions among species by the charge scaling. When using the same input value E_x of the electric field, the external force acting on an ECC ion is only 75% of the force exerted on a full, nominal charge. However, the force due to the external electric field should be proportional to the nominal charge in both cases, since the external forces are not reduced by either the electronic or nuclear part of the permittivity. Since the effect of the electric field E_x on a scaled charge is equivalent to the effect of a reduced field $E_{x,\mathrm{eff}}$ on a full charge, we must correct eq 2 by adding the charge scaling factor k (which is 0.75 in our case)

$$\mu_x = \frac{v_x}{E_{x,\mathrm{eff}}} = \frac{v_x}{E_x k} \tag{4}$$

Note that throughout this work we report the electric fields E_x that were applied in our simulations and appear as input values in simulation packages.

Having the mobility profile as a function of distance from the surface (see, e.g., Figure 2C), we need to determine the average mobility of bulk water. For most of the systems, the

https://dx.doi.org/10.1021/acs.jpcc.9b11371
J. Phys. Chem. C 2020, 124, 3159−3170

constant bulklike mobility is reached already at 15−20 Å from the solid. To provide a reliable and uniform analysis, in all cases, we were averaging mobilities of water that is at least 20 Å away from the surface. Using the obtained values, we were able to calculate the ZP using the Helmholtz−Smoluchowski eq 1.[14] For the SPC/E water model employed in our work, the relative permittivity and dynamic viscosity are 68 and 7.29 × 10^{-4} Pa s at 298.15 K and 51 and 2.69 × 10^{-4} Pa s at 373.15 K, respectively,[72,73] but we used the experimental values (79 and 8.9 × 10^{-4} Pa s at 298.15 K and 56 and 2.84 × 10^{-4} Pa s at 373.15 K, respectively),[72,73] since bulk experimental values are commonly used to convert directly observed electrophoretic mobilities into the ZP. Note that any of these constants do not account for changes related to concentration effects in the solution, not to mention the fact that the interfacial values of ε_r and η can differ from their bulk values significantly.[74,75]

3. RESULTS AND DISCUSSION

Our results obtained following the NEMD approach are divided into several parts: (i) the effect of ECC on the ZP when compared to a full charges approach; (ii) the difference in the ZP of TiO_2 and SiO_2 particles; (iii) concentration and temperature effects on the ZP of quartz (101) surfaces; and (iv) the effect of cooperative adsorption of sodium and oxalate by rutile (110) surfaces on the resulting ZP.

3.1. Scaled vs Full Charges. Figure 4 shows the resulting ZP for a NaCl solution at rutile (110) and quartz (101) surfaces, using two types of force fields: "full" that carries nominal charges for ions and the corresponding full charge force field for the surfaces, and ECC that employs 75% charges for both ions and charged surfaces. As one can see, the type of a charge model does not change the shape of the ZP curves, though ZP values from simulations with scaled charges are in some cases larger, particularly when surfaces are more negatively or positively charged, i.e., when there is a large number of strongly adsorbed counterions. In general, with charge scaling, the ionic sorption is less firm[54] and ions are more mobile and can induce a larger mobility of water molecules. Previously, we have also shown[54] that the ECC model of sodium[69] significantly overestimates the diffusivity of that cation, i.e., the mobility is also supposed to be higher, and eventually, that should result in larger ZP values. The same behavior is expected for most monovalent cations, e.g., Rb^+, at least for this generation of ECC ionic models.[54] Although we were aware of this drawback, which we reported previously,[54] the fact that the ZP is still very similar, regardless of an employed force field, should definitely be treated as a positive sign. Our results actually recommend to utilize ECC force fields in simulating ions that require a charge scaling to a much greater extent (for example, oxalate)[61] than sodium does, but still Na^+ should be present in the system as, e.g., a counterion or part of a background salt and consequently must be modeled using the same charge scaling factor. Any simulation setup must be consistent within the force field, i.e., all species including surfaces must have the same charge scaling factor (0.75, 1, or another). However, the performance of ECC force fields should be carefully verified in the context of ZP determination for both structural and dynamic properties. The charge scaling may lead to many significant improvements in the atomic description of aqueous solutions, especially ion pairing. There is an ongoing debate on which scaling factor should be applied;[54,59,60] particularly, 85% scaling for NaCl[76] and other solutions containing, e.g., sulfate anions[60] has been recently suggested. In this work, we did not aim to explore all possible scaling factors and limited our comparison to standard "full" models and originally proposed 75% scaling in ECC.

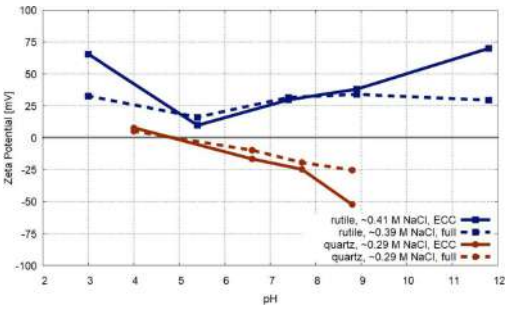

Figure 4. ζ-Potential as a function of pH for rutile (101) and quartz (101) surfaces in NaCl solutions using full and ECC force fields.

3.2. TiO_2 vs SiO_2. We have extensively studied rutile (110)[51,52,54,56,57] and quartz (101)/water[53,55] interfaces by MD simulations. Briefly summarizing, TiO_2 surfaces are much stronger sorbents than SiO_2 surfaces over the whole range of pH. For example, Kroutil et al.[53] compared the adsorption on both surfaces using the adsorption data as a function of SCD and concluded that the rutile (110) surface could adsorb 1.5−3 times more ions than quartz (101) when both have similar SCD and interact with aqueous solutions of comparable bulk ionic concentrations. This difference is even more pronounced when comparing adsorption at similar pH, so it obviously should result in the contrasting behavior of those NPs in aqueous solutions, and particularly, it should affect electrokinetic properties including the ZP.

In Figure 5A, we compare the ZP obtained from NEMD simulations of rutile (110) and quartz (101) surfaces

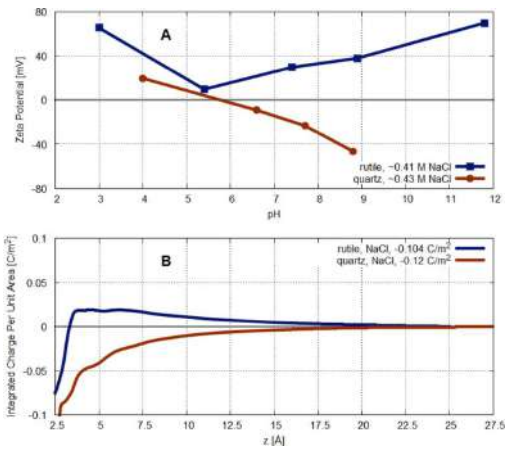

Figure 5. (A) ζ-Potential as a function of pH for quartz (101) and rutile (110) surfaces in NaCl solution. (B) Running integral of interfacial charge per unit area without the contribution of water molecules for quartz (101) and rutile (110) surfaces of similar surface charge densities in NaCl solution.

https://dx.doi.org/10.1021/acs.jpcc.9b11371
J. Phys. Chem. C 2020, 124, 3159−3170

interacting with NaCl aqueous solutions of similar concentrations. The data differ completely in the overall shapes of the ZP curves. The ZP of TiO_2 is consistently positive over the studied range of pH. From previous studies,[25,52,54] we know that sodium is a strong adsorbent on rutile (110) surfaces, which readily overcompensates a negative surface charge if the ionic concentration is high enough. Such overcharging causes charge reversal of the interface[77] and leads in this case to anomalous positive ZP at negative surfaces. While one might expect the ZP to be zero at neutral surfaces, the ZP is positive due to the negative water mobility dominated by a more mobile weak adsorbent, i.e., Cl^-, in contrast to strongly adsorbed Na^+. At positively charged surfaces, the behavior is already trivial, i.e., chloride is unable to overcompensate a positive surface charge and sodium poorly adsorbs due to repulsive electrostatics, so the ZP is again positive due to mobile Cl^-, now in the role of counterions. We hypothesized[25] that this ZP behavior should be common for strongly adsorbing cations at high ionic concentrations, while under low ionic strength, the ZP curve should follow the textbooklike behavior, i.e., decreasing ZP and changing the sign at pH_{iep}, close to pH_{zpc}. For example, rubidium, a weakly adsorbing monovalent cation, does not overcompensate a surface charge even at high salt concentrations.[25] These phenomena were not only observed in simulations but were also confirmed by experimental measurements.[45,47,78−80] In general, our data are nicely in line with experiments, even though they differ in absolute values of ZP and ionic concentrations, at which we observe the vanishing of pH_{iep}. However, this discrepancy could be easily explained by the different morphological structures of TiO_2 (rutile in simulations and usually anatase in referenced experimental studies) or due to existing limits of utilized force fields.

The ZP of quartz (101) behaves completely differently with increasing pH; it follows the buildup of SCD and gets more negative with increasing pH. This means that Na^+ does not overcompensate a surface charge even at ∼0.4 M concentration. This behavior was previously shown by experimental studies with silica, and even the positive ZP at the pH of neutral surfaces was measured,[17,81−84] in agreement with our simulation data. The positive ZP at neutral surfaces can be explained, as for rutile (110), by stronger adsorption of Na^+ compared to that of Cl^-; see Figure S8. On the contrary, the neutral fully hydroxylated quartz (101) surface is not so attractive for positively charged divalent cations with a strong solvation shell, e.g., Sr^{2+} or Ca^{2+}, which results in negative or nearly zero ZP at pH_{zpc} (Figure 6).

The contrasting behaviors of TiO_2 and SiO_2 could be predicted from distance-dependent profiles of the electrostatic field, which is proportional to the integrated interfacial charge. Figure 5B shows the overcompensation of surface charges for rutile (110) surfaces but a gradual compensation of surface charges for quartz (101) surfaces. None of the studied cations revealed strong adsorption on quartz (101) surfaces, so a surface charge is never overcompensated, and the ZP is always negative at $pH > pH_{zpc}$, regardless of the salt; see again Figure 6. The magnitudes of ZPs are larger for monovalent cations (Na^+ and Rb^+) than for divalent (Ca^{2+} and Sr^{2+}), and this difference gets larger with increasing pH. This agrees with the recent microelectrophoretic measurements of the ZP of silica in saltwater by Romero et al.,[85] who showed that in the presence of $CaCl_2$ and $MgCl_2$ solutions the ZP of silica is lower than when the salt metal is monovalent. For instance, they

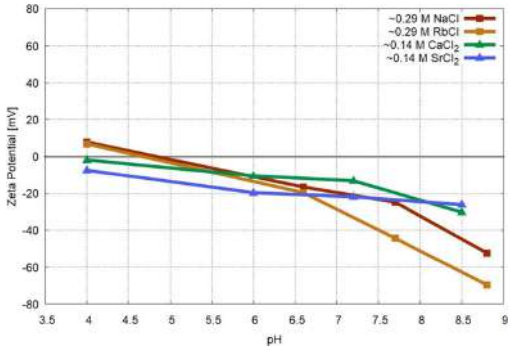

Figure 6. ζ-Potential as a function of pH for quartz (110) surfaces in various ionic solutions.

reported the ZP for 0.05 M $CaCl_2$ to be around −3 mV at pH 7 and 9, while for 0.05 M NaCl, the values were −40 and −45 mV at pH 7 and 9, respectively. Our simulation data estimate the ZP at pH 6.6 to be around −49, −21, and −17 mV for 0.05, 0.16, and 0.28 M NaCl solutions, respectively, which is in good agreement with the experiment. At pH 8.8, we obtained larger values, namely, −91, −75, and −52 mV for 0.07, 0.14, and 0.33 M NaCl, respectively. For $CaCl_2$ solution, we report −13 and −30 mV at pH 7.2 and 8.5, at 0.14 and 0.15 M concentrations, respectively. In general, we qualitatively reproduce the tendency that stronger adsorption of divalent cations gives rise to lower ZP, with the effect of $SrCl_2$ being similar to that of $CaCl_2$.

3.3. Concentration and Temperature Dependences.

Increasing the salt concentration leads to two main ZP-related features. First, the magnitudes of the ZP decrease, and second, in some cases, the isoelectric point disappears, with ZP having the same sign throughout the investigated pH range. Both phenomena have been found and discussed in detail in our original study[25] for TiO_2, so in this work, we focus on SiO_2 surfaces. Figure 7A shows that the ZP of negatively charged quartz (101) surfaces decreases in magnitude with increasing bulk concentration of NaCl solution. This finding agrees not only with theoretical arguments (if there is enough salt, it is easier to compensate a surface charge, i.e., decrease the ZP) but also with many experimental studies.[16,17,32,81−85] Note that to reach the lowest possible bulk ionic concentration for systems of our size, the lowest presented concentration ∼0.06 M was gained by having in the system only Na^+ ions that are needed to compensate a surface charge and only four ion pairs for the neutral surface; see SI. The same approach has been used previously when modeling NaCl at rutile (110).[25]

Interestingly, at neutral surfaces with increasing ionic strength, the ZP changes from near-zero to positive values. This means that at pH_{zpc} the surface prefers sodium to chloride, which is in line with different adsorption properties of these ions, although overall SiO_2 is a weak adsorbent, especially compared to many other metal oxides including TiO_2.

Depending on the type of NP, the surrounding solution and its concentration, and also accompanying dissolution processes,[86−89] it has been observed experimentally that a higher temperature can increase as well as decrease (or not affect) the ZP. From the molecular point of view, we expect at least few primary factors causing these changes or their absence. First of

https://dx.doi.org/10.1021/acs.jpcc.9b11371
J. Phys. Chem. C 2020, 124, 3159−3170

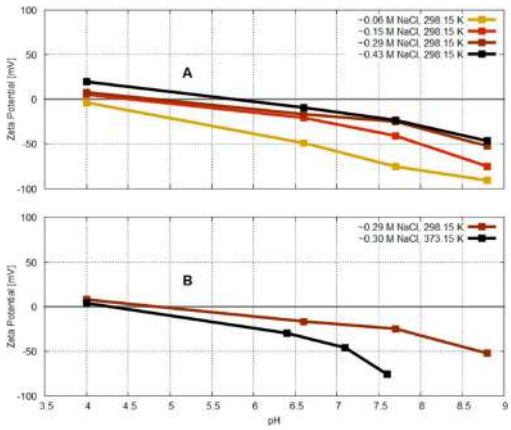

Figure 7. ζ-Potential as a function of pH for quartz (101) surfaces by (A) varying the bulk concentration of a NaCl solution at constant temperature or (B) varying the temperature at similar NaCl concentrations.

all, the relative motion of NPs in aqueous solutions is more rapid at higher temperatures, and generally, it is inversely proportional to the viscosity of the fluid (see SI of ref 25), which decreases with increasing temperature. When the ZP is being calculated, the resulting rise in the mobility should cancel out in the H−S equation by the viscosity itself if the temperature effect on the interfacial viscosity[74] influencing the ZP is the same as the temperature effect on the bulk viscosity entering the H−S equation. However, a lower dielectric constant of water should eventually lead to higher ZP values at higher temperatures. Another important concern is that temperature can cause structural changes at the solid/liquid interface and particularly alter the distribution of ions among various adsorption sites.[52] Moreover, the water structure can also experience changes. It is therefore difficult or almost impossible to predict the temperature effect on ZP without a detailed molecular picture of the interface.

For silica and quartz particles, there is not a solid inference yet on how the ZP changes with temperature. Ramachandran and Somasundaran[90] revealed a gradual increase in the ZP of quartz NPs when temperature was increased up to 75 °C. Recently, Duffy et al. concluded the same for both crystalline and amorphous silica up to 150 °C.[91] Other studies on amorphous silica also reported larger ZP values for higher temperatures.[92,93] On the contrary, Vinogradov et al., who were working with natural sand packs, claimed that when increasing the temperature, the ZP should decrease at low ionic concentrations and remain the same at fairly high ionic concentrations.[94,95] Our simulation data, Figure 7B, that compare the ZP of quartz (101) surfaces at two temperatures, 298.15 and 373.15 K, indicate that the ZP is larger at the higher temperature over the studied pH range. If density profiles from simulations at selected temperatures, Figure S9, are compared, one can see that sodium ions are less adsorbed at the interface when the temperature is higher, i.e., the surface charges are less effectively screened, which accordingly leads to larger ZP. The water structure, in turn, exhibits rather minor changes.

3.4. Effect of Cooperative Adsorption of Sodium and Oxalate. Another set of simulations was performed with the adsorption of oxalic acid anions on rutile (110) surfaces. Charged forms of oxalic acid are oxalate, $(COO^-)_2$, which is present over a whole range of studied pH, and hydrogenoxalate, $H^+(COO^-)_2$, which is significant only at the lowest modeled pH, i.e., at +0.208 C/m^2 rutile (110) surface. These ions, particularly their intramolecular and intermolecular structures in bulk water and adsorption on TiO_2, were intensively studied by us.[56,57,61] Oxalate has been found to be a very strong adsorbent on the positively charged rutile (110) surface,[56,57] so we expected the overcompensation of a positive surface charge by these anions. Available experimental data support this hypothesis: Janusz and Matysek showed that the adsorption of oxalate should result in negative ZP of anatase NPs over a whole range of pH if the salt concentration is not extremely low,[96] while the experimental study by Erdemoğlu and Sarikaya indicated the same for magnetite (Fe_3O_4), which is another strongly adsorbing metal oxide.[97] Besides, Nguyen et al. measured negative ZP for kaolinite with adsorbed oxalate at pH between 2 and 11,[98] and the same was shown for oxalate adsorbed on some variable-charged soils.[99]

Figure 8 compares the ZP of oxalate at rutile (110) surfaces from our NEMD simulations with the experimental data.[96,97]

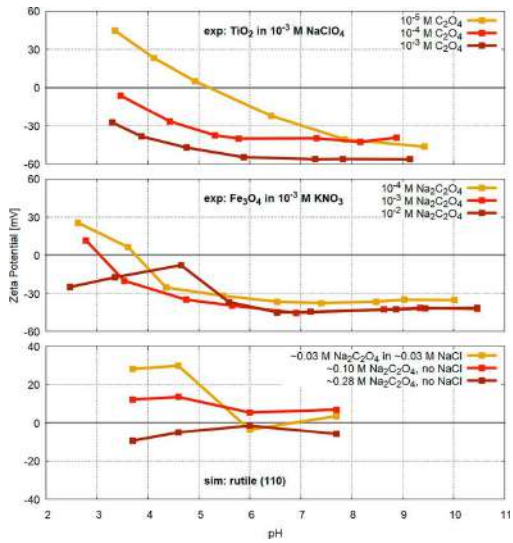

Figure 8. Experimentally measured ζ-potential as a function of pH for TiO_2 (top)[96] and Fe_3O_4 (middle)[97] in presence of oxalic acid compared to the data from simulations with rutile (110) surfaces (bottom). Note different vertical scales of the bottom graph.

Simulation data are represented by three ZP lines as a function of pH: (i) for low concentration of $Na_2C_2O_4$ in NaCl medium, (ii) for a $Na_2C_2O_4$ solution of relatively low concentration without a background salt, and (iii) for a concentrated $Na_2C_2O_4$ solution without a background salt. Simulated ionic concentrations are still much higher than in experiments, but we are already at the limit of our capabilities due to system size and statistics. However, even under these conditions, we capture several trends as in the experiments. First, in our

https://dx.doi.org/10.1021/acs.jpcc.9b11371
J. Phys. Chem. C 2020, 124, 3159−3170

simulations, with the increasing concentration of oxalate, the ZP changes its sign at a lower pH, and the same happens in the experiment, although at much lower concentrations. Second, the ZP is indeed constantly negative at the highest modeled concentration but still smaller in amplitude over the studied pH range. A lower amplitude could be explained purely by a concentration difference like that shown in experimental studies of oxalate adsorbed by anatase[100] and corundum.[101] However, the explanation misses so far a part of the puzzle, mainly what happens at medium concentrations and why we observe identical trends in very different concentration ranges but cannot interpolate behavior in between them. Particularly, looking at the experimental data, one might guess that the ZP should always be negative with further increasing oxalate concentration, but we do not observe this in our simulations at around 0.1 M. To address this issue, we recall few things discussed previously. As we already know, with increasing NaCl concentration without oxalate in the system, the ZP of TiO_2 becomes at some concentration constantly positive due to the overcompensation of surface charges. At the same time, experimental measurements are usually performed under low ionic strength of both oxalate and background salts, and the latter usually contains a heavily adsorbing cation like Na^+ or K^+ (see legends of the experimental data in Figure 8). The overcompensation by these cations does not occur at their low concentrations, but we argue that there is already enough oxalate to overcompensate a positive surface charge, which leads to negative ZP. Having in our simulations high concentrations of all ionic species, we observe the strong adsorption of both Na^+ and oxalate. At lower modeled concentrations, this results in dual overcompensation of a surface charge, and only then, with further increasing ionic concentration, oxalate becomes dominant at the interface. Primarily, all of this explains the near-zero ZP at the neutral surface, positive values at a lower pH and lower ionic concentrations, and less negative ZP than in experiments at a higher pH. The role of Cl^- (or another rather inert anion in terms of adsorption) in defining the ZP seems small, since other species dictate the adsorption. The role of hydrogenoxalate, which at a lower pH should be present in the bulk in a similar amount as that of oxalate, is less clear. On the one hand, its role could also be minor like that of Cl^-. On the other hand, hydrogenoxalate, which also adsorbs quite well on rutile (110) surfaces,[56] although weaker than oxalate, electrostatically weakens the adsorption of Na^+ because it carries a proton on one of the COO^- groups, and this eventually could lead to more negative ZP and the Λ-shape of the curve at a lower pH as we see in the experimental data for magnetite at the highest concentration. However, due to the complexity of oxalate-containing systems (in some cases, we model four different simultaneously adsorbing ionic species), this part should be further investigated in the future, best together with modeling the adsorption of other oxyanions for additional comparison.

4. CONCLUSIONS

ζ-Potential is a widely used theoretical concept that characterizes the stability and electrokinetic motion of colloidal particles in organic solutions. The role of the whole inhomogeneous interface in the resulting ZP, as well as the emphasis on the dynamic component of electrokinetic phenomena (quantified by the distance-dependent mobility of ions and water) as opposed to purely electrostatic interpretation of the ZP (as the word "potential" might infer), has been already formulated in our seminal work on predicting the ZP from NEMD simulations.[25] Here, we extensively applied the method to a range of systems, including (for the first time) molecular ions, namely, oxalate and hydrogenoxalate. These ions also represent strongly adsorbing anions, which allows discussing differences with respect to weakly adsorbing Cl^- anions studied so far. Comparison between (110) rutile (TiO_2) and (101) quartz (SiO_2) surfaces allows exploring the behavior of stronger and weaker adsorbents, respectively, with the latter exhibiting more textbooklike behavior and the former exhibiting anomalous behavior (ultimately leading to the ZP being only positive or only negative throughout the pH range) at high concentrations of ions in the solution. Additionally, our NEMD simulations supply valuable insights into how and why the ZP of quartz surfaces changes with the increasing temperature or how the simultaneous adsorption of strongly adsorbing but oppositely charged ions (in our case, sodium and oxalate) can in turn alter the ZP at rutile surfaces. The discussion of these differences and the observed trends provide a deeper understanding of interfacial phenomena, essential for designing nanodevices and controlling their functions.

Even though the computer models are always imperfect, it is worth stressing that we obtained a satisfactory agreement with experimental data in all cases, where available. This strongly highlights the universality of the proposed approach. Moreover, with the growing popularity of nonpolarizable force fields that utilize scaled ionic charges, it is important to understand how the charge scaling should be treated if one runs simulations with an applied electric field. We showed that the effective electric field in simulations with reduced charges is lower than the one applied in standard simulations with full charges, and this inequality must be taken into account when calculating streaming mobilities. This effort significantly contributes to the integration of ECC theory into molecular simulations of not only solid/liquid interfaces[54] but also other systems where electrokinetic phenomena are of interest.

Finally, we have implemented the method for the ZP determination from NEMD simulations[25] to two common simulation packages, Gromacs and LAMMPS, which makes this method accessible to a much wider range of scientists as well as explored systems. A more technical paper devoted to technical issues of this method and discussing the recommended parameters for processing/postprocessing the trajectories and making the method public is currently under preparation.

■ ASSOCIATED CONTENT

Supporting Information

The Supporting Information is available free of charge at https://pubs.acs.org/doi/10.1021/acs.jpcc.9b11371.

Example Gromacs and LAMMPS input files; summary of force field parameters employed in this work; additional density, velocity, mobility, and ζ-potential profiles; and more detailed technical information about simulations (PDF)

■ AUTHOR INFORMATION

Corresponding Author

Milan Předota − *Institute of Physics, Faculty of Science, University of South Bohemia, České Budějovice 370 05, Czech Republic;* orcid.org/0000-0003-3902-0992; Email: predota@prf.jcu.cz

https://dx.doi.org/10.1021/acs.jpcc.9b11371
J. Phys. Chem. C 2020, 124, 3159−3170

Other Authors

Denys Biriukov − *Institute of Physics, Faculty of Science, University of South Bohemia, České Budějovice 370 05, Czech Republic;* orcid.org/0000-0003-1007-2203

Pavel Fibich − *Department of Botany, Faculty of Science, University of South Bohemia, České Budějovice 370 05, Czech Republic*

Complete contact information is available at: https://pubs.acs.org/10.1021/acs.jpcc.9b11371

Notes

The authors declare no competing financial interest.

■ ACKNOWLEDGMENTS

This work was supported by the Czech Science Foundation (project 17-10734S). Computational resources were provided by the CESNET LM2015042 and the CERIT Scientific Cloud LM2015085 under the program "Projects of Large Research, Development, and Innovations Infrastructures". The authors thank Moira K. Ridley for important inputs and comments on available pH titration data with quartz nanoparticles.

■ REFERENCES

(1) Lyklema, J. *Fundamentals of Interface and Colloid Science*; Academic Press, 1995; Vol. 2, pp 1−232.

(2) Skoglund, S.; Hedberg, J.; Yunda, E.; Godymchuk, A.; Blomberg, E.; Wallinder, I. O. Difficulties and Flaws in Performing Accurate Determinations of Zeta Potentials of Metal Nanoparticles in Complex Solutions−Four Case Studies. *PLoS One* **2017**, *12*, No. e0181735.

(3) Wang, Y.; Zhao, Q.; Han, N.; Bai, L.; Li, J.; Liu, J.; Che, E.; Hu, L.; Zhang, Q.; Jiang, T.; et al. Mesoporous Silica Nanoparticles in Drug Delivery and Biomedical Applications. *Nanomedicine* **2015**, *11*, 313−327.

(4) Honda, R. J.; Keene, V.; Daniels, L.; Walker, S. L. Removal of TiO_2 Nanoparticles During Primary Water Treatment: Role of Coagulant Type, Dose, and Nanoparticle Concentration. *Environ. Eng. Sci.* **2014**, *31*, 127−134.

(5) Morfesis, A.; Jacobson, A. M.; Frollini, R.; Helgeson, M.; Billica, J.; Gertig, K. R. Role of Zeta (ζ) Potential in the Optimization of Water Treatment Facility Operations. *Ind. Eng. Chem. Res.* **2009**, *48*, 2305−2308.

(6) Wilhelm, P.; Stephan, D. On-line Tracking of the Coating of Nanoscaled Silica with Titania Nanoparticles via Zeta-Potential Measurements. *J. Colloid Interface Sci.* **2006**, *293*, 88−92.

(7) Greenwood, R. Review of the Measurement of Zeta Potentials in Concentrated Aqueous Suspensions using Electroacoustics. *Adv. Colloid Interface Sci.* **2003**, *106*, 55−81.

(8) Kozak, D.; Anderson, W.; Vogel, R.; Chen, S.; Antaw, F.; Trau, M. Simultaneous Size and ζ-Potential Measurements of Individual Nanoparticles in Dispersion using Size-Tunable Pore Sensors. *ACS Nano* **2012**, *68*, 6990−6997.

(9) Sikora, A.; Bartczak, D.; Geißler, D.; Kestens, V.; Roebben, G.; Ramaye, Y.; Varga, Z.; Palmai, M.; Shard, A. G.; Goenaga-Infante, H.; et al. A Systematic Comparison of Different Techniques to Determine the Zeta Potential of Silica Nanoparticles in Biological Medium. *Anal. Methods* **2015**, *7*, 9835−9843.

(10) Sikora, A.; Shard, A. G.; Minelli, C. Size and ζ-Potential Measurement of Silica Nanoparticles in Serum using Tunable Resistive Pulse Sensing. *Langmuir* **2016**, *32*, 2216−2224.

(11) Vogel, R.; Pal, A. K.; Jambhrunkar, S.; Patel, P.; Thakur, S. S.; Reátegui, E.; Parekh, H. S.; Saá, P.; Stassinopoulos, A.; Broom, M. F. High-Resolution Single Particle Zeta Potential Characterisation of Biological Nanoparticles using Tunable Resistive Pulse Sensing. *Sci. Rep.* **2017**, *7*, No. 17479.

(12) Bhattacharjee, S. DLS and Zeta Potential − What They are and What They are Not? *J. Controlled Release* **2016**, *235*, 337−351.

(13) Sze, A.; Erickson, D.; Ren, L.; Li, D. Zeta-Potential Measurement using the Smoluchowski Equation and the Slope of the Current−Time Relationship in Electroosmotic Flow. *J. Colloid Interface Sci.* **2003**, *261*, 402−410.

(14) Delgado, A. V.; Gonsalez-Caballero, E.; Hunter, R. J.; Koopal, L. K.; Lyklema, J. Measurement and Interpretation of Electrokinetic Phenomena (IUPAC Technical Report). *Pure Appl. Chem.* **2005**, *77*, 1753−1805.

(15) Leroy, P.; Tournassat, C.; Bizi, M. Influence of Surface Conductivity on the Apparent Zeta Potential of TiO_2 Nanoparticles. *J. Colloid Interface Sci.* **2011**, *356*, 442−453.

(16) Leroy, P.; Devau, N.; Revil, A.; Bizi, M. Influence of Surface Conductivity on the Apparent Zeta Potential of Amorphous Silica Nanoparticles. *J. Colloid Interface Sci.* **2013**, *410*, 81−93.

(17) Berli, C. L. A.; Piaggio, M. V.; Deiber, J. A. Modeling the Zeta Potential of Silica Capillaries in Relation to the Background Electrolyte Composition. *Electrophoresis* **2003**, *24*, 1587−1595.

(18) Park, H. M.; Hong, S. M.; Lee, J. S. Estimation of Zeta Potential of Electroosmotic Flow in a Microchannel using a Reduced-Order Model. *Biomed. Microdevices* **2007**, *9*, 751−760.

(19) Kulsing, C.; Yang, Y.; Matyska, M. T.; Pesek, J. J.; Boysen, R. I.; Hearn, M. T. W. Prediction of the Zeta Potentials and Ionic Descriptors of a Silica Hydride Stationary Phase with Mobile Phases of Different pH and Ionic Strength. *Anal. Chim. Acta* **2015**, *859*, 79−86.

(20) Batalioto, F.; Figueiredo Neto, A. M.; Barbero, G. Ion Trapping on Silica Nanoparticles: Effect on the ζ-potential. *J. Appl. Phys.* **2017**, *122*, No. 164303.

(21) Mikolajczyk, A.; Gajewicz, A.; Rasulev, B.; Schaeublin, N.; Maurer-Gardner, E.; Hussain, S.; Leszczynski, J.; Puzyn, T. Zeta Potential for Metal Oxide Nanoparticles: A Predictive Model Developed by a Nano-Quantitative Structure−Property Relationship Approach. *Chem. Mater.* **2015**, *27*, 2400−2407.

(22) Doane, T. L.; Chuang, C.-H.; Hill, R. J.; Burda, C. Nanoparticle ζ −Potentials. *Acc. Chem. Res.* **2012**, *45*, 317−326.

(23) Huang, D. M.; Cottin-Bizonne, C.; Ybert, C.; Bocquet, L. Ion-Specific Anomalous Electrokinetic Effects in Hydrophobic Nanochannels. *Phys. Rev. Lett.* **2007**, *98*, No. 177801.

(24) Brkljača, Z.; Namjesnik, D.; Lützenkirchen, J.; Předota, M.; Preočanin, T. Quartz/Aqueous Electrolyte Solution Interface: Molecular Dynamic Simulation and Interfacial Potential Measurements. *J. Phys. Chem. C* **2018**, *122*, 24025−24036.

(25) Předota, M.; Machesky, M. L.; Wesolowski, D. J. Molecular Origins of the Zeta Potential. *Langmuir* **2016**, *32*, 10189−10198.

(26) Alixadeh, A.; Wang, M. Flexibility of Inactive Electrokinetic Layer at Charged Solid-Liquid Interface in Response to Bulk Ion Concentration. *J. Colloid Interface Sci.* **2019**, *200*, 195−204.

(27) Preočanin, T.; Namjesnik, D.; Brown, M. A.; Lützenkirchen, J. The Relationship between Inner Surface Potential and Electrokinetic Potential from an Experimental and Theoretical Point of View. *Environ. Chem.* **2017**, *14*, 295−309.

(28) Jesionowski, T. Influence of Aminosilane Surface Modification and Dyes Adsorption on Zeta Potential of Spherical Silica Particles Formed in Emulsion System. *Colloids Surf., A* **2003**, *222*, 87−94.

(29) Erdemoğlu, M. Zeta Potential of Pyrophyllite in Aqueous Solutions of Alkaline and Alkaline Earth Metal Cations and Low-Molecular-Weight Organic Anions. *J. Dispersion Sci. Technol.* **2007**, *28*, 689−695.

(30) Hanaor, D.; Michelazzi, M.; Leonelli, C.; Sorrell, C. C. The Effects of Carboxylic Acids on the Aqueous Dispersion and Electrophoretic Deposition of ZrO_2. *J. Eur. Ceram. Soc.* **2012**, *32*, 235−244.

(31) Holmberg, J. P.; Ahlberg, E.; Bergenholtz, J.; Hassellöv, M.; Abbas, Z. Surface Charge and Interfacial Potential of Titanium Dioxide Nanoparticles: Experimental and Theoretical Investigations. *J. Colloid Interface Sci.* **2013**, *417*, 168−176.

(32) Jalil, A. H.; Pyell, U. Quantification of Zeta-Potential and Electrokinetic Surface Charge Density for Colloidal Silica Nanoparticles Dependent on Type and Concentration of the Counterion:

Probing the Outer Helmholtz Plane. *J. Phys. Chem. C* **2018**, *122*, 4437−4453.
(33) Kirby, B. J.; Hasselbrink, E. F., Jr. Zeta Potential of Microfluidic Substrates: 1. Theory, Experimental Techniques, and Effects on Separations. *Electrophoresis* **2004**, *25*, 203−213.
(34) Kirby, B. J.; Hasselbrink, E. F., Jr. Zeta Potential of Microfluidic Substrates: 2. Data for Polymers. *Electrophoresis* **2004**, *25*, 187−202.
(35) Darlington, A. M.; Jarisz, T. A.; DeWalt-Kerian, E. L.; Roy, S.; Kim, S.; Azam, MdS.; Hore, D. K.; Gibbs, J. M. Separating the pH-Dependent Behavior of Water in the Stern and Diffuse Layers with Varying Salt Concentration. *J. Phys. Chem. C* **2017**, *121*, 20229−20241.
(36) Gómez-Merino, A. I.; Rubio-Hernández, F. J.; Velázquez-Navarro, J. F.; Aguiara, J. Assessment of ζ-potential in TiO_2 Aqueous Suspensions: A Comparative Study Based on Thermodynamic and Rheological Methods. *Ceram. Int.* **2015**, *41*, 5331−5340.
(37) Hartkamp, R.; Biance, A.-L.; Fu, L.; Dufrêche, J.-F.; Bonhommeb, O.; Joly, L. Measuring Surface Charge: Why Experimental Characterization and Molecular Modeling should be Coupled. *Curr. Opin. Colloid Interface Sci.* **2018**, *37*, 101−114.
(38) Fu, L.; Merabia, S.; Joly, L. What Controls Thermo-osmosis? Molecular Simulations Show the Critical Role of Interfacial Hydrodynamics. *Phys. Rev. Lett.* **2017**, *119*, No. 214501.
(39) Siboulet, B.; Hocine, S.; Hartkamp, R.; Dufrêche, J.-F. Scrutinizing Electro-Osmosis and Surface Conductivity with Molecular Dynamics. *J. Phys. Chem. C* **2017**, *121*, 6756−6769.
(40) English, N. J.; Long, W. F. Estimation of Zeta Potentials of Titania Nanoparticles by Molecular Simulation. *Phys. A* **2009**, *388*, 4091−4096.
(41) Van der Spoel, D.; Lindahl, E.; Hess, B.; Groenhof, G.; Mark, A. E.; Berendsen, H. J. C. GROMACS: Fast, Flexible, and Free. *J. Comput. Chem.* **2005**, *26*, 1701−1718.
(42) Plimpton, S. Fast Parallel Algorithms for Short-Range Molecular Dynamics. *J. Comput. Phys.* **1995**, *117*, 1−19.
(43) Kosmulski, M. The Role of the Activity Coefficients of Surface Groups in the Formation of Surface Charge of Oxides. Part II: Ion Exchange and Potentials. *Colloid Polym. Sci.* **1993**, *271*, 1076−1082.
(44) Kosmulski, M.; Maczka, E.; Rosenholm, J. B. Isoelectric Points of Metal Oxides at High Ionic Strengths. *J. Phys. Chem. B* **2002**, *106*, 2918−2921.
(45) Kosmulski, M.; Rosenholm, J. B. High Ionic Strength Electrokinetics. *Adv. Colloid Interface Sci.* **2004**, *112*, 93−107.
(46) Kosmulski, M.; Dahlsten, P. High Ionic Strength Electrokinetics of Clay Minerals. *Colloids Surf., A* **2006**, *291*, 212−218.
(47) Kosmulski, M.; Prochniak, P.; Rosenholm, J. B. Electroacoustic Study of Titania at High Concentrations of 1-2, 2-1 and 2-2 Electrolytes. *Colloids Surf. A* **2009**, *345*, 106−111.
(48) Bouhaik, I. S.; Leroy, P.; Ollivier, P.; Azaroual, M.; Mercury, L. Influence of Surface Conductivity on the Apparent Zeta Potential of TiO_2 Nanoparticles: Application to the Modeling of their Aggregation Kinetics. *J. Colloid Interface Sci.* **2013**, *406*, 75−85.
(49) Wang, N.; Hsu, C.; Zhu, L.; Tseng, S.; Hsu, J.-P. Influence of Metal Oxide Nanoparticles Concentration on their Zeta Potential. *J. Colloid Interface Sci.* **2013**, *407*, 22−28.
(50) Sun, D.; Kang, S.; Liu, C.; Lu, Q.; Cui, L.; Hu, B. Effect of Zeta Potential and Particle Size on the Stability of SiO_2 Nanospheres as Carrier for Ultrasound Imaging Contrast Agents. *Int. J. Electrochem. Sci.* **2016**, *11*, 8520−8529.
(51) Předota, M.; Bandura, A. V.; Cummings, P. T.; Kubicki, J. D.; Wesolowski, D. J.; Chialvo, A. A.; Machesky, M. L. Electric Double Layer at the Rutile (110) Surface. 1. Structure of Surfaces and Interfacial Water from Molecular Dynamics by Use of ab Initio Potentials. *J. Phys. Chem. B* **2004**, *108*, 12049−12060.
(52) Předota, M.; Machesky, M. L.; Wesolowski, D. J.; Cummings, P. T. Electric Double Layer at the Rutile (110) Surface. 4. Effect of Temperature and pH on the Adsorption and Dynamics of Ions. *J. Phys. Chem. C* **2013**, *117*, 22852−22866.
(53) Kroutil, O.; Chval, Z.; Skelton, A. A.; Předota, M. Computer Simulations of Quartz (101)−Water Interface over a Range of pH Values. *J. Phys. Chem. C* **2015**, *119*, 9274−9286.
(54) Biriukov, D.; Kroutil, O.; Předota, M. Modeling of Solid-Liquid Interfaces using Scaled Charges: Rutile (110) Surfaces. *Phys. Chem. Chem. Phys.* **2018**, *20*, 23954−23966.
(55) Marchioro, A.; Bischoff, M.; Lütgebaucks, C.; Biriukov, D.; Předota, M.; Roke, S. Surface Characterization of Colloidal Silica Nanoparticles by Second Harmonic Scattering: Quantifying the Surface Potential and Interfacial Water Order. *J. Phys. Chem. C* **2019**, *123*, 20393−20404.
(56) Biriukov, D.; Kroutil, O.; Kabeláč, M.; Ridley, M. K.; Machesky, M. L.; Předota, M. Oxalic Acid Adsorption on Rutile: Molecular Dynamics and Ab Initio Calculations. *Langmuir* **2019**, *35*, 7617−7630.
(57) Machesky, M. L.; Ridley, M. K.; Biriukov, D.; Kroutil, O.; Předota, M. Oxalic Acid Adsorption on Rutile: Experiments and Surface Complexation Modeling to 150 °C. *Langmuir* **2019**, *35*, 7631−7640.
(58) Leontyev, I.; Stuchebrukhov, A. A. Accounting for Electronic Polarization in Non-Polarizable Force Fields. *Phys. Chem. Chem. Phys.* **2011**, *13*, 2613−2626.
(59) Smith, W. R.; Nezbeda, I.; Kolafa, J.; Moučka, F. Recent Progress in the Molecular Simulation of Thermodynamic Properties of Aqueous Electrolyte Solutions. *Fluid Phase Equilib.* **2018**, *466*, 19−30.
(60) Zeron, I. M.; Abascal, J. L. F.; Vega, C. A Force Field of Li^+, Na^+, K^+, Mg^{2+}, Ca^{2+}, Cl^-, and SO_4^{2-} in Aqueous Solution Based on the TIP4P/2005 Water Model and Scaled Charges for the Ions. *J. Chem. Phys.* **2019**, *151*, No. 134504.
(61) Kroutil, O.; Předota, M.; Kabeláč, M. Force Field Parametrization of Hydrogenoxalate and Oxalate Anions with Scaled Charges. *J. Mol. Model.* **2017**, *23*, No. 327.
(62) Leontyev, I.; Vener, M.; Rostov, I.; Basilevsky, M.; Newton, M. D. Continuum Level Treatment of Electronic Polarization in the Framework of Molecular Simulations of Solvation Effects. *J. Chem. Phys.* **2003**, *119*, 8024−8037.
(63) Leontyev, I. V.; Stuchebrukhov, A. A. Electronic Polarizability and the Effective Pair Potentials of Water. *J. Chem. Theory Comput.* **2010**, *6*, 3153−3161.
(64) Kitamura, A.; Fujiwara, K.; Yamamoto, T.; Nishikawa, S.; Moriyama, H. Analysis of Adsorption Behavior of Cations onto Quartz Surface by Electrical Double-layer Model. *J. Nucl. Sci. Technol.* **1999**, *36*, 1167−1175.
(65) Berendsen, H. J. C.; Grigera, J. R.; Straatsma, T. P. The Missing Term in Effective Pair Potentials. *J. Phys. Chem. A.* **1987**, *91*, 6269−6271.
(66) Lee, S. H.; Rasaiah, J. C. Molecular Dynamics Simulation of Ion Mobility. 2. Alkali Metal and Halide Ions using the SPC/E Model for Water at 25 °C. *J. Phys. Chem. A.* **1996**, *100*, 1420−1425.
(67) Joung, I. S.; Cheatham, T. E. Determination of Alkali and Halide Monovalent Ion Parameters for Use in Explicitly Solvated Biomolecular Simulations. *J. Phys. Chem. B* **2008**, *112*, 9020−9041.
(68) Pluhařová, E.; Fischer, H. E.; Mason, P. E.; Jungwirth, P. Hydration of the Chloride Ion in Concentrated Aqueous Solutions using Neutron Scattering and Molecular Dynamics. *Mol. Phys.* **2014**, *112*, 1230−1240.
(69) Kohagen, M.; Mason, P. E.; Jungwirth, P. Accounting for Electronic Polarization Effects in Aqueous Sodium Chloride via Molecular Dynamics Aided by Neutron Scattering. *J. Phys. Chem. B* **2015**, *120*, 1454−1460.
(70) Martinek, T.; Duboué-Dijon, E.; Timr, S.; Mason, P. E.; Baxová, K.; Fischer, H. E.; Schmidt, B.; Pluharova, E.; Jungwirth, P. Calcium Ions in Aqueous Solutions: Accurate Force Field Description Aided by Ab Initio Molecular Dynamics and Neutron Scattering. *J. Chem. Phys.* **2018**, *148*, No. 222813.
(71) Hoover, W. G. Canonical Dynamics: Equilibrium Phase-Space Distributions. *Phys. Rev. A* **1985**, *31*, 1695−1697.

https://dx.doi.org/10.1021/acs.jpcc.9b11371
J. Phys. Chem. C 2020, 124, 3159−3170

(72) Vega, C.; Abascal, J. L. F. Simulating Water with Rigid Non-Polarizable Models: a General Perspective. *Phys. Chem. Chem. Phys.* **2011**, *13*, 19663−19688.
(73) Rami Reddy, M.; Berkowitz, M. The Dielectric Constant of SPC/E Water. *Chem. Phys. Lett.* **1989**, *155*, 173−176.
(74) Předota, M.; Cummings, P. T.; Wesolowski, D. J. Electric Double Layer at the Rutile (110) Surface. 3. Inhomogeneous Viscosity and Diffusivity Measurement by Computer Simulations. *J. Phys. Chem. C* **2007**, *111*, 3071−3079.
(75) Parez, S.; Předota, M.; Machesky, M. L. Dielectric Properties of Water at Rutile and Graphite Surfaces: Effect of Molecular Structure. *J. Phys. Chem. C* **2014**, *118*, 4818−4834.
(76) Benavides, A. L.; Portillo, M. A.; Chamorro, V. C.; Espinosa, J. R.; Abascal, J. L. F.; Vega, C. A Potential Model for Sodium Chloride Solutions Based on the TIP4P/2005 Water Model. *J. Chem. Phys.* **2017**, *147*, No. 104501.
(77) Lyklema, J. Quest for Ion-ion Correlations in Electric Double Layers and Overcharging Phenomena. *Adv. Colloid Interface Sci.* **2009**, *147−148*, 205−213.
(78) Sprycha, R. Zeta Potential and Surface Charge Components at Anatase/Electrolyte Interface. *J. Colloid Interface Sci.* **1986**, *110*, 278−281.
(79) Gustafsson, J.; Mikkola, P.; Jokinen, M.; Rosenholm, J. B. The Influence of pH and NaCl on the Zeta Potential and Rheology of Anatase Dispersions. *Colloids Surf., A* **2000**, *175*, 349−359.
(80) Kosmulski, M.; Gustafsson, J.; Rosenholm, J. B. Ion Specificity and Viscosity of Rutile Dispersions. *Colloid Polym. Sci.* **1999**, *277*, 550−556.
(81) Kosmulski, M.; Matijevic, E. ζ-Potentials of Silica in Water-Alcohol Mixtures. *Langmuir* **1992**, *8*, 1060−1064.
(82) Kosmulski, M. Positive Electrokinetic Charge of Silica in the Presence of Chlorides. *J. Colloid Interface Sci.* **1998**, *208*, 543−545.
(83) Xu, G.; Zhang, J.; Song, G. Effect of Complexation on the Zeta Potential of Silica Powder. *Powder Technol.* **2003**, *134*, 218−222.
(84) Peng, L.; Qisui, W.; Xi, L.; Chaocan, Z. Zeta-Potentials and Enthalpy Changes in the Process of Electrostatic Self-Assembly of Cations on Silica Surface. *Powder Technol.* **2009**, *193*, 46−49.
(85) Romero, C. P.; Jeldres, R. I.; Quezada, G. R.; Concha, F.; Toledo, P. G. Zeta Potential and Viscosity of Colloidal Silica Suspensions: Effect of Seawater Salts, pH, Flocculant, and Shear Rate. *Colloids Surf., A* **2018**, *538*, 210−218.
(86) Tosha, T.; Matsushima, N.; Ishido, T. Zeta Potential Measured for an Intact Granite Sample at Temperatures to 200 °C. *Geophys. Res. Lett.* **2003**, *30*, 28-1−28-4.
(87) López Valdivieso, A.; Reyes Bahena, J. L.; Song, S.; Herrer Urbina, R. Temperature Effect on the Zeta Potential and Fluoride Adsorption at the α-Al_2O_3/Aqueous Solution Interface. *J. Colloid Interface Sci.* **2006**, *298*, 1−5.
(88) Al-Mahrouqi, D.; Vinogradov, J.; Jackson, M. D. Temperature Dependence of the Zeta Potential in Intact Natural Carbonates. *Geophys. Res. Lett.* **2016**, *43*, 578−587.
(89) Liu, X.; Mäki-Arvela, P.; Aho, A.; Vajglova, Z.; Gun'ko, V. M.; Heinmaa, I.; Kumar, N.; Eränen, K.; Salmi, T.; Murzin, D. Yu. Zeta Potential of Beta Zeolites: Influence of Structure, Acidity, pH, Temperature and Concentration. *Molecules* **2018**, *23*, 946−959.
(90) Ramachandran, R.; Somasundaran, P. Effect of Temperature on the Interfacial Properties of Silicates. *Colloids Surf.* **1986**, *21*, 355−369.
(91) Duffy, T. S.; Raman, B.; Hall, D. M.; Machesky, M. L.; Johns, R. T.; Lvov, S. N. Experimentation and Modeling of Surface Chemistry of the Silica-Water Interface for Low Salinity Waterflooding at Elevated Temperatures. *Colloids Surf., A* **2019**, *570*, 233−243.
(92) Rodriguez-Santiago, V.; Fedkin, M. V.; Lvov, S. N. Electrophoresis System for High Temperature Mobility Measurements of Nanosize Particles. *Rev. Sci. Instrum.* **2008**, *79*, No. 093302.
(93) Wiśniewska, M. The Temperature Effect on Electrokinetic Properties of the Silica−Polyvinyl Alcohol (PVA) System. *Colloid Polym. Sci.* **2011**, *289*, 341−344.
(94) Vinogradov, J.; Jackson, M. D. Zeta Potential in Intact Natural Sandstones at Elevated Temperatures. *Geophys. Res. Lett.* **2015**, *42*, 6287−6294.
(95) Vinogradov, J.; Jackson, M. D.; Chamerois, M. Zeta Potential in Sandpacks: Effect of Temperature, Electrolyte pH, Ionic Strength and Divalent Cations. *Colloids Surf. A* **2018**, *553*, 259−271.
(96) Janusz, W.; Matysek, M. Coadsorption of Cd(II) and Oxalate Ions at the TiO_2/Electrolyte Solution Interface. *J. Colloid Interface Sci.* **2006**, *296*, 22−29.
(97) Erdemoğlu, M.; Sarikaya, M. Effects of Heavy Metals and Oxalate on the Zeta Potential of Magnetite. *J. Colloid Interface Sci.* **2006**, *300*, 795−804.
(98) Nguyen, M. N.; Dultz, S.; Tran, T. T. T.; Bui, A. T. K. Effect of Anions on Dispersion of a Kaolinitic Soil Clay: A Combined Study of Dynamic Light Scattering and Test Tube Experiments. *Geoderma* **2013**, *209−210*, 209−213.
(99) Xu, R.; Li, C.; Ji, G. Effect of Low-Molecular-Weight Organic Anions on Electrokinetic Properties of Variable Charge Soils. *J. Colloid Interface Sci.* **2004**, *277*, 243−247.
(100) Kosmulski, M.; Prochniak, P.; Rosenholm, J. B. Surface-Induced Electrolytic Dissociation of Oxalic Acid in Polar Organic Solvents. *Langmuir* **2010**, *26*, 1904−1909.
(101) Nero, M. D.; Galindo, C.; Bucher, G.; Georg, S.; Mazan, V.; Barillon, R. Speciation of Oxalate at Corundum Colloid−Solution Interfaces and its Effect on Colloid Aggregation under Conditions Relevant to Freshwaters. *Colloids Surf., A* **2013**, *418*, 165−173.

https://dx.doi.org/10.1021/acs.jpcc.9b11371
J. Phys. Chem. C 2020, 124, 3159−3170

Article DB6

Bischoff, M.; **Biriukov, D.**; Předota, M.; Roke, S.; Marchioro, A.

Surface Potential and Interfacial Water Order at the Amorphous TiO_2 Nanoparticle/Aqueous Interface

Submitted to Journal of Physical Chemistry C **2020**;
IF (2018) = 4.309

Participation of Denys Biriukov:

DB performed all the molecular simulations, analyzed the results, and participated in the paper writing.

Surface Potential and Interfacial Water Order at the Amorphous TiO_2 Nanoparticle/Aqueous Interface

Marie Bischoff[1], Denys Biriukov[2], Milan Předota[2], Sylvie Roke[1]* and Arianna Marchioro[1]*

[1] *Laboratory for fundamental BioPhotonics (LBP), Institute of Bioengineering (IBI), and Institute of Materials Science (IMX), School of Engineering (STI), École polytechnique fédérale de Lausanne (EPFL), CH-1015 Lausanne, Switzerland.*

* *E-mail : arianna.marchioro@epfl.ch, sylvie.roke@epfl.ch*

[2] *Institute of Physics, Faculty of Science, University of South Bohemia, 370 05 České Budějovice, Czech Republic*

Abstract

Colloidal nanoparticles exhibit unique size-dependent properties differing from their bulk counterpart, which can be particularly relevant for catalytic applications. To optimize surface-mediated chemical reactions, the understanding of the microscopic structure of the nanoparticle-liquid interface is of paramount importance. Here we use polarimetric angle-resolved second harmonic scattering to determine surface potential values as well as interfacial water orientation of ~100 nm diameter amorphous TiO_2 nanoparticles dispersed in aqueous solutions, without any initial assumption on the distribution of interfacial charges. We find three regions of different behavior with increasing NaCl concentration. At very low ionic strengths (0-10 μM), the Na^+ ions are preferentially adsorbed at the TiO_2 surface as inner sphere complexes. At low ionic strengths (10-100 μM), a distribution of counterions equivalent to a diffuse layer is observed, while at higher ionic strengths (>100 μM), an additional layer of hydrated condensed ions is formed. We find a similar behavior for TiO_2 nanoparticles in solutions of different basic pH. Compared to identically-sized SiO_2 nanoparticles, the TiO_2 interface has a higher affinity for Na^+ ions, which we further confirm with molecular dynamics simulations. With its ability to monitor ion adsorption at the surface with micromolar sensitivity and changes in the surface potential, AR-SHS is a powerful tool to investigate interfacial properties in a variety of (photo)catalytic applications.

Introduction

Titanium dioxide (TiO_2) is a semiconductor material with a high physical and chemical stability[1,2] which makes it particularly interesting for use in aqueous environments. Titania has a broad range of applications: It is widely used as white pigment in paints, in food coloring, as well as in cosmetics and personal care products, such as sunscreen and toothpaste.[3–6] Furthermore, TiO_2 is a well-known photocatalyst, used amongst others in environmental remediation through photocatalytic waste water treatment,[6–9] as building material for self-cleaning glass[7,10,11] and for energy applications, such as photocatalytic water splitting.[12–14] The understanding of the surface chemical reactivity of TiO_2 is key to develop highly efficient, low-cost and environmentally-friendly photocatalytic devices. Thus, it is of fundamental interest to understand the microscopic structure of this semiconductor-liquid interface and how it is affected by the composition of the surrounding aqueous environment.

As colloidal nanoparticles possess a high surface to volume ratio, which is beneficial in order to enhance surface-mediated chemical reactions, they are an attractive and relevant system to study in this context. Colloids in water or another fluid are only stable in solution if they develop a charged layer at their surface, so that the repulsive forces between the particles are strong enough to prevent aggregation or flocculation. The surface charge of the particles depends on the pH and ionic strength of the aqueous environment and is compensated by counterions in the surrounding solution.[15,16] This charged surface together with its counterions is called “electrical double layer” (EDL). The EDL plays a fundamental role in driving physical and chemical processes at the interface. However, a complete picture of the EDL is still missing. Multiple models describing the EDL have been put forward, which usually simplify the complex structure of the interface by assuming a uniformly charged interface, by reducing the aqueous environment to a uniform dielectric and by representing the ions as point charges. A model frequently referred to is the Gouy-Chapman model in which the counterions are distributed in the fluid surrounding a charged surface in such a way that the potential inside the electrolyte decays exponentially.[2,16] This charge distribution inside the EDL is called the diffuse layer (DL). As this model fails for high charge densities of counterions near the interface, a modification was proposed by Stern, which involves the formation of a layer of hydrated counterions at the surface, the so called “Stern Layer”. This layer of countercharges close to the charged surface is expected to act like a parallel plate capacitor, causing a steep linear potential drop within the Stern layer.[2,16–19] Nevertheless, a complete realistic description of the EDL remains challenging, as the electrostatic environment of the interface depends on many factors, such as individual material properties comprising the local chemical nature of the surface, the

amount and the type of ions as well as their solvation shells and the behavior of the solvent, as for example the orientation of water molecules at the interface.[2,16,19–24] Most of those parameters are difficult to access experimentally, especially without using the assumptions implied by the presented models.[20]

The simplest approach to investigate the EDL is to use techniques measuring electrokinetic mobilities. The velocity of a suspension of particles in an applied electric field is measured and can be converted into zeta potential via the Hückel or Smoluchowski equation.[16,17,19,25] In a simplified picture[26] the zeta potential is the potential at the boundary between the solvent shell of ions and water molecules moving with the particle when an electric field is applied, and the rest of the static solution. This boundary is commonly termed the shear plane. However, as the shear plane is presumed to be situated 0.3 to 1 nm away from the charged particle surface,[16,17,19] the knowledge of the zeta potential alone does not provide a full picture of the electrostatic environment of the investigated sample. In order to have a more complete picture of the EDL, one can also measure the surface charge density of the particle, which can be obtained by potentiometric titrations.[27–31] Yet this technique requires larger quantities of sample (in the order of hundreds of milligrams) and assumes that ions only adsorb on the surface (i.e. the sample is non-porous) [27] therefore providing, at best, an upper limit for the surface charge density.

A more direct indicator of the electrostatic environment around a charged particle in solution is the surface potential. With current experimental methods, this is a rather complicated parameter to access. Kelvin Probe Force Microscopy (KPFM) can probe surface potentials of semiconductor/air or semiconductor/vacuum interfaces on flat surfaces. In this case, the surface potential is defined as the work function difference of the semiconductor surface and the metal tip probing the surface.[32] However, applying this technique to solid/liquid interfaces brings up practical challenges[33,34] and is not to date applicable to particles in solution. So far, a method that has been proved to be suitable for the measurement of surface potential of particles in aqueous environments is X-ray photoelectron spectroscopy (XPS). XPS measurements were done on colloidal SiO_2 particles in a liquid microjet by Brown et al.,[35–38] assigning the charge divided binding energy difference between the Si 2p photoelectrons in an environment containing salt and the Si 2p photoelectrons at the point of zero charge to the value of the surface potential. Nevertheless, this method requires small-sized colloidal nanoparticles (~3-20 nm) and high salt concentrations of ~>50 mM, in addition to synchrotron facilities. First ambient pressure XPS studies on anatase TiO_2 particles in a liquid jet were performed by Makowski et al.,[39] examining the role of surface charge in the electronic surface band banding of the semiconductor particles in contact with an electrolyte. Soft-X-ray photoelectron

spectroscopy measurements with a liquid microjet were also applied to anatase TiO_2 particles in another study by Ali et al. to investigate the interaction between specific surface sites and water molecules in the aqueous environment in different pH conditions.[40] However, to the best of our knowledge no direct surface potential measurements have been performed on TiO_2 particle dispersions until now.

Second-order nonlinear optical techniques are suitable to study processes at surfaces and interfaces of centrosymmetric systems as second harmonic generation (SHG) is forbidden in centrosymmetric and isotropic media and therefore the signal arises only from the non-centrosymmetric regions at the interface.[41–44] Nonlinear second-order scattering was used to obtain information about the interfacial properties of particles in liquids by the Eisenthal group,[45] including TiO_2 particles.[46] A first attempt to measure the surface potential of particles in solution was done in the same group by Yan et al.[47] They collected SHG of polystyrene sulfate spheres with a wide collection angle in the forward scattering direction and extracted the surface potential by fitting their data to the Gouy-Chapman model. Yang et al.[48] were the first to measure resonant angular-resolved second harmonic scattering (AR-SHS) patterns from polystyrene colloids with surface-adsorbed malachite green in water. The angular-dependent scattering pattern is strongly polarization-dependent and holds information about the size and shape of the particles.[48–50]

We recently showed the universal applicability of polarimetric angle-resolved second harmonic scattering (AR-SHS) in non-resonant conditions to extract values for the surface potential Φ_0 of a particle with respect to bulk liquid,[51–55] with no *a priori* theoretical treatment to model the distribution of charges in the electrical double layer. Furthermore, AR-SHS enables to obtain absolute values for the surface susceptibility $\mathbf{C}_{S,2}^{(2)}$, which contains information about the orientation of interfacial water molecules. This non-resonant SHS technique has the advantage of being non-invasive, and performed at ambient pressure on particles of a broad size range that are directly dispersed in solution. In this work we apply AR-SHS to semiconductor particles, showing how the surface potential and surface susceptibility of ~100 nm diameter amorphous TiO_2 particles evolve as a function of NaCl and pH. Three different regions can be identified with increasing ionic strength. We compare the results to SiO_2 particles of the same size investigated in different ionic strength conditions. Our findings are further supported with molecular information gathered by molecular dynamics (MD) simulations. The knowledge of surface potential and surface susceptibilty, together with the zeta potential and MD simulations, allow to get a deeper

understanding of the microscopic structure of the EDL around colloidal TiO_2 and SiO_2 in different salt and pH conditions.

Materials and Methods

A. Chemicals

Sodium hydroxide, (NaOH, > 99.99% trace metals basis, Sigma-Aldrich) and sodium chloride (NaCl, >99.999%, abcr GmbH) were used as received. TiO_2 colloids (~100 nm diameter) were purchased already dispersed in solution from Corpuscular Microspheres Nanospheres (2.5% w/v). SiO_2 microspheres of 100 nm diameter were purchased from Polysciences, Inc. (5.9% w/w). The particles were washed as described in the sample preparation section.

B. Sample preparation

All procedures described hereafter used ultrapure water (MilliQ, Millipore, Inc., electrical resistance of 18.2 $M\Omega \cdot cm$). The 2.5 w/v% stock solution of colloidal TiO_2 particles was sonicated for 30 min (35 kHz, 400 W, Bandelin) and vortexed 2 min prior to usage. The stock was then diluted in water to a 0.5 w/v% solution, where the particles were stabilized by addition of NaOH up to a final concentration of 80 μM. The 0.5 w/v% dilution was then further sonicated for 10 min and vortexed 2 min. In order to remove residual ions from the synthetic procedure, nanoparticles were then collected via centrifugation and resuspended in MilliQ water at the same concentration of 0.5 w/v%. The pellet was resuspended by vortexing 5 min and ultrasonicating for 10 minutes. The conductivity of the washed particles was measured as described in section **C** to ensure that the initial ionic strength of the particle solution was as low as possible. The TiO_2 particles were further diluted to 0.05 w/v% solutions (corresponding to approximately $4.3 \cdot 10^{11}$ particles/ml) containing the desired amount of NaOH or NaCl. The pH or ionic strength of the solutions was adjusted using 0.1 mM or 1 mM solutions of NaOH and NaCl. The 0.05 w/v% solutions were vortexed 2 min and sonicated 10 min, then filtered using four 0.2 μm PES syringe filters (Filtropur Sarstedt) per 10 ml tube to remove particle aggregates. After filtering, each sample was sonicated another 10 min and vortexed 2 minutes. The TiO_2 solutions were prepared and measured on the same day. Corresponding water references at the same

pH/ionic strength were prepared for each TiO_2 sample. For SiO_2 particle solutions and references a similar preparation procedure was employed. The particles were washed twice but no additional NaOH was added. The SiO_2 stock solution was diluted to a 0.06% (w/v) solution (corresponding to approximately $2.9 \cdot 10^{11}$ particles/ml) containing the desired amount of NaOH or NaCl. No filtering of the particles was necessary. All preparation steps and measurements were performed at room temperature.

C. Sample characterization

The particle size distribution was determined by dynamic light scattering (DLS) and the zeta potential was measured by electrophoretic measurements (Zetasizer Nano ZS, Malvern). After the filtering process, the TiO_2 colloids had a mean hydrodynamic diameter of ~ 120 nm with a uniform size distribution (for most samples, polydispersity index (PDI) ~ 0.1). The SiO_2 particles had a mean hydrodynamic diameter of ~ 125 nm with a uniform size distribution (polydispersity index (PDI) < 0.05). Average radii and zeta potentials are given as the average of 3 measurements. The pH of the samples was determined using a pH-meter (HI 5522 pH/ISE/EC bench meter and HI 1330 pH electrode, Hanna Instruments) calibrated with the appropriate buffer solutions. In order to control the amount of salt added to the samples and the initial ionic strength of the washed TiO_2 particles in water, the conductivity was measured by two different means. Firstly, using a conductivity-meter (HI 5522 pH/ISE/EC bench meter and HI 76312 conductivity electrode, Hanna Instruments) calibrated with the appropriate buffer solutions and secondly, using the conductivity obtained from the zeta potential measurements (Zetasizer Nano ZS, Malvern). Knowing the conductivity σ, the average ionic strength, represented by the concentration of ions in solution *c* was calculated using the equivalent (molar) ionic conductivity Λ_m [56]:

$$c = \frac{\sigma}{\Lambda_m} = \frac{\sigma}{\sum_i \upsilon_i \lambda_i}$$

Here λ_i are the equivalent ionic conductivities of the cations and anions present in the electrolyte that were taken from reference [57] and υ_i refers to the number of moles of each ion. In cases where the theoretical salt concentration of the sample is below 0.5 mM, the ionic molar conductivity at infinite dilution Λ_m° can be used, whereas for a theoretical concentration of above 0.5 mM the ionic molar conductivity Λ_m should be calculated

according to the Debye-Hückel-Onsager equation. For all the samples considered here with a salt concentration below 0.5 mM, the ionic molar conductivity at infinite dilution Λ_m° was used.

For TiO_2 samples diluted in ultrapure water where no salt was added, the average conductivity was assumed to be due to residual Na^+ and OH^- ions from the preparation process. The measured conductivity values of washed and filtered samples at pH 7 without additional salt of the same particle batch varied from 9.7 to 11.3 μS/cm (corresponding to an ionic strength of $3.9 \cdot 10^{-5}$ and $4.6 \cdot 10^{-5}$ mol/l). This conductivity, attributed to residual Na^+ and OH^- ions in solution, was subtracted from the conductivity measured for TiO_2 samples where salt was added, in order to calculate the pure contribution of Na^+ and Cl^- ions to the ionic strength of the solution. The total ionic strength value of the samples used in the fitting procedure includes the ionic strength originating from the Na^+ and Cl^- ions, as well as the residual Na^+ and OH^- ions.

D. AR-SHS model and theory

In the following we want to briefly summarize some of the important aspects of the AR-SHS model and the nonlinear optics theory that are relevant for the fitting procedure. A more detailed description can be found elsewhere.[51–53,58,59] In a non-resonant AR-SHS experiment, the fundamental frequency of a high energy femtosecond laser pulse interacts with an aqueous solution that contains particles. The intense femtosecond laser pulses distort the electron clouds of all non-centrosymmetric molecules which causes a displacement of charge with a frequency component of $2w$. These induced charge oscillations are to leading order the origin of molecular dipole moments. The sum of the molecular SH dipoles results in a macroscopic polarization $\mathbf{P}^{(2)}$. This polarization $\mathbf{P}^{(2)}$ is defined as:

$$\mathbf{P}^{(2)}{}_{2\omega} = \varepsilon_0 \chi^{(2)} : \mathbf{E}(\omega)\mathbf{E}(\omega) \tag{1}$$

where ε_0 is the permittivity of free space, $\chi^{(2)}$ is the second order susceptibility, which describes the local second harmonic response of the medium, and $\mathbf{E}(\omega)$ is the incoming electromagnetic field for SHS. The generated electromagnetic wave has double the frequency $(2w)$ of the incoming light. In the electric dipole approximation, the emission of SH light is forbidden in the bulk of centrosymmetric media as they possess inversion

symmetry. Considering a spherical particle with an isotropic amorphous interior, and water as an isotropic liquid, the SH signal originates specifically from the non-centrosymmetric regions at the interface. Under non-resonant conditions, the second-order polarization $\mathbf{P}^{(2)}$ depends on the molecular electron density in the interfacial region. Therefore, every non-centrosymmetric molecule in the non-centrosymmetric region around the particle contributes equally to the SH polarization. However, since the SH intensity scales quadratically with the number density of molecules, the majority of the SH signal intensity originates from water molecules at the interface, as the number of non-centrosymmetrically distributed surface groups of the particle is much smaller than the number of oriented water molecules at the interface. The SHS signal then arises from the net orientational order of water molecules along the surface normal. Besides the $\chi^{(2)}$ contribution to the SHS signal that describes the orientational order induced by all (chemical) interactions confined to the particle surface plane, the electrostatic field E_{DC} generated between the counterions and the charged surface affects the SHS signal. The effective third-order susceptibility tensor $\chi^{(3)'}$ represents all processes that lead to the emission of SH light and require an interaction with E_{DC}. This includes the reorientation of water molecules in the interfacial region and in the bulk solution (main $\chi^{(3)'}$ contributions) as well as a pure third-order interaction that arises from the isotropic third-order susceptibility of bulk water. The resulting effective third-order polarization $\mathbf{P}^{(3)'}$ is defined as:

$$\mathbf{P}^{(3)'}{}_{2\omega} \propto \varepsilon_0 \chi^{(3)'} : \mathbf{E}(\omega)\mathbf{E}(\omega)\Phi_0 \tag{2}$$

with $\Phi_0 = \int_0^{+\infty} E_{DC}(z)dz$ being the surface potential. We then obtain for the total SHS intensity $I_{2\omega} = \left|\mathbf{P}^{(2)}_{2\omega} + \mathbf{P}^{(3)'}_{2\omega}\right|^2$. Thus, within the Rayleigh-Gans-Debye-(RGB) approximation, which assumes no reflection nor absorption by the scatterer, the SHS intensity can be given as:

$$I_{2w} \mu \left| G^{(2)}(R, c_S^{(2)}, q) + G^{(3)'}(R, c^{(3)'}, q, k^{-1}) \times F_0 \right|^2 \tag{3}$$

where R is the particle radius, θ the scattering angle, k^{-1} the Debye length (directly correlated to the ionic strength of the solution). The Debye length is defined as $k^{-1} = \sqrt{(e_0 e_r k_B T)/(2000 e^2 z^2 N_{Av} c)}$ and takes into account the vacuum and relative permittivity ε_0 and ε_r respectively, the Bolzmann constant k_B, the temperature T, the elementary charge *e*, the valency z, Avogadro's number N_{Av} and the ionic concentration *c*. $G^{(2)}$ and $G^{(3)'}$ are respectively the effective second- and third-order susceptibilities that are connected to the two SHS contributions $\chi^{(2)}$ and $\chi^{(3)'}$ through multiplication of geometrical form factors that are specific to the geometry of the scatterer and the geometry of the incoming and outgoing electromagnetic fields. The geometrical form factors for spheres are shown in the Supplementary Information. In the experimental geometry that we use, we obtain nonzero normalized SHS signal in two independent polarization combinations of light: PPP and PSS=SSP=SPS. Here the first letter refers to the polarization state of the SH beam and the second and third letter refer to that of the fundamental incoming beam. P polarized light is parallel and S polarized light is perpendicular to the scattering plane. Within the aforementioned RGD approximation, the scattered intensity from a sphere or shell in the two independent polarization combinations normalized by the bulk water signal can analytically be expressed as:

$$\frac{I_{PPP}(w)}{I_{SSS}(w)} = \frac{e_0^2 \left(E_P(w)^2 \left[\cos\left(\frac{q}{2}\right)^3 (G_1^{(2)}) + \cos\left(\frac{q}{2}\right)(G_2^{(2)} + G_2^{(3)'})(2\cos(q)+1) \right] \right)^2}{\bar{m}^2 N_b / N_p} \quad (4)$$

$$\frac{I_{PSS}(w)}{I_{SSS}(w)} = \frac{e_0^2 \left(E_S(w)^2 \left[\cos\left(\frac{q}{2}\right)(G_2^{(2)} + G_2^{(3)'}) \right] \right)^2}{\bar{m}^2 N_b / N_p} \quad (5)$$

where $\bar{m} = \bar{b}^{(2)}_{H_2O} E(w)^2$ is the averaged induced second-order dipole moment with $\bar{b}^{(2)}_{H_2O}$ being the averaged hyperpolarizability of water. N_p is the number of particles and N_b is the density of bulk water ($3.34 \cdot 10^{28}$ molecules/m^3), so that N_b / N_p is the number of bulk water molecules per particle. A summary of all the relevant constants and analytical expressions used can be found in Tables S1 and S2 in the Supplementary Information for completeness. Note that the effective third-order susceptibility $G^{(3)'}$ is directly related to

the surface potential Φ_0 and the effective second-order susceptibility $G^{(2)}$ is related to the orientation of water molecules at the interface given by $\chi^{(2)}$ as described in equation 3. By fitting the measured and normalized AR-SHS patterns in two different polarization combinations according to equations 4 and 5 absolute values for the surface potential and the orientation of water molecules at the surface can be extracted. More information about the measurements and the normalization procedure can be found in the next section.

E. AR-SHS measurements

The second harmonic scattering measurements were performed on the same SHS setup previously described in detail in Refs.[53,55,60] To measure AR-SHS, a pulsed 190 fs Yb:KGW laser (Pharos-SP system) with a center wavelength of 1028 nm, a repetition rate of 200 kHz and an average power of 80 mW was focused into a cylindrical glass sample cell (4.2 mm inner diameter, high precision cylindrical glass cuvettes, LS instruments). The input- (output-) polarization was controlled by a Glan-Taylor polarizer (GT10-B, Thorlabs) and a zero-order half wave plate (WPH05M-1030), and another Glan Taylor polarizer (GT10-A, Thorlabs), respectively. The beam waist was about $2w_0 \sim 36\,\mu m$; the corresponding Rayleigh length was ~ 0.94 mm. The scattered SH light was collected, collimated with a plano-convex lens (f = 5 cm), polarization analyzed and filtered (ET525/10, Chroma) before being focused into a gated photomultiplier tube (H7421-40, Hamamatsu). The acceptance angle was set to 3.4° for scattering patterns. Patterns were obtained in steps of 5° from θ=-90° to θ=90° with 0° being the forward direction of the fundamental beam. Data points were acquired using 20 x 1.5 s acquisition time with a gate width of 10 ns. To correct for incoherent hyper Rayleigh scattering (HRS) from the solvent phase, both the SHS response from the sample solution $I(q)_{SHS,\,sample}$ and the HRS response from a solution of identical ionic strength/pH but without nanoparticles $I(q)_{HRS,\,solution}$ are collected. The HRS is subtracted from the SHS signal of the sample and the obtained difference is then normalized to the isotropic SSS signal of pure water $I(q)_{HRS,\,water,\,SSS}$ to correct for differences in the beam profile on a day-to-day basis:

$$I_{PPP}^{Norm}(q) = \left[\frac{I(q)_{SHS,\,sample,\,PPP} - I(q)_{HRS,\,solution,\,PPP}}{I(q)_{HRS,\,water,\,SSS}} \right] \qquad (6)$$

Here, the normalized signal of the sample $I^{Norm}(\theta)$ is given for SHS in PPP polarization combination. The normalization procedure was applied in the same way for SHS measured in PSS polarization combination. In order to obtain absolute values for the surface potential Φ_0 and the surface susceptibility $C_{S,2}^{(2)}$ as a measure of surface molecular orientation of water molecules, the relative measured SHS signal needs to be related to absolute quantities. Here we use the fact that the second order hyperpolarizability $\beta^{(2)}$ and the third order hyperpolarizability $\beta^{(3)}$ of uncorrelated water are known, so that through normalization by $I(q)_{HRS,\,water,\,SSS}$, the measured SHS response can directly be linked to an absolute value of the $\beta^{(2)}$ component of the particle solution. The second order hyperpolarizability $\beta^{(2)}$ is connected to the second order susceptibility $\chi^{(2)}$, which than can be used to determine the orientation of water molecules at the interface. The particle interface of a spherical scatterer can be considered as isotropic in the interfacial plane (tangential coordinates are degenerate). This reduces the 27 possible $\chi^{(2)}$ tensor elements to only 4 non-zero $\chi^{(2)}$ elements ($C_{S,1}^{(2)}$, $C_{S,2}^{(2)}$, $C_{S,3}^{(2)}$, $C_{S,4}^{(2)}$). Considering a lossless medium (appropriate for non-resonant SHG) and Kleinman symmetry, 3 of the 4 remaining elements are degenerate ($C_{S,2}^{(2)} = C_{S,3}^{(2)} = C_{S,4}^{(2)}$). Assuming that the orientational distribution of water molecules at the interface is broad, $C_{S,1}^{(2)}$ can be neglected. Knowing $C_{S,2}^{(2)}$ is therefore sufficient to describe the molecular ordering at the surface. As a sign convention for $C_{S,2}^{(2)}$ we use the following: negative values for water molecules with O atoms pointing towards the surface (dipole moment pointing away from the surface) and positive values for water molecules with H atoms pointing towards the surface (dipole moment pointing in direction of the surface). This sign convention arises from a comparison to values obtained from SFG studies.[61]

The fitting procedure using the AR-SHS model that allows to determine Φ_0 and $C_{S,2}^{(2)}$ is described in detail elsewhere.[53–55] It uses the analytical equations 4 and 5 and takes into consideration the particle radius R, as it was measured by dynamic light scattering (DLS), the ionic strength, as determined from conductivity measurements, the refractive indices of water (1.33)[62] and TiO_2 (2.61)[63] or SiO_2 (1.46)[64], the SH wavelength λ = 514 nm, the temperature T and the number of particles/ml.

We note that the errors that we report for the surface potential Φ_0 and the $C_{S,2}^{(2)}$ are based on the statistical errors of the measured AR-SHS patterns prior to normalization. The errors on Φ_0 and $C_{S,2}^{(2)}$ are numerical errors on the fitting procedure.

Other sources of error may contribute to the total error, such as the variations in the experimentally determined parameters (i.e. the particle radius, the number of particles or the ionic strength). An estimation of the influence of those uncertainties on the surface potential Φ_0 and the surface susceptibility $C_{S,2}^{(2)}$ was done for oil droplets in water and can be found in ref.[53]

F. Molecular dynamics simulations

TiO_2 was modeled as a negatively charged (-0.104 C/m^2) hydroxylated rutile (110) surface,[65] while as SiO_2 model we used a negatively charged (-0.12 C/m^2) quartz (101) surface.[66] Water was modeled as rigid SPC/E,[67] whereas parameters for Na^+ ions were taken from the literature.[68] All employed models utilize the electronic continuum correction (ECC) theory,[69] which in a mean-field way incorporates electronic polarization effects into classical, nonpolarizable MD simulations. Other technical details of the simulations are the same or similar to those in our previous works.[55,65,66]

Results and Discussion

Surface potential and water order under different ionic strength conditions

Part **A** of Figure 1 shows AR-SHS patterns of colloidal ~100 nm diameter amorphous TiO_2 particles in two different polarization combinations (PPP and PSS). The scattering patterns were measured for different concentrations of NaCl ranging from 0 to 300 μM.

Both PPP and PSS AR-SHS patterns show a decrease of the normalized SHS intensity with increasing salt concentration. At a higher ionic strength, more counterions will be situated in proximity of the charged interface of the particle, leading to a reduced penetration of the electrostatic field E_{DC} in the electrolyte solution. As a consequence, the

volume of the overall probed water shell around the particles is reduced, resulting in a lower SHS intensity with increasing ionic strength. The solid lines represent the fit of the corresponding data points using the AR-SHS model described in Materials and Methods Section D. The results of the fits for the surface potential Φ_0 and the surface susceptibility $C_{S,2}^{(2)}$ as a function of added NaCl are shown graphically in Figure 1**B** and are given in Table **1**. Tables S3 and S5 (Supplementary Information) summarize all the parameters used for the fitting. Note that the radius obtained through DLS measurements indicated in Table **1** is slightly larger than the nominal radius of the particles.

The zeta potential ζ of the TiO_2 samples in different ionic strength conditions is presented in Figure 1**B** for comparison to the surface potential. The zeta potential is a common measure for the stability of a particle suspension, and values around +/- 30 mV are generally indicative of stable suspensions.[70] The isoelectric point ($\zeta = 0$) was determined through electrophoretic mobility measurements and is close to pH 4 for the here used colloidal ~100 nm diameter amorphous TiO_2 particles. It can be seen that the zeta potential does not change in magnitude and remains between -24 mV to -30 mV, whereas the surface potential varies from -12 mV to -326 mV in the investigated ionic strength range. For the behavior of the surface potential three different regions can be identified: i) 0-10 μM NaCl, where $|\Phi_0| > |\zeta|$, ii) 10-100 μM NaCl, where $|\Phi_0| \approx |\zeta|$ and iii) above 100 μM NaCl where $|\Phi_0| >> |\zeta|$. At the same time, the surface susceptibility shown in the bottom part of Figure 1**B** changes in sign between 10 and 50 μM NaCl. Negative values of $C_{S,2}^{(2)}$ indicate that the net dipole moment of water molecules points away from the surface (oxygens towards the surface), while positive values of $C_{S,2}^{(2)}$ indicate that the average orientation of water molecules is with their dipole moment facing the surface (hydrogens towards the surface).

As all the ionic strength measurements were carried out at pH 7, above the isoelectric point of the TiO_2 particles, the particle surface is expected to be mainly composed of hydroxyl groups, with only a few deprotonated hydroxyl groups. We estimate the deprotonation to be between 1% and 8% at pH 7 using surface charge densities values from the literature (See Supplementary Material). This estimation is only meant as a guidance as very different surface charge density values have been reported by different groups[28–31] These values can greatly differ depending on the size and the crystal phase of the particles, as well as the synthetic procedure. For the less known amorphous phase, no record of surface charge density values could be found so far. Our results show negative values of zeta potentials, as anticipated for a negatively charged surface. In the very low ionic strength

range (0-10 μM NaCl), where $|\Phi_0| > |\zeta|$, we observe that the magnitude of the surface potential decreases until a value of the same magnitude of the zeta potential is reached (see Figure 2**A**,**B)**. We assign this behavior to arise from positively charged Na^+ ions that directly adsorb at the O^- surface groups of the colloids (inner sphere complex), as it is illustrated in Figure 2**B**. Because of the reduction of the effective negative surface charge by the adsorbed counterions, the magnitude of the surface potential will decrease accordingly. Additionally, in this ionic strength region the surface susceptibility is negative, which indicates that the interfacial water molecules are oriented with their net dipole moment away from the surface (oxygens towards the surface). This behavior can be explained by hydrogen bonding between the hydroxyl surface groups of the TiO_2 particles and the oxygen atoms of the water molecules.

In the low ionic strength region (10-100 μM NaCl), the surface potential reaches a minimum in magnitude and is close to zero. This suggests that once all the favorable sites have been occupied by direct adsorption of the counterions, further addition of salt does not affect the surface potential, and thus neither the surface charge density in this concentration range. Our experiment cannot provide insights on the nature of these favorable sites. However, it evidences that only a fraction of the deprotonated hydroxyls is occupied by direct adsorption of Na^+, as a complete coverage would result in a neutral particle ($\Phi_0 = 0$), which could not be stable in solution and would precipitate. Furthermore, the surface potential remains very close to the zeta potential up to 100 μM NaCl. As the zeta potential is considered to be located a few water layers away from the surface,[16,17,19] a value of surface potential close to the zeta potential suggests that there are no mobile counterions accumulated in between the shear plane and the surface, but that they are rather distributed in solution. In the Gouy-Chapman model, this would be equivalent to a diffuse layer forming around the TiO_2 particles, which is illustrated in Figure 2**C**. At the same time, we observe a change in sign of the surface susceptibility between 10 μM and 50 μM of added NaCl. This reflects a change in orientation of the water molecules situated directly at the interface, as the surface susceptibility describes the orientational order induced by all (chemical) interactions confined to the particle surface plane (see Materials and Methods). The average surface molecular directionality changes from the net dipole moment pointing away from the surface (oxygens toward the surface) to the net dipole moment pointing towards the surface (hydrogens toward the surface). Therefore, it can be argued that, above a certain threshold, the presence of Na^+ near the interface is responsible for the change in directionality of interfacial water. This phenomenon can be rationalized by the rearrangement of the H-bonding network between the Ti-OH groups and the surface water molecules caused by the Na^+ ions.

In the higher ionic strength region above 100 μM NaCl, where $|\Phi_0| >> |\zeta|$, we observe a strong increase in magnitude of the surface potential with salt concentration. This large deviation from the zeta potential suggests the formation of a condensed layer of ions at the interface, which is further supported by the observation of the drastic reduction in the SHS intensity. This charge condensation layer is also predicted by the Gouy-Chapman-Stern model, where the steep potential drop in the very first interfacial layers is approximated to the linear potential drop in a parallel plate capacitor. Taking the distance between the surface and the zeta potential plane to be between 0.3 and 0.9 nm (1 to 3 water molecules),[16,17,19] the electric field can be estimated here to be ca. $3 \cdot 10^8$ to $1 \cdot 10^9$ V/m for an ionic strength of 300 μM NaCl. This large value of the electric field in the interfacial region provides additional evidence of the presence of a condensed layer of ions. The latter is schematically illustrated in Fig. 2**D**. Note that in this case the ions cannot be directly adsorbed at the TiO_2 surface. The absence of water molecules between the negatively charged surface and the counterions would lead to charge neutralization and a consequent decrease in surface potential, as already observed for the very low ionic strength case. As such, the ions are present as outer sphere complexes and likely have one or more layers of water in between them and the surface.

The surface susceptibility has a positive sign in this higher ionic strength region. As a consequence, the net dipole moment of the interfacial water is oriented towards the surface with the hydrogen atoms facing the surface. This behavior further confirms the presence of a strong electric field forming in between the condensed layer of positively charged ions at the interface and the negatively charged TiO_2 particle surface groups. Analogously to the previous case, we expect the net dipole moment to be influenced by the rearrangement of the H-bonding network between the surface hydroxyl groups and the interfacial water molecules, as well as by the presence of additional oriented water molecules belonging to the Na^+ hydration shell. Both the diffuse region and the condensed layer region have been previously experimentally determined for 300 nm diameter SiO_2 particles in a previous report by our group.[55] However interestingly, the direct counterion adsorption was not observed in that case, most likely because the initial ionic strength of the nanoparticles was much higher (0.1 mM, vs. tens of μM here).

Surface potential and water order in different pH conditions

In order to investigate the influence of different surface charge densities on the molecular water order and the surface potential, similar AR-SHS measurements were performed as a function of pH. The pH was adjusted by adding NaOH to the particle

suspension, resulting in a more negatively charged surface. No additional salt was added. The initial TiO_2 dispersion in water prior to NaOH addition had a pH = 7. The results for the AR-SHS patterns of colloidal ~100 nm diameter amorphous TiO_2 in different basic pHs are shown in part **A** of Figure 3. It can be seen that the normalized SHS signal decreases with increasing pH for both polarization combinations, as also observed for increasing salt concentrations in Figure 1**A**, which reflects a smaller number of oriented water molecules. Figure 3**B** shows the surface potential Φ_0 and the surface susceptibility $C_{S,2}^{(2)}$ as a function of the pH of the aqueous environment. A list of the exact values can be found in Table 2. A summary of all the parameters used for the fitting is given in Tables S3 and S6 (Supplementary Information). In this experiment, the range of pH tested was limited by the signal-to-noise ratio for pH > 10.7 and pH < 3. For the 3 < pH < 7, no SHS patterns could be obtained due to particle aggregation that occurs close to the isoelectric point (pH = 4), when the particles become unstable. Despite these limitations, the three behaviors found in Fig.1 are also seen here: Close to pH 7 the magnitude of the surface potential Φ_0 is larger than the zeta potential. For more basic pH (9.5), the surface potential decreases in magnitude and becomes comparable to the zeta potential. For the highest pH investigated here the surface potential increases again in magnitude. A change of sign in the surface susceptibility is observed between pH 9.5 and pH 10.7, indicative of the reorientation of the net dipole moment of interfacial water molecules from oxygens facing the surface to hydrogens facing the surface.

Between pH 7 and pH 11, the surface charge of the colloids is expected to be increasingly negative due to deprotonation of hydroxyl groups at the surface, while the same counterion (Na^+) is expected to interact with the negatively charged groups. As for the neutral pH case, we can estimate the approximate percentage of deprotonation at pH = 9.5 using surface charge density values from the literature (see Supplementary Information) and find it to be between 10% and 35%. This indicates that while the surface is approximately three to ten times more charged than at pH = 7, the majority of the surface groups remain protonated. Given the similarities with the results as a function of ionic strength, we assign these findings to the same mechanisms of counterion adsorption (for pH 7 to pH 9.5), the creation of a diffuse layer (around pH 9.5) and the creation of a layer of condensed ions (for pH > 9.5) as it was discussed in detail above. The change in orientation of the interfacial water molecules from the net dipole moment pointing away from the surface to the net dipole moment pointing towards the surface occurs here between pH 9.5 and pH 10.7. Converting these pH values to the corresponding ionic strength values, we find that the change in sign occurs above 30 μM added NaOH, which is in good agreement with the change in sign observed for the NaCl case (between 10 and 50 μM added NaCl). The fact

that the surface potential values are very similar and that the change in water orientation occurs for similar ionic strengths shows that in the here investigated range of pH and salt, the surface charge density for a given ionic strength is similar, and does not depend on the use of a salt (NaCl) or a base (NaOH). This behavior was already observed for SiO2 particles.[55] It also suggests that the surface charge density at pH 7, pH at which the AR-SHS patterns as a function of salt are recorded, is already negative enough to permit the formation of a layer of condensed counterions.

Comparison of SiO_2 and TiO_2 interfacial properties

In order to determine if the evolution of the surface potential and the water orientation with increasing ionic strength and pH is specific to the nature of the investigated surface, we performed AR-SHS on SiO_2 particles of the same size (~100 nm diameter). SiO_2 was chosen in order to have a comparison with another metal oxide surface bearing the same potential determining ions (H^+ and OH^-). The SiO_2 colloids were found to have a stronger SHS signal than the amorphous TiO_2 particles (both relative to neat water, ~10 times higher, see Supplementary Material) even though the particle density of the two particle suspensions was in the same order of magnitude ($2.9 \cdot 10^{11}$ particles/ml in the case of SiO_2 and $4.3 \cdot 10^{11}$ particles/ml for TiO_2). Figure 4**A** shows the surface potential Φ_0 of 100 nm diameter SiO_2 particles in different NaCl concentrations compared to 100 nm diameter amorphous TiO_2 particles. Three regions of surface potential behavior can also be distinguished for SiO_2 particles. (i) It can be seen that the surface potential of the SiO_2 particles decreases in magnitude with increasing salt concentration for low ionic strength (< 300 μM). (ii) At 300 μM NaCl concentration, the surface potential value is similar to the zeta potential, which is not shown here for clarity but lies in the order of -32 to -48 mV (See Table 3). (iii) For ionic strength > 300 μM the magnitude of the surface potential rises again to values of $|\Phi_0| > |\zeta|$. Compared to TiO_2, the increase in magnitude of the surface potential in region (iii) occurs at a higher ionic strength for SiO_2. Likewise, the decay in magnitude of the surface potential in region (i) until the surface potential $|\Phi_0| \approx |\zeta|$ in region (ii) spans over a wider ionic strength range for SiO_2 compared to TiO_2.

In Figure 4**B** the surface susceptibility $C_{S,2}^{(2)}$ of SiO_2 and TiO_2 can be seen. A change in sign of $C_{S,2}^{(2)}$ from negative values to positive values happens in between a NaCl concentration of 100 μM to 300 μM. This indicates that the reorientation of the net dipole moment of the water molecules from oxygens facing the surface to hydrogens facing the

surface happens at higher ionic strength for SiO_2 than for TiO_2. The surface susceptibility of SiO_2 is one order of magnitude higher than the surface susceptibility of TiO_2, which implies a larger net dipole moment of the interfacial water molecules near the SiO_2 surface compared to the water molecules close to the TiO_2 surface. This larger net dipole moment translates into a stronger ordering of the interfacial water molecules which contributes to the higher SHS intensity observed in the SiO_2 case. Such an effect could be caused by the different molecular surface groups (e.g. bridging or terminal hydroxyls for TiO_2 vs. different siloxane and silanol groups for SiO_2) and their different occurrences, with consequential influence on the interfacial H-bonding network.

The same mechanisms of ion adsorption, formation of a diffuse layer and creation of a layer of condensed charges, which were discussed in detail for the ionic strength dependency of TiO_2 particles and further confirmed in the case of pH variation, can explain the three regions of surface potential and surface susceptibility behavior for the SiO_2 particles. Even though the general behavior is similar for both surfaces, the onset of the three regions as a function of ionic strength is clearly different in the case of SiO_2 particles. Counterion adsorption is more gradual and requires up to 300 μM to reach a minimum in the surface potential magnitude, indicative of a saturation of all the favorable deprotonated hydroxyls. Analogously to the TiO_2, we note here that all the deprotonated hydroxyls cannot be occupied, as this would result in a neutral, unstable particle. It is interesting to see that for both materials, the change in sign of $C_{S,2}^{(2)}$ occurs just before the minimum in the surface potential magnitude is reached. This result suggests that the hypothesized rearrangement of the H-bonding network at the surface by the counterions is already significant enough before the favorable deprotonated hydroxyls are saturated with Na^+ ions. Furthermore, the increase of surface potential magnitudes, which implies the formation of a layer of condensed charges, occurs at ionic strengths above 300 μM in the case of the SiO_2 particles, compared to above 100 μM in the case of TiO_2 particles. Knowing that the density of OH groups per surface area is similar for both surfaces (4.8 OH/nm^2 for TiO_2 [71] and 4.9 OH/nm^2 for SiO_2 [72]), this implies that the TiO_2 surface has a higher affinity to adsorb Na^+ ions than SiO_2, which has been already observed by our simulations comparing the amount of adsorbed cations at negatively charged (and even neutral) rutile and quartz surfaces.[66]

In order to decipher the molecular origin of our experimental results, we performed molecular dynamics (MD) calculations following the same strategy as in our previous study.[55] We adopted our molecular dynamics models of TiO_2 and SiO_2 to investigate and compare the effect of ionic concentration on the orientation of water molecules at these interfaces. TiO_2 was modeled as a negatively charged (-0.104 C/m^2)

hydroxylated rutile (110) surface, while as SiO_2 model we used a negatively charged (-0.12 C/m^2) quartz (101) surface, as described in the Materials and Methods section. A similar negative surface charge density, which is constant in a single simulation, was chosen to fairly compare properties above the point of zero charge for both TiO_2 and SiO_2, when a portion of surface hydroxyls is deprotonated, corresponding to neutral or slightly basic pH.

Despite the fact that the behavior of crystal and amorphous solids used in experiments may differ, the comparison of two crystal forms by simulations still can provide valuable information on sorption properties of both materials. To probe concentration effects, we prepared a set of three systems for each modeled surface. To mimic extremely low concentrations studied in the experiments (μM concentrations) that are not directly accessible in simulations, the number of Na^+ ions in the system was set to be equal to the amount of negative surface charges (and there were no anions). However, the number of ions allowed in the vicinity of the negative surface up to 10 Å varied between 0% compensation (i.e. all the counterions were forced to be further away from the surface), 50% compensation (only half of the ions were allowed in the region up to 10 Å), and 100% compensation (no restriction on the position of ions, i.e. a surface charge could be fully compensated). In the latter case the surface charge could be fully (100%) compensated up to 10 Å. However, due to the equilibrium between the distribution of ions at regions closest to the surface and further away (including the bulk region), in conjunction with the low total number of ions allowed in the simulation, even in this 100% case part of the surface charge remains uncompensated up to 10 Å. This situation resembles our experimental low ionic concentration conditions when, even in the presence of a sufficient number of cations to compensate the surface charge, the particles remain negatively charged and stable.

The measure that can be compared to the experimental data is the integral of the "dipole concentration", which is a product of the average number density of water molecules and the perpendicular component of the water dipole moment with respect to the surface (with positive values indicating hydrogens facing the surface, i.e. as in the experiment). The running integral of the dipole concentration provides an indicator for the buildup of the SHS intensity as a function of distance. The SHS intensity is proportional to the square of this running integral along the z-axis perpendicular to the surface.[55] The plane at z=0 corresponds to the average position of the last TiO layer. Figure 5 shows the running integrals of dipoles as a function of distance for TiO_2 and SiO_2 surfaces. Both surfaces exhibit a similar behavior as a function of sodium concentration as observed in region (i) of SHS experiments: addition of ions to the interface, resulting in inner-sphere complexes (or outer-sphere complexes adsorbed at the surface), shifts the signal towards negative values, i.e. less water molecules are oriented, which is consistent with the effect of adsorbed Na^+

compensating a negative surface charge. Moreover, the rate of change in the interfacial region (up to ≈10 Å from the surface) is more drastic for TiO_2. At 50% compensation, the integrated dipole value at 10 Å is 0.094 D/Å² for TiO_2 and 0.130 D/Å² for SiO_2. At 100% compensation, the integrated dipole value at 10 Å decreases down to 0.026 D/Å² for TiO_2 and to 0.096 D/Å² for SiO_2. This steeper decrease of the integrated dipole moment with the amount of counterions indicates that the surface charge of TiO_2 is more efficiently screened by Na^+ counterions. In other words, less ions are required at the TiO_2 surface to result in similar changes as in the case of SiO_2. This observation is also in line with the SHS experiments, where a minimum in the surface potential magnitude is reached at lower ionic strengths for TiO_2 than for SiO_2. Note also the flat profile of the curve allowing 100% compensation of the TiO_2 surface, compared to the same curve for SiO_2, which is still growing, i.e. gaining further contributions to the SHS signal, with increasing distance from the surface. That clearly documents that while in both cases the ions can fully compensate the surface charge (and eventually do so at large distances), for TiO_2 nearly all the compensation occurs in the nearest vicinity of the surface, while for SiO_2 we observe a wide diffuse layer.

Conclusions

In summary, non-resonant polarimetric AR-SHS was applied for the first time to semiconductor nanoparticles in aqueous environments. By collecting two different polarization combinations of light from a colloidal suspension, the two analytical expressions from nonlinear optical theory containing Φ_0 and $C_{S,2}^{(2)}$ can be solved without assuming any model for the distribution of the ions at the interface. The surface potential and molecular orientation of interfacial water molecules of ~100 nm diameter spherical TiO_2 particles in different NaCl and pH conditions are reported and compared to the results for insulating SiO_2 particles as a function of NaCl concentration. By comparison of the surface potential to the zeta potential, three different regions can be identified: at very low ionic strengths (0-10 μM), Na^+ ions preferentially adsorb as inner sphere complexes. At low ionic strengths (10-100 μM), we observe the presence of a distribution of counterions equivalent to a diffuse layer in the GC model, while at higher ionic strengths (>100 μM), the presence of an additional layer of condensed charges, similar to a Stern layer in the GCS model, is detected. Changes in interfacial water orientation as a consequence of counterions accumulating in proximity of the charged surface further support this picture and indicate a rearrangement of the water H-bond network caused by the Na^+ ions. This rearrangement

occurs already for small amounts of counterions present in solution (below 50 μM added Na^+). Regions of equivalent behavior are observed for TiO_2 particles in varying basic pH conditions. Comparing TiO_2 and the SiO_2 particles as a function of NaCl concentration show that the TiO_2 surface has a higher affinity to adsorb Na^+ ions than SiO_2. These findings are in line with data obtained by MD simulations of the rutile and quartz surfaces interacting with aqueous solutions, where the rate of change of the integrated dipole with increasing Na^+ adsorption at the surface is faster for TiO_2 than for SiO_2.

Overall, these results pave the way to a better understanding of processes taking place at the surface of semiconductor nanoparticles in solution. In particular, they highlight the potential of AR-SHS to monitor ion adsorption at the surface, changes in the surface effective charge, and general interfacial properties in a variety of (photo)catalytic applications.

Acknowledgments

This work was supported by the Swiss National Science Foundation (Ambizione grant number PZ00P2_174146 to A.M.), the Julia Jacobi Foundation and by the Czech Science Foundation (project 17-10734S to D.B. and M.P.).

References

(1) Memming, R. *Semiconductor Electrochemistry*, 2nd ed.; WILEY-VCH: Weinheim, 2015. https://doi.org/10.1002/9783527688685.

(2) Sharon, M. *An Introduction to the Physics and Electrochemistry of Semiconductors: Fundamentals and Applications*; Scrivener Publishing LLC, John Wiley & Sons, Inc.: Beverly ,Hoboken, 2016. https://doi.org/10.1002/9781119274360.

(3) *Nanomaterial: Impacts on Cell Biology and Medicine*; Capco, D. G., Chen, Y., Eds.; Advances in Experimental Medicine and Biology; Springer: New York, 2014. https://doi.org/10.1007/978-94-017-8739-0.

(4) *Application of Titanium Dioxide*; Janus, M., Ed.; InTech: Rijeka, 2017. https://doi.org/10.5772/intechopen.70121.

(5) Braun, J. H.; Baidins, A.; Marganski, R. E. TiO_2 Pigment Technology: A Review. *Prog. Org. Coat.* **1992**, *20* (2), 105–138. https://doi.org/10.1016/0033-0655(92)80001-D.

(6) Banerjee, A. N. The Design, Fabrication, and Photocatalytic Utility of Nanostructured Semiconductors: Focus on TiO_2-Based Nanostructures. *Nanotechnol. Sci. Appl.* **2011**, *4*, 35–65. https://doi.org/10.2147/NSA.S9040.

(7) Fujishima, F. TiO_2 Photocatalysis Fundamentals and Applications. *Revolut. Clean. Technol.* **1999**, 14–21.

(8) *Application of Nanotechnology in Membranes for Water Treatment*, 1st ed.; Figoli, A., Hoinkis, J., Altinkaya, S. A., Bundschuh, J., Eds.; CRC Press: Boca Raton, 2017.

(9) Milošević, I.; Rtimi, S.; Jayaprakash, A.; van Driel, B.; Greenwood, B.; Aimable, A.; Senna, M.; Bowen, P. Synthesis and Characterization of Fluorinated Anatase Nanoparticles and Subsequent N-Doping for Efficient Visible Light Activated Photocatalysis. *Colloids Surf. B Biointerfaces* **2018**, *171*, 445–450. https://doi.org/10.1016/j.colsurfb.2018.07.035.

(10) Náfrádi, B.; Náfrádi, G.; Martin-Hamka, C.; Forró, L.; Horváth, E. Superior Water Sheeting Effect on Photocatalytic Titania Nanowire Coated Glass. *Langmuir* **2017**, *33* (36), 9043–9049. https://doi.org/10.1021/acs.langmuir.7b01790.

(11) *Application of Titanium Dioxide Photocatalysis to Construction Materials: State-of-the-Art Report of the RILEM Technical Committee 194-TDP*; Ohama, Y., van Gemert, D., Eds.; RILEM state of the art reports; Springer: Dordrecht, 2011.

(12) *Photoelectrochemical Hydrogen Production*; van de Krol, R., Grätzel, M., Eds.; Electronic Materials: Science & Technology; Springer: New York, 2012.

(13) Bagotsk̆iĭ, V. S.; Skundin, A. M.; Volfkovich, Y. V. *Electrochemical Power Sources: Batteries, Fuel Cells, and Supercapacitors*; John Wiley & Sons, Inc.: Hoboken, New Jersey, 2015.

(14) Fujishima, A.; Honda, K. Electrochemical Photolysis of Water at a Semiconductor Electrode. *Nature* **1972**, *238*, 37–38.

(15) Ohshima, H. *Theory of Colloid and Interfacial Electric Phenomena*; Interface Science and Technology; Elsevier, Academic Press: Amsterdam, 2006; Vol. 12.

(16) Hiemenz, P. C.; Rajagopalan, R. *Principles of Colloid and Surface Chemistry*, 3rd ed.; Marcel Dekker: New York, 1997.

(17) Hunter, R. J. *Zeta Potential in Colloid Science. Principles and Applications*; Academic Press: London, 1981.

(18) Hunter, R. J. *Foundations of Colloid Science*, 2nd ed.; Oxford University Press: Oxford, 2000.

(19) *Fundamentals of Interface and Colloid Science*; Lyklema, J., Ed.; Academic Press: London, 2005; Vol. 5. https://doi.org/10.1016/S1874-5679(05)80019-4.

(20) Schmickler, W.; Santos, E. *Interfacial Electrochemistry*, 2nd ed.; Springer: Berlin, Heidelberg, 2010.

(21) Ataka, K.; Yotsuyanagi, T.; Osawa, M. Potential-Dependent Reorientation of Water Molecules at an Electrode/Electrolyte Interface Studied by Surface-Enhanced Infrared Absorption Spectroscopy. *J. Phys. Chem.* **1996**, *100* (25), 10664–10672. https://doi.org/10.1021/jp953636z.

(22) Bockris, J. O.; Khan, S. U. M. *Surface Electrochemistry: A Molecular Level Approach*; Springer Science & Business Media: Berlin, Heidelberg, 2013.

(23) Lange, E.; Miščenko, K. P. Zur Thermodynamik Der Ionensolvatation. *Ztg. Für Phys. Chem. A* **1930**, *149*.

(24) YazdanYar, A.; Aschauer, U.; Bowen, P. Interaction of Biologically Relevant Ions and Organic Molecules with Titanium Oxide (Rutile) Surfaces: A Review on Molecular Dynamics Studies. *Colloids Surf. B Biointerfaces* **2018**, *161*, 563–577. https://doi.org/10.1016/j.colsurfb.2017.11.004.

(25) Fedkin, M. V.; Zhou, X. Y.; Kubicki, J. D.; Bandura, A. V.; Lvov, S. N.; Machesky, M. L.; Wesolowski, D. J. High Temperature Microelectrophoresis Studies of the Rutile/Aqueous Solution Interface. *Langmuir* **2003**, *19* (9), 3797–3804. https://doi.org/10.1021/la0268653.

(26) Předota, M.; Machesky, M. L.; Wesolowski, D. J. Molecular Origins of the Zeta Potential. *Langmuir* **2016**, *32* (40), 10189–10198. https://doi.org/10.1021/acs.langmuir.6b02493.

(27) Lützenkirchen, J.; Preočanin, T.; Kovačević, D.; Tomišić, V.; Lövgren, L.; Kallay, N. Potentiometric Titrations as a Tool for Surface Charge Determination. *Croat. Chem. Acta* **2012**, *85* (4), 391–417. https://doi.org/10.5562/cca2062.

(28) Holmberg, J. P.; Ahlberg, E.; Bergenholtz, J.; Hassellöv, M.; Abbas, Z. Surface Charge and Interfacial Potential of Titanium Dioxide Nanoparticles: Experimental and Theoretical Investigations. *J. Colloid Interface Sci.* **2013**, *407*, 168–176. https://doi.org/10.1016/j.jcis.2013.06.015.

(29) Machesky, M. L.; Wesolowski, D. J.; Palmer, D. A.; Ichiro-Hayashi, K. Potentiometric Titrations of Rutile Suspensions to 250°C. *J. Colloid Interface Sci.* **1998**, *200* (2), 298–309. https://doi.org/10.1006/jcis.1997.5401.

(30) Akratopulu, K. Ch.; Kordulis, C.; Lycourghiotis, A. Effect of Temperature on the Point of Zero Charge and Surface Charge of TiO_2. *J. Chem. Soc. Faraday Trans.* **1990**, *86* (20), 3437. https://doi.org/10.1039/ft9908603437.

(31) Yates, D. E. *The Structure of the Oxide/Aqueous Electrolyte Interface*; PhD Dissertation. Faculty of Science. Chemistry. University Melbourne, 1975.

(32) Nonnenmacher, M.; O'Boyle, M. P.; Wickramasinghe, H. K. Kelvin Probe Force Microscopy. *Appl. Phys. Lett.* **1991**, *58*, 2921–2923.

(33) Umeda, K.; Kobayashi, K.; Oyabu, N.; Hirata, Y.; Matsushige, K.; Yamada, H. Practical Aspects of Kelvin-Probe Force Microscopy at Solid/Liquid Interfaces in Various Liquid Media. *J. Appl. Phys.* **2014**, *116* (13), 134307. https://doi.org/10.1063/1.4896881.

(34) Collins, L.; Jesse, S.; Kilpatrick, J. I.; Tselev, A.; Okatan, M. B.; Kalinin, S. V.; Rodriguez, B. J. Kelvin Probe Force Microscopy in Liquid Using Electrochemical Force Microscopy. *Beilstein J. Nanotechnol.* **2015**, *6*, 201–214. https://doi.org/10.3762/bjnano.6.19.

(35) Brown, M. A.; Abbas, Z.; Kleibert, A.; Green, R. G.; Goel, A.; May, S.; Squires, T. M. Determination of Surface Potential and Electrical Double-Layer Structure at the Aqueous Electrolyte-Nanoparticle Interface. *Phys. Rev. X* **2016**, *6* (1), 011007. https://doi.org/10.1103/PhysRevX.6.011007.

(36) Brown, M. A.; Goel, A.; Abbas, Z. Effect of Electrolyte Concentration on the Stern Layer Thickness at a Charged Interface. *Angew. Chem. Int. Ed.* **2016**, *55* (11), 3790–3794. https://doi.org/10.1002/anie.201512025.

(37) Brown, M. A.; Beloqui Redondo, A.; Sterrer, M.; Winter, B.; Pacchioni, G.; Abbas, Z.; van Bokhoven, J. A. Measure of Surface Potential at the Aqueous–Oxide Nanoparticle Interface by XPS from a Liquid Microjet. *Nano Lett.* **2013**, *13* (11), 5403–5407. https://doi.org/10.1021/nl402957y.

(38) Brown, M. A.; Jordan, I.; Beloqui Redondo, A.; Kleibert, A.; Wörner, H. J.; van Bokhoven, J. A. In Situ Photoelectron Spectroscopy at the Liquid/Nanoparticle Interface. *Surf. Sci.* **2013**, *610*, 1–6. https://doi.org/10.1016/j.susc.2013.01.012.

(39) Makowski, M. J.; Galhenage, R. P.; Langford, J.; Hemminger, J. C. Liquid-Jet X-Ray Photoelectron Spectra of TiO_2 Nanoparticles in an Aqueous Electrolyte Solution. *J. Phys. Chem. Lett.* **2016**, *7* (9), 1732–1735. https://doi.org/10.1021/acs.jpclett.6b00445.

(40) Ali, H.; Seidel, R.; Bergmann, A.; Winter, B. Electronic Structure of Aqueous-Phase Anatase Titanium Dioxide Nanoparticles Probed by Liquid Jet Photoelectron Spectroscopy. *J. Mater. Chem. A* **2019**, *7* (12), 6665–6675. https://doi.org/10.1039/C8TA09414D.

(41) Shen, Y. R. Surfaces Probed by Nonlinear Optics. *Surf. Sci.* **1994**, *299–300*, 551–562. https://doi.org/10.1016/0039-6028(94)90681-5.

(42) Shen, Y. R. Surface Properties Probed by Second-Harmonic and Sum-Frequency Generation. *Nature* **1989**, *337* (6207), 519–525. https://doi.org/10.1038/337519a0.

(43) Wang, C. C. Second-Harmonic Generation of Light at the Boudary of an Isotropic Medium. *Phys. Rev.* **1969**, *178*, 1457–1461.

(44) Boyd, R. *Nonlinear Optics*, 3rd ed.; Academic Press, Elsevier Science: Amsterdam, 2008.

(45) Wang, H.; Yan, E. C. Y.; Borguet, E.; Eisenthal, K. B. Second Harmonic Generation from the Surface of Centrosymmetric Particles in Bulk Solution. *Chem. Phys. Lett.* **1996**, *259* (1), 15–20. https://doi.org/10.1016/0009-2614(96)00707-5.

(46) Liu, Y.; Dadap, J. I.; Zimdars, D.; Eisenthal, K. B. Study of Interfacial Charge-Transfer Complex on TiO_2 Particles in Aqueous Suspension by Second-Harmonic Generation. *J. Phys. Chem. B* **1999**, *103* (13), 2480–2486. https://doi.org/10.1021/jp984288e.

(47) Yan, E. C. Y.; Liu, Y.; Eisenthal, K. B. New Method for Determination of Surface Potential of Microscopic Particles by Second Harmonic Generation. *J. Phys. Chem. B* **1998**, *102*, 6331–6336.

(48) Yang, N.; Angerer, W. E.; Yodh, A. G. Angle-Resolved Second-Harmonic Light Scattering from Colloidal Particles. *Phys. Rev. Lett.* **2001**, *87*, 103902.

(49) Dadap, J. I.; de Aguiar, H. B.; Roke, S. Nonlinear Light Scattering from Clusters and Single Sparticles. *J. Chem. Phys.* **2009**, *130*, 214710.

(50) de Beer, A. G. F.; Roke, S.; Dadap, J. I. Theory of Optical Second-Harmonic and Sum-Frequency Scattering from Arbitrarily Shaped Particles. *J. Opt. Soc. Am. B* **2011**, *28*, 1374–1384.

(51) de Beer, A.; Kramer Campen, R.; Roke, S. Separating Surface Structure and Surface Change with Second-Harmonic and Sum-Frequency Scattering. *Phys. Rev. B* **2010**, *82*, 235431.

(52) Gonella, G.; Lütgebaucks, C.; de Beer, A. G. F.; Roke, S. Second Harmonic and Sum-Frequency Generation from Aqueous Interfaces Is Modulated by Interference. *J. Phys. Chem. C* **2016**, *120* (17), 9165–9173. https://doi.org/10.1021/acs.jpcc.5b12453.

(53) Lütgebaucks, C.; Gonella, G.; Roke, S. Optical Label-Free and Model-Free Probe of the Surface Potential of Nanoscale and Microscopic Objects in Aqueous Solution. *Phys. Rev. B* **2016**, *94* (19). https://doi.org/10.1103/PhysRevB.94.195410.

(54) Lütgebaucks, C.; Macias-Romero, C.; Roke, S. Characterization of the Interface of Binary Mixed DOPC:DOPS Liposomes in Water: The Impact of Charge Condensation. *J. Chem. Phys.* **2017**, *146*, 044701.

(55) Marchioro, A.; Bischoff, M.; Lütgebaucks, C.; Biriukov, D.; Předota, M.; Roke, S. Surface Characterization of Colloidal Silica Nanoparticles by Second Harmonic Scattering: Quantifying the Surface Potential and Interfacial Water Order. *J. Phys. Chem. C* **2019**, *123* (33), 20393–20404. https://doi.org/10.1021/acs.jpcc.9b05482.

(56) *Electrochemical Dictionary*, 2nd ed.; Bard, A. J., Inzelt, G., Scholz, F., Eds.; Springer: Heidelberg, 2012.

(57) Lide, D. R. *Handbook of Chemistry and Physics*, 84th ed.; CRC Press: Boca Raton, 2004.

(58) Roke, S.; Bonn, M.; Petukhov, A. V. Nonlinear Optical Scattering: The Concept of Effective Susceptibility. *Phys. Rev. B* **2004**, *70* (11). https://doi.org/10.1103/PhysRevB.70.115106.

(59) de Beer, A. G. F.; Roke, S. Obtaining Molecular Orientation from Second Harmonic and Sum Frequency Scattering Experiments in Water: Angular Distribution and Polarization Dependence. *J. Chem. Phys.* **2010**, *132* (23), 234702. https://doi.org/10.1063/1.3429969.

(60) Gomopoulos, N.; Lütgebaucks, C.; Sun, Q.; Macias-Romero, C.; Roke, S. Label-Free Second Harmonic and Hyper Rayleigh Scattering with High Efficiency. *Opt. Express* **2013**, *21* (1), 815. https://doi.org/10.1364/OE.21.000815.

(61) Nihonyanagi, S.; Yamaguchi, S.; Tahara, T. Direct Evidence for Orientational Flip-Flop of Water Molecules at Charged Interfaces: A Heterodyne-Detected Vibrational Sum Frequency Generation Study. *J. Chem. Phys.* **2009**, *130* (20), 204704. https://doi.org/10.1063/1.3135147.

(62) Hale, G. M.; Querry, M. R. Optical Constants of Water in the 200nm to 200μm Wavelength Region. *Appl. Opt.* **1973**, *12*, 555–563.

(63) Martin, P. Review of the Filtered Vacuum Arc Process and Materials Deposition. *Thin Solid Films* **2001**, *394* (1–2), 1–14. https://doi.org/10.1016/S0040-6090(01)01169-5.

(64) Malitson, I. H. Interspecimen Comparison of the Refractive Index of Fused Silica. *J. Opt. Soc. Am. B* **1965**, *55* (10), 1205–1209. https://doi.org/10.1364/JOSA.55.001205.

(65) Biriukov, D.; Kroutil, O.; Předota, M. Modeling of Solid–Liquid Interfaces Using Scaled Charges: Rutile (110) Surfaces. *Phys. Chem. Chem. Phys.* **2018**, *20* (37), 23954–23966. https://doi.org/10.1039/C8CP04535F.

(66) Kroutil, O.; Chval, Z.; Skelton, A. A.; Předota, M. Computer Simulations of Quartz (101)–Water Interface over a Range of PH Values. *J. Phys. Chem. C* **2015**, *119* (17), 9274–9286. https://doi.org/10.1021/acs.jpcc.5b00096.

(67) Berendsen, H. J. C.; Grigera, J. R.; Straatsma, T. P. The Missing Term in Effective Pair Potentials. *J. Phys. Chem.* **1987**, *91* (24), 6269–6271. https://doi.org/10.1021/j100308a038.

(68) Kohagen, M.; Mason, P. E.; Jungwirth, P. Accounting for Electronic Polarization Effects in Aqueous Sodium Chloride via Molecular Dynamics Aided by Neutron Scattering. *J. Phys. Chem. B* **2016**, *120* (8), 1454–1460. https://doi.org/10.1021/acs.jpcb.5b05221.

(69) Leontyev, I.; Stuchebrukhov, A. Accounting for Electronic Polarization in Non-Polarizable Force Fields. *Phys. Chem. Chem. Phys.* **2011**, *13* (7), 2613–2626. https://doi.org/10.1039/C0CP01971B.

(70) Zeta Potential - An Introduction in 30 Minutes. Malvern Instruments.

(71) Mueller, R.; Kammler, H. K.; Wegner, K.; Pratsinis, S. E. OH Surface Density of SiO_2 and TiO_2 by Thermogravimetric Analysis. *Langmuir* **2003**, *19* (1), 160–165.

(72) Zhuravlev, L. T. Concentration of Hydroxyl Groups on the Surface of Amorphous Silicas. *Langmuir* **1987**, *3* (3), 316–318. https://doi.org/10.1021/la00075a004.

TOC graphic

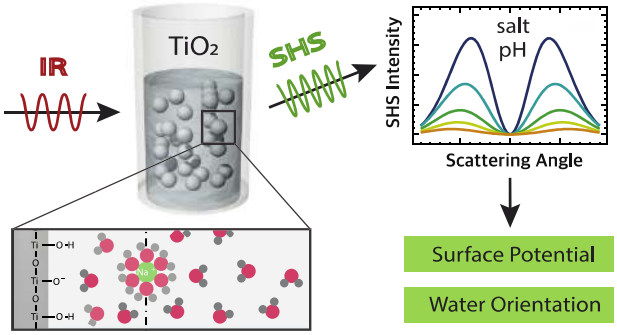
IR
TiO2
SHS
SHS Intensity
salt
pH
Scattering Angle
Surface Potential
Water Orientation

Table 1: Surface potential Φ_0 and surface susceptibility $C_{S,2}^{(2)}$ values that were obtained by fitting the AR-SHS patterns of ~100 nm diameter amorphous TiO_2 nanoparticles in aqueous solutions for different NaCl concentrations. The radius *R* was measured by DLS and the zeta potential ζ was obtained from electrophoretic mobility measurements.

added NaCl [μM]	R [nm]	ζ [mV]	Φ_0 [mV]	$\chi_{s,2}^{(2)}$ [$10^{-24}\frac{\mathrm{m}^2}{\mathrm{V}}$]
0	59 ± 21	-24 ± 21	-182 ± 13	-8.1 ± 0.4
10	60 ± 19	-27 ± 20	-57 ± 23	-39.6 ± 0.5
50	60 ± 19	-25 ± 17	-12 ± 19	46.1 ± 2.7
100	60 ± 15	-26 ± 20	-57 ± 40	45.3 ± 6.9
300	59 ± 28	-30 ± 22	-326 ± 163	94.1 ± 16.3

Table 2: Surface potential Φ_0 and surface susceptibility $C_{S,2}^{(2)}$ values obtained from fitting the AR-SHS patterns of 100 nm diameter amorphous TiO_2 nanoparticles in aqueous solutions of different pH. The pH was adjusted through NaOH addition. The radius *R* was measured by DLS and the zeta potential ζ was obtained from electrophoretic mobility measurements.

pH	R [nm]	ζ [mV]	Φ_0 [mV]	$\chi_{s,2}^{(2)}$ [$10^{-24}\frac{\mathrm{m}^2}{\mathrm{V}}$]
7	63 ± 17	-27 ± 19	-138 ± 15	-18.1 ± 0.5
9.5	63 ± 14	-32 ± 19	-47 ± 48	-32.3 ± 4.6
10.7	59 ± 19	-34 ± 22	-137 ± 91	66.2 ± 31.9

Table 3: Surface potential Φ_0 and surface susceptibility $C_{S,2}^{(2)}$ values obtained from fitting the AR-SHS patterns of ~100 nm diameter SiO_2 nanoparticles in aqueous solutions of different NaCl concentrations. The radius *R* was measured by DLS and the zeta potential ζ was obtained from electrophoretic mobility measurements.

added NaCl [μM]	R [nm]	ζ [mV]	Φ_0 [mV]	$\chi_{s,2}^{(2)}$ [$10^{-24}\frac{\mathrm{m}^2}{\mathrm{V}}$]
0	65 ± 12	-48 ± 31	-163 ± 5	-2.2 ± 0.1
10	64 ± 11	-41 ± 22	-130 ± 5	-2.8 ± 0.08
50	62 ± 7	-36 ± 24	-92 ± 7	-3.2 ± 0.08
100	61 ± 7	-35 ± 23	-54 ± 15	-3.4 ± 0.01
300	60 ± 5	-32 ± 23	-19 ± 50	3.9 ± 0.7
600	58 ± 5	-34 ± 26	-430 ± 90	9.1 ± 0.7

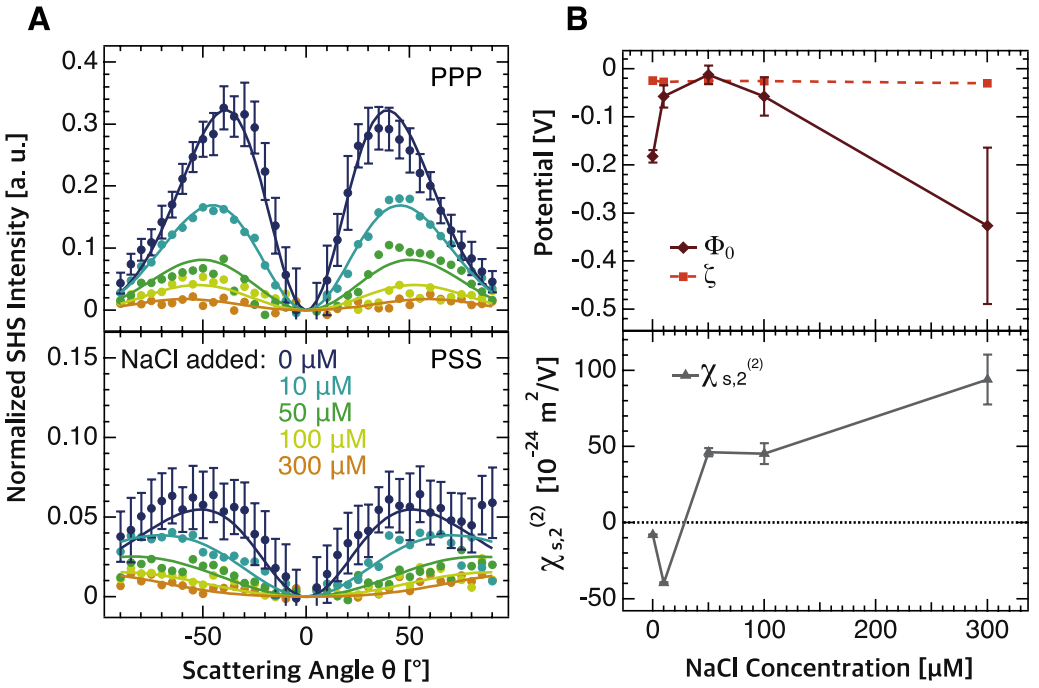

Figure 1: (A) AR-SHS patterns of amorphous ~100 nm diameter TiO_2 particles as a function of ionic strength in PPP polarization combination (top) and PSS polarization combination (bottom). Plain data points of different colors represent different salt concentrations of the aqueous environment. The ionic strength was adjusted through NaCl addition. The particle density was kept constant for each sample and equal to $4.3 \cdot 10^{11}$ particles/ml. All measurements were performed at T = 296.15 K. Solid lines represent the fits to the corresponding data points using the AR-SHS model. A summary of all the parameters used for the fits can be found in Tables S3 and S5. **(B)** Surface potential Φ_0 (dark red diamonds) and surface susceptibility $C_{S,2}^{(2)}$ (grey triangles) as a function of ionic strength. Φ_0 and $C_{S,2}^{(2)}$ were obtained by fitting the corresponding AR-SHS patterns of ~100 nm diameter amorphous TiO_2 particles in solution in PPP and PSS polarization combination (see (a)). The light red squares represent the zeta potential ζ values measured for the different ionic strength conditions using electrophoretic mobility measurements.

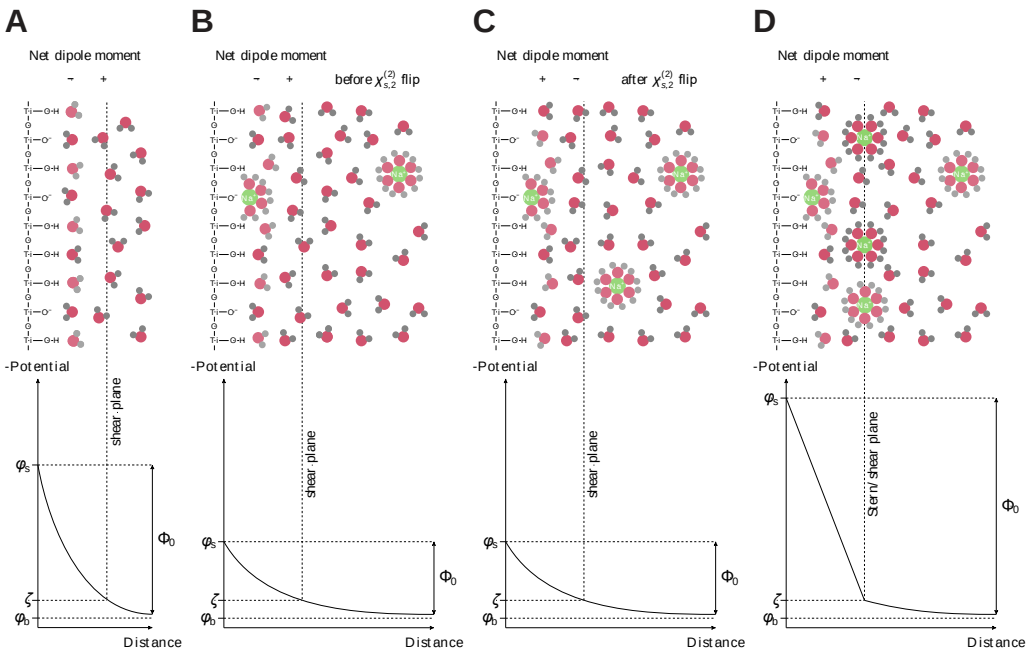

Figure 2: The EDL around a TiO_2 particle surface and the corresponding surface potential Φ_0 and zeta potential ζ over the distance to the surface with **(A)** No added salt, and **(B)** Under very low ionic strength, **(C)** Low ionic strength and **(D)** High ionic strength conditions. The particle surface is approximated to a flat surface for clarity and no anions are displayed. The mean orientation of water molecules in direct proximity of the slightly deprotonated surface is given by the net dipole moment pointing away or towards the surface, reflecting average water orientation with the hydrogens away (**(A)** and **(B)**) or towards (**(C)** and **(D)**) the surface. Scheme **(B)** displays the direction of the net dipole moment before the sign of the surface susceptibility $\chi^{(2)}_{S,2}$ flips to positive values, while scheme **(C)** shows the net dipole moment after the $\chi^{(2)}_{S,2}$ flip. The surface potential Φ_0 is the potential difference between the potential at the surface of the particle Φ_S and the potential of the bulk solution Φ_b. Note that this schematic illustration shows the magnitudes of the before mentioned potentials. ζ is the potential at the shear plane. In this simplistic scheme, the Stern plane is approximated to be equal to the shear plane in the high ionic strength situation where a condensed layer of counterions is formed in **(D)**.

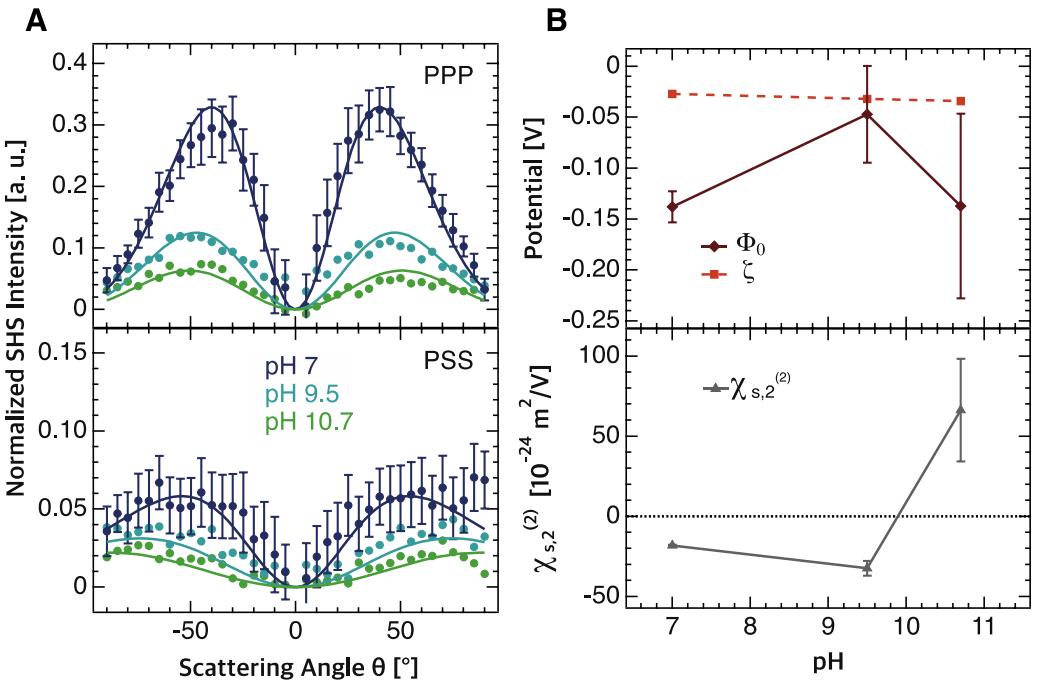

Figure 3: (A) AR-SHS patterns of amorphous 100 nm diameter TiO_2 particles in solutions of different pH in PPP polarization combination (top) and PSS polarization combination (bottom). Plain data points of different colors represent different pH conditions of the aqueous environment. For pHs above 7, the pH was adjusted through NaOH addition. The particle density was kept constant for each sample and equal to $4.3 \cdot 10^{11}$ particles/ml. All measurements were performed at T = 296.15 K. Solid lines represent the fits to the corresponding data points using the AR-SHS model. A summary of all the parameters used for the fits can be found in Tables S3 and S6. **(B)** Surface potential Φ_0 (dark red diamonds) and surface susceptibility $\chi_{S,2}^{(2)}$ (grey triangles) as a function of pH as they were obtained by fitting the corresponding AR-SHS patterns of 100 nm diameter amorphous TiO_2 particles in solution in PPP and PSS polarization combination (see Figures 2). The light red squares represent the zeta potential-values ζ that were measured for the different pH conditions of the aqueous environment using electrophoretic mobility measurements.

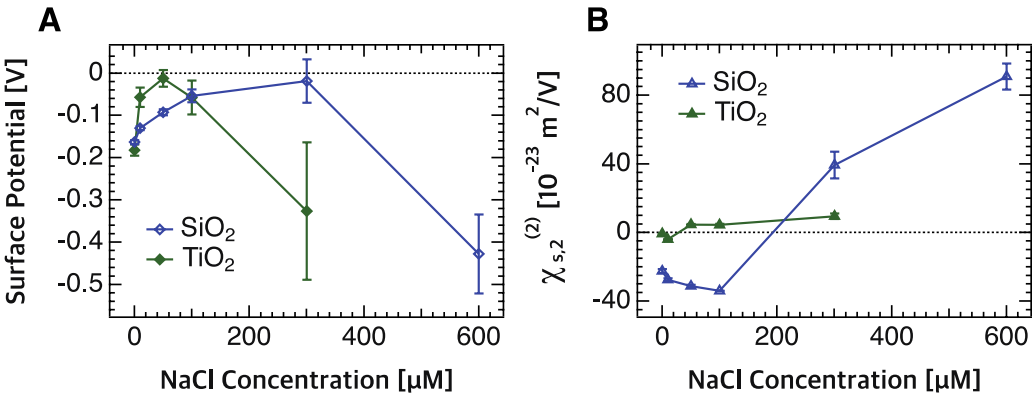

Figure 4: (A) Surface potential Φ_0 and **(B)** surface susceptibility $C_{S,2}^{(2)}$ of ~100 nm diameter SiO_2 particles and ~100 nm diameter amorphous TiO_2 particles as a function of ionic strength. The ionic strength was adjusted through NaCl addition. The particle density was kept constant and equal to $2.9 \cdot 10^{11}$ particles/ml for the SiO_2 and equal to $4.3 \cdot 10^{11}$ particles/ml for the TiO_2 samples. All measurements were performed at T = 296.15 K and pH=7. Dark blue open diamonds and triangles represent the SiO_2 samples and dark green diamonds and triangles represent the TiO_2 particles in aqueous environment. A summary of all the parameters used for the fits through which Φ_0 and $C_{S,2}^{(2)}$ were extracted can be found in Tables S3, S4, S5 and S7.

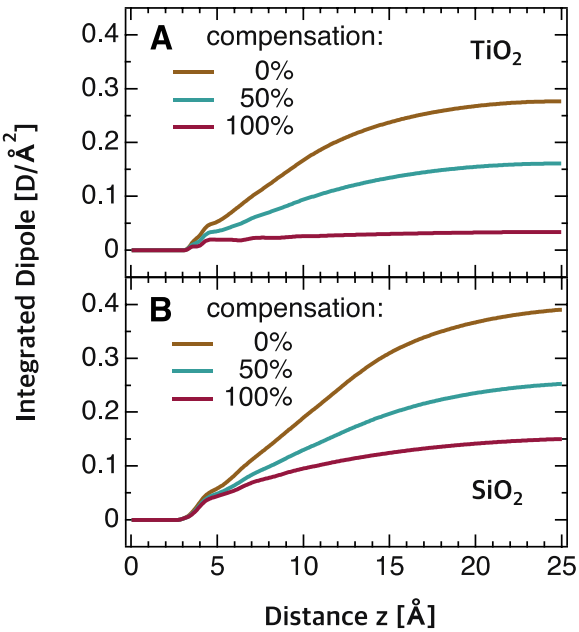

Figure 5: Integrated dipole as a function of distance from negatively charged (**A)** (110) rutile (-0.104 C/m^2) and (**B**) (101) quartz (-0.12 C/m^2) surfaces. The brown line represents simulations allowing 0% compensation of the surface charge (i.e. all the counterions were forced to be at least 10 Å away from the surface), the turquois line represents 50% compensation (only half of the ions were allowed in the region up to 10 Å from the surface), and the purple line is from simulations allowing 100% compensation (no restriction on the positions of ions).

Surface Potential and Interfacial Water Order at the Amorphous TiO_2 Nanoparticle/Aqueous Interface

Marie Bischoff[1], Denys Biriukov[2], Milan Předota[2], Sylvie Roke[1]* and Arianna Marchioro[1]*

[1] *Laboratory for fundamental BioPhotonics (LBP), Institute of Bioengineering (IBI), and Institute of Materials Science (IMX), School of Engineering (STI), École polytechnique fédérale de Lausanne (EPFL), CH-1015 Lausanne, Switzerland.*

[*] *E-mail : arianna.marchioro@epfl.ch, sylvie.roke@epfl.ch*

[2] *Institute of Physics, Faculty of Science, University of South Bohemia, 370 05 České Budějovice, Czech Republic*

Supplementary Information

AR-SHS model and theory – relevant constants, analytical expressions and assumptions

The geometrical form factor functions for spheres, as they are shown in Table S1 can also be found in Refs.[1,2] They depend on the radius of the particles R and the scattering vector |**q**| = q. The third form factor also depends on the inverse Debye length κ and therefore the ionic strength of the solvent. The Debye length is defined as $k^{-1} = \sqrt{(\varepsilon_0 \varepsilon_r k_B T)/(2000 e^2 z^2 N_{Av} c)}$ and takes into account the vacuum and relative permittivity ε_0 and ε_r respectively, the Bolzmann constant k_B, the temperature T, the elementary charge *e*, the valency z, Avogadro's number N_{Av} and the ionic concentration *c*. The constants used to calculate the scattered intensity from spherical particles in equations 4 and 5 are the dipole moment of water μ_{DC}, and the hyperpolarizability tensor elements of water $\overline{b}^{(2)}$ and $\overline{b}^{(3)}$. The values of the hyperpolarizability tensor elements were computed from an ab-initio model (using 1064 incoming light, Table 4, Model IIIa, of Ref. [3]). Although there are 3 $\beta^{(2)}$ or 6 $\beta^{(3)}$ nonzero hyperpolarizability tensor elements for a single water molecule, a single mean value can be obtained by averaging over many water molecules in an isotropic liquid, here indicated as $\overline{b}^{(2)}$ and $\overline{b}^{(3)}$.

Table S2 summarizes some important equalities as well as the surface and effective particle susceptibility elements needed to compute the second harmonic scattering intensity from spherical particles in solution. The non-zero second- and third-order susceptibility elements $c_{s,1}^{(2)}$, $c_{s,2}^{(2)}$ and $c_2^{(3)'}$ are corrected for changes in the refractive index occurring at the particle/liquid interface following Refs.[4,5] so that dispersion can be neglected. It was found in previous studies that a linear correction term as proposed by Dadap et al.[5] is sufficient to correct for the changes in the orthogonal coordinate of the electromagnetic field when it crosses the particle/liquid interface.[6] The corrected susceptibility elements $c_{s,1}^{(2)"}$, $c_{s,2}^{(2)"}$ and $c_2^{(3)"}$ are than inserted into the analytical expressions for the non-zero effective particle susceptibility elements $G_1^{(2)}$, $G_2^{(2)}$ and $G_2^{(3)'}$ needed to calculate the scattering intensity in equations 4 and 5. The effective particle susceptibilities represent the combined symmetry of the incoming electromagnetic fields, the geometry of the scatterers (here: spherical), the interfacial structure and the electrostatic field in the aqueous phase. Note that the scattering intensity equations 4 and

5 are only valid under the assumption that dispersion from the difference in the refractive indices of the particles (n_p) and the liquid (n_{H2O}) can be neglected and that no multiple scattering events occur. Dynamic light scattering experiments and second harmonic scattering experiments as a function of particle concentration (not shown here) proved that the intensity scales linearly with the particle concentration ensuring that those assumptions hold. The expressions for the surface and effective particle susceptibilities, presented in Table S2, are derived using five commonly used assumptions [7] that are related to the optical properties of isotropic materials and their behavior in nonresonant second harmonic scattering experiments:

1. The liquids can be considered as spatially isotropic reducing the number of possible 81 elements (considering a loss-less medium and that the electric fields are real) of the $\chi^{(3)'}$ and $\Gamma^{(3)'}$ tensors to only 4 remaining non-zero elements (Ref. [7] page 53).
2. Applying that the material is loss-less and that the electric fields are real, reduces the amount of possible elements for $\chi^{(2)}$ and $\Gamma^{(2)}$ to 27. As the particle interface can be considered as isotropic in the interfacial plane, meaning that tangential coordinates are interchangeable, the number of non-zero elements reduces to 4 elements for $\chi_s^{(2)}$ and $\Gamma^{(2)}$.
3. Assuming the absence of dispersion due to the probing being off-resonant, three of the four tensor elements of $\chi_s^{(2)}$ ($\Gamma^{(2)}$) and $\chi^{(3)'}$ ($\Gamma^{(3)'}$) are equal to one another ($\chi_{s,2}^{(2)} = \chi_{s,3}^{(2)} = \chi_{s,4}^{(2)}$ and $\chi_2^{(3)'} = \chi_3^{(3)'} = \chi_4^{(3)'}$) so that only two independent tensor elements remain. Those are $\chi_{s,1}^{(2)}$ and $\chi_{s,2}^{(2)}$, and $\chi_1^{(3)'}$ and $\chi_2^{(3)'}$ respectively. This assumption was verified by confirming that the polarization combinations PSS and SPS (or SSP) generate the same SHS response within experimental uncertainty. Mind that SPS and SSP are the same in SHS as we are using a single incoming frequency $\omega_1 = \omega_2 = \omega$ which makes the last two indices interchangeable.
4. Additionally, the element $\chi_1^{(3)'}$ is equal to zero due to symmetry properties of the third-order susceptibility tensor of an isotropic medium (namely

$\chi_1^{(3)'} = \chi_{\perp\perp\perp,\perp}^{(3)'} - \chi_{\parallel\parallel\perp,\perp}^{(3)'} - \chi_{\parallel\perp\parallel,\perp}^{(3)'} - \chi_{\perp\parallel\parallel,\perp}^{(3)'} = 0$).[8,9] Thus also $G_1^{(3)'} = 0$ (Ref. [2]).

5. We finally assume that $C_{s,1}^{(2)}$ = 0, which is the case for a broad orientational distribution of water molecules at the interface. See Ref. [9] for details.

Table S1: Constants, geometrical form factor functions and scattering vector used for calculating the scattered intensity from spherical particles (equations 4 and 5).

Geometrical form factors
$F_1(qR) = 2\pi R^2 i \left(\frac{\sin(qR)}{(qR)^2} - \frac{\cos(qR)}{qR} \right)$
$F_2(qR) = 4\pi R^2 i \left(3\frac{\sin(qR)}{(qR)^4} - 3\frac{\cos(qR)}{(qR)^3} - \frac{\sin(qR)}{(qR)^2} \right)$
$F_3(\kappa R, qR) = 2\pi R^2 i \frac{qR\cos(qR) + \kappa R \sin(qR)}{(qR)^2 + (\kappa R)^2}$
Scattering vector
$\mathbf{q} \equiv \mathbf{k_0} - 2\mathbf{k_1}, \;\; q = \left\lvert \frac{4\pi n_{\mathrm{H_2O}}}{\lambda_{\mathrm{SH}}} \sin\frac{\theta}{2} \right\rvert$
Constants
$\mu_{DC} = 8.97 \cdot 10^{-30}\,\mathrm{Cm}$
$\bar{\beta}^{(2)} = 3.09 \cdot 10^{-52}\,\mathrm{C^3 m^3 J^{-2}}$
$\bar{\beta}^{(3)} = 4.86 \cdot 10^{-62}\,\mathrm{C^4 m^4 J^{-3}}$

Table S2: Effective particle susceptibilities and surface susceptibility elements and their equalities used for computing the scattering intensity from spherical particles (equations 4 and 5). ⊥ refers to the direction perpendicular to the particle surface and ∥ to the direction parallel to the particle surface. The second- and third-order susceptibility elements are corrected for changes in the refractive index occurring at the particle/liquid interface following Ref. [4,5] so that dispersion can be neglected.

Second-order surface susceptibilities and their equalities
$\chi_{s,1}^{(2)} = \chi_{s,\perp\perp\perp}^{(2)} - \chi_{s,\parallel\parallel\perp}^{(2)} - \chi_{s,\parallel\perp\parallel}^{(2)} - \chi_{s,\perp\parallel\parallel}^{(2)}, \;\; \chi_{s,1}^{(2)} \to 0$
$\chi_{s,2}^{(2)} = \chi_{s,\parallel\parallel\perp}^{(2)}, \;\; \chi_{s,2}^{(2)} = \chi_{s,3}^{(2)} = \chi_{s,4}^{(2)}$
Effective third-order susceptibilities and their equalities
$\chi_1^{(3)'} = \chi_{\perp\perp\perp,\perp}^{(3)'} - \chi_{\parallel\parallel\perp,\perp}^{(3)'} - \chi_{\parallel\perp\parallel,\perp}^{(3)'} - \chi_{\perp\parallel\parallel,\perp}^{(3)'}, \quad \chi_1^{(3)'} = 0$
$\chi_2^{(3)'} = \frac{N_b}{\epsilon_0}\left(\bar{\beta}^{(3)} + \frac{\bar{\beta}^{(2)}\mu_{DC}}{3k_BT}\right) = 10.3 \cdot 10^{-22}\,\mathrm{m^2V^{-2}}, \quad \chi_2^{(3)'} = \chi_3^{(3)'} = \chi_4^{(3)'}$
Corrected surface- and effective third-order susceptibilities
$\chi_{s,1}^{(2)''} = 27\eta\frac{\left(\chi_{s,1}^{(2)}\eta^2 + 3\chi_{s,2}^{(2)}\left(\eta^2-1\right)\right)}{(2+\eta)^3}, \quad \eta = \left(\frac{n_p}{n_{\mathrm{H_2O}}}\right)^2$
$\chi_{s,2}^{(2)''} = 27\eta\frac{\chi_{s,2}^{(2)}}{(2+\eta)^3}$
$\chi_2^{(3)''} = 27\eta\frac{\chi_2^{(3)'}}{(2+\eta)^3}$
Effective particle susceptibilities
$\Gamma_1^{(2)} = \left(2F_1(qR) - 5F_2(qR)\right)\chi_{s,1}^{(2)''}$
$\Gamma_2^{(2)} = F_2(qR)\chi_{s,1}^{(2)''} + 2F_1(qR)\chi_{s,2}^{(2)''}$
$\Gamma_2^{(3)'} = 2\chi_2^{(3)''}\Phi_0\left(F_1(qR) + F_3(qR,\kappa R)\right)$

Experimental parameters used for fitting the AR-SHS patterns

Table S3: Parameters used for fitting the normalized second harmonic scattering patterns applying the AR-SHS model. These parameters are common to all the TiO_2 sets of data presented and fitted.

Second harmonic wavelength λ [nm]	515
Refractive index n_{H_2O} (@ 515 nm)	1.33
Refractive index n_{TiO_2} (@ 515 nm)	2.61
Temperature [°C]	23
Number of particles	$4.26 \cdot 10^{11}$

Table S4: Parameters used for fitting the normalized second harmonic scattering patterns applying the AR-SHS model. These parameters are common to all sets of SiO_2 data presented and fitted.

Second harmonic wavelength λ [nm]	515
Refractive index n_{H_2O} (@ 515 nm)	1.33
Refractive index n_{SiO_2} (@ 515 nm)	1.46
Temperature [°C]	23
Number of particles	$2.91 \cdot 10^{11}$

Table S5: Parameters used for fitting the normalized second harmonic scattering patterns of 100 nm amorphous TiO_2 particles applying the AR-SHS model. The values presented are specifically used for fitting the NaCl concentration series.

added NaCl [μM]	0	10	50	100	300
Radius [nm]	59	60	60	60	59
Ionic strength [μM]	40.4	46.5	91.2	134.7	311. 0

Table S6: Parameters used for fitting the normalized second harmonic scattering patterns of 100 nm amorphous TiO_2 particles applying the AR-SHS model. The values presented are specifically used for fitting the pH series.

pH	7	9.5	10.7
Radius [nm]	63	63	59
Ionic Strength [μM]	39.1	98.0	569.7

Table S7: Parameters used for fitting the normalized second harmonic scattering patterns of 100 nm SiO_2 particles applying the AR-SHS model. The values presented are specifically used for fitting the NaCl concentration series.

added NaCl [μM]	0	10	50	100	300	600
Radius [nm]	65	64	62	61	60	58
Ionic strength [μM]	13.0	23.0	57.5	96.6	288. 0	561. 0

Surface charge densities and deprotonation

From surface charge density values found in the literature[10–13] that were measured by potentiometric titration, we calculated the percentage of deprotonation at pH 7 using an initial density of 4.8 OH/nm^2 as determined for the hydroxylated surface of P25 TiO_2 particles (Degussa) taken from Ref. [14] The radius of the particles was taken as 60 nm, which is close to what was measured in our dynamic light scattering experiments for amorphous TiO_2 particles. We obtain a deprotonation of 1% using the reported surface charge densities of - 0.00763 C/m^2 for 21 nm diameter P25 TiO_2 particles (Degussa) at pH 7.10 by Holmberg et al.,[10] and - 0.00833 C/m^2 for ≈ 72 nm diameter rutile TiO_2 particles (CL/D 528 Tioxide International Limited) at pH 7.13 by Yates.[11] Values up to - 0.06417 C/m^2 have been reported by Machesky et al.[12] for ≈ 83 nm diameter rutile TiO_2 particles (Tioxide Specialities Ltd.) at pH 7.02, which correspond to deprotonation values of 8%. Similar values were reported by Akratopulu et al.[13] for 30 nm diameter P25 TiO_2 particles (Degussa) at pH 6.93 who obtained a surface charge density of - 0.05074 C/m^2 which corresponds to a deprotonation of 7%.

Calculating the percentage of deprotonation in the same way for pH 9.5 by using the reported surface charge densities of - 0.06250 C/m^2 for 21 nm diameter P25 TiO_2 particles (Degussa) at pH 9.3 (Holmberg et al.)[10] and - 0.07431 C/m^2 for ≈ 72 nm rutile TiO_2 particles synthesized at pH 9.6 (Yates)[11] we obtain a deprotonation of 8-10%. Higher deprotonation values, up to 35% are calculated using a surface charge density of - 0.27644 C/m^2 reported at pH 9.4 by Akratopulu et al.[13] for 30 nm diameter P25 TiO_2 particles. Machesky et al.[12] found similar values for the surface charge density of ≈ 83 nm diameter rutile TiO_2 particles at pH 9.63 (- 0.22686 C/m^2) translating into 30% deprotonation. Given the fact that the measurements in Holmberg et al.,[10] Yates,[11] Machesky et al.[12] and Akratopulo et al.[13] were performed at higher ionic strength of 0.1 M $NaNO_3$, 1 mM KNO_3, 0.03M NaCl and 0.1M KNO_3, respectively, the calculated deprotonation values can be regarded as an upper limit for the real deprotonation that we expect for our amorphous TiO_2 particles in the lower ionic strength region.

AR-SHS patterns of 100 nm diameter SiO_2 particles as a function of NaCl concentration

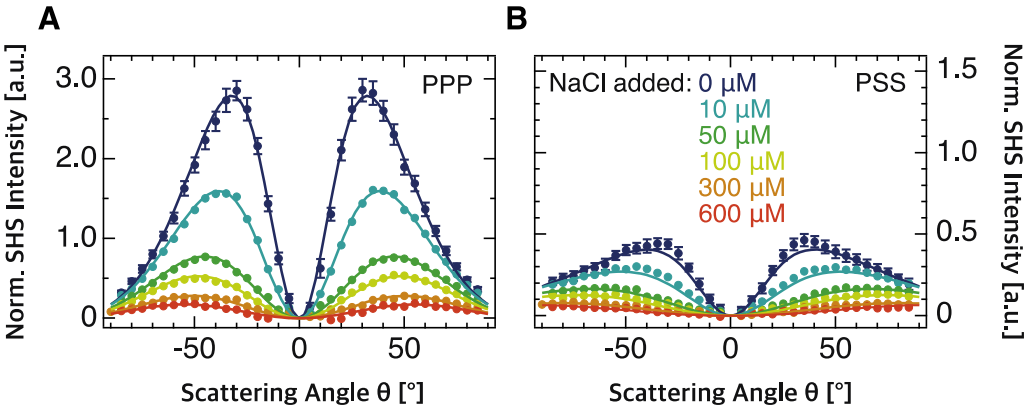

Figure S8: AR-SHS patterns of 100 nm diameter SiO_2 particles as a function of ionic strength in PPP (**A**) and PSS (**B**) polarization combination. Plain data points of different colors represent different salt concentrations of the aqueous environment. The ionic strength was adjusted through NaCl addition. The particle density was kept constant for each sample and equal to $2.9 \cdot 10^{11}$ particles/ml. All measurements were performed at T = 296.15 K. Solid lines represent the fits to the corresponding data points using the AR-SHS model. A summary of all the parameters used for the fits can be found in Tables S4 and S7.

References

(1) de Beer, A. G. F.; Roke, S. Obtaining Molecular Orientation from Second Harmonic and Sum Frequency Scattering Experiments in Water: Angular Distribution and Polarization Dependence. *J. Chem. Phys.* **2010**, *132* (23), 234702. https://doi.org/10.1063/1.3429969.

(2) Gonella, G.; Lütgebaucks, C.; de Beer, A. G. F.; Roke, S. Second Harmonic and Sum-Frequency Generation from Aqueous Interfaces Is Modulated by Interference. *J. Phys. Chem. C* **2016**, *120* (17), 9165–9173. https://doi.org/10.1021/acs.jpcc.5b12453.

(3) Gubskaya, A. V.; Kusalik, P. G. The Multipole Polarizabilities and Hyperpolarizabilities of the Water Molecule in Liquid State: An Ab Initio Study. *Mol. Phys.* **2001**, *99* (13), 1107–1120. https://doi.org/10.1080/00268970110041218.

(4) Dadap, J. I. Second-Harmonic Rayleigh Scattering from a Sphere of Centrosymmetric Material. *Phys. Rev. Lett.* **1999**, *83*, 4045–4048.

(5) Dadap, J. I.; Shan, J.; Heinz, T. F. Theory of Optical Second-Harmonic Generation from a Sphere of Centrosymmetric Material: Small-Particle Limit. *J. Opt. Soc. Am. B* **2004**, *21* (7), 1328. https://doi.org/10.1364/JOSAB.21.001328.

(6) Lütgebaucks, C.; Gonella, G.; Roke, S. Optical Label-Free and Model-Free Probe of the Surface Potential of Nanoscale and Microscopic Objects in Aqueous Solution. *Phys. Rev. B* **2016**, *94*, 195410-1-195410–195416.

(7) Boyd, R. *Nonlinear Optics*, 3rd ed.; Academic Press, Elsevier Science: Amsterdam, 2008.

(8) de Beer, A.; Kramer Campen, R.; Roke, S. Separating Surface Structure and Surface Change with Second-Harmonic and Sum-Frequency Scattering. *Phys. Rev. B* **2010**, *82*, 235431.

(9) de Beer, A. G. F.; Roke, S. What Interactions Can Distort the Orientational Distribution of Interfacial Water Molecules as Probed by Second Harmonic and Sum Frequency Generation? *J. Chem. Phys.* **2016**, *145* (4), 044705. https://doi.org/10.1063/1.4959033.

(10) Holmberg, J. P.; Ahlberg, E.; Bergenholtz, J.; Hassellöv, M.; Abbas, Z. Surface Charge and Interfacial Potential of Titanium Dioxide Nanoparticles: Experimental and Theoretical Investigations. *J. Colloid Interface Sci.* **2013**, *407*, 168–176. https://doi.org/10.1016/j.jcis.2013.06.015.

(11) Yates, D. E. *The Structure of the Oxide/Aqueous Electrolyte Interface*; PhD Dissertation. Faculty of Science. Chemistry. University Melbourne, 1975.

(12) Machesky, M. L.; Wesolowski, D. J.; Palmer, D. A.; Ichiro-Hayashi, K. Potentiometric Titrations of Rutile Suspensions to 250°C. *J. Colloid Interface Sci.* **1998**, *200* (2), 298–309. https://doi.org/10.1006/jcis.1997.5401.

(13) Akratopulu, K. Ch.; Kordulis, C.; Lycourghiotis, A. Effect of Temperature on the Point of Zero Charge and Surface Charge of TiO_2. *J. Chem. Soc. Faraday Trans.* **1990**, *86* (20), 3437. https://doi.org/10.1039/ft9908603437.

(14) Mueller, R.; Kammler, H. K.; Wegner, K.; Pratsinis, S. E. OH Surface Density of SiO_2 and TiO_2 by Thermogravimetric Analysis. *Langmuir* **2003**, *19* (1), 160–165. https://doi.org/10.1021/la025785w.

denysbiriukov@gmail.com

Application of Electronic Continuum Correction to Molecular Simulations of Nano/Bio Interfaces
Ph.D. Thesis Series, 2020, No. 10

Printed in the Czech Republic by Typodesign
Edition of 15 copies

University of South Bohemia in České Budějovice
Faculty of Science
Branišovská 1760
CZ-37005 České Budějovice, Czech Republic
Phone: +420 387 776 201
www.prf.jcu.cz, e-mail: sekret-fpr@prf.jcu.cz